Structural and magnetic properties of V_2O_3-based magnetic heterostructures

Ignatova Kristina

Faculty of Science
University of Iceland
2024

Structural and magnetic properties of V_2O_3-based magnetic heterostructures

Ignatova Kristina

Dissertation submitted in partial fulfillment of a
Philosophiae Doctor degree in Physics

Advisor
Unnar Bjarni Arnalds

PhD Committee
Unnar Bjarni Arnalds
Friðrik Magnus
Gunnar Karl Pálsson

Opponents
Arantxa Fraile Rodríguez
Wolfgang Kuch

Faculty of Science
School of Engineering and Natural Sciences
University of Iceland
Reykjavik, May 2024

Structural and magnetic properties of V_2O_3-based magnetic heterostructures

Dissertation submitted in partial fulfillment of a *Philosophiae Doctor* degree in Physics

Faculty of Science
School of Engineering and Natural Sciences
University of Iceland
Dunhaga 3
107, Reykjavík, Reykjavik
Iceland

Telephone: 525-4000

Bibliographic information:
Ignatova Kristina, 2024, *Structural and magnetic properties of V_2O_3-based magnetic heterostructures*, PhD dissertation, Faculty of Science, University of Iceland, 148 pp.

ISBN 978-9935-9768-3-3

Printing: Háskólaprent, Fálkagata 2, 107 Reykjavík
Reykjavik, Iceland, May 2024

Somewhere, something incredible is waiting to be known.
– *Carl Sagan*

Dedicated to my beloved mother and father, Galina and Igor, the dearest hearts in my life. With all my love, always and forever.

Посвящается моим любимым маме и папе, Галине и Игорю, самым дорогим сердцам в моей жизни. Со всей моей любовью, навсегда.

Abstract

Vanadium sesquioxide, typified by its first-order metal-insulator transition, structural phase transition, and magnetic changes, transition from a high-temperature rhombohedral metallic and paramagnetic state to a low-temperature insulating monoclinic antiferromagnet. The three transitions occur simultaneously, presenting a complex, intertwined phenomenon. Investigating the phase coexistence region in V_2O_3 is crucial, as its transition is intrinsically inhomogeneous, offering a unique scenario where two phases exist simultaneously within a narrow temperature range. This characteristic, coupled with the ability to manipulate it through various parameters, not only underscores V_2O_3's distinctiveness but also amplifies its appeal from an applications standpoint, signaling a rich avenue for further research into this material's potential. The complex nature of V_2O_3, characterized by simultaneous transitions, offers a unique opportunity to explore the properties of bilayers and observe how overlying layers are affected by the transitions through the interface. For instance, it allows for the creation of a system with a ferromagnet/paramagnet interface at room temperature and a ferromagnet/antiferromagnet interface at low temperatures. Particularly at low temperatures, interfacing a ferromagnetic layer with V_2O_3 introduces the potential for an exchange bias effect, which arises from the ferromagnetic/antiferromagnetic interface interaction. Exchange bias systems are extensively researched for their capacity to increase ferromagnetic coercivity and stabilize magnetization from thermal fluctuations, thus providing a method to manipulate magnetic properties. V_2O_3 demonstrates that alterations in crystal structure due to structural phase transitions can be leveraged to influence magnetic characteristics, thereby introducing an extra dimension of control via its magnetic transition phenomena.

This thesis delves into the study of phase transitions in V_2O_3 and their inherent characteristics, as well as the subsequent impact on the magnetic properties of overlying magnetic layers. Specifically, we investigate the coercivity response to the phase transitions in V_2O_3 and emergence of exchange bias within a bilayer system incorporating a nickel (Ni) or a permalloy (Py) layer. The first part of the project was dedicated to optimizing the V_2O_3 layer on various substrates, including silicon and sapphire with different crystallographic orientations, aiming to achieve the highest crystallinity and effective epitaxy of V_2O_3. This optimization was crucial for observing the most pronounced metal-insulator transition and structural phase transition. To maintain a focused and concise discussion, these optimization details are not included in this thesis; however, they are documented and presented in the publications referenced herein that are not discussed in this thesis (Paper V and Paper VI). The second part of

the project was devoted to investigating the coupling effects between phase transitions in V_2O_3 and magnetism of the Ni layer. Following the first part, a decision was made to grow a magnetic heterostructure on a sapphire substrate, specifically on two distinct crystallographic directions. This resulted in differing crystallographic and microstructural properties of V_2O_3, which in turn impacted the magnetic layer in various ways, as detailed in Paper I and Paper III. Concurrently, a different study focused on a magnetic layer composed of Py ($Ni_{80}Fe_{20}$), presented in Paper II. However, studying magnetic Py films on V_2O_3 presented challenges—discussed later in this thesis—and thus far, no significant magnetic response or effect of the SPT has been observed in the Py films. The bilayer structure, composed of Ni and V_2O_3, grown on sapphire *r*-plane, exhibited the most sensitive response to the phase transition, manifested in enhanced coercivity and tunable exchange bias. Consequently, a comprehensive study of the structural phase transition of V_2O_3 grown on *r*-plane sapphire was conducted, the findings of which are detailed in Paper III. Subsequently, the research emphasis shifted to a more detailed analysis of exchange bias, which is discussed in Paper IV, thus highlighting another facet of this thesis with equal foundational and practical significance.

Útdráttur

Vanadínoxíð (V_2O_3) er hálfmálsoxíð sem fer í gegnum fasabreytingu þar sem kristalgerð þess, seguleiginleikar og rafeiginleikar breytast með hitastigi. Við stofuhita hefur það tígulflötungskristalgerð, er málmleiðandi og hefur meðseglandi seguleiginleika en ef það er kælt niður fyrir 150 K breytist það í einangrara með einhalla kristalgerð og andjárnseglandi segulgerð. Allar þessar þrjár fasabreytingar gerast samtímis og rannsóknir á þeim veita því innsýn í flókið samspil þeirra, sérstaklega þegar bæði háhita og lághita fasarnir eru til staðar samtímis. Með því að tvinna saman vanadíumoxíð við önnur efni í lagskiptum efnum má rannsaka hvernig fasabreytingarnar hafa áhrif á eiginleika nærliggjandi efna yfir samskeyti þeirra. Þannig má til dæmis byggja samskeyti efna sem eru járnseglandi/meðseglandi við stofuhita en járnseglandi/andjárnseglandi við lág hitastig. Sérstaklega er áhugavert að skoða slík samskeyti við lág hitastig því andjárnseglandi ástand vanadínoxíðs getur valdið skiptavíxlverkun á samskeytunum sem veldur hliðrun í seguleiginleikum. Vanadíumoxíð í lagskiptum efnum sýna því vel hvernig breytingar í kristalgerð nýtast til að hafa áhrif segulgerð og jafngilda því nýrri aðferð til að stjórna seguleiginleikum efna. Í þessari rannsókn er fasabreyting vanadínoxíðs skoðuð og áhrif hennar á seguleiginleika nærliggjandi efna.

Í fyrri hluta verkefnisins var unnið að ræktun vanadínoxíð kristalla á ólík undirlög með það að markmiði að hámarka kristalgæði efnisins en kristalgerð vanadínoxíðs ræður miklu um eiginleika fasabreytingarinnar í efninu. Ritgerðin sjálf fjallar ekki sérstaklega um þennan hluta verkefnisins en vísindagreinar sem tengjast þessum rannsóknarhluta verkefnisins er hafðar með til hliðsjónar (greinar V og VI).

Í seinni hluta verkefnisins var unnið að rannsóknum á hvernig fasabreytingar í vanadínoxíðihafa áhrif á seguleiginleika segulefna í tvílögum (greinar I, II, III og IV). Unnið var með vanadínoxíð húðir ræktaðar á safír undirlög og skoðað hvernig kristalgerð, fasabreytingar og kristalbygging vanadínoxíðs hefur áhrif á breytingar á eiginleikum segulhúða. Tvílög af vanadínoxíði og Ni segulhúðum sýndu sterkustu áhrif fasabreytingarinnar á seguleiginleikana sérstaklega hvað varðar segulheldnisvið og skiptavíxlverkun.

Table of Contents

List of Original Papers

I **Reversible exchange bias in epitaxial V_2O_3/Ni hybrid magnetic heterostructures.**

K. Ignatova, E.B. Thorsteinsson, B.A. Jósteinsson, N. Strandqvist, C. Vantaraki, V. Kapaklis, A. Devishvili, G.K. Pálsson, U.B. Arnalds

Journal of Physics: Condensed Matter **34**, 495001, 2022.

II **Structural and magnetic characterization of epitaxial V_2O_3/$Ni_{80}Fe_{20}$ hybrid magnetic structures.**

K. Ignatova, M.T. Sultan, A.O. Elvarsson, S. Ingvarsson, U.B. Arnalds

International Semiconductor Conference (CAS), 2022.

III **Phase coexistence induced surface roughness in V_2O_3/Ni magnetic heterostructures.**

K. Ignatova, E. Vlasov, S.D. Seddon, N. Gauquelin, J. Verbeeck, D. Wermeille, S. Bals, T.P.A. Hase, U.B. Arnalds

APL Materials **12**, 041118, 2024.

IV **Angular-dependent exchange bias in V_2O_3/Ni magnetic heterostructures.**

K. Ignatova, E.B. Thorsteinsson, U.B. Arnalds

In manuscript, 2024.

Other publications not discussed in this thesis:

V **Structural and electrical properties of V_2O_3 thin films on c-plane Al_2O_3 fabricated by reactive-HiPIMS and dcMS techniques.**

M.T. Sultan, **K. Ignatova**, E.B. Thorsteinsson, F. Magnus, U.B. Arnalds

Journal of Physics D: Applied Physics, **54**, 425302, 2021.

VI **Structural morphology and electrical transitions of V_2O_3 thin films grown on SiO_2/Si by high power impulse magnetron sputtering.**

M.T. Sultan, **K. Ignatova**, E.B. Thorsteinsson, U.B. Arnalds

Thin Solid Films, **742**, 139048, 2022.

Acknowledgments

First and foremost, Unnar, you are undoubtedly responsible for one of the most amazing and memorable periods of my life, known as the 'PhD student' period. I am endlessly grateful for your support, the countless opportunities you provided, your guidance, and your supervision. I am grateful to you for who I have become today, as I have transitioned and changed significantly over the past 3.5 years. Although I initially accepted the PhD position in Grenoble and was set to do my PhD there, I ultimately changed my mind and chose Iceland. Ironically, I ended up back in Grenoble for beam time on four separate occasions — so much for escaping it! :) Since then, I would make the same decision every day and wouldn't change a thing. So, a massive thank you to you! Gunnar, I would also like to express my sincere gratitude for your oversight and contributions throughout this project.

Ah, the thrilling beam times! Tom, I am truly blessed to have met you and had the opportunity to work alongside you. I want to express my heartfelt thanks for the delightful 'beam times' and our stimulating science discussions. You've given me the right words when I needed them, and your endless enthusiasm for research and science has kept my motivation up. Learning from you has been an enriching experience, both academically and personally. I really hope I will have many more beam times with you, or any chance to collaborate again. I deeply appreciate your scientific expertise, honesty, openness, and genuine empathy. From the bottom of my heart, thank you, Tom!

Anton, you are one of the reasons why my PhD has been one of the most rewarding periods of my life. I deeply value both our scientific and casual conversations. Thank you for your consistent support, care, and compassion. Though I've expressed everything to you personally, I also want to formally acknowledge you here, as you hold significant importance in both my personal and academic life.

Zhenya, you know everything... even more! Without you, nothing would have been possible—absolutely nothing! You were always there for me, spending hours discussing science and sharing in my excitement about my results and frustrations. Here, I specifically want to acknowledge the period of our PhD times we shared, facing the same challenges and supporting each other. I have no words to express my gratitude to you!

Asgeir, thank you for our friendship, support, and I am glad we shared many lab and non-lab moments and experiences together. Your kindness, encouragement, and all the laughs we've shared have made every moment unforgettable. Kristbjörg, thank you for your support and assistance, as

well as for sharing moments outside of work and our small adventures. Your help has been very useful, and I appreciate all of it. Einar, our late nights in the lab were great, fixing cold moke, dealing with clean room flood, and doing all the measurements in between. Your assistance and sharing your expert lab hacks meant a lot to me. Those moments were a mix of fun and learning. Thank you for being my partner in science and adventure! Kristjan, thank you for your support in the lab! Ira, Rustam, Taha, Kibbi, Bing, thank you for our chats and for bringing a smile to my face! Swetha and Elli, it's tough for me to be at this part of the chapter where I have to think about how much space to give each person and how to group everyone. But I can't help but mention both of you separately because you've both been incredibly special to me during my PhD. Whenever we talked, it felt like a warm hug and a moment of tranquility, knowing we were all in this together. You're more than just colleagues; you're amazing friends with your beautiful, kind, and fun personalities. Thank you for everything! Andre, I won't say much, just this: Let's celebrate this day! It's my defence day! And to the VR3 people, thank you for being part of this journey. Your presence and support have created lasting memories.

Alina, meeting you here has been one of the best things that's happened to me, and your support has been incredible. Our journey has been truly unforgettable, always on the edge of something wild and incredible. Your friendship means so much to me because you've made every moment exciting and memorable. Joan, Bonni, Johan, you've been an integral part of this journey, and you hold a special place in my heart. Each of you impacted me in your own unique way, which was so important when I needed it most. Your support means the world to me. Thank you for being in my life during this incredible path.

Igor, I want you to know that your contribution has been invaluable to my journey. You were the starting point for everything amazing that has happened in the past seven years. Your influence has shaped my path, and I am deeply grateful for your presence in my life.

Nina Vladimirovna, I must acknowledge you for something truly significant — you've made one of the most important impacts on me — you set the bar for the quality of research. I'm deeply grateful for your acceptance as my master thesis mentor.

Мама, Папа, Женя, Соня, Тетя Света, Ирина, вы - моя опора и поддержка. Вы переживали и поддерживали меня больше всего. Поэтому я хочу посвятить эту скромную научную работу вам. Когда мне казалось, что я не справлюсь, вы всегда были рядом, не давая мне сдаться. Спасибо вам за все!

Chapter 1

Introduction

Vanadium (III) oxide (V_2O_3) stands out in the realm of transition metal oxides (TMOs) for its distinctive and multifaceted phase transitions, offering a rich ground for exploration in the context of structural and magnetic properties. Unlike the more commonly discussed Metal-Insulator Transition (MIT) typically investigated in TMOs such as VO_2, the primary focus of this research is the structural phase transition (SPT) of V_2O_3 from a rhombohedral to a monoclinic phase, and its intricate magnetic transition. These transitions are a critical part of the material's complex behavior and potential for tailoring properties for advanced technological applications

At room temperature, V_2O_3 is in a rhombohedral phase, exhibiting paramagnetic properties. However, under specific conditions such as varying temperature, pressure, or chemical doping, V_2O_3 undergoes a structural phase transition to a monoclinic phase. This transition is closely coupled with a magnetic transition, leading to significant changes in the material's magnetic properties. The study of these transitions, especially in thin film form, poses a fascinating challenge due to the sensitivity of V_2O_3 to external conditions and the subtle interplay of factors governing its phase behavior.

The importance of these transitions extends beyond academic curiosity, holding the potential to be utilized in applications in fields such as spintronics, magnetic storage devices, and smart materials. The structural phase transition from rhombohedral to monoclinic, in particular, impacts the magnetic ordering in the material, which can be exploited in designing devices that leverage these magnetic properties. However, achieving a comprehensive understanding and control of these phase transitions in V_2O_3, especially when engineered as thin films, remains a challenge. The response of materials to external stimuli, along with the balance of factors influencing its structural and magnetic phases, therefore, requires meticulous investigation.

This thesis aims to shed light on the structural and magnetic transitions of V_2O_3, with a special emphasis on thin film applications. By focusing

on the nuanced interactions between the structural phase transitions and corresponding magnetic changes, this research seeks to contribute to the broader understanding of TMOs and their potential in advancing modern technology. The following chapters will delve into the methodology, experimental findings, and the broader implications of this study, ultimately underscoring the significance of V_2O_3's structural and magnetic transitions in the context of advanced material science.

Chapter 2

Survey

2.1 Vanadium sesquioxide V_2O_3

Vanadium oxides, known for their strong electron correlations, have garnered significant interest for their potential applications stemming from their phase transitions. These materials can be fabricated using conventional deposition methods such as physical vapor deposition, chemical vapor deposition or atomic layer deposition. Vanadium oxides display a diverse array of stoichiometries, each correlating with distinct crystal structures that can profoundly influence the dynamics and characteristics of their phase transitions. These variations in composition and atomic arrangement often lead to markedly different behaviors in phase transitions of the materials, impacting their physical and chemical properties in significant ways. The temperature at which the phase transitions occur varies across different oxidation states of vanadium oxides [1, 2]. Among the different stoichiometric forms, V_2O_3, VO_2, and V_2O_5 are the most extensively studied vanadium oxides for their potential in real-world applications (highlighted in red in Figure. 2.1). Vanadium dioxide (VO_2) has been the subject of more extensive study primarily because its MIT occurs just above room temperature, making it particularly appealing from an application standpoint. Vanadium Sesquioxide (V_2O_3) is relatively less explored compared to VO_2. Another aspect that makes V_2O_3 intriguing is its specific magnetic phase transition, which is not seen in VO_2. Many experimental approaches applied to VO_2 could be replicated with V_2O_3. It's plausible to anticipate that V_2O_3 may exhibit physical properties similar to those of VO_2, given that the MIT in both VO_2 and V_2O_3 are first-order phase transitions. Nonetheless, physical properties of V_2O_3 might differ from those of VO_2 and V_2O_5. As for V_2O_5, it is recognized as the most oxidized and stable form among vanadium oxides. Yet, in most cases, V_2O_5 does not undergo an MIT; however, certain studies have identified an MIT in V_2O_5, while also noting a suppressed SPT [3, 4].

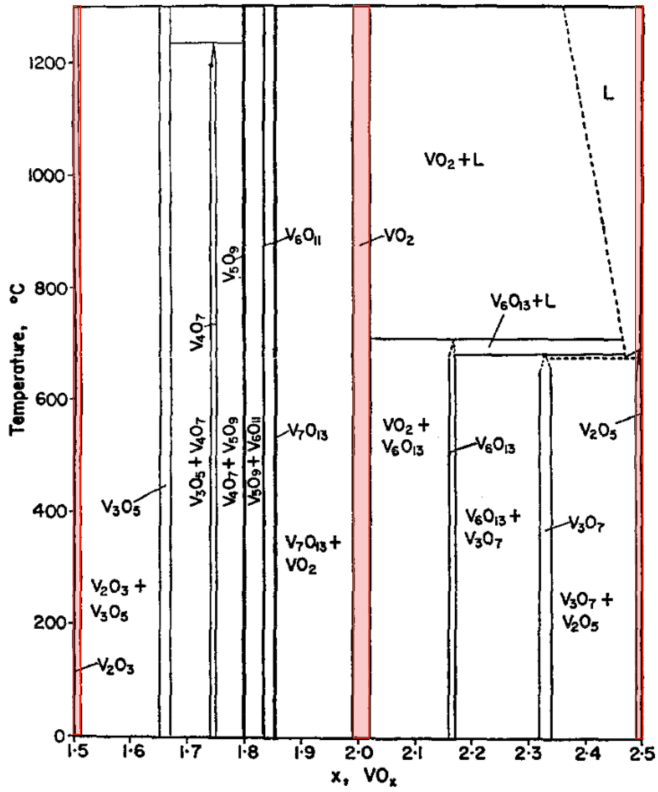

Figure 2.1: The proposed phase diagram of the vanadium oxides with different stoichiometries in the temperature range up to 1200 °C. The red columns highlight the vanadium oxide phases that are the most extensively studied, specifically VO_2, V_2O_3, and V_2O_5. Reprinted from [5] with permission from Elsevier.

2.2 Metal-Insulator and Structural Phase Transitions

Vanadium sesquioxide, V_2O_3, known for its distinct Mott phase transition around 150 K, has been the subject of substantial research due to its intriguing transition properties. Generally it is identified as a Mott insulator. It exhibits a temperature-dependent Metal-Insulator Transition that is closely linked to its crystal structure. V_2O_3 possesses a rhombohedral (hexagonal) corundum structure, $R\bar{3}c$, at room temperature and transforms into a less symmetric monoclinic structure, adopting the $I2/a$ symmetry at $\sim$ 155 K (see Fig. 2.3). Both transitions are hysteretic with a quite narrow temperature width of the transition which typically ranges between 5 to

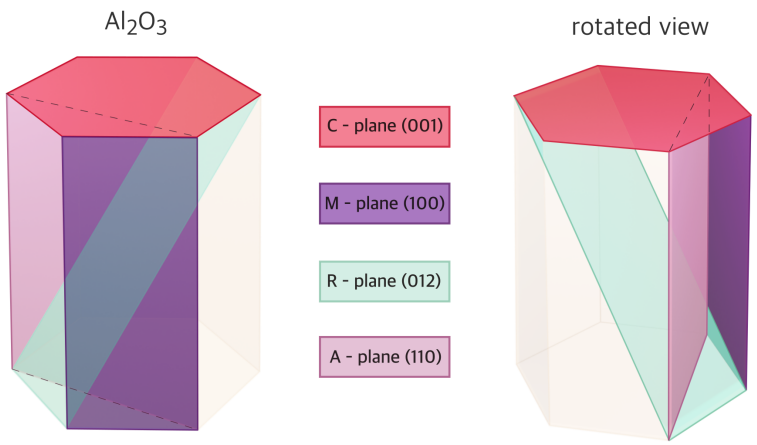

Figure 2.2: Visual representation of the crystallographic planes for substrates of Al_2O_3 sapphire with varying crystallographic orientations, such as c, m, r, and a planes.

10 K, making them intriguing for different applications.

A crucial aspect of understanding the physics behind these transitions is determining whether the phase change is primarily driven by the structural or the electronic transition. The transition temperatures and magnitude can be modified through the selection of the substrate or the conditions of deposition. V_2O_3, having a corundum rhombohedral structure at room temperature, is identical to that of sapphire (α-Al_2O_3), facilitating its epitaxial growth on single-crystal α-Al_2O_3 substrates. Depositing V_2O_3 on sapphire substrates with varied crystallographic orientations, such as a, m, c, and r planes (depicted in Fig. 2.2), enables the exploration of diverse structural and electronic characteristics of V_2O_3 [7]. This approach allows for a tailored investigation into the unique properties of V_2O_3. The underlying structural phase transition properties of V_2O_3 are illustrated in Figure 2.3, which shows how the transition for V_2O_3 films grown on sapphire r-plane can be observed with temperature-dependent X-ray diffraction measurements. The properties of the film are influenced by factors such as crystallographic orientation, oxygen content, and thickness of the layer [8–11]. Different studies suggest that it becomes possible to decouple the transitions and observe each independently, by suppressing either the MIT or the SPT. This approach has been explored in previous research, including

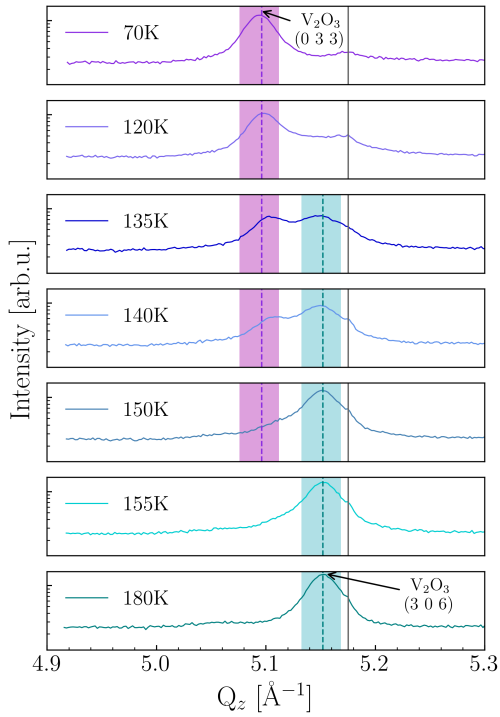

Figure 2.3: Temperature-dependent x-ray diffraction scans recorded for a V_2O_3/Ni film deposited onto an r-plane Al_2O_3 substrate as a function of temperature across the SPT of V_2O_3. Pink and cyan bars indicate the diffraction peaks for the monoclinic and rhombohedral phases of the V_2O_3 at low and high temperatures, respectively. Broken lines indicate the XRD peak positions derived by fitting with a Pearson type VII function of the monoclinic V_2O_3 (0 3 3) at low temperatures and the rhombohedral V_2O_3 (3 0 6) at high temperatures [6].

doping and high-pressure experiments on V_2O_3 single crystals [12–15].

As was shown by Drain et al. [16], throughout the SPT, the c-axis of the hexagonal cell shifts by $\sim 1.8°$ towards the hexagonal basal plane, following the trajectory of three equivalent basal-plane (hexagonal cell) directions, specifically $(1\bar{1}0)$, (010), and $(\bar{1}00)$. A rhombohedral reflection such as $(116)_H$ splits into three monoclinic ones, arranged in the form of a spherical equilateral triangle (indicated by a red triangle in the Figure 2.4) [17]. Such a threefold degeneracy leads to the formation of a triply twinned monoclinic structure as it cools below the transition temperature. To convert hexagonal reflection indices to their corresponding monoclinic reflection indices, the following transformation matrices should be applied [16]:

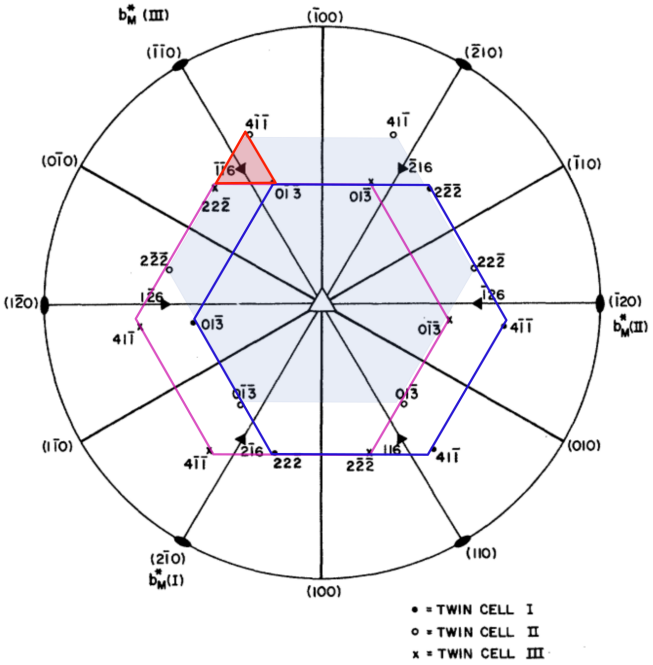

Figure 2.4: A stereographic projection showcases the hexagonal cell alongside its three equivalent monoclinic cells (exaggerated for clarity). Reprinted figure with permission from [16]. Copyright 2024 by the American Physical Society. The highlighted figures serve to enhance visual comprehension.

$$\begin{pmatrix} \vec{a}_m \\ \vec{b}_m \\ \vec{c}_m \end{pmatrix} = \begin{pmatrix} \frac{2}{3} & \frac{4}{3} & \frac{1}{3} \\ 1 & 0 & 0 \\ \frac{1}{3} & \frac{2}{3} & -\frac{1}{3} \end{pmatrix} \begin{pmatrix} \vec{a}_H \\ \vec{b}_H \\ \vec{c}_H \end{pmatrix},$$

$$\begin{pmatrix} \frac{4}{3} & \frac{2}{3} & \frac{1}{3} \\ 0 & 1 & 0 \\ \frac{2}{3} & -\frac{1}{3} & -\frac{1}{3} \end{pmatrix} \quad \text{and} \quad \begin{pmatrix} \frac{2}{3} & \frac{2}{3} & \frac{1}{3} \\ -1 & -1 & 0 \\ \frac{1}{3} & \frac{1}{3} & -\frac{1}{3} \end{pmatrix}.$$

These matrices provide a direct method to determine the monoclinic indices from given hexagonal indices. The twinning is evident at the nanoscale level, occurring over a few nanometers. However, methods such as nearfield

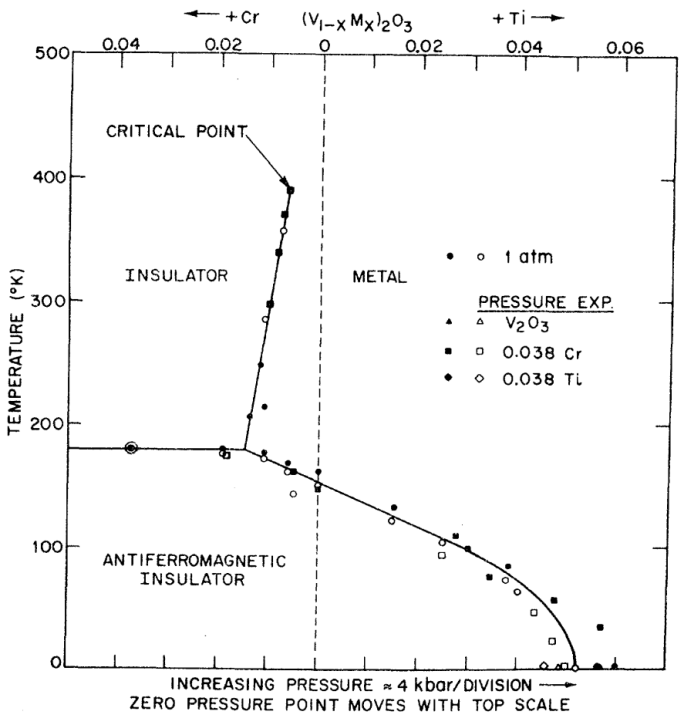

Figure 2.5: The phase diagram for the metal-insulator transition in V_2O_3, influenced by doping with Cr or Ti and pressure variations. Reprinted figure with permission from [20]. Copyright 2024 by the American Physical Society.

infrared spectroscopy [18] or low-temperature conductive scanning electron microscopy [19] reveal that phase separation takes place on a significantly larger scale, in the vicinity of 100 nm, meaning that in both the SPT and the MIT, factors at length scales larger than twinning are significantly influential.

The occurrence of the MIT in V_2O_3 varies across a spectrum of temperatures and pressure (see Figure 2.5). When vanadium sesquioxide is doped with transition metals like Cr or Ti, the behavior of its MIT can be significantly altered [17, 20]. Specifically, Ti doping has been found to favor the metallic phase, whereas Cr doping tends to maintain the insulating phase, showcasing the tunability of V_2O_3's electrical properties through selective doping. The SPT and MIT in V_2O_3 exhibit significantly higher sensitivity to disorder and growth conditions [13], such as oxygen content, pressure, and substrate temperature, compared to VO_2. This is evidenced

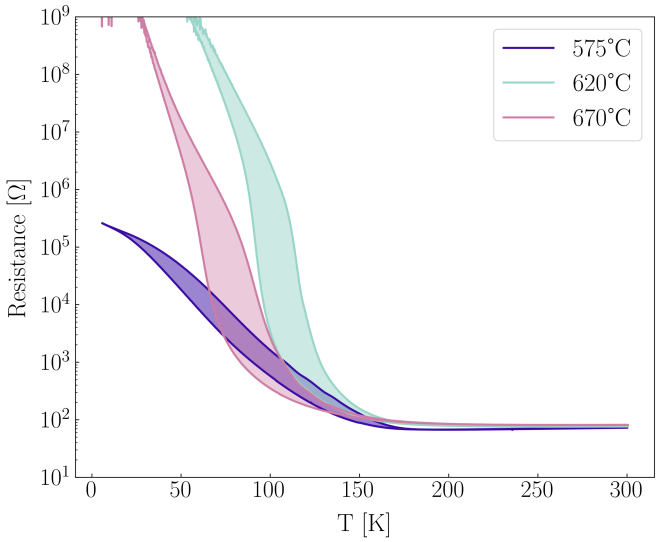

Figure 2.6: Resistance measurements as a function of temperature for V_2O_3 single layer films deposited under different substrate temperatures on *c*-plane Al_2O_3 sapphire [21].

in Figure 2.6, which shows that work conducted in our group demonstrates the highly tunable and sensitive nature of these transitions in response to substrate temperature variations [21], with both the magnitude and width of hysteresis undergoing drastic changes even with minor temperature adjustments. Typically the MIT takes place within a similar temperature range to the SPT, often viewed as a classic manifestation of a Mott-Hubbard transition [22]. First identified over fifty years ago, this phenomenon represents an electronic first-order phase transition, characterized by pronounced hysteretic behavior, these transitions exhibit a significant region where both phases coexist. Undergoing MIT, the resistivity can change by more than 6 orders of magnitude. Exemplary measurements of the MIT conducted by our group on a V_2O_3 single layer deposited on a *c*-plane Al_2O_3 sapphire substrate with optimized deposition parameters, are depicted in Figure 2.6 [21].

Phenomena such as phase coexistence and nanoscale phase separation in transition metal oxides can often be attributed to the presence of inhomogeneities resulting from both intrinsic and extrinsic factors. These inhomogeneities play a crucial role in electrical, magnetic, and structural properties, including colossal magnetoresistance in manganites [23] and

avalanches in VO_2 [24]. Properties like crystal structure and magnetization can undergo dramatic changes in response to external conditions such as temperature, magnetic field, and stress, leading to events of varying magnitudes, which are termed "avalanches". Therefore, the MIT in these materials occurs through multiple abrupt jumps or avalanche-like events [24, 25]. A proposed theoretical model seeks to clarify the phenomenon of avalanches in VO_2, attributing them to a voltage-induced breakdown [26]. The model suggests that at low applied voltages, avalanches stem from random percolation, whereas at higher voltages, they result from the formation of conductive filaments. Since V_2O_3 exhibits a first-order MIT similar to those seen in VO_2 [27], including phase coexistence [18], one might also expect similar avalanche jumps in V_2O_3. This expectation has been strongly corroborated by findings indicating that such avalanche jumps in V_2O_3 are highly dependent on the dimensions of the device [25]. Based on the varying power law distributions characterizing these jumps, it seems plausible that the mechanisms driving the MIT in VO_2 and V_2O_3 are distinct, suggesting that the percolative process during the MIT in V_2O_3 is correlated [25] and that the MIT in V_2O_3 is associated with the percolative process.

2.3 The Magnetic Phase Transition

The magnetic transition in V_2O_3 is characterized by a shift from a paramagnetic (PM) state at ambient temperatures to the emergence of an antiferromagnetic (AFM) phase as temperatures decrease. This change occurs alongside the MIT and the SPT, illustrating a sophisticated interaction between the magnetic and electronic states of the material. Previous studies highlight the role of magnetic correlations in V_2O_3, particularly noting that the spin degree of freedom becomes active above the MIT [29, 30]. Studies using techniques like low-energy muon spin relaxation have revealed that this magnetic transition is closely intertwined with the structural shift from rhombohedral to monoclinic symmetry [28]. The observations indicate a stable coexistence of both high- and low-temperature phases over a broad temperature range. This coexistence underscores the significance of magnetic interactions in the overall phase transition of V_2O_3. A significant difference of a 10 K higher onset at around 185 K for the drop in the paramagnetic fraction below unity, compared to the rhombohedral phase transition at approximately 175 K, is noted in [28] (see Fig. 2.7), it is theorized to be linked to the presence of short-range critical antiferromagnetic fluctuations above the Néel temperature (T_N) [31, 32]. This suggests

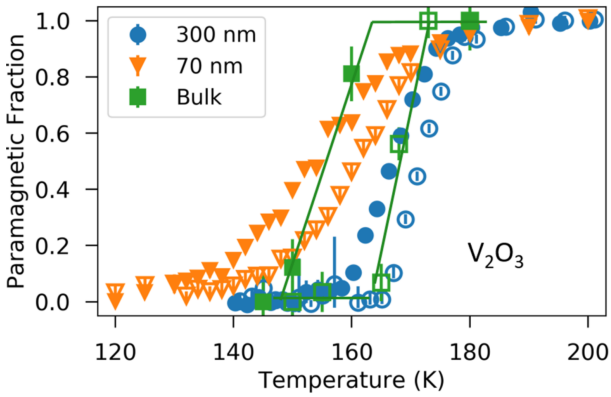

Figure 2.7: The temperature-dependent change in the paramagnetic phase fraction of V_2O_3 across the SPT in samples of 300 nm, 70 nm, and bulk size. The study illustrates this evolution with both cooling and warming cycles. The cooling sequence data is denoted by filled symbols, whereas the warming sequence data is represented by open symbols. Reprinted figure with permission from [28]. Copyright 2024 by the American Physical Society.

the reduction in the paramagnetic fraction at higher temperatures might be due to the partial pinning of these AFM fluctuations. Nevertheless, the critical point for both the structural phase transition and magnetic transition, where phase changes are most pronounced (midpoint of the transition), are essentially the same within the margin of error. This indicates a close coupling between the two transitions in terms of temperature and emphasizes the intricate connection among magnetic, structural, and electronic aspects in this material, which is known for its strong electron correlation. The existence of such short-range AFM fluctuations at higher temperatures is more typical of continuous phase transitions, even though the AFM transition in V_2O_3 is of the first order. However, the gradual evolution is abruptly disrupted in a manner characteristic of first-order transitions near the SPT temperature. This suggests that while the magnetic transition nearly behaves as continuous, it becomes first order due to the influence of the SPT [28]. It's important to note that the antiferromagnetic ordering appears spatially inhomogeneous during the transition, indicating a gradual and complex evolution of the magnetic state.

2.4 Magnetic anisotropy in thin films

Magnetic anisotropy is a fundamental concept in the study of magnetic materials, essential for understanding their behavior under various conditions. Anisotropy refers to the variation of a property depending on the direction in which it is measured. In the context of magnetic anisotropy, it is the energy density observed along a specific direction of a crystal or sample, typically expressed in J/m^3 [33]. This characteristic, or its absence, significantly influences the development and performance of spintronic devices, acting as a critical constraint. In ferromagnets (FMs), a range of factors encapsulated under magnetic anisotropy influence the direction of magnetization. This concept is quantified by the energy density E, with the magnetization vector $\vec{M}$ aligning itself with the local minimum of E. This aligns with the classic Stoner-Wohlfarth model, relevant in the study of magnetization and applies particularly to situations where the magnetization undergoes coherent rotation [34]. This model is most effective in cases where the material is in a monodomain state, meaning it behaves as a single magnetic domain. The energy density E is defined as:

$$E = -\vec{H} \cdot \vec{M} + \sum_i E_i$$

where the term $-\vec{H} \cdot \vec{M}$ is the Zeeman energy term, and E_i symbolizes different anisotropy contributions. The fundamental anisotropy contributions in magnetic thin films include shape anisotropy, magnetocrystalline anisotropy, growth-induced uniaxial anisotropy, magnetoelastic anisotropy, interface anisotropy, and exchange bias. In this chapter, we will discuss the most relevant ones.

Shape anisotropy

Magnetic shape anisotropy emerges from long-range dipolar interactions in ferromagnetic and ferrimagnetic materials [35], linked to the demagnetization field resulting from the surface divergence of magnetization. This anisotropy's energy per unit volume, denoted as E_A, is formulated as $\frac{\mu_0}{2} M^2 \cos^2 \theta$, where θ is the angle between the saturation magnetization M and the normal to the plane.

Magnetocrystalline Anisotropy

Magnetocrystalline anisotropy arises due to the film's crystalline structure and refers to the energy needed to redirect magnetization within a single

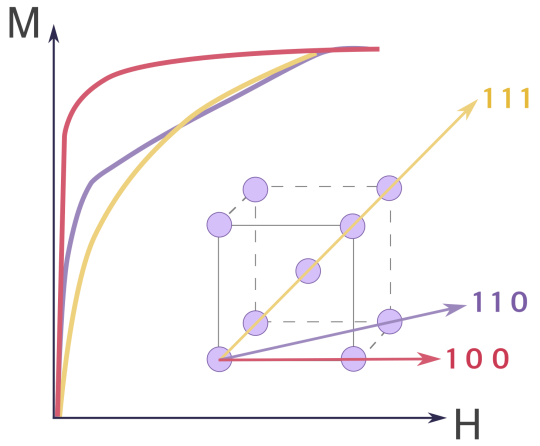

Figure 2.8: The magnetisation with applied feild for body-centred cubic Fe, possessing an easy axis along the ⟨100⟩ directions, a medium axis in the ⟨110⟩, and a hard axis on the ⟨111⟩.

crystal from a preferred (easy) direction to a less favorable (hard) direction. This phenomenon primarily arises due to the spin-orbit interaction, heavily influenced by the crystalline structure of the material. In a lattice, the orbits of an atom are determined by the lattice's structure and pinned in place by the bonds. This situation causes the orbital component of magnetization to be fixed, a state often described as 'quenched.' Consequently, the spin moments dominate magnetization behavior in an external field. This magnetization is influenced by the orientation of the lattice due to spin-orbit coupling, leading to the establishment of certain crystal directions as 'easy' and others as 'hard' for magnetization. The variation in energy needed to disrupt the spin-orbit coupling gives rise to these distinct magnetization pathways. The orientation of the magnetic easy axis differs across various material systems and crystallographic structures. For example, in body-centred cubic (bcc) iron, this results in an easy axis along the ⟨100⟩ direction, a medium axis in the ⟨110⟩, and a hard axis on the ⟨111⟩, as shown in Fig. 2.8. For a cubic system the magnetocrystalline energy term in spherical coordinates is given by [36]:

$$\begin{aligned} E =& K_1 \left(\frac{1}{4} \sin^2(\theta) \sin^2(2\phi) + \cos^2(\theta) \right) \sin^2(\theta) \\ &+ \frac{K_2}{16} \left(\sin^2(2\phi) \sin^2(2\theta) \sin^2(\theta) \right) \end{aligned} \tag{2.1}$$

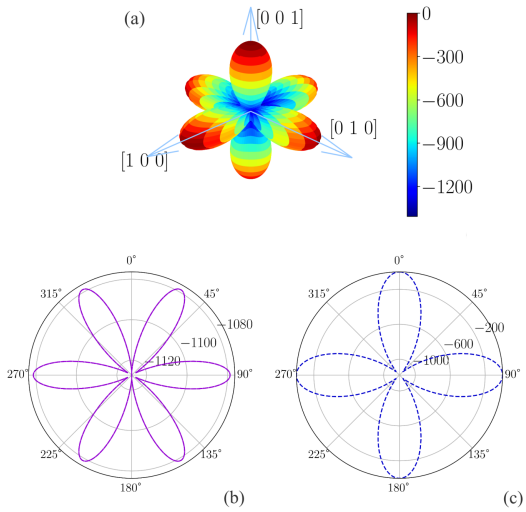

Figure 2.9: (a) Anisotropy energy (in Jm^{-3}) surface for Ni (FCC) according to equation (1) using the first and second anisotropy constants for nickel $K_1 = -4.5{\times}10^3$ Jm^{-3} and $K_2 = 2.3{\times}10^3$ Jm^{-3} [37]. The [1 0 0], [0 1 0] and [0 0 1] crystallographic directions are indicated in the image. (b) Anisotropy energy around the [1 1 1] direction. (c) Anisotropy energy around the [1 0 0] direction.

where K_1 and K_2 are the first and second order anisotropy constants (higher order terms have been left out), θ is the polar angle and ϕ is the azimuthal angle, in a coordinate system aligned to the crystallographic axes. When K_1 is larger than zero in a cubic crystal the directions of the magnetic easy axes are <100>. However, when K_1 is negative and $K_2 < 9|K_1|\ /4$, as in Ni, the magnetic easy axes are <111> and the hard axes are <100>. Figure 2.9 illustrates the magnetocrystalline energy of Ni, calculated using equation (2.1), with the first and second order anisotropy constants for Ni set at $K_1 = -4.5{\times}10^3$ Jm^{-3} and $K_2 = 2.3{\times}10^3$ Jm^{-3}, as referenced in Paper I [37]. Rotating Ni around the [111] axis, reveals a sixfold symmetry in the magnetocrystalline energy. As depicted in Figure 2.9, this energy variation is relatively modest. In contrast, a more significant change in energy is observed when Ni is rotated around the [100] direction.

Growth-induced Uniaxial Anisotropy

During the sample preparation process, a preferred axis for magnetization can be established through methods like oblique deposition or the application of external magnetic fields. Factors such as the shape of the

substrate, terrace structure of the substrate, or strain within the substrate also contribute to this growth-induced anisotropy [38, 39].

Interface Anisotropy

Breaking inversion symmetry at interfaces, where the orientation of "up" differs from "down" at any bilayer, creates a distinct axis perpendicular to the interface, thereby causing a uniaxial anisotropy related to the surface. When anistropy energy is positive, this phenomenon induces perpendicular magnetic anisotropy, promoting magnetization alignment perpendicular to the interface. This effect acts in opposition to the dipolar-induced shape anisotropy typically observed in planar films.

Exchange anisotropy

Exchange anisotropy results from the interaction of spins between FM and AFM materials at their boundary. This phenomenon, as described by the microscopic Heisenberg model, involves FM spins orienting themselves at right angles to the AFM's preferred direction, leading to spin-flop coupling [40]. In the case of a smooth interface, this interaction doesn't produce a unidirectional anisotropy nor the related exchange bias effect (described delow). Rather, it creates a uniaxial anisotropy, which subsequently increases the coercivity (H_C) and alters the magnetization ($M(H)$) curve's profile. The theoretical calculations of exchange anisotropy energy generally far exceed actual measurements, which are significantly influenced by the characteristics of the FM and AFM materials, as well as the nature of their interface, including factors like AFM anisotropy energy, spin canting, interface roughness, and dislocation density [41, 42].

2.5 Exchange bias

Exchange bias refers to the shifting of the hysteresis loop along the magnetic field axis in a system typically composed of two magnetically distinct materials. This shift commonly occurs in a bilayer or multilayer structure where a ferromagnet is in direct contact with an antiferromagnet. The term "exchange bias" is used because this shift in the hysteresis loop is influenced by a bias field, which is additional to the external applied field. This bias field originates from the exchange interactions between the two different magnetic materials [43, 44].

In 1956, Meiklejohn and Bean [45, 46] discovered a new type of magnetic anisotropy, best described as exchange anisotropy and more commonly

referred to as exchange bias. The effect arises from the coupling between the ferromagnetic and antiferromagnetic spins at the interface. It results in a shift of the FM hysteresis loop along the magnetic field axis with respect to the applied magnetic field. The discovery originated from studies on cobalt (Co) particles surrounded by a cobalt oxide (CoO) shell, revealing that the interaction between the ferromagnetic cobalt core and the antiferromagnetic CoO shell at their interface crucially altered the magnetic properties, resulting in a shift in the hysteresis loop. This led to the identification of a new type of exchange anisotropy. To detect EB, the experimental method involved cooling the Co/CoO system below the Néel temperature (T_{N}) of the antiferromagnetic CoO in a magnetic field, a crucial step due to the transition of both FM and AFM materials to a paramagnetic state above their Curie and Néel temperatures, respectively. The Néel temperature for an AFM material and the Curie temperature for a FM material refer to the threshold temperatures above which these magnetic materials transition into a paramagnetic state. This cooling process starts between the AFM's Néel temperature and the FM's Curie temperature. EB observations are conducted at temperatures below the Curie temperature (or blocking temperature for superparamagnetic particles), after which the EB effect becomes undetectable. The intensity of the EB effect is measured in terms of the EB field and the coercivity within the hysteresis loop. Meiklejohn and Bean compared torque curves of the Co-CoO system to a system with uniaxial anisotropy. They described the anisotropy energy in the Co-CoO particle system with the term $K_u \cos\Theta$, in contrast to the $K_1 \sin^2\Theta$ term used for uniaxial anisotropy. Here, Θ represents the angle between the FM magnetization and its easy axis, while K_1 and K_u are constants representing uniaxial and unidirectional anisotropy, respectively. This formulation indicates that the particles are in a stable state at one specific angle. Unlike uniaxial anisotropy, which has two stable states at two angles, the hysteresis loop shift in these systems is attributed to what's termed as unidirectional anisotropy. This means that, unlike uniaxial anisotropy where magnetization is energetically favorable in two opposite directions (along the easy axis), the net magnetization in an exchange bias system prefers a single direction, demonstrating its favorability to one direction energetically.

2.6 Models of exchange bias

The modeling of EB systems has historically led to disagreements between experimentalists and theorists in the field, due to divergent results. A

key issue is the absence of a unified model capable of accounting for all experimental findings. Despite over forty years of research into the EB phenomenon, its microscopic underpinnings are still debated and subject to ongoing investigation. This chapter briefly describes different possible models to explain the exchange bias phenomenon. Despite the numerous models proposed to describe the exchange bias phenomenon, it's crucial to recognize that exchange bias is highly composition-dependent, with each system displaying unique characteristics. This diversity contributes to the contradictory results observed and underscores the continuous development of new models. Considering the inherent complexity of materials like V_2O_3, which exhibit simultaneous structural, magnetic, and electronic phase transitions in a unique manner with a coexistence region where interface characteristics can significantly vary with temperature, the development of a new model may be even necessary to more accurately capture its features. The models applied to EB systems can be divided into three distinct groups based on the length scale of the region sharing the same magnetic moment: macroscopic, mesoscopic, and microscopic. Generally, comparison of mesoscopic models with experimental data indicates a more accurate alignment. The following chapters will provide an overview of these models.

The phenomenological model

A basic qualitative model can be constructed based on the macroscopic phenomena of the hysteresis loop shift, attributed to unidirectional anisotropy. This model, depicted in Figure 2.10, utilizes the Curie temperature of the ferromagnetic layer and the T_N of the antiferromagnetic layer, with the AFM entering a long-range state below T_N. For the EB system to function correctly, it's essential that $T_N < T_C$ during the cooling process. Initially, the system's temperature is set between T_N and T_C, where the AFM exhibits a paramagnetic state with randomly oriented spins, and the FM spins align with an external magnetic field, resulting in a hysteresis loop centered around zero magnetic field, unaffected by the AFM presence. The cooling process includes applying a strong external magnetic field to fix the magnetization direction of the FM layer while lowering the temperature below the AFM's Néel temperature. After cooling, the exchange interaction at the interface, influenced by the external magnetic field and the magnetization direction of the overlying FM layer, positions the AFM in a long-range state. This state features uncompensated layers that are anti-parallel to each other, with the interface layer aligned either ferromagnetically or antiferromagnetically with the FM interface layer. This

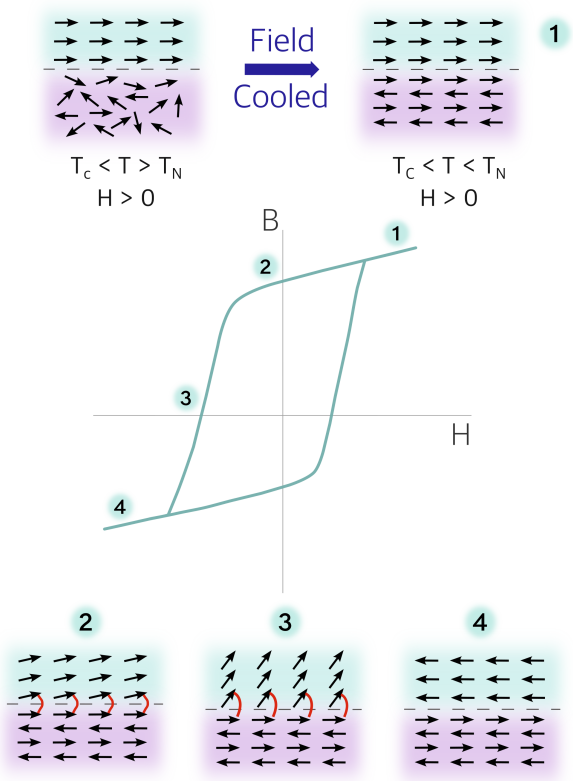

Figure 2.10: Illustrative schematic of ferromagnetic and antiferromagnetic moment alignment during field cooling and subsequent hysteresis loop stages.

results in a net magnetization at the interface due to the uncompensated layer. Throughout the hysteresis loop, both the FM and AFM layers are considered to remain in a single domain state.

Figure 2.10 graphically presents the development of exchange bias and the associated shift in the hysteresis loop. Initially, the system is depicted (top left) with the AFM material in a paramagnetic state, owing to the temperature being above its Néel temperature. The transformation of this state occurs when the system is cooled below T_N in the presence of a magnetic field. This leads to the alignment of AFM spins with those in the FM layer, influenced by interfacial interactions. The neighboring spin arrays align in a staggered manner, balancing out to achieve zero net magnetization, as shown in Figure 2.10(1). This arrangement also aligns with the saturation path in the hysteresis loop. When the magnetic field is cycled in this setup and its direction reverses (2), the FM spins begin

to pivot either out-of-plane (as depicted in Figure 2.10) or in-plane. The AFM spins, however, remain stable due to their substantial anisotropy. The interface interactions between AFM and FM spins exert a torque on the latter, attempting to maintain their initial orientation (3). This interfacial interaction is what establishes the unidirectional anisotropy, predisposing the FM-spins towards a singular alignment. Ultimately, a sufficiently strong applied field can overcome this anisotropy, resulting in the reversal of the FM-layer (4). It's important to note that in cases where the AFM anisotropy is relatively weak, only an increase in coercivity (H_c) might be observed, without a shift in the loop.

Based on the phenomenology outlined previously, Meiklejohn and Bean developed a model based on the following assumptions:

- The FM layer rotates coherently and exhibits uniaxial anisotropy with the easy axis oriented in-plane.
- The AFM layer also exhibits uniaxial anisotropy with the easy axis in-plane.
- The spins within the AFM layer are rigid, remaining unchanged during the magnetization reversal process of the FM layer.
- The AFM layers are in an uncompensated state, resulting in a net magnetic moment at the interface layer.
- The interface between the FM and AFM layers is considered to be perfectly smooth.
- A single domain state is assumed for both the AFM and FM layers.
- At the interface, the AFM and FM layers are coupled through an exchange interaction.

Mesoscopic Non-Interactive Kouvel model

Mesoscopic models often explore spin configurations in the in-plane direction of the sample, effectively segmenting the sample's in-plane area into smaller sections, each distinguished by its unique magnetization orientation. Crucial methodologies in this domain include the investigation of the granular structure of antiferromagnetic materials and the application of finite element methods for comprehensive examination. Over the years, numerous mesoscopic models focusing on grains have been developed, with

the majority drawing on the Fulcomer-Charap and Kouvel models as foundational concepts. Therefore, this chapter will focus on these two pivotal ideas.

In examining magnetic hysteresis loops within concentrated CuMn and AgMn spin glass alloys, Kouvel introduced a straightforward model to explain the unique behaviors observed [47]. This model highlighted the presence of inhomogeneous regions composed of both ferromagnetically and antiferromagnetically aligned spins interacting with one another. In this model, the phenomenon known as magnetic viscosity was observed, highlighting the dynamic and time-dependent behavior of magnetic systems. Such non homogeneous interactions between FM and AFM domains were crucial in explaining phenomena like the loop's displacement along the field axis after field cooling, a linear relationship at higher fields, and an increase in remanent magnetization with a higher cooling field. Kouvel attributed these magnetic properties to an exchange anisotropy mechanism, conceptualizing the hysteresis loops as comprising both a linear and an asymmetrical component. He suggested that the area under the curve, shifted by the asymmetrical component, correlates with the unidirectional anisotropy energy, in line with Mickeljohn and Bean's exchange anisotropy model [45, 48]:

$$J = \frac{\mu_0}{2} \int_{-H_{\max}}^{0} (M + M_s)\, dH \tag{2.2}$$

where M denotes the magnetization and M_s the saturation magnetization, both adjusted by removing the linear component from the offset loop.

By analyzing both intra-domain and inter-domain interactions and positing that exchange interactions within domains are significantly stronger than those between domains, it is possible to conceptualize the effective field acting on each domain as a combination of the applied field and a molecular field [49]. From this basis, an angle-dependent energy formula for each domain can be derived, incorporating the magnetization of the ferromagnetic domains, the uniaxial anisotropy energy per domain, and the molecular field. In its ground state, the system possesses no net magnetization; however, a non-zero net moment emerges when the system is cooled in an applied magnetic field. Consequently, the system's properties are markedly influenced by the disparity between the number of spin pairs that align and those that anti-align at the domain boundary interfaces.

Fulcomer and Charap [50] later contributed to this line of research in 1972 by proposing a grain model to describe the EB system, grounded

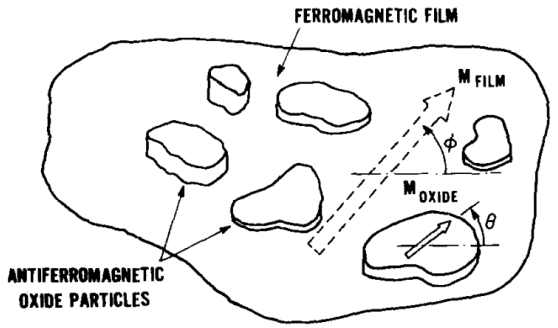

Figure 2.11: Illustrative diagram of the Fulcomer-Charap model of isolated AFM particles that are coupled to the FM layer beneath them. Reprinted figure with permission from [50]. Copyright 2024 by the AIP Publishing via Copyright Clearance Center's RightsLink.

in the theory of magnetic aftereffects of small particles. They specifically focused on small uniaxial AFM particles, which are exchange coupled to the FM but do not interact magnetically among themselves. These particles were characterized by a variety of sizes, shapes, and orientations of their magnetization relative to the FM's easy axis, effectively capturing the complexity and diversity of interactions within the EB system (depicted in Figure 2.11). The contact fraction of grains is based on Néel's idea [51] that the surface magnetic moment of grains with identical area can vary from one grain to another. This model incorporates a term for magnetic viscosity. This phenomenon, also known as magnetic aftereffect, is significant in scenarios where a material's magnetization does not immediately respond to changes in the magnetic field, but rather exhibits a delayed reaction. In an EB system, the AFM component may exhibit a magnetic aftereffect under the influence of the effective field from the FM component. This effect becomes evident when the moment of the FM is reversed, altering the exchange coupling term's sign and initiating the switching of AFM grains through thermal fluctuations. Fulcomer and Charap observed that within each grain distribution, the smaller grains exhibit superparamagnetic behavior due to thermal fluctuations, and grains of different sizes have varying degrees of coupling with the FM component.

Mesoscopic non-ideal models

Non-ideal models first appeared in studies of medium-sized (mesoscopic) systems. Unlike traditional models that assume everything is perfect and

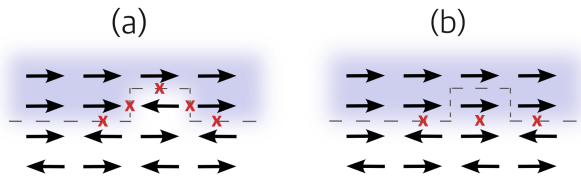

Figure 2.12: Schematic side view of possible spin configurations of spin in a FM-AFM layered structure with a non-flat interface. (a) The arrangement of spins prior to the FM reversal, and (b) the arrangement following the FM reversal. The atomic step should be depicted on a two-dimensional interface for visualization. Frustrated bonds are indicated by crosses. The schematic illustration is recreated from [54].

simple, non-ideal models aim to be more realistic by including features like uneven surfaces and impurities that are not magnetic in the whole volume of AFM materials.

Imry and Ma [52] were among the first to suggest that the orderly magnetic arrangement found in AFM materials could become unstable due to these imperfections, such as impurities that don't magnetize, either within the material or at the boundary between AFM and FM materials. This kind of instability often leads to the formation of separate magnetic regions, or domains, in the AFM material. Building on this, Nowak and others [53] showed that when AFM materials are placed in strong magnetic fields, these domains form because of differences between two types of sites within the AFM, caused by the impurities. The creation of these domain walls, or boundaries, helps lower the overall energy of the system and allows the walls to move more easily past the non-magnetic impurities. It's important to highlight that these insights were gained through the use of microscopic models, focusing on the very small scale.

The most notable mesoscopic model that incorporates non-ideal elements is proposed by Malozemoff [54–56], which builds upon the concepts introduced by Imry and Ma [52] for EB systems with blurred boundaries. In Malozemoff's approach, domain walls, oriented perpendicular to the boundary between AFM and FM materials, are favored energetically due to the surface irregularities at this interface (see Figure 2.12). These irregularities generate a random field that triggers the formation of domain walls within the AFM material. Specifically, the model focuses on a rough, atomic-scale interface in a compensated AFM, which can induce uncompensated spins necessary for the shift in the hysteresis loop. The randomness at the atomic

level of the interface, coupled with the assumption that the FM remains in a single-domain state, makes it energetically beneficial for the AFM to segment into domains. This segmentation minimizes the overall random unidirectional interfacial anisotropy. As a result, domain walls perpendicular to the interface and throughout the AFM's bulk are a permanent feature of the AFM layer. This is in contrast to the Mauri model, where parallel domain walls near the interface are temporarily formed during the reversal of the FM. The EB field in this model is described by:

$$H_{\mathrm{eb}} = \frac{2z\sqrt{A_{\mathrm{AFM}}K_{\mathrm{AFM}}}}{\pi^2 M_{\mathrm{FM}} t_{\mathrm{FM}}}$$

where:

- z is a factor close to one, influenced by the interface's roughness level,
- A_{AFM} and K_{AFM} are constants related to the antiferromagnetic material,
- M_{FM} and t_{FM} are the magnetization and thickness of the ferromagnetic layer, respectively.

Comparing the EB field values derived from these models with experimental data reveals a high level of accuracy [57–60].

Chapter 3

Experimental methods

This chapter provides a brief overview of the primary experimental methods utilized in the fabrication and characterization of vanadium oxide-based thin film heterostructures. The films were meticulously prepared using reactive DC magnetron sputtering, with precise control over parameters such as oxygen and argon flow rates, substrate temperature, DC power, and substrate orientation. A suite of characterization techniques, including X-ray diffraction (XRD), Reciprocal Space Mapping (RSM), and X-ray Reflectometry (XRR), was employed to investigate the crystal structure. The surface morphology of the films was examined using Atomic Force Microscopy (AFM). Magnetic properties were assessed using Vibrating Sample Magnetometry (VSM) and Magneto-Optical Kerr Effect (MOKE) measurements. Additionally, Polarized Neutron Reflectometry (PNR) was employed to study magnetic depth profiles, while Scanning Transmission Electron Microscopy (STEM) with advanced techniques such as High-Angle Annular Dark-Field (HAADF) imaging, Electron Energy Loss Spectroscopy (EELS) and Energy-Dispersive X-ray Spectroscopy (EDXS) were introduced to evaluate layer homogeneity and interface quality. This chapter provides a brief overview of the experimental framework employed in this study.

3.1 Thin film deposition

It is important to mention that in the process of depositing V_2O_3 thin films, one of the foremost challenges lies in the inherent complexity of the material's stoichiometry. V_2O_3 is known for its multiple non-stoichiometric phases, each with unique properties and behaviors. Controlling the deposition environment, particularly the oxygen partial pressure in the chamber, becomes critical to steer the thin film towards the desired phase. The oxygen level not only affects the sputtering and oxidation rates but also determines the final stoichiometric composition of the films. This aspect of V_2O_3 thin film deposition demands a high degree of precision and understanding, as the slightest deviation in stoichiometry can lead to the

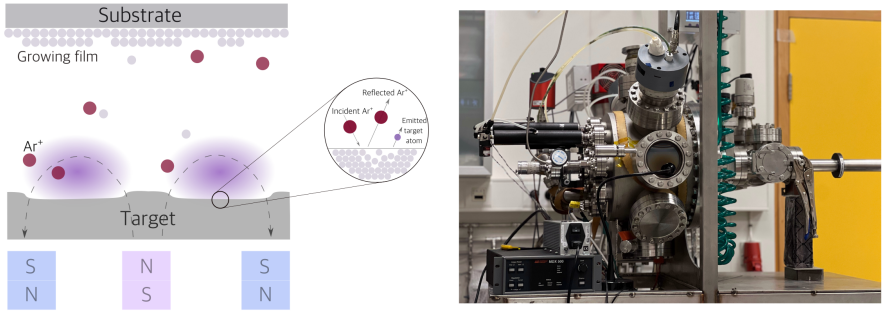

Figure 3.1: Left: Schematic representation of a DC magnetron sputtering equipment and deposition process. A direct current is used to create a plasma in a magnetically confined space, causing atoms to be sputtered from a target material onto a substrate. Right: The experimental sputtering chamber — SPIKE — used for the film depositions.

emergence of unintended phases, thereby impacting the film's overall properties and applicability. Magnetron sputtering is employed as a method that enables precise control over various deposition parameters, essential for the successful fabrication of thin films.

3.1.1 DC magnetron sputtering

Direct current magnetron sputtering is a physical vapor deposition technique used extensively to produce thin films. In this process, a target is bombarded with ions within a high-vacuum environment. The efficiency of this ion bombardment is significantly enhanced by a magnetron-generated magnetic field, which confines the plasma, thereby increasing the ionization rate and the subsequent sputtering of the target material.

A key aspect of this process, especially when depositing materials like vanadium sesquioxide (V_2O_3), is the flow rate of reactive gases, particularly oxygen and argon. The stoichiometry of vanadium oxide is highly sensitive to the oxygen content, as vanadium can exist in multiple oxidation states, each leading to different phases of the oxide. Precise control over the oxygen flow is essential to achieve the desired phase and properties of the V_2O_3 film. Insufficient oxygen can lead to oxygen-deficient phases, while excess oxygen can lead to higher oxidation states of vanadium. Other important factors include sputtering power and substrate temperature, which affect the mobility and arrangement of atoms on the surface, influencing the film's crystallinity and phase. The gas pressure in the chamber determines

the energy and density of the sputtered atoms, impacting the film's microstructure. Additionally, the deposition setup's geometry, such as the target-to-substrate distance and the angle of deposition, affects the film's uniformity and thickness. The growth process was carried out in a custom-built chamber, equipped with three 3-inch magnetrons (see Fig. 3.1(Right)) [61]. The base pressure of the chamber was kept below 4×10^{-6} Pa.

3.1.2 Sample composition

The composition and deposition procedures in the study were initially aimed at enhancing the structural qualities and the MIT in single V_2O_3 films. Single layers of V_2O_3 were deposted on various sapphire substrates (*a*-cut, *m*-cut, *c*-cut, *r*-cut) at different temperatures and with varying thicknesses to determine the optimal conditions for achieving the best structural qualities. This step was crucial in establishing a baseline for optimizing the structural properties and the MIT. Following this, heterostructures composed of V_2O_3 and magnetic layers (either Ni or Py) were deposited. These were aligned with the reference single V_2O_3 layers, maintaining identical deposition conditions to ensure consistency. For each magnetic heterostructure, a reference sample composed solely of the magnetic layer was prepared under the same deposition parameters, serving as a benchmark for comparison.

In this thesis, the results predominantly feature films grown on sapphire Al_2O_3 *c*-plane [0001] and *r*-plane [$1\bar{1}02$] substrates. All samples were grown using a reactive direct current (DC) magnetron sputtering. Some of these substrates were annealed in air at 1200 °C for a duration of 24 hours, while others were used without undergoing any annealing process. This distinction in substrate preparation allowed for a comparative analysis of the effects of annealing on the film growth and properties. The substrates underwent pre-baking under vacuum in the sputtering chamber at a temperature of 610 °C for $\sim$ 60 minutes prior to any growth. The V_2O_3 was deposited at different temperatures, whilst the magnetic layers (Ni or Py) and Zr layers were deposited predominantly at room temperature after allowing the sample to cool down under ultra-high vacuum. A Zr capping layer was added to the films to prevent oxidation.

3.2 Structural characterization

The study of material characterization is integral for assessing the stoichiometry, homogeneity, and crystallinity of materials, playing a pivotal role in understanding their properties and behaviors. This chapter covers

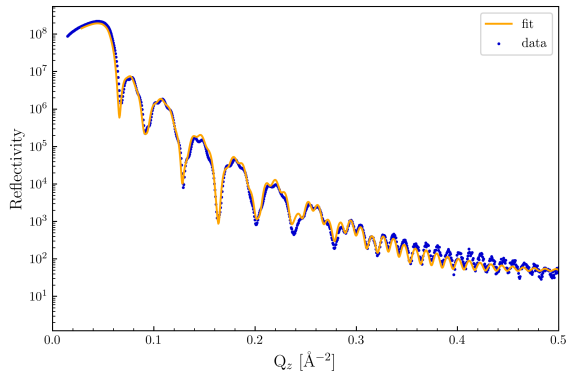

Figure 3.2: The exemplary XRR scan at room temperature with the fit for the V_2O_3/Ni/Zr film grown on *c*-plane Al_2O_3 [0 0 0 6] of thickness V_2O_3 = 58.1 nm, Ni = 9.4 nm, and Zr = 5.4 nm.

various material characterization techniques, including traditional methods like X-Ray Reflectivity, X-Ray Diffraction, and Reciprocal Space Mapping, along with advanced techniques like Scanning Transmission Electron Microscopy - High-Angle Annular Dark-Field, Electron Energy Loss Spectroscopy, Energy-Dispersive X-ray Spectroscopy, and Atomic Force Microscopy, offering a deeper understanding of the microstructural features.

3.2.1 X-Ray Reflectivity

X-ray Reflectometry is a robust and non-invasive technique widely used to measure film thickness, interface and surface roughness and density of films, excelling in determining electron density profiles perpendicular to the surface at scales ranging from 0.1 to 100 nm. In XRR measurements of thin films, the interference fringe pattern that is observed typically contains contributions from every layer within the film structure. This interference pattern arises from the constructive and destructive interference of X-rays that are scattered from different interfaces within the film. Figure 3.2 shows an exemplary XRR scan at room temperature, including the fit, for the V_2O_3/Ni/Zr film grown on *c*-plane Al_2O_3 [0 0 0 6]. The film has thicknesses of V_2O_3 = 58.1 nm, Ni = 9.4 nm, and Zr = 5.4 nm. XRR is particularly effective in analyzing hybrid heterostructures due to its sensitivity to electron density variations at interfaces and within individual layers. In this study, XRR was employed to determine the thickness, film mass density, and surface roughness of the samples.

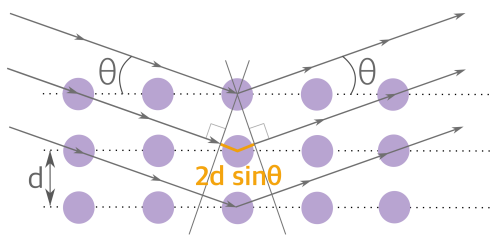

Figure 3.3: Visualisation of Braggs' Equation depicting the constructive interference of X-rays interacting with a crystal lattice, where an X-ray beam with wavelength λ hits atomic planes spaced at a distance d at an angle θ.

3.2.2 X-Ray Diffraction

X-ray Diffraction is a technique fundamentally based on the principle of constructive interference of X-rays, utilized for analyzing the crystallographic structure of materials. Throughout this research, XRD was employed to investigate the crystallinity, phase identification, and texture of both reference samples and bilayer structures. In XRD, the fundamental principle involves the oscillation of electrons within the atoms of a material in response to the alternating electromagnetic field of incident X-rays. This electron oscillation occurs at the same frequency as the incident X-rays, leading to constructive interference and the generation of a diffraction pattern that reveals the material's crystalline structure. Figure 3.3 provides a visualization of X-ray diffraction, where an X-ray beam with wavelength λ hits atomic planes, spaced at distance d, at an angle θ. This beam then deflects off these planes at the same angle θ relative to the crystalline plane. The phase difference between X-rays scattered from the first and second planes can be seen in the figure, highlighted in orange. Constructive interference occurs at specific angles, known as θ_B, which vary based on the spacing between these planes, d. This principle is defined in Equation 3.1, commonly known as the Bragg Equation.

$$n\lambda = 2d_{hkl} \sin \theta_B \tag{3.1}$$

In this equation, θ_B represents the Bragg angle, while the hkl subscript in the interplanar spacing d denotes the Miller indices of the crystallographic plane. The integer n denotes the order of the diffraction maxima, with $n = 1$ indicating the first order, $n = 2$ the second order, and so on. The Bragg Equation fundamentally links the angular position of diffracted X-rays to the lattice spacing, forming the basis of all XRD measurements.

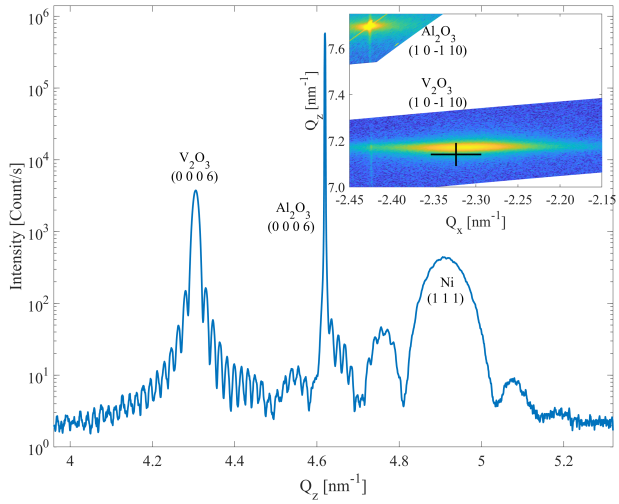

Figure 3.4: Representative X-ray diffraction scan and Reciprocal Space map in the inset recorded for the $Al_2O_3/V_2O_3/Ni/Zr$ film structure. The results reveal a well defined out-of-plane crystal growth with strong V_2O_3 (0 0 0 6) and Ni (1 1 1) peaks with Laue oscillations extending from both sides of the peaks. The reciprocal space map is perfomed around the (1 0 -1 10) peaks of V_2O_3 and Al_2O_3. The cross indicates the bulk V_2O_3 peak position.

A representative XRD scan recorded for the $V_2O_3/Ni/Zr$ film structure grown on *c*-plane Al_2O_3 sapphire is depicted in Figure 3.4.

3.2.3 Reciprocal Space Mapping

Reciprocal-space mapping is a measurement technique employed in X-ray diffraction. Reciprocal-space mapping is characterized by how X-ray diffraction intensity changes concerning variations in both an incident angle to the surface of the sample, ω, and 2θ angles. This mapping is achieved through a process where the incident angle ω and the diffraction angle 2θ are systematically adjusted to modify the direction and magnitude of the scattering vector within a specified range. Subsequently, X-ray diffraction measurements are conducted for each scattering vector within this range. This technique possesses significant capabilities, enabling the extraction of crucial information such as the in-plane and out-of-plane lattice constants of a film, the lateral correlation length, and mosaicity. The inset in Figure 3.4 displays an exemplary RSM scan recorded for the $V_2O_3/Ni/Zr$ film structure grown on *c*-plane Al_2O_3 sapphire substrate. This technique was used to examine the in-plane structural properties of the films relative to the substrate at room temperature (see Fig. 3.4). Additionally, High-

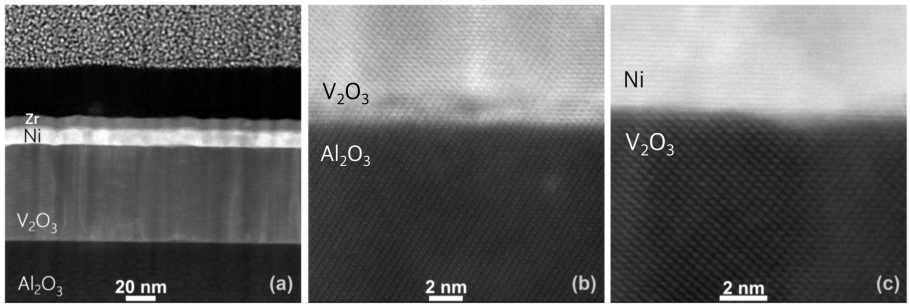

Figure 3.5: Experimental HAADF-STEM image of (a) the cross-section of the V_2O_3/Ni/Zr thin film on Al_2O_3 *c*-plane substrate, (b) the Al_2O_3/V_2O_3 interface, and (c) the V_2O_3/Ni interface. HAADF-STEM signal intensity (image grayscale) is proportional to atomic number.

resolution 3-dimensional reciprocal space mapping (3D-RSM), along with XRD and XRR, were employed to investigate the crystal microstructure and its structural evolution across the temperature-driven phase transition in V_2O_3 and V_2O_3/Ni films. The measurements across the transition utilizing 3D-RSM, XRD, and XRR were conducted at the BM28 (XMaS) beamline at the European Synchrotron Radiation Facility (ESRF) in Grenoble, France.

3.2.4 Scanning Transmission Electron Microscopy - High-Angle Annular Dark-Field

In the context of thin films, Transmission Electron Microscopy and its variant, Scanning Transmission Electron Microscopy, are especially valuable. When applying these techniques to thin films, a high-energy electron beam, typically in the range of 60 to 300 keV, is directed onto an ultra-thin, electron-transparent sample of the film. As electrons pass through the thin film, they experience both elastic and inelastic scattering due to interactions with the material's atoms. This scattering is crucial for image formation. In converting a conventional TEM to a STEM, an added system rasterizes a focused electron beam across the sample. This 'probe' is methodically scanned over the thin film, and the resulting electron scatter is detected and correlated with the probe's position to create an image. This approach is particularly useful for thin films as it allows for detailed analysis at high resolution [62].

The imaging modes in STEM are adapted based on the scattering angle of the electrons. For thin films, low-angle scattering (less than 10 mrad) is used in Bright-Field STEM and electron diffraction, offering insights into the crystalline structure of the film. This is particularly useful for

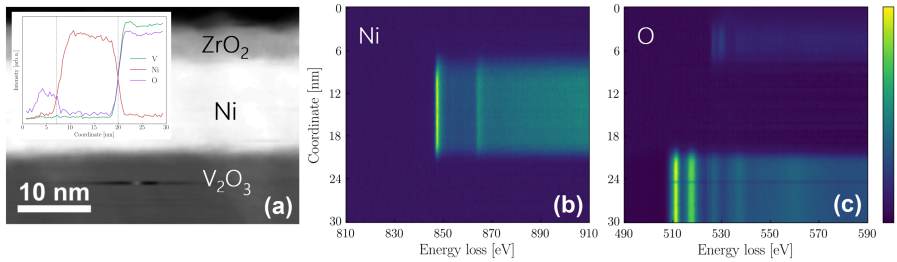

Figure 3.6: (a) Experimental HAADF-STEM image of the cross-section of the V_2O_3/Ni/Zr film; the inset shows corresponding V-, Ni-, and O- elemental profiles obtained by EELS. EELS structure evolution across the film and the interfaces for (b) Ni $L_{2,3}$-edge, (c) O K-edge. After extended exposure, the top capping layer undergoes oxidation, as confirmed by the analysis. Consequently, all scans were analyzed using a model that incorporates ZrO_2 atop the heterostructure. Notably, there is no presence of a NiO layer across the film.

understanding the film's composition and phase distribution. High-angle scattering (more than 50 mrad), used in High-Angle Annular Dark Field Scanning TEM, provides mass-thickness contrast, which is instrumental in visualizing variations in the film's density and thickness. An exemplary HAADF-STEM image is presented in Figure 3.5. In this project, HAADF-STEM was utilized to provide detailed information at the atomic scale, enabling the visualization of defects and the microstructure of the film. Additionally, it allowed for an examination of the interface quality and the verification of the presence of any interfacial layers or significant diffusion between layers that might impact the film's properties.

3.2.5 Energy-Dispersive X-ray Spectroscopy

During the process of inelastic scattering in electron microscopy, the electron beam transfers energy to the specimen's atoms. This transfer of energy can lead to the ionization of atoms and cause electrons within the atom to move between different energy levels. Such interactions generate various types of signals including energy-loss electrons, which are key in Electron Energy Loss Spectroscopy, as well as characteristic X-rays used in Energy-Dispersive X-ray Spectroscopy, and even visible light.

In the case of EDXS, inelastic interactions prompt the excitation and subsequent ejection of inner shell electrons from atoms. When these electrons are ejected, electrons from higher energy shells drop down to fill the vacancies created, releasing X-ray photons in the process. The energy of these emitted photons is specific to the difference between the two energy levels involved, and is unique for each element. By employing an

energy-dispersive spectrometer, it's possible to measure both the number and energy of these emitted X-rays, providing valuable information about the elemental composition of the specimen. In this research, EDXS was employed to analyze both the qualitative and quantitative elemental composition within layers and served as a complementary method for examining the elemental composition at interfaces.

3.2.6 Electron Energy Loss Spectroscopy

EELS, or Electron Energy Loss Spectroscopy, functions by detecting electrons that have interacted with the specimen. In this process, electrons that have lost energy due to these interactions are separated based on their kinetic energies using a magnetic prism. The distribution of these energy losses offers insights into several aspects of the specimen, such as its local elemental composition, the nature of chemical bonds, optical characteristics, and vibrational modes. Both EDXS and EELS techniques are capable of producing spectra that can be converted into quantitative images. In this project, using EELS enabled the verification of the chemical composition and oxidation state of V_2O_3 across the entire layer, confirming the consistent stoichiometry throughout the film. Additionally, it facilitated the examination of interface quality, specifically resolving whether an oxide interfacial NiO layer exists between the V_2O_3 and magnetic Ni layer, a factor significantly important for studying interface effects such as exchange bias. An illustrative scan showcasing these findings for the V_2O_3/Ni/Zr thin film on the Al_2O_3 r-plane substrate is presented in Figure 3.6. As can be observed from the line profiles and the evolution of elemental profiles across the film, there is no interfacial oxidation layer of NiO.

3.2.7 Atomic Force Microscopy

Atomic Force Microscopy is a high-resolution imaging technique that operates without the need for optics. It involves a flexible cantilever with a tip at its free end, controlled by a piezoelectric ceramic scanner for precise lateral and vertical positioning relative to the sample's surface. As the AFM tip moves across surface features of varying heights, it causes the cantilever to deflect. This deflection is monitored using a laser beam reflected from the cantilever's backside, which is directed into a position-sensitive photodetector. By combining the coordinates tracked by the atomic force microscopy tip during scanning, a 3D topographic image with subnanometer resolution of the surface is generated. In this work, AFM was employed to examine both the surface roughness and morphology of samples.

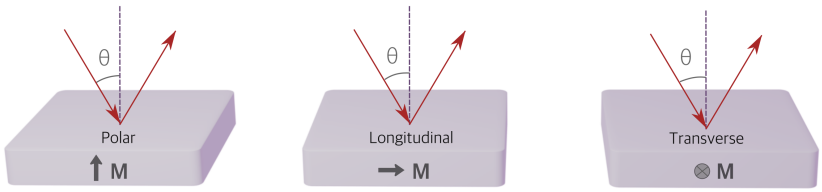

Figure 3.7: Various configurations of the magneto-optical Kerr effects: polar, longitudinal, and transverse.

3.3 Magnetic characterization

3.3.1 Magneto-Optical Kerr Effect

The Magneto-Optical Kerr Effect serves as a common technique employed to explore magnetic characteristics. MOKE is a phenomenon that is sensitive to surface properties and involves the use of linearly polarized light reflected from a magnetized surface. Upon interaction with the sample, the light undergoes ellipsoidal polarization, leading to a shift in the principal axis of polarization. This rotation is directly related to the magnetization of the reflecting surface and can be quantified, especially in the presence of a magnetic field, which results in the observation of hysteresis loops. In the context of MOKE configurations, three distinct types can be identified: polar, longitudinal, and transverse MOKE, , as shown in Fig. 3.7. The polar MOKE involves magnetization within the plane of incidence and perpendicular to the sample's surface. In the longitudinal MOKE, the magnetization also lies in the plane of incidence but aligns with the sample's plane. The transverse MOKE, meanwhile, features magnetization perpendicular to the plane of incidence and within the sample's plane. This setup enables localized measurements of magnetization changes in the sample, such as hysteresis loops, facilitated by the focused laser spot. In this study, a longitudinal MOKE setup is employed, offering the capability to adjust the azimuth angle of the sample, thereby allowing the examination of in-plane magnetic anisotropy. Another custom-built longitudinal MOKE setup without continuous rotation, at a fixed angle, was used for temperature-dependent measurements. This setup facilitated, for example, the measurement of coercivity behavior of the magnetic layer across the transition temperature of V_2O_3.

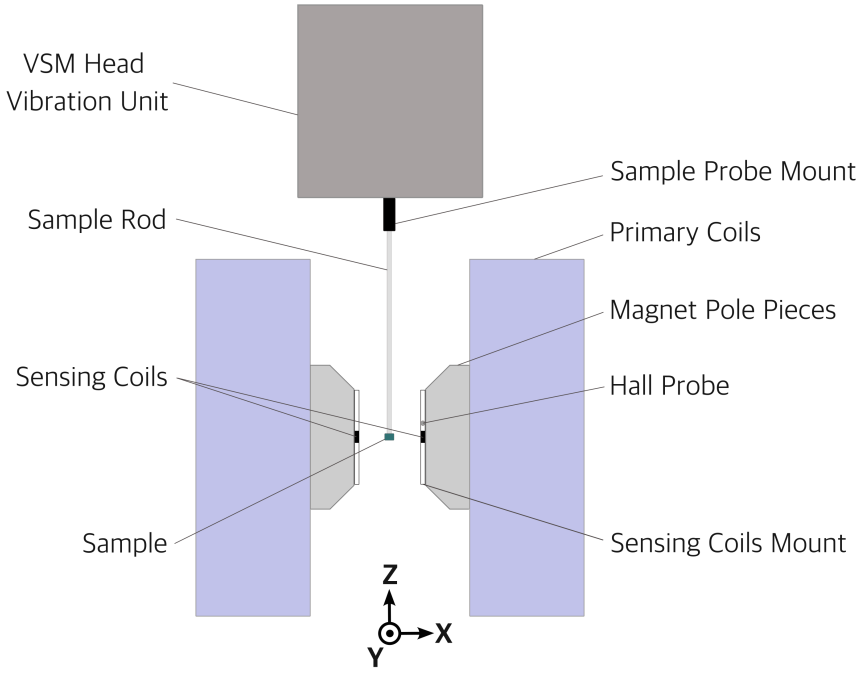

Figure 3.8: Schematic diagram of the Lakeshore 8600 Vibrating Sample Magnetometer.

3.3.2 Vibrating Sample Magnetometer

Vibrating sample magnetometers remain among the most adaptable systems for magnetic measurements. The basic design has remained consistent since its initial introduction in 1956 by Forner [63]. In the VSM technique [64, 65], a sample is positioned within specially designed coils, referred to as detection or pick-up coils. When a uniform magnetic field is applied, the sample develops a magnetic moment that correlates with its susceptibility and the applied field's intensity. As the sample vibrates, this creates an electrical signal in the coils in accordance with Faraday's law of induction. This signal is directly proportional to the sample's magnetic moment.

In this study, two commercial VSM systems were used. The first VSM, provided by Cryogenic Inc., features a cryogen-free magnet setup in a longitudinal configuration, where the pick-up coils are aligned with the applied magnetic field. This system is capable of producing magnetic fields of up to approximately 5 T and operates across a temperature range from 3 K to 325 K. The second one, the Lakeshore Model 8600, was the main

magnetometer used, as illustrated in Figure 3.8. The system includes sensing coils, an electromagnet with adjustable pole piece separation, a single-stage variable temperature (SSVT) option, a continuous flow cryostat, and a high-temperature oven. For the temperature-dependent measurements in a range of 300 K to 80 K, a single-stage variable temperature option was used alongside an electromagnet, being able to generate magnetic fields up to 2 T. Due to the small distance between the coils, specialized sample holders are required. A quartz bottom mount sample holder with a diameter of 5 mm was used to measure in-plane magnetization curves. The sample size is limited by 8 mm opening of the SSVT stage. Before measuring each distinct sample, an adjustment of the Z direction (see Fig. 3.8) was carried out to ensure the saturation magnetization was maximized, indicating proper placement. Accounting for the space between the opening gap and the sample rod, which has a 3 mm tolerance, it was assumed that the sample was centered in the X and Y directions without the need for adjustment measurements. Two main types of measurements were simultaneously conducted on each sample using the VSM system: simple magnetization curves measured at various temperature states across the V_2O_3 transition, and hysteresis loops recorded at different azimuthal angles at each temperature step. While measuring, the SSVT stage, cooled by liquid nitrogen, has a temperature stability of $\pm$ 1 K.

3.3.3 Polarized Neutron Reflectometry

The investigation of the magnetic profile's depth-dependence and its variation with temperature can be conducted using the Polarized Neutron Reflectivity method. A crucial distinction between X-rays and neutrons lies in the fact that neutrons possess a spin of $\frac{1}{2}$ and an associated magnetic moment. This unique property enables neutrons to scatter off the magnetic moments in the material being examined, a capability not present with X-rays. This method involves examining both nuclear and magnetic interactions, with a particular emphasis on the latter for the study of magnetic materials. In PNR techniques, the nuclear and magnetic Scattering Length Density (SLD) parameters are crucial for analyzing the structure and magnetic properties of layered materials. The magnetic SLD reveals the depth profile of the magnetization within the sample. Both profiles are derived from fitting models of the reflectivities profile. The interaction of neutrons in PNR is shaped by the relationship between the magnetization of the material and an external magnetic field. This relationship determines how the neutron's spin state will be affected during the scattering process. In simple terms, when the magnetization is parallel to the external field,

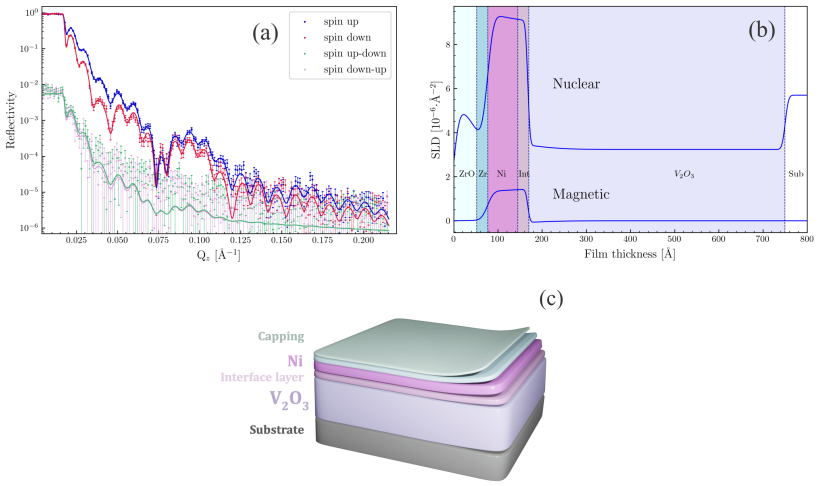

Figure 3.9: Representative polarized neutron reflectivities recorded for the V_2O_3/Ni/Zr film. (a) Specular neutron reflectivities at a temperature of 10 K and 5 kG. The solid lines show the best fit to the experimental data obtained using the BoToFit software [66, 67]. (b) Corresponding scattering length density profiles derived from the fit. (c) Schematic illustration of the fitting model.

the neutron retains its spin state. In contrast, when the magnetization is perpendicular, the neutron undergoes a change in its spin state. This leads to different types of scattering: non-spin flip when the spin state is retained, and spin flip when it changes. PNR uses a combination of devices like polarizers, spin-flippers, and analyzers to differentiate these scattering types. The polarizer and analyzer are designed to filter neutrons based on their spin state, relative to the external magnetic field's direction. Spin flippers, on the other hand, can alter the spin state of the neutrons. In PNR, the capability to distinguish four unique reflectivity types is based on the varying combinations of the neutron's spin state before and after its interaction with the sample. These combinations include up-up (uu), down-down (dd), down-up (du), and up-down (ud), corresponding to the different orientations of the two incoming and outgoing spin states of the neutrons. [68]. Figure 3.9(a) presents representative reflectivity curves for all four spin channels - *uu*, *dd*, *ud*, and *du*, obtained for the V_2O_3/Ni/Zr film. The fitting, using BoToFit software [66, 67], allowed for the extraction of both magnetic and nuclear scattering length density profiles across different depths, as depicted in Figure 3.9(b).

Chapter 4

V_2O_3-based hybrid magnetic heterostructures

Hybrid heterostructures offer a versatile approach to engineering material properties through the strategic combination of different materials, enabling the exploration of emergent phenomena with broad scientific and technological implications. Incorporating vanadium sesquioxide (V_2O_3) as part of hybrid heterostructures provides an intriguing opportunity to customize material capabilities through subtle manipulation of interfacial interactions, as V_2O_3 undergoes phase transitions. Combining V_2O_3 with magnetic layers, offers the possibility of novel functionalities driven by the interplay between the inherent electronic, structural, and magnetic changes in V_2O_3 and magnetic properties of the overlying layer. Controlling magnetism with external magnetic fields has its limits, leading to a growing need for non-magnetic methods to switch and adjust magnetism. In recent decades, there has been a significant effort to enhance the control of magnetism, primarily aimed at advancing magnetic storage technologies. Various methods like electric fields [69–71], currents [72, 73], pressure [74–76], thermal changes [77, 78], acoustic [79, 80], and light [81, 82] have been applied to alter magnetization. However, material options that meet all magnetic recording standards are limited. Utilizing the phase transitions in V_2O_3 present a novel method for adjusting the magnetic properties of the overlying magnetic layer. In this chapter, we delve into the experimental exploration of bilayer samples, each comprising a consistent V_2O_3 layer paired with different magnetic materials, namely Ni and Py ($Ni_{80}Fe_{20}$), across varying sapphire substrate planes. The choice of different crystalline orientations of the Al_2O_3 substrate, on which the V_2O_3 layer is grown, plays a pivotal role in shaping the microstructure and epitaxial quality of the V_2O_3 layer. This, in turn, has significant implications for the subsequent magnetic layer's properties.

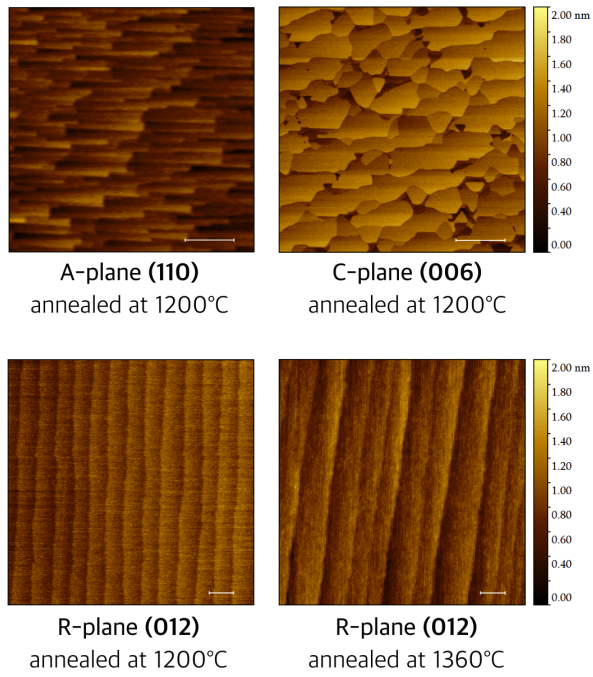

Figure 4.1: 5×5 μm^2 AFM images of different crystallographic planes of sapphire Al_2O_3 substrates annealed at various temperatures. The scale bars for *a*- and *c*-plane are 1 μm; for the *r*-plane, the scale bar is 100 nm.

4.1 Coercivity behaviour across the SPT

The choice of substrate plane significantly influences the microstructure of the V_2O_3 layer, thereby affecting the overall properties of bilayers. Various Al_2O_3 substrate orientations differ in surface terracing (as shown in Fig. 4.1) and lattice mismatches, which influence the V_2O_3 grain morphology and strain. This strain can be altered by annealing the substrate prior to growth, affecting the overall film properties. The smaller lattice mismatch between V_2O_3 and Al_2O_3 *c*-plane substrates enables the formation of highly epitaxial V_2O_3 (001) oriented films. Similarly, observed Laue oscillations in the Ni (111) peak confirms a well-defined crystalline structure of the Ni layer, indicating that the film layering is exceptionally defined with minimal roughness, as shown on Fig. 3.4. RSM, as shown in the inset of Fig. 3.4, reveals that the presence of a fully strained component in V_2O_3 originates from a fully strained interface layer with the substrate during the initial stages of growth. This is followed by film relaxation, leading to the appearance of a relaxed peak in the RSM. The magnetic response of such

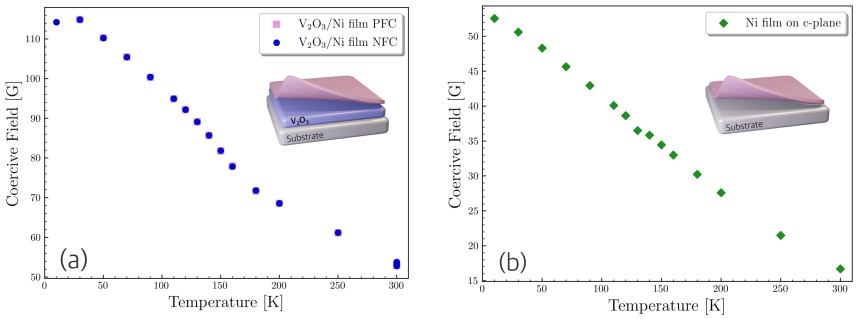

Figure 4.2: (a) Coercivity of the V_2O_3/Ni/Zr film recorded using VSM as a function of increasing temperature. The Ni layer deposited on V_2O_3 exhibits a notable strain-related increase in coercivity around 150 K, coinciding with the transition temperature of V_2O_3 (b) A reference single Ni layer sample directly deposited onto the Al_2O_3 substrate exhibits the typical increase in coercivity with temperature and shows no enhancement.

a highly crystalline heterostructure, as detailed in Paper I, temperature-dependent measurements under various field-cooling protocols unveiled an anticipated enhancement in coercivity upon cooling, accompanied by a noticeable change in the slope coinciding with the SPT of V_2O_3, as can be seen in Figure 4.2. This enhancement in coercivity, similar to observations by Polewczyk and De la Venta [83, 84], underscores the impact of strain in the Ni layer, a result of the structural transition within V_2O_3. This variation in the coercivity slope is attributed to the strain in the Ni layer induced by structural changes within V_2O_3.

Following the same recipe to achieve consistent crystallinity in the films, we shifted our focus to another magnetic layer - Permalloy (Py), composed of $Ni_{80}Fe_{20}$ (Paper II). High crystallinity of such hybrid structures can be achieved not only at room temperature but also at elevated temperatures (up to 400°C). However, Py did not exhibit any distinguishable magnetic response to the phase transition in V_2O_3. Furthermore, recent analyses using HAADF-STEM, EELS, and EDXS reveal that the Py layer consists of somewhat granular structures composed of Py ($Ni_{80}Fe_{20}$) with oxidized regions in between, according to EELS and STEM (see Figure 4.3). The roughness of the magnetic layer closely correlates with the roughness of both the substrate and the V_2O_3 layer, demonstrating a direct influence of the underlying surface properties on the topography of the magnetic layer. This correlation is consistent across all films fabricated on Al_2O_3 sapphire substrates. From recorded EELS spectra from O-K edges across different

regions—namely, the top Zr layer, inside Py grains, and the intergranular spaces, identified by cyan, blue, and pink squares respectively—it is evident that there is a complete absence of oxide within the Py grains (see Fig. 4.3 (b) - (d)). In contrast, the regions between the grains show signs of oxygen presence, similar to that observed in the upper portion of the oxidized Zr capping layer. The Py layer absorbs oxygen from V_2O_3, inferred from the presence of a 5-6 nm Zr capping layer initially intended to protect against oxygen intrusion from outside the film. We suggest that the oxygen migration occurs within the V_2O_3 layer towards Py, rather than from external sources. Consequently, while there could be a magnetic response to the structural transition in V_2O_3, accurately interpreting the changes occurring within the magnetic layer is challenging due to the complexity of the structure and elemental composition of the magnetic layer.

Growing V_2O_3 on *r*-plane sapphire, which has a larger lattice mismatch, results in increased roughness of the V_2O_3 layer and diminished epitaxial quality of the film with the formation of a textured Ni layer atop the V_2O_3, as evidenced by XRD in Figure 2.3. This also contributes to the altered microstructure of the V_2O_3 layer, observable in STEM Figure 4.4. Specifically, this includes the development of staircase-like features within the V_2O_3 layer and anti-phase boundaries (APBs) originating at the Al_2O_3/V_2O_3 interface, with the displacement vector aligned parallel to the *c*-plane <001> direction. After examining the structural properties of the V_2O_3/Ni film at room temperature, we then turned our focus to the low-temperature phase transition of V_2O_3/Ni films on sapphire *r*-plane substrates (detailed results outlined in Paper III). We assumed that the higher roughness of the V_2O_3 layer on the *r*-plane, combined with a larger mismatch between V_2O_3 and the substrate, and the presence of structural defects such as APBs, could have a more significant impact on the magnetic layer during the SPT than observed on the *c*-plane. The transition was studied through temperature-dependent RSM, XRD and XRR techniques at the BM28 (XMaS) beamline at the ESRF in Grenoble, France. The transition from the low temperature phase begins at about 110 K and extends up to about 155 K at which point the layer has fully transformed to the rhombohedral phase (see Fig. 2.3). Figure 4.5(a) shows the rhombohedral and monoclinic phase fractions determined from fits to the peaks shown in Figure 2.3 and normalized by their sum. The phase fractions' temperature dependency was analyzed using a cumulative skewed normal distribution, capturing the transition well with $\alpha = -0.1 \pm 0.6$ indicating minimal skewness. The transition width of 12.7 ± 0.3 K with a central point at 131.4 ± 0.5 K, illustrating the fit's effectiveness despite

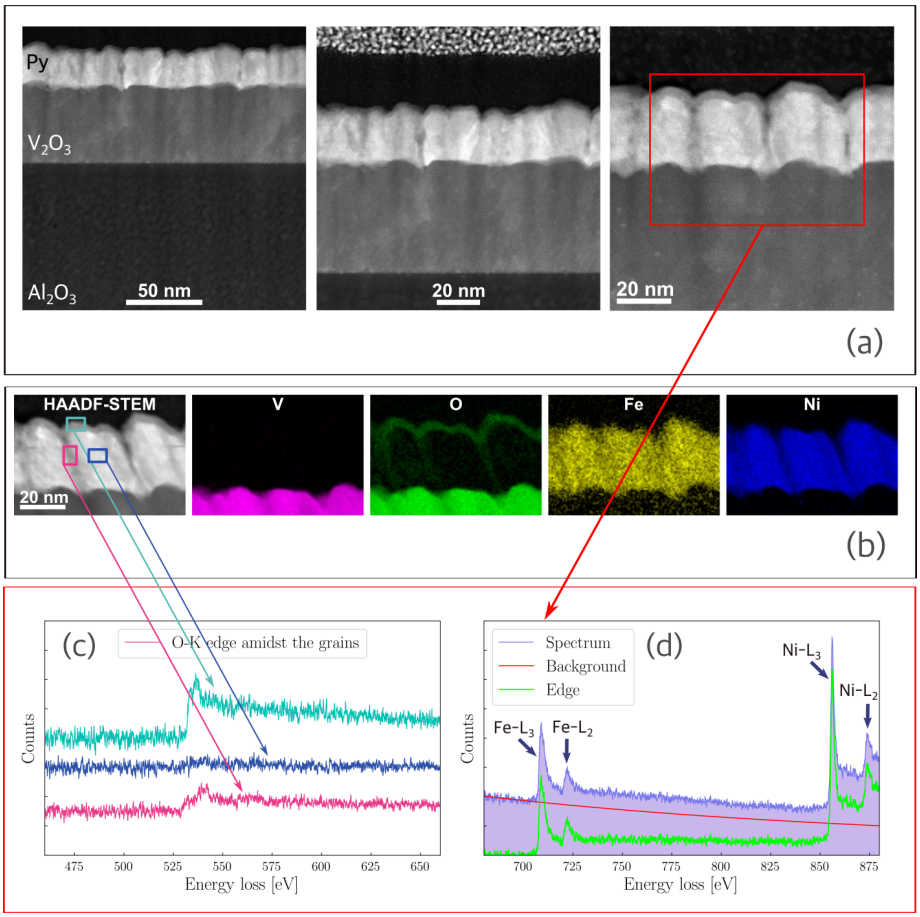

Figure 4.3: HAADF-STEM images of (a) the cross-section of the V_2O_3/Py/Zr thin film on the Al_2O_3 *r*-plane substrate and (b) EDX elemental mapping and (c), (d) STEM-EELS spectra taken from highlighted zones with indicated energy loss V-L and O-K edges. The HAADF-STEM signal intensity is proportional to atomic number and portrayed in the greyscale of the images.

its abstract nature. The thickness of the V_2O_3 layer follows the same trend as the phase fraction, indicating a correlation between the two. The temperature dependence of the V_2O_3 layer's roughness, extracted from the fitting of XRR profiles at different temperatures across the SPT upon heating, was modeled using the derivative of the cumulative skewed normal distribution, as shown in Figure 4.5 (b), (c). The following illustrates the conventional form of the skewed normal distribution:

$$f(x) = \frac{2}{\omega}\phi\left(\frac{x-\xi}{\omega}\right)\Phi\left(\alpha\left(\frac{x-\xi}{\omega}\right)\right) \tag{4.1}$$

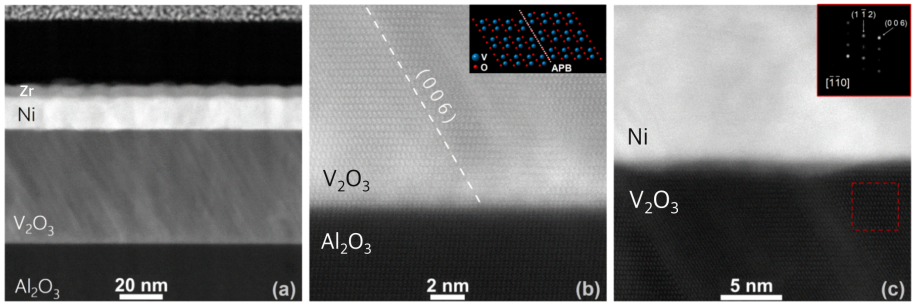

Figure 4.4: HAADF-STEM images of (a) the cross-section of the V_2O_3/Ni/Zr thin film on the Al_2O_3 r-plane substrate and (b) the Al_2O_3/V_2O_3 and (c) the V_2O_3/Ni interfaces. The HAADF-STEM signal intensity is proportional to atomic number and portrayed in the greyscale of the images. The dashed line in (b) illustrates the placement of an anti-phase boundary in the V_2O_3, schematically illustrated in the inset. The inset in (c) shows a diffractogram obtained Fourier transforming the image from the red square region in the V_2O_3 layer indexed as rhombohedral V_2O_3.

where:

- x is the variable,
- μ is the location parameter (mean),
- σ is the scale parameter (standard deviation),
- α is the shape parameter (skewness),
- $\phi(\cdot)$ is the standard normal PDF,
- $\Phi(\cdot)$ is the standard normal CDF.

Figure 4.5 shows a clear correlation between the phase fraction, the thickness, and the roughness of the V_2O_3 layer, especially across the phase coexistence region. During the phase coexistence region there is an increase in the surface roughness of the V_2O_3 layer, peaking at the midpoint of the transition. The RSM scans across the SPT reveal no secondary peaks or alterations in the lateral spread of the RSM peaks, ruling out any short-length scale periodicity in this specific case with a structure grown on the r-plane, where V_2O_3 has a thickness of around 50 nm. Consequently, it indicates that domain formation during the nanoscale phase formation does not occur, and the peak structure is dominated by the mosaic at all temperatures, remaining consistent throughout the phase transition. Therefore, we conclude that significant structural changes, associated with the competing phases, occur at a mesoscale. Interestingly, the coercivity

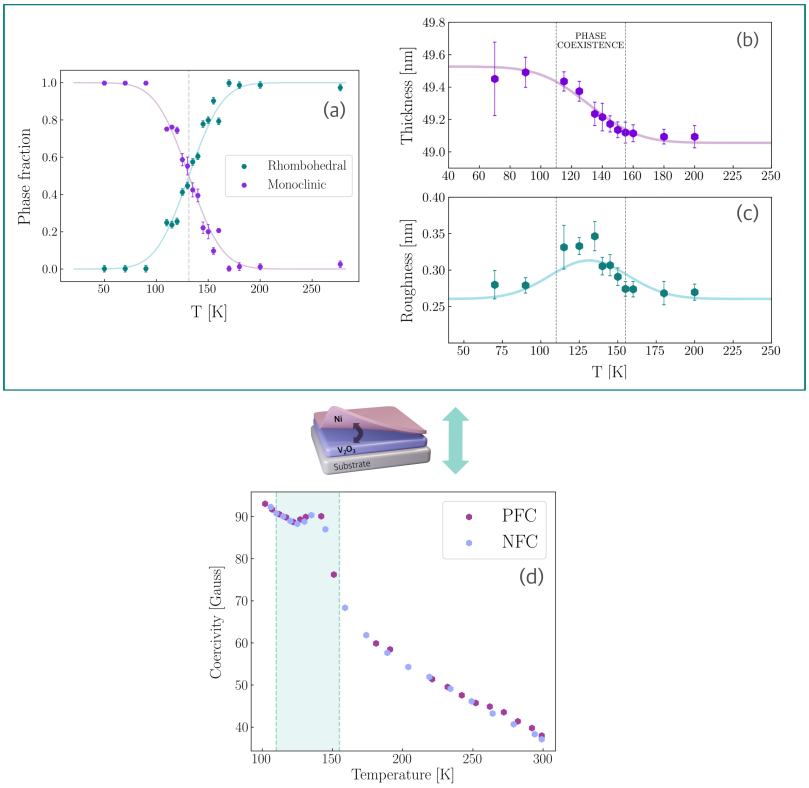

Figure 4.5: (a) Rhombohedral and monoclinic phase fractions of the V_2O_3 observed upon heating in the V_2O_3/Ni film. The dashed line indicates the temperature where the ratio of monoclinic and rhombohedral V_2O_3 phases are equal and it is at $\sim$ 131 K. (b) and (c) show the thickness and the roughness values of the V_2O_3 layer derived from the fit of the XRR profiles as a function of temperature, respectively. The error bars represent estimated systematic errors calculated in the fitting. Dashed lines indicate where the fractions of either of the two coexisting phases correspond to 5 %. (d) Coercivity of the V_2O_3/Ni film after PFC and NFC along the easy axis.

of the magnetic Ni layer in the film grown on the *r*-plane substrate is noticeably affected by the SPT of the V_2O_3. In the temperature range of 110 K to 155 K, where different phases of V_2O_3 coexist, there is a distinct peak in coercivity (see Figure 4.5 (d)). This peak is observed in the region where both phases coexist, along with an increase in roughness on the surface of the V_2O_3 layer, which puts strain on the nearby magnetic Ni layer. Ni that comes into contact with different phases of V_2O_3 experiences different strain. This uneven strain distribution leads to disorder in the Ni that depends on temperature, reaching its highest point when the volume fractions of the two phases are equal (around 131 K – 135 K). If the size

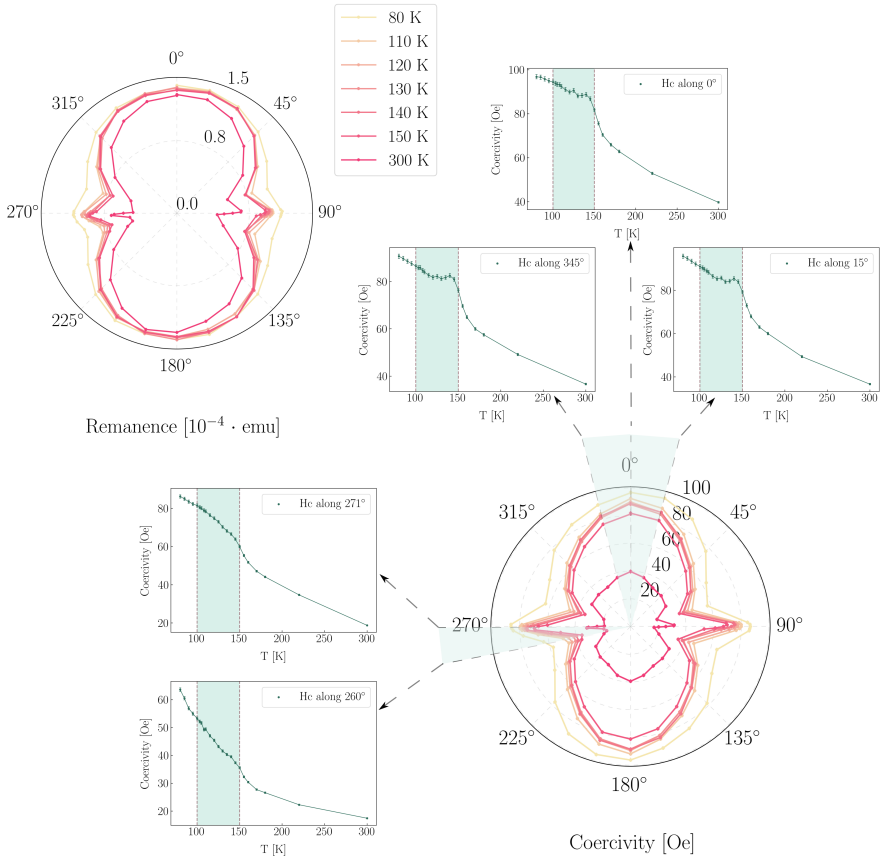

Figure 4.6: Temperature and azimuth angular dependence of magnetic properties: Coercivity and remanent magnetization M_{rem} for the V_2O_3/Ni film grown on the r-plane of Al_2O_3 substrate annealed at 1200°C. The effective magnetic anisotropy exhibits a gradual transition throughout the SPT of V_2O_3, without any abrupt changes. Insets show representative scans of detailed behavior of the coercive field across the SPT of the V_2O_3 along the hard and easy axes. The error bars in the figures are determined based on field accuracy measurements, defined as 1 % of the reading. Cyan dashed line areas indicate phase coexistence regions in the V_2O_3 during the SPT.

of the V_2O_3 domains is smaller than the size of the magnetic domains in Ni, the V_2O_3 domains can act as barriers at the boundary, separating the magnetic domains of Ni and pin the magnetic domain wall.

The enhancement of coercivity, shown as a peak in the phase coexistence region, was observed along a specific direction. A few studies have been performed to examine the effect of the SPT on the anisotropy of the mag-

netic layer, yet the results remain inconsistent, highlighting the complexity of each system and the need for further investigations [38, 85]. Following our initial discussions, we proceeded with a comprehensive study of the temperature dependence of coercivity along different in-plane directions across the SPT. Figure 4.6 shows results for the temperature-dependent evolution of the in-plane magnetic anisotropy within the V_2O_3/Ni magnetic heterostructure across the SPT. Insets detail the coercive field behavior across the SPT along the 0° and 90° in-plane angles, and in their vicinity. The magnetic anisotropy does not exhibit abrupt changes during the SPT of the V_2O_3, contrary to previous findings where a significant change in anisotropy occurred during the structural phase transition of the V_2O_3 [85, 86]. In our case, as the temperature decreases across the SPT, the magnetic anisotropy becomes slightly less pronounced, accompanied by the anticipated temperature-dependent increase in the coercivity of the Ni layer upon cooling. One possible reason for this might be the reduced thickness of the V_2O_3 layer. A thickness of 50 nm could be critical, lessening the impact of the structural phase transition on the coercive field and anisotropy of the magnetic layer [87]. As depicted in Figure 4.6, having two easy axes at 0° (180°) and 90° (270°), the coercivity's temperature-dependent behavior shows a distinct peak at the phase coexistence region exclusively along the primary easy axis at 0° (180°), whereas along the 90° (270°) easy axis and its vicinity, the changes in coercivity are significantly more gradual, indicating a strong directional dependence of Ni's magnetic properties on the SPT of the V_2O_3. Such directional differences in coercivity can be explained by the inhomogeneous distribution of metallic rhombohedral and insulating monoclinic states in the V_2O_3 layer during the phase coexistence region [18], which leads to an uneven stress distribution in the Ni layer. Previous experimental findings demonstrate that the SPT significantly influences the magnetic domain configuration within the Ni layer. Specifically, the spatial variability in V_2O_3's domain structure leads to localized variations in the magnetic properties of the Ni layer [86]. Such variability in stress distribution causes differential stress transfer to the Ni layer, resulting in distinct magnetic responses depending on the orientation. The angular dependence of coercivity changes can therefore be attributed to the coexistence of diverse magnetic anisotropies within the Ni layer, induced by this interfacial stress transfer during the V_2O_3's first-order SPT.

4.2 Exchange bias in V_2O_3/Ni films

In the previous discussion, we highlighted the influence of depositing films on the Al_2O_3 *c*-plane, which notably results in high crystallinity and a noticeable change in the temperature dependence of coercivity of the magnetic Ni layer. When cooling the heterostructures through the transition in V_2O_3 towards an AFM/FM interface at low temperatures, one can anticipate an exchange bias emerging at the transition temperature. This phenomenon has been reported by Sass et al. [88], who observed an exchange bias field in V_2O_3/Ni films grown on *c*-plane sapphire substrate. The exchange bias field appeared at the transition temperature of V_2O_3 in their case as well, with a strength of about 70 Oe. This was observed with a magnetic layer only 5 nm thick and a V_2O_3 layer that was about three times thinner. It's important to highlight that the phenomenon of exchange bias is roughly inversely proportional to the thickness of the FM layers [44] and it was also demostrated that EB correlates with the thickness of the AFM layer [89–92]. The magnetic transition in V_2O_3, as demonstrated by [28], is also sensitive to the V_2O_3 layer's thickness. Thus, with a magnetic layer almost three times thicker (13 - 14 nm), we anticipate a reduced magnitude of exchange bias in our system.

Coercivity, extracted from magnetization loops recorded using VSM as a function of increasing temperature after positive field cooling (PFC) and negative field cooling (NFC), was used to calculate the exchange field. The exchange bias was calculated using the following equation:

$$H_{\mathrm{EB}} = \frac{H_{c1} + H_{c2}}{2} \tag{4.2}$$

where H_{c1} and H_{c2} are the coercive fields measured for the ascending and descending branches of the hysteresis loop, respectively.

At first, exchange bias was observed in V_2O_3/Ni heterostructures grown on not annealed Al_2O_3 sapphire *c*-plane substrate, as described in Paper I [94]. As can be seen from Figure 4.7, there is a clear onset of exchange bias within this heterostructure at the SPT temperature of the V_2O_3. By changing the field cooling conditions from negative to positive, we effectively reverse the direction of the exchange bias, a characteristic behavior observed in exchange-biased systems. Additional measurements were conducted along a 90° orientation owing to the initial limitations of our first VSM setup (Cryogenic Inc.), which doesn't allow adjustments in the in-plane angle during measurement. It is important to mention that applying the field along 90° did not affect the exchange bias, demonstrating its angular

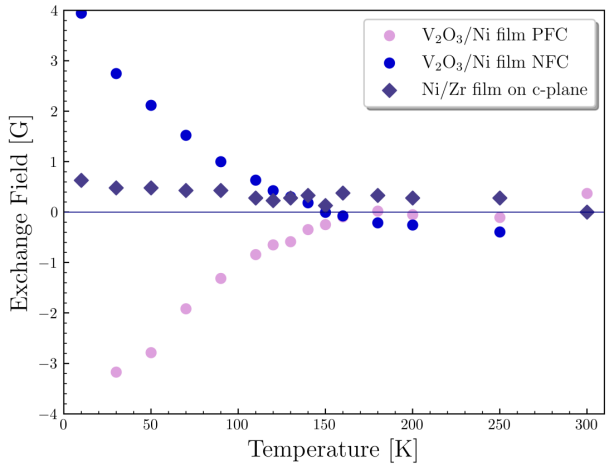

Figure 4.7: Exchange field for the V_2O_3/Ni/Zr film extracted from magnetization loops recorded using VSM as a function of increasing temperature after positive field cooling (PFC) under an applied field of 50 kG and negative field cooling (NFC) with a field of −50 kG. The reference sample (single Ni layer) showed no indication of an exchange bias. The presence of the in-plane exchange bias for the V_2O_3/Ni/Zr film was verified by carrying out both MOKE and VSM measurements. No differences are observed for both normal and field-cooled states as well as for sample orientations rotated in-plane 90°.

independence (not shown). As the onset of exchange bias coincides with the SPT temperature, we attribute the exchange bias to the phase transition occurring in the V_2O_3. The reference sample, consisting of a single layer of Ni (Fig. 4.7, violet squares), does not exhibit any onset of exchange bias. Analysis from PNR measurements for this hybrid heterostructure suggests that there's a roughly 2 nm thick layer at the V_2O_3/Ni interface, according to the model that fits the data best (see Fig. 3.9). Observations from HAADF-STEM and EELS measurements showed a sharp interface between V_2O_3 and Ni without any oxidized Ni layer. However, fitting the PNR model across the SPT presented challenges and further investigations are needed to investigate the magnetic interface properties in a more detailed manner.

Proceeding with the V_2O_3/Ni film grown on Al_2O_3 *r*-plane substrate, which exhibits a peak in coercivity and an increase in roughness within the phase coexistence region, this heterostructure similarly exhibits exchange bias at the SPT temperature of V_2O_3, yet with more complex behavior (Paper IV). Specifically, it shows dependence on both the in-plane angular direction and the direction of the applied field during cooling. Figure 4.8

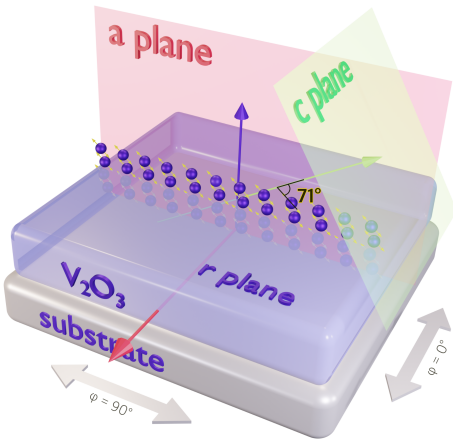

Figure 4.8: 3D schematic illustration of a film stack with the orientation of crystallographic planes and corresponding axes (based on XRD and FFT analyses from HAADF-STEM [6]. The yellow arrows suggest the general direction of vanadium magnetic moments in the AFM phase (perpendicular to the rhombohedral a-axis and inclined at an angle of 71° to the rhombohedral c-axis [93]). The grey arrows denote the azimuthal φ angles with respect to in-plane coercivity and exchange bias measurements. The cooling field was applied at distinct orientations of $\varphi = 0°$, 45°, and 90°. The illustration magnifies the position of vanadium atoms above the layer for visual emphasis.

presents a three-dimensional schematic of a film stack, highlighting both the crystallographic planes' orientations and the corresponding axes as determined by XRD and FFT from HAADF-STEM, detailed in Paper III. This figure further illustrates the orientation of vanadium magnetic moments in the low-temperature monoclinic phase, which align perpendicularly to the rhombohedral a-axis and form a 71° angle with the rhombohedral c-axis, according to [93]. The grey arrows represent the in-plane azimuthal φ angles. The cooling field was applied at orientations of 0°, 45°, and 90°. The magnitude of the applied magnetic field was ±5 kOe. Notably, altering the field strength to ±15 kOe did not influence the exchange bias's direction or magnitude under any cooling state. Regarding field cooling states, whether the applied field is positive or negative, it only affects the direction of the exchange bias. From Figure 4.9, it is evident that the application of a cooling field along 0° (180°) induces an exchange bias at 80 K, characterized by a complex unidirectional symmetry due to the field cooling-induced phase shift. Applying cooling field at 45° leads to a minor realignment of the exchange bias in the cooling field's direction, yet its

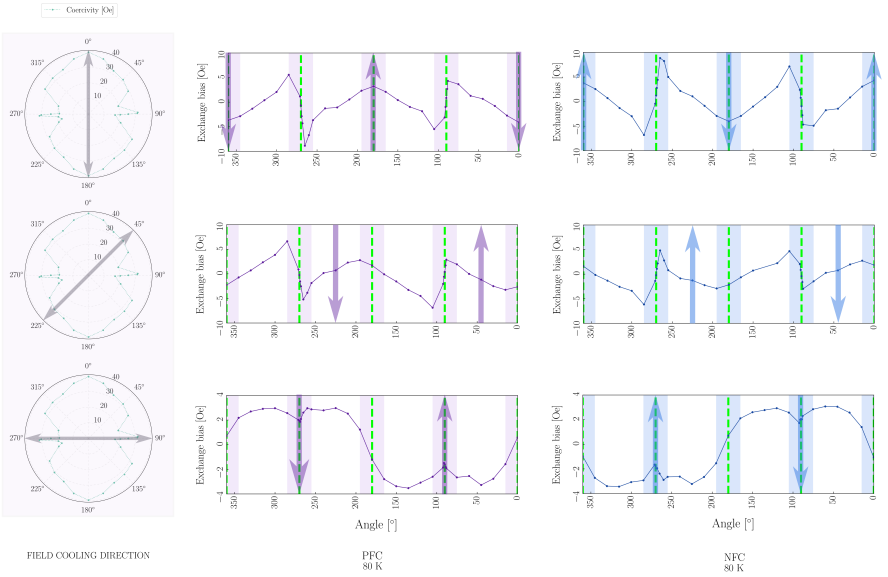

Figure 4.9: The in-plane angle dependence of H_{EB} at 80 K in response to both positive and negative field cooling modes with different applied field directions along 0°, 45°, and 90°. The applied magnetic field was -5 kOe (NFC) and +5 kOe (PFC). Measurements were conducted for increasing temperature. Arrows indicate the direction of field cooling. Dashed green lines denote the position of the easy axes of the film at 0° (180°) and 90° (270°).

unidirectional symmetry is preserved. A significant alteration occurs when the cooling field is applied along 90° (270°), as shown in the lowest row of Figure 4.9, where the exchange bias undergoes a notable change, becoming almost fully unidirectional in nature.

The impact of the field cooling direction is further illustrated in Figures 4 and 5 of Paper IV, which feature contour plots depicting the exchange bias intensity as a function of temperature and azimuthal angle under distinct field cooling conditions: along the primary easy axis at 0° (180°) and along the easy axis at 90° (270°), respectively, including detailed temperature and angular exchange bias behavior plots at various angles. The onset of exchange bias appears to be always at the transition temperature in V_2O_3 for all the cooling states, as can be seen from the detailed exchange bias plots along specific angles. Notably, applying field cooling along the 90° (270°) axis shows a more uniform intensity across the phase transition, in contrast to the primary easy axis at 0° (180°) direction, which exhibits significant intensity variation with azimuthal angle, especially in the transition region where both phases coexist, as illustrated in Fig. 4 (Paper IV). When

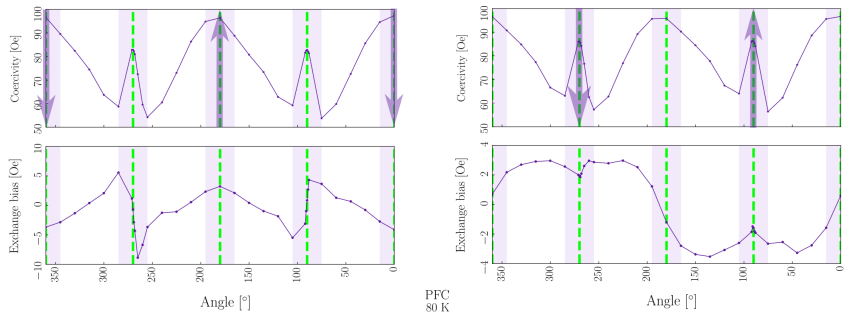

Figure 4.10: The azimuthal dependence of coercivity and exchange bias in Oe at 80 K for two positive field cooling states of +5 kOe: along the primary easy axis at 0° (180°) and along the secondary axis at 90° (270°). Arrows represent the field cooling direction. Dashed green lines denote easy axes at 0° (180°) and 90° (270°).

cooling the sample with an applied field along 0° (180°), the exchange bias exhibits peaks along and in the vicinity of the axis at 90° (270°), where coercivity behaves rather smoothly without displaying any peaks. Conversely, along the primary easy axes, where coercivity exhibits peaks in the phase coexistence region, the peaks in exchange bias are less pronounced. This observation suggests a strong correlation between the coercivity and exchange bias behavior along different crystallographic directions. This pronounced correlation fades when the cooling field is oriented along the 90° (270°) axis and it exhibits a more stable behavior across the temperature range with reduced anisotropy (see Figure 5 in Paper IV). Here, the exchange bias incrementally increases during cooling, with the absence of sharp changes during the phase transition in V_2O_3. Figure 4.10 displays coercivity and exchange bias as functions of azimuthal angles at 80 K across various cooling states, showcasing a correlation between exchange bias and coercivity akin to that identified in prior studies [95–97]. Cooling with an applied field along the 90° (270°) direction, coinciding with the spin alignment plane of the V moments, leads to a more commonly expected in-plane angular behavior of the exchange bias, correlated with the coercivity [95–97]. Conversely, a cooling field applied along the primary easy axis, perpendicular to the V moment alignment and presumably less effective for coupling, exhibits increased sensitivity to structural changes during the SPT, culminating in a less uniform and more inhomogeneous exchange bias across the coexistence region.

In conclusion, our research consistently shows that exchange bias in V_2O_3/Ni heterostructures emerges at the transition temperature of V_2O_3, independent of the substrate used (Al_2O_3 *c*-plane or *r*-plane), the cooling

state or along which in-plane angle magnetic hysteresis loops were recorded. However, we observed significant variations in the behavior of exchange bias and coercivity. For heterostructures with high epitaxial quality, the exchange bias and coercivity remain consistent regardless of the angle at which the cooling field is applied, as confirmed by measurements taken in-plane angles at 0° and 90° (due to the limitations of our first VSM system). Conversely, magnetic heterostructures of V_2O_3/Ni grown on Al_2O_3 *r*-plane exhibit a more complex dependence on the states of the cooling field and angular orientation. The intricate relationship between the structural composition of V_2O_3/Ni heterostructures and phase transitions of V_2O_3 plays a pivotal role in their magnetic coupling, which further underscores the complicated interplay affecting exchange bias. This dependency on the system's composition extends to the phenomena observed when considering the effects of field cooling states and the angles at which these fields are applied. The high sensitivity of exchange bias to these factors can be attributed to how the structural and microstructural properties of the antiferromagnetic V_2O_3 layer influence the magnetic coupling mechanisms at the interface with the Ni layer.

Chapter 5

Conclusion & Outlook

In conclusion, this thesis delves into the intricate world of V_2O_3, a material whose crystal properties are significantly influenced by how it is deposited and the type of underlying surfaces (substrates) used. Depending on these factors, V_2O_3 displays varied crystal qualities and microstructural characteristics, which in turn, distinctly affect its SPT and MIT (and potentially its magnetic transition as well). Small differences in its microstructure have a significant effect, leading to diverse interactions and coupling with the magnetic layer placed on top of the V_2O_3. By carefully adjusting the deposition conditions and choosing specific substrates, we can control these microstructural, structural and electronic properties of the V_2O_3. This manipulation allows us to control the SPT within V_2O_3 more precisely. As a result, we uncover a broader range of possibilities for influencing and controlling the magnetism in the overlying magnetic layer throughout the SPT. Additionaly, it uncovers more complexity in how V_2O_3 interacts magnetically with the layer on top of it. This could lead to fresh ideas on how we can control and manipulate magnetic properties more effectively. Essentially, I hope this research shows us new insights on possibilities of how to adjust and use the magnetism in materials put on V_2O_3. By learning about and controlling the small changes in V_2O_3, we can make materials with magnetic properties that we can set as we like.

The study of vanadium oxides, especially V_2O_3, represents a promising frontier in the exploration of phase transitions in correlated electron systems and the control of magnetic properties. For a deeper understanding of V_2O_3's unique behaviors, it's clear that a more detailed examination of the phase coexistence area is needed, especially considering layers with varying microstructures and thicknesses. The presence of microstructural defects, such as antiphase boundaries, could significantly impact the material's properties, including its MIT and SPT. The presence of such defects can alter the local electronic structure, potentially stabilizing one phase over another or affecting the transition's kinetics by providing nucleation sites. In V_2O_3, which experiences both a MIT and a SPT, these defects could

change not only when the transition happens but also how abrupt and pronounced these changes are. Investigating the phase coexistence more closely, particularly in layers of varying thickness on highly crystalline films (such as on sapphire *c*-plane), could reveal how thickness affects this transition region. The thickness might influence how much the insulating domains of the material are stressed, especially closer to the substrate, which in turn could dictate the shape that domains take. Such stressing effect, and how it potentially could vary with the thickness of the V_2O_3 layer, could prevent the phases from evolving independently or with different dynamics. Therefore, a more detailed exploration of the phase coexistence region, looking into the distribution of phase fractions and microstrain, could be valuable. Techniques like high-resolution RSM and STEM could offer precise insights across these transitions, shedding light on the intricate coexistence of phases in V_2O_3.

The interaction between Ni and V_2O_3 in their combined magnetic structure offers a promising research frontier, especially in understanding and controlling magnetism. By studying the magnetic domains in Ni as V_2O_3 undergoes its SPT, we can gain insights into how these transitions influence magnetism at a very detailed level. Techniques like neutron scattering and advanced STEM, including analysis of strain through 4D STEM where each pixel contains convergent beam electron diffraction data, Lorentz electron microscopy and off-axis holography [98–100], are valuable tools. Employing these methods will allow the observation of the magnetic field distribution in Ni during the V_2O_3 transition revealing the distribution of magnetic fields within Ni domains, providing valuable information on which exchange bias mechanisms might work in such a complex system. This consideration of phase coexistence regions, which display a spatial inhomogeneity particularly relevant to magnetic transitions in V_2O_3, underscores the importance of understanding these interactions. Such understanding can lead to more precise control over the magnetic properties of hybrid structures, opening up new possibilities for applications in technology and research. Further examination is essential for the exchange bias measurements, for instance, utilizing Lorentz microscopy within 4D STEM can enable the detailed study of reversal mechanisms in exchange-biased V_2O_3/Ni bilayers. Having the opportunity to examine both strain and magnetic field distribution will facilitate a deeper understanding of the direction of exchange anisotropy, particularly in terms of exchange bias and its dependence on strain, which, as previously demonstrated, exhibits significant coupling [101].

Additionally, exploring the magnetic transition in V_2O_3 and its coupling with the SPT is crucial, as limited research has been conducted in this area,

especially in thin film form, highlighting the need for further investigation to fully understand these complex interactions.

Bibliography

[1]C. Griffiths and H. Eastwood, "Influence of stoichiometry on the metal-semiconductor transition in vanadium dioxide," Journal of Applied Physics **45**, 2201–2206 (1974).

[2]Z. Yang, C. Ko, and S. Ramanathan, "Annu. rev. mater. res," Annu. Rev. Mater. Res **41** (2011).

[3]R.-P. Blum, H. Niehus, C. Hucho, R. Fortrie, M. V. Ganduglia-Pirovano, J. Sauer, S. Shaikhutdinov, and H.-J. Freund, "Surface metal-insulator transition on a vanadium pentoxide (001) single crystal," Physical review letters **99**, 226103 (2007).

[4]M. Kang, I. Kim, S. W. Kim, J.-W. Ryu, and H. Y. Park, "Metal-insulator transition without structural phase transition in V_2O_5 film," Applied physics letters **98** (2011).

[5]K. Kosuge, "The phase diagram and phase transition of the V_2O_3 - V_2O_5, system," Journal of Physics and Chemistry of Solids **28**, 1613–1621 (1967).

[6]K. Ignatova, E. Vlasov, S. D. Seddon, N. Gauquelin, J. Verbeeck, D. Wermeille, S. Bals, T. P. A. Hase, and U. B. Arnalds, "Phase coexistence induced surface roughness in V_2O_3/Ni magnetic heterostructures," Submitted to APL Materials, under review, 2024.

[7]I. Yamaguchi, T. Manabe, T. Kumagai, W. Kondo, and S. Mizuta, "Preparation of epitaxial V_2O_3 films on C-, A-and R-planes of α-Al_2O_3 substrates by coating-pyrolysis process," Thin Solid Films **366**, 294–301 (2000).

[8]J. Brockman, M. Samant, K. Roche, and S. Parkin, "Substrate-induced disorder in V_2O_3 thin films grown on annealed c-plane sapphire substrates," Applied Physics Letters **101** (2012).

[9]E. B. Thorsteinsson, S. Shayestehaminzadeh, and U. B. Arnalds, "Tuning metal-insulator transitions in epitaxial V_2O_3 thin films," Applied Physics Letters **112**, 161902 (2018).

[10]H. Hajihoseini, E. B. Thorsteinsson, V. V. Sigurjonsdottir, and U. B. Arnalds, "Strained interface layer contributions to the structural and electronic properties of epitaxial V_2O_3 films," Applied physics letters **118** (2021).

[11]M. Sultan, K. Ignatova, E. Thorsteinsson, and U. Arnalds, "Structural morphology and electrical transitions of V_2O_3 thin films grown on SiO_2/Si by high power impulse magnetron sputtering," Thin Solid Films **742**, 139048 (2022).

[12]D. McWhan, J. Remeika, T. Rice, W. Brinkman, J. Maita, and A. Menth, "Electronic specific heat of metallic Ti-doped V_2O_3," Physical review letters **27**, 941 (1971).

[13]J. G. Ramirez, T. Saerbeck, S. Wang, J. Trastoy, M. Malnou, J. Lesueur, J.-P. Crocombette, J. E. Villegas, and I. K. Schuller, "Effect of disorder on the metal-insulator transition of vanadium oxides: local versus global effects," Physical Review B **91**, 205123 (2015).

[14]F. Mazzola, S. K. Chaluvadi, V. Polewczyk, D. Mondal, J. Fujii, P. Rajak, M. Islam, R. Ciancio, L. Barba, M. Fabrizio, et al., "Disentangling structural and electronic properties in V_2O_3 thin films: A genuine nonsymmetry breaking Mott transition," Nano Letters **22**, 5990–5996 (2022).

[15]A. Ronchi, P. Franceschini, A. De Poli, P. Homm, A. Fitzpatrick, F. Maccherozzi, G. Ferrini, F. Banfi, S. S. Dhesi, M. Menghini, et al., "Nanoscale self-organization and metastable non-thermal metallicity in mott insulators," Nature Communications **13**, 3730 (2022).

[16]P. Dernier and M. Marezio, "Crystal structure of the low-temperature antiferromagnetic phase of V_2O_3," Physical Review B **2**, 3771 (1970).

[17]D. McWhan and J. Remeika, "Metal-insulator transition in $(V_{(1-x)}Cr_x)_2O_3$," Physical Review B **2**, 3734 (1970).

[18]A. McLeod, E. Van Heumen, J. Ramirez, S. Wang, T. Saerbeck, S. Guenon, M. Goldflam, L. Anderegg, P. Kelly, A. Mueller, et al., "Nanotextured phase coexistence in the correlated insulator V_2O_3," Nature Physics **13**, 80–86 (2017).

[19]S. Guénon, S. Scharinger, S. Wang, J. Ramırez, D. Koelle, R. Kleiner, and I. K. Schuller, "Electrical breakdown in a V_2O_3 device at the insulator-to-metal transition," Europhysics Letters **101**, 57003 (2013).

[20]D. McWhan, A. Menth, J. Remeika, W. Brinkman, and T. Rice, "Metal-insulator transitions in pure and doped V_2O_3," Physical Review B **7**, 1920 (1973).

[21]E. B. Thorsteinsson, S. Shayestehaminzadeh, A. S. Ingason, F. Magnus, and U. B. Arnalds, "Controlling metal–insulator transitions in reactively sputtered vanadium sesquioxide thin films through structure and stoichiometry," Scientific Reports **11**, 1–10 (2021).

[22]N. F. Mott, "The basis of the electron theory of metals, with special reference to the transition metals," Proceedings of the Physical Society. Section A **62**, 416 (1949).

[23]M. Fath, S. Freisem, A. Menovsky, Y. Tomioka, J. Aarts, and J. Mydosh, "Spatially inhomogeneous metal-insulator transition in doped manganites," Science **285**, 1540–1542 (1999).

[24]A. Sharoni, J. G. Ramırez, and I. K. Schuller, "Multiple avalanches across the metal-insulator transition of vanadium oxide nanoscaled junctions," Physical Review Letters **101**, 026404 (2008).

[25]S. Wang, J. G. Ramırez, and I. K. Schuller, "Avalanches in vanadium sesquioxide nanodevices," Physical Review B **92**, 085150 (2015).

[26]A. Shekhawat, S. Papanikolaou, S. Zapperi, and J. P. Sethna, "Dielectric breakdown and avalanches at nonequilibrium metal-insulator transitions," Physical Review Letters **107**, 276401 (2011).

[27]F. Morin, "Oxides which show a metal-to-insulator transition at the neel temperature," Physical review letters **3**, 34 (1959).

[28]B. A. Frandsen, Y. Kalcheim, I. Valmianski, A. S. McLeod, Z. Guguchia, S. C. Cheung, A. M. Hallas, M. N. Wilson, Y. Cai, G. M. Luke, et al., "Intertwined magnetic, structural, and electronic transitions in V_2O_3," Physical Review B **100**, 235136 (2019).

[29]E. R. Fletcher, K. Higashi, Y. Kalcheim, H. Kageyama, and B. A. Frandsen, "Uniform structural phase transition in V_2O_3 without short-range distortions of the local structure," Physical Review B **104**, 184115 (2021).

[30]J. Trastoy, A. Camjayi, J. Del Valle, Y. Kalcheim, J.-P. Crocombette, D. A. Gilbert, J. Borchers, J. Villegas, D. Ravelosona, M. Rozenberg, et al., "Magnetic field frustration of the metal-insulator transition in V_2O_3," Physical Review B **101**, 245109 (2020).

[31]W. Bao, C. Broholm, G. Aeppli, S. Carter, P. Dai, T. Rosenbaum, J. Honig, P. Metcalf, and S. Trevino, "Magnetic correlations and quantum criticality in the insulating antiferromagnetic, insulating spin liquid, renormalized Fermi liquid, and metallic antiferromagnetic phases of the Mott system V_2O_3," Physical Review B **58**, 12727 (1998).

[32]W. Bao, C. Broholm, G. Aeppli, P. Dai, J. Honig, and P. Metcalf, "Dramatic switching of magnetic exchange in a classic transition metal oxide: evidence for orbital ordering," Physical review letters **78**, 507 (1997).

[33]D. Mapps, "Magnetoresistive sensors," Sensors and Actuators A: Physical **59**, 9–19 (1997).

[34]E. C. Stoner and E. Wohlfarth, "A mechanism of magnetic hysteresis in heterogeneous alloys," Philosophical Transactions of the Royal Society of London. Series A, Mathematical and Physical Sciences **240**, 599–642 (1948).

[35]W. F. Brown, "Magnetostatic principles in ferromagnetism," (1962).

[36]S. Blundell, *Oxford master series in condensed matter physics*, 2001.

[37]D. Jiles, *Introduction to magnetism and magnetic materials*, 1998.

[38]D. A. Gilbert, J. G. Ramırez, T. Saerbeck, J. Trastoy, I. K. Schuller, K. Liu, and J. de la Venta, "Growth-induced in-plane uniaxial anisotropy in V_2O_3/Ni films," Scientific reports **7**, 1–9 (2017).

[39]X. Xu, L. Jin, T. Wen, Y. Liao, X. Tang, H. Zhang, and Z. Zhong, "Effects of substrate annealing on uniaxial magnetic anisotropy and ferromagnetic resonance frequency of $Ni_{80}Fe_{20}$ films deposited on self-organized periodically rippled sapphire substrates," Vacuum **186**, 110047 (2021).

[40]T. Schulthess and W. Butler, "Consequences of spin-flop coupling in exchange biased films," Physical review letters **81**, 4516 (1998).

[41]B. Miller and E. D. Dahlberg, "Use of the anisotropic magnetoresistance to measure exchange anisotropy in Co/CoO bilayers," Applied physics letters **69**, 3932–3934 (1996).

[42]N. Koon, "Calculations of exchange bias in thin films with ferromagnetic/antiferromagnetic interfaces," Physical review letters **78**, 4865 (1997).

[43]J. Nogués, J. Sort, V. Langlais, V. Skumryev, S. Suriñach, J. Muñoz, and M. Baró, "Exchange bias in nanostructures," Physics reports **422**, 65–117 (2005).

[44]J. Nogués and I. K. Schuller, "Exchange bias," Journal of Magnetism and Magnetic Materials **192**, 203–232 (1999).

[45]W. H. Meiklejohn and C. P. Bean, "New magnetic anisotropy," Physical review **102**, 1413 (1956).

[46]W. Meiklejohn, "Exchange anisotropy—a review," Journal of Applied Physics **33**, 1328–1335 (1962).

[47]I. Jacobs and J. Kouvel, "Exchange anisotropy in mixed manganites with the hausmannite structure," Physical Review **122**, 412 (1961).

[48]W. H. Meiklejohn and C. P. Bean, "New magnetic anisotropy," Physical Review **105**, 904 (1957).

[49]J. Kouvel, "A ferromagnetic-antiferromagnetic model for copper-manganese and related alloys," Journal of Physics and Chemistry of Solids **24**, 795–822 (1963).

[50]E. Fulcomer and S. Charap, "Thermal fluctuation aftereffect model for some systems with ferromagnetic-antiferromagnetic coupling," Journal of Applied Physics **43**, 4190–4199 (1972).

[51]L. Néel, "Étude théorique du couplage ferro-antiferromagnétique dans les couches minces," in Annales de physique, Vol. 14, 2 (1967), pp. 61–80.

[52]Y. Imry and S.-k. Ma, "Random-field instability of the ordered state of continuous symmetry," Physical Review Letters **35**, 1399 (1975).

[53]U. Nowak, K.-D. Usadel, J. Keller, P. Miltényi, B. Beschoten, and G. Güntherodt, "Domain state model for exchange bias. i. theory," Physical review B **66**, 014430 (2002).

[54]A. Malozemoff, "Random-field model of exchange anisotropy at rough ferromagnetic-antiferromagnetic interfaces," Physical review B **35**, 3679 (1987).

[55]A. Malozemoff, "Mechanisms of exchange anisotropy," Journal of Applied Physics **63**, 3874–3879 (1988).

[56]A. Malozemoff, "Heisenberg-to-ising crossover in a random-field model with uniaxial anisotropy," Physical Review B **37**, 7673 (1988).

[57]E. Maniv, R. A. Murphy, S. C. Haley, S. Doyle, C. John, A. Maniv, S. K. Ramakrishna, Y.-L. Tang, P. Ercius, R. Ramesh, et al., "Exchange bias due to coupling between coexisting antiferromagnetic and spin-glass orders," Nature Physics **17**, 525–530 (2021).

[58]P. Miltényi, M. Gierlings, J. Keller, B. Beschoten, G. Güntherodt, U. Nowak, and K.-D. Usadel, "Diluted antiferromagnets in exchange bias: proof of the domain state model," Physical Review Letters **84**, 4224 (2000).

[59]Z. Liu and S. Adenwalla, "Closely linear temperature dependence of exchange bias and coercivity in out-of-plane exchange-biased [pt/co] 3/nio (11 Å) multilayer," Journal of applied physics **94**, 1105–1109 (2003).

[60]H. Béa, M. Bibes, F. Ott, B. Dupé, X.-H. Zhu, S. Petit, S. Fusil, C. Deranlot, K. Bouzehouane, and A. Barthélémy, "Mechanisms of exchange bias with multiferroic bifeo 3 epitaxial thin films," Physical review letters **100**, 017204 (2008).

[61]U. Arnalds, J. Agustsson, A. Ingason, A. Eriksson, K. B. Gylfason, J. Gudmundsson, and S. Olafsson, "A magnetron sputtering system for the preparation of patterned thin films and in situ thin film electrical resistance measurements," Review of Scientific Instruments **78**, 103901 (2007).

[62]B. W. David and C. B. Carter, *Transmission electron microscopy: a textbook for materials science* (Springer Science + Business Media, LLC, 1996).

[63]S. Foner, "Vibrating sample magnetometer," Review of Scientific Instruments **27**, 548–548 (1956).

[64]S. Foner, "Versatile and sensitive vibrating-sample magnetometer," Review of Scientific Instruments **30**, 548–557 (1959).

[65]F. Fiorillo, "Measurements of magnetic materials," Metrologia **47**, S114 (2010).

[66]A. Klechikov, *BoToFit, Neutron Reflectivity fitting software*, `https://github.com/Alexey-Klechikov/BoToFit`.

[67]B. Toperverg and V. Derizlazov, "Softwares for fitting of specular reflection and simulations of off-specular scattering are available on the instrument site, or from Boris.Toperverg@RUB.de," Unpublished.

[68]H. Zabel, K. Theis-Bröhl, and B. Toperverg, *Handbook of magnetism and advanced magnetic materials (novel techniques for characterization and preparing samples vol 3) ed h kronmuller and s parkin*, 2007.

[69]J. Heron, M. Trassin, K. Ashraf, M. Gajek, Q. He, S. Yang, D. Nikonov, Y. Chu, S. Salahuddin, and R. Ramesh, "Electric-field-induced magnetization reversal in a ferromagnet-multiferroic heterostructure," Physical review letters **107**, 217202 (2011).

[70]R. Cherifi, V. Ivanovskaya, L. Phillips, A. Zobelli, I. Infante, E. Jacquet, V. Garcia, S. Fusil, P. Briddon, N. Guiblin, et al., "Electric-field control of magnetic order above room temperature," Nature materials **13**, 345–351 (2014).

[71]V. Laukhin, V. Skumryev, X. Martı, D. Hrabovsky, F. Sánchez, M. Garcıa-Cuenca, C. Ferrater, M. Varela, U. Lüders, J.-F. Bobo, et al., "Electric-field control of exchange bias in multiferroic epitaxial heterostructures," Physical review letters **97**, 227201 (2006).

[72]J. Katine and E. E. Fullerton, "Device implications of spin-transfer torques," Journal of Magnetism and Magnetic Materials **320**, 1217–1226 (2008).

[73]A. Fert, "Nobel lecture: origin, development, and future of spintronics," Reviews of modern physics **80**, 1517 (2008).

[74]T. Li, S. Jiang, N. Sivadas, Z. Wang, Y. Xu, D. Weber, J. E. Goldberger, K. Watanabe, T. Taniguchi, C. J. Fennie, et al., "Pressure-controlled interlayer magnetism in atomically thin CrI_3," Nature materials **18**, 1303–1308 (2019).

[75]J. Kouvel and R. Wilson, "Magnetization of iron-nickel alloys under hydrostatic pressure," Journal of Applied Physics **32**, 435–441 (1961).

[76]J. Kouvel and C. Hartelius, "Pressure dependence of the magnetization of cobalt," Journal of Applied Physics **35**, 940–941 (1964).

[77]J. C. Slonczewski, "Initiation of spin-transfer torque by thermal transport from magnons," Physical Review B **82**, 054403 (2010).

[78]J.-U. Thiele, S. Maat, and E. E. Fullerton, "Ferh/fept exchange spring films for thermally assisted magnetic recording media," Applied Physics Letters **82**, 2859–2861 (2003).

[79]W. Li, B. Buford, A. Jander, and P. Dhagat, "Acoustically assisted magnetic recording: a new paradigm in magnetic data storage," IEEE transactions on magnetics **50**, 37–40 (2014).

[80]W.-G. Yang and H. Schmidt, "Acoustic control of magnetism toward energy-efficient applications," Applied Physics Reviews **8** (2021).

[81]S. Mangin, M. Gottwald, C. Lambert, D. Steil, V. Uhlıř, L. Pang, M. Hehn, S. Alebrand, M. Cinchetti, G. Malinowski, et al., "Engineered materials for all-optical helicity-dependent magnetic switching," Nature materials **13**, 286–292 (2014).

[82]P. Zhang, T.-F. Chung, Q. Li, S. Wang, Q. Wang, W. L. Huey, S. Yang, J. E. Goldberger, J. Yao, and X. Zhang, "All-optical switching of magnetization in atomically thin CrI_3," Nature materials **21**, 1373–1378 (2022).

[83]V. Polewczyk, S. Chaluvadi, P. Orgiani, G. Panaccione, G. Vinai, G. Rossi, and P. Torelli, "Tuning the magnetic properties of V_2O_3/CoFeB heterostructures across the V_2O_3 structural transition," Physical Review Materials **5**, 034413 (2021).

[84]J. De La Venta, S. Wang, T. Saerbeck, J. Ramırez, I. Valmianski, and I. K. Schuller, "Coercivity enhancement in V_2O_3/Ni bilayers driven by nanoscale phase coexistence," Applied Physics Letters **104**, 062410 (2014).

[85]C. T. Wolowiec, J. G. Ramırez, M.-H. Lee, N. Ghazikhanian, N. M. Vargas, A. C. Basaran, P. Salev, and I. K. Schuller, "Stress-tailoring magnetic anisotropy of V_2O_3/Ni bilayers," Physical Review Materials **6**, 064408 (2022).

[86]I. Valmianski, A. F. Rodrıguez, J. Rodrıguez-Álvarez, M. G. Del Muro, C. Wolowiec, F. Kronast, J. G. Ramırez, I. K. Schuller, A. Labarta, and X. Batlle, "Driving magnetic domains at the nanoscale by interfacial strain-induced proximity," Nanoscale **13**, 4985–4994 (2021).

[87]A. Pofelski, S. Valencia, Y. Kalcheim, P. Salev, A. Rivera, C. Huang, M. A. Mawass, F. Kronast, I. K. Schuller, Y. Zhu, et al., "Domain nucleation across the metal-insulator transition of self-strained V_2O_3 films," arXiv preprint arXiv:2312.09051 (2023).

[88]B. Sass, S. Buschhorn, W. Felsch, D. Schmitz, and P. Imperia, "Thin layers of Fe, Co and Ni on V_2O_3 (112
0) and V_2O_3 (0 0 0 1): A comparison of the interfacial magnetic interactions," Journal of magnetism and magnetic materials **303**, 167–177 (2006).

[89]O. Allegranza and M.-M. Chen, "Effect of substrate and antiferromagnetic film's thickness on exchange-bias field," Journal of applied physics **73**, 6218–6222 (1993).

[90]J. Van Driel, F. De Boer, K.-M. Lenssen, and R. Coehoorn, "Exchange biasing by $Ir_{19}Mn_{81}$: Dependence on temperature, microstructure and antiferromagnetic layer thickness," Journal of Applied Physics **88**, 975–982 (2000).

[91]R. Stamps, "Mechanisms for exchange bias," Journal of Physics D: Applied Physics **33**, R247 (2000).

[92]H. Xi and R. M. White, "Exchange coupling of NiFe/CrMnPt x bilayers prepared by a substrate bias sputtering method," Journal of Applied Physics **87**, 410–415 (2000).

[93]R. Moon, "Antiferromagnetism in V_2O_3," Journal of Applied Physics **41**, 883–883 (1970).

[94]K. Ignatova, E. B. Thorsteinsson, N. Strandqvist, C. Vantaraki, V. Kapaklis, A. Devishvili, G. K. Pálsson, U. B. Arnalds, et al., "Reversible exchange bias in epitaxial V_2O_3/Ni hybrid magnetic heterostructures," Journal of Physics: Condensed Matter (2022).

[95]T. Ambrose, R. Sommer, and C. Chien, "Angular dependence of exchange coupling in ferromagnet/antiferromagnet bilayers," Physical Review B **56**, 83 (1997).

[96]H. Xi, M. H. Kryder, and R. M. White, "Study of the angular-dependent exchange coupling between a ferromagnetic and an antiferromagnetic layer," Applied physics letters **74**, 2687–2689 (1999).

[97]F. Radu, A. Westphalen, K. Theis-Bröhl, and H. Zabel, "Quantitative description of the azimuthal dependence of the exchange bias effect," Journal of Physics: Condensed Matter **18**, L29 (2005).

[98]L. Wu, M.-G. Han, and Y. Zhu, "Toward accurate measurement of electromagnetic field by retrieving and refining the center position of non-uniform diffraction disks in Lorentz 4D-STEM," Ultramicroscopy **250**, 113745 (2023).

[99]P. Midgley, "An introduction to off-axis electron holography," Micron **32**, 167–184 (2001).

[100]P. A. Midgley and R. E. Dunin-Borkowski, "Electron tomography and holography in materials science," Nature materials **8**, 271–280 (2009).

[101]A. Masseboeuf, C. Gatel, P. Bayle-Guillemaud, Y. Lamy, and B. Viala, "The use of Lorentz microscopy for the determination of magnetic reversal mechanism of exchange-biased $Co_{30}Fe_{70}$/NiMn bilayer," Journal of magnetism and magnetic materials **321**, 3080–3083 (2009).

Abbreviations

AFM	Antiferromagnetic
bcc	Body-centered cubic
DC	Direct current
EB	Exchange bias
EDXS	Energy-dispersive x-ray spectroscopy
EELS	Electron energy loss spectroscopy
FM	Ferromagnetic
HAADF	High-angle annular dark-field
MOKE	Magneto-optic Kerr effect
MIT	Metal-insulator transition
PM	Paramagnetic
PNR	Polarized neutron reflectometery
RSM	Reciprocal space mapping
SLD	Scattering length density
SPT	Structural phase transition
STEM	Scanning transmission electron microscopy
TMOs	Transition metal oxides
VSM	Vibrating sample magnetometer
XRD	X-ray diffraction
XRR	X-ray reflectivity

Chapter 6
Original papers

Paper I

Reversible exchange bias in epitaxial V_2O_3/Ni hybrid magnetic heterostructures

K. Ignatova, E.B. Thorsteinsson, B.A. Jósteinsson, N. Strandqvist, C. Vantaraki, V. Kapaklis, A. Devishvili, G. K. Pálsson, U.B. Arnalds

Journal of Physics: Condensed Matter (2022)

Reversible exchange bias in epitaxial V_2O_3/Ni hybrid magnetic heterostructures

K. Ignatova,[1] E. B. Thorsteinsson,[1] B. A. Jósteinsson,[1] N. Strandqvist,[2] C. Vantaraki,[2] V. Kapaklis,[2] A. Devishvili,[2,3] G. K. Pálsson,[2] and U. B. Arnalds[1]

[1]*Science Institute, University of Iceland, Dunhaga 3, 107 Reykjavik, Iceland*
[2]*Department of Physics, Uppsala University, Uppsala SE-751 20, Sweden*
[3]*Institut Laue-Langevin, BP 156, 38042 Grenoble, France*

In this work we present a temperature and angular dependent study of the structural and magnetic properties in highly crystalline V_2O_3/Ni/Zr magnetic heterostructure films. Our investigation focuses on the coupling between the ferromagnetic Ni layer and V_2O_3 layer which undergoes an antiferromagnetic/paramagnetic phase transition coupled to the structural phase transition of the material at around 150 K. Structural investigations using x-ray diffraction reveal highly crystalline films of a quality which has previously not been reported in the literature. The Ni layers display an absence of in-plane magnetic anisotropy owing to the highly textured (1 1 1) layering of the Ni films on the underlying V_2O_3(0 0 0 1) oriented layer. During the transition we observe a strain related enhancement of the coercivity and the onset of a weak exchange bias for cooling under an external magnetic field. Heating the films to above the transition temperature, the exchange bias in the Ni is removed and can be reversed upon subsequent cooling under an inverted external magnetic field. Using temperature dependent polarized neutron reflectometry we investigate the film structure at the interface, capturing the magnetic and nuclear profiles.

I. INTRODUCTION

Hybrid magnetic heterostructures composed of vanadium sesquioxide (V_2O_3) and magnetic layers have drawn growing research interest regarding the role of interface strain and surface induced roughness on the magnetic properties of ferromagnetic layers [1, 2]. Interest in exchange coupled multilayers and hybrid structures arises from interface effects such as exchange bias [4, 5], magnetic proximity [6] and exchange spring effects [7, 8] affecting the magnetic properties [9]. Here we present an experimental investigation of a simple epitaxial bilayer model composed of a ferromagnetic layer and vanadium sesquioxide. This highly crystalline hybrid heterostructure allows us to investigate magnetic anisotropy effects as well as exchange bias occurring at the interface [4, 10].

The V_2O_3 undergoes a reversible structural transition from a high temperature paramagnetic metal to a low temperature antiferromagnetic insulator, wherein the crystal structure changes from a rhombohedral to a monoclinic phase. For hybrid heterostructures composed of V_2O_3 and an overlying magnetic layer the transition can induce direct effects via strain, affecting the properties of the magnetic material [1, 2, 11, 12]. Additionally, a surface induced roughness has been observed to occur during the structural transition as the transition progresses with temperature in nanoscale domains, inducing a roughness in the magnetic film and thereby an increased coercivity of the magnetic layer [12–14]. Although these previous results have shown direct effects on the magnetic properties of the magnetic layers in the hybrid heterostructures, evidence of exchange bias between the oxide and magnetic layer has been limited. As the V_2O_3 undergoes a paramagnetic to antiferromagnetic transition while the temperature is lowered below the transition temperature, an induced exchange bias with an onset at the structural transition can be expected upon cooling the heterostructures under an applied magnetic field. Such results have been reported by Sass *et al.*[15], where an exchange bias field was observed for V_2O_3/Ni films grown on *c*- and *a*-plane sapphire substrates with an onset of the exchange field coinciding with the temperature of the metal–insulator transition (MIT) of the V_2O_3 layer. In spite of a substantial effort in the literature to reproduce these findings, the exchange bias effect remains elusive [2, 6, 12].

The exchange bias effect could potentially be due to the crystal and interface quality of the films and changes in the intermixing region between the magnet and the oxide. We therefore focus our attention here on highly crystalline heterostructures of the V_2O_3/Ni system, investigating the possible correlation between temperature/angular dependent structural, magnetic and morphological characteristics of the deposited films. Using polarized neutron reflectometry we evaluate the structural and magnetic profile at the buried interface between the Ni and the V_2O_3 as a function of temperature with high spatial resolution.

Our results show that highly crystalline hybrid magnetic heterostructures of Ni layers of (1 1 1) orientation can be deposited onto V_2O_3 films on *c*-plane sapphire substrates. Our results reveal the presence of a $\sim$ 2 nm thick interfacial layer at the V_2O_3/Ni interface although no anomalous changes in this layer and the magnetic structure of the films are observed through the structural transition of the V_2O_3 layer. The high (1 1 1) texture of the magnetic layer results in a weak in plane magneto-crystalline anisotropy compared to the main crystallographic axes resulting in highly isotropic magnetic behaviour of the films. We observe a clear reversible exchange bias effect in the Ni layer with an onset at the paramagnetic/antiferromagnetic transition of the underlying V_2O_3 layer. The exchange bias direction can be reversed upon heating to above the structural transi-

tion temperature and subsequent cooling under applied field of inverse direction. Coupled to the onset of the exchange bias we observe a concomitant change in the coercivity of the films (with temperature) with a noticeable increase occurring at $\sim$ 150 K. We attribute this increase to strain, induced by the structural transition occurring in the V_2O_3 layer [11, 14].

II. EXPERIMENTAL

The heterostructure film stack is composed of a 60 nm thick V_2O_3 layer, a 10 nm Ni layer and finally a 5 nm thick Zr capping layer to prevent oxidation of the Ni layer. The thin films used in this study were grown by a combination of dc-magnetron sputtering and reactive dc-magnetron sputtering in a custom-built chamber [16]. Prior to deposition the base pressure of the chamber was below 4×10^{-6} Pa. The films were deposited onto 1×1 cm^2 single-crystalline [0 0 0 1] oriented (c-plane) sapphire substrates with a working pressure of 0.4 Pa of 5N Ar and O_2 gases at 20 sccm and 1.05 sccm flow rates, respectively. Before growth the substrates were pre-baked in vacuum at a temperature of 650°C for $\sim$ 30 minutes.

The V_2O_3 was deposited at a temperature of 485°C which has previously been shown to yield highly epitaxial (0 0 1) oriented films [17]. The Ni and Zr layers were deposited after cooling down to room temperature under ultra-high vacuum. Identical reference samples composed of only the Ni and Zr layers were deposited following the same recipe directly onto c-plane sapphire substrates.

The structural properties of the films were investigated with x-ray diffraction (XRD), x-ray reflectometry (XRR) and pole figure measurements on a PANalytical X'Pert Pro using CuK_α radiation. Reciprocal space maps were recorded on a Panalytical Empyrean with a PIXcel^{3D} detector using CuK_α radiation. The magnetic properties of the V_2O_3/Ni bilayers were characterized at room temperature using the longitudinal magneto-optical Kerr effect (MOKE) as a function of the azimuth angle (revealing the in-plane magnetic anisotropy). Magnetic behavior as a function of temperature was recorded using vibrating sample magnetometry (VSM) and a custom-built system for measuring the longitudinal MOKE signal at low temperatures. Polarized neutron reflectivity data was recorded at different temperatures and external field values at the reflectometer SuperADAM at the Institute Laue-Langevin (ILL) using a monochromatic neutron beam with wavelength 5.21 Å[18, 19]. Polarized neutron reflectivity data was recorded at different temperatures and external field values at the reflectometer SuperADAM at the Institute Laue-Langevin (ILL) using a monochromatic neutron beam with wavelength 5.21 Å[18, 19]. The fitting of neutron data was performed using the BoToFit software [20, 21].

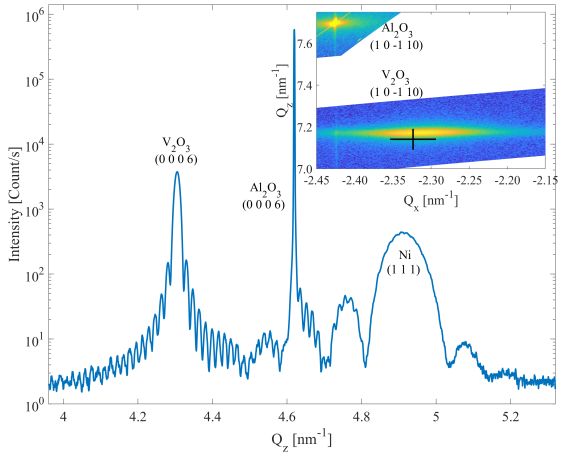

FIG. 1: X-ray diffraction scan recorded for the Al_2O_3/V_2O_3/Ni/Zr film structure. The results reveal a well defined out-of-plane crystal growth with strong V_2O_3 (0 0 0 6) and Ni (1 1 1) peaks with Laue oscillations extending from both sides of the peaks. The inset shows the reciprocal space map around the (1 0 -1 10) peaks of V_2O_3 and Al_2O_3. The cross indicates the bulk V_2O_3 peak position.

III. RESULTS AND DISCUSSION

A. Structural properties

Figure 1 shows an XRD scan of the V_2O_3/Ni heterostructure. Only V_2O_3 (0 0 0 6) and Ni (1 1 1) peaks are seen in the scan along with the substrate Al_2O_3 (0 0 0 6) peak. The absence of any additional peaks in the scanned 2θ range (full scan range from 10° to 100°) reveals no other vanadium phases to be present in the film and that the Ni is fully textured with a (1 1 1) orientation.

The highly epitaxial nature of the V_2O_3 is confirmed with a strong (0 0 0 6) peak and Laue oscillations extending from both sides of the peak. A similar argument can be made with respect to the Ni (1 1 1) peak which also shows clear Laue oscillations therefore verifying a well defined crystalline structure of the Ni layer. Such highly crystalline hybrid heterostructures of this type have not been reported previously in the literature. Previously, we have shown that the epitaxial nature of V_2O_3 films grown by dc-magnetron sputtering is strongly dependent on the power settings, O_2 flow rate and other deposition parameters [22]. These results reveal the film layering to be extremely well defined with very low roughness. The inset shows a reciprocal space map scan performed on the film around the strongest relative intensity asymmetrical (1 0 -1 10) peak for V_2O_3. Two layer peaks can be observed, one corresponding to a fully strained component of the film and one corresponding to a relaxed part positioned close to bulk values. The presence of the fully

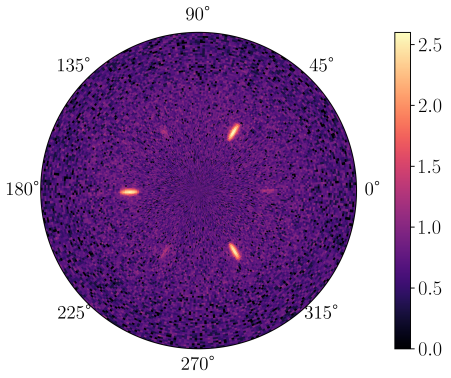

FIG. 2: Pole figure on a logarithmic scale [counts/sec] recorded for the V_2O_3 [104] peak at $2\theta = 33.0°$. Three peaks with epitaxial relation to the substrate are visible. The other three weaker peaks, discernible in the graph, are associated with 180° rotated domains. The ratio of the intensities of the peaks reveals that ∼ 97 % of the film is in the primary domain state.

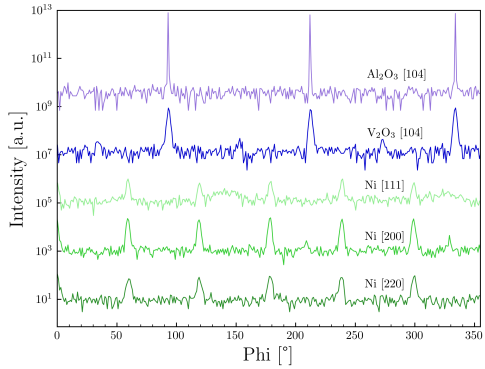

FIG. 3: Individual ϕ-scans on the Al_2O_3 (1 0 4) and the V_2O_3 (1 0 4) peaks and the Ni (1 1 1), (2 0 0) and (2 2 0) peaks. The V_2O_3 peaks align to the Al_2O_3 peak positions indicating an epitaxial growth. V_2O_3 (1 0 4) peaks rotated 60° are associated with 180° rotated domains. The Ni layer displays an epitaxial relation with two types of grains equally likely.

strained component arises from a fully strained interface layer forming during the initial stages of growth, subsequently the film relaxes leading to the formation of the relaxed peak in the RSM reciprocal space map. A detailed discussion of the fully strained component can be found elsewhere [17, 23]. *Ex situ* atomic force microscopy (AFM) of the top V_2O_3 interface was conducted by depositing a series of V_2O_3 films, without depositing the subsequent Ni and capping Zr layers, with results presented in references [24, 25]. The RMS roughness of the films, determined from the AFM scans, was between 0.2 - 0.5 nm in agreement with values for the buried interface derived from the XRR and PNR fits described further below.

To confirm the epitaxial in-plane relations of the V_2O_3 and Ni layers to the substrate, pole figures were recorded. Figure 2 shows the pole figure recorded for the V_2O_3 (1 0 4) reflection. Three high intensity peaks are observed at $\chi = 39.2°$ and three low intensity peaks rotated 60° from the high intensity ones. The high-intensity peaks align to the sapphire, Al_2O_3 (0 0 0 6), and arise therefore from epitaxial grains (see Fig. 3). The low intensity peaks are from 180° rotated domains [26]. The intensities of the peaks indicate that ∼ 97 % of the film is in the primary domain. Figure 3 shows in-plane ϕ-scans recorded for the Ni (1 1 1), (2 0 0), and (2 2 0) peaks, and the Al_2O_3 (1 0 4) and V_2O_3 (1 0 4) peaks. For the V_2O_3 three intense peaks are observed that align to the substrate peaks indicating the well defined in-plane crystal structure. Three much less intense peaks are seen rotated 60° from the main peaks from 180° rotated domains as described before [26]. In-plane ϕ-scans recorded for the Ni (1 1 1), (2 0 0) and (2 2 0) reflections reveal six peaks shifted 30° from the V_2O_3 (1 0 4) peaks. The occurrence of six peaks indicates that the Ni is composed of two types of epitaxial grains rotated 60° with respect to each other.

B. Magnetic properties

Figure 4 shows the coercivity and relative remanence ($M_{\rm rem}/M_{\rm sat}$) extracted from hysteresis loops as a function of the in plane sample angle recorded using MOKE at room temperature. The results show only minor changes as a function of angle for both the coercivity (which varies between 55 G and 57 G) and remanence illustrating the lack of anisotropy in the system. We attribute this lack of anisotropy to the high (1 1 1) texture of the film. These results are consistent with anisotropy energy calculations around the Ni [1 1 1] direction. The calculations reveal a sixfold symmetry with minor energy changes as a function of in-plane angle (see supplementary material Figure S1).

Several VSM and temperature-dependent MOKE measurements were performed for the V_2O_3/Ni/Zr and Ni/Zr reference samples. The measurements were made in field-cooled (FC) states produced by cooling from room temperature through the transition temperature in an external field of ±50 kG (VSM) and ±400 G (MOKE).

Figure 5 shows recorded hysteresis loops for selected temperatures during heating after field cooling. The exchange bias is illustrated in the loop at 30 K which is offset by 5.5 G, i.e., it is shifted along the H-axis by 2.75 G, in the opposite direction to the cooling field, as seen in Figure 5. The bias field and coercivity derived from the hysteresis are shown as a function of temperature in

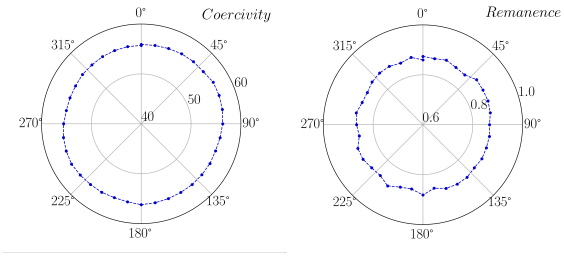

FIG. 4: Coercivity in Gauss and relative remanent magnetization ($M_{\rm rem}/M_{\rm sat}$) for the hybrid heterostructure as a function of the in plane sample angle. Even though the structures exhibit a high crystallinity, the magnetic nature of the film in plane is highly isotropic.

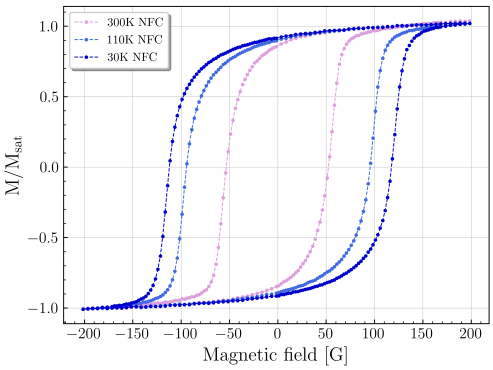

FIG. 5: Normalized hysteresis loops of the V_2O_3/Ni/Zr film measured in plane at 30 K, 110 K and room temperature after negative field cooling (NFC). The sample was cooled in an external magnetic field of −50 kG applied parallel to the film plane. The VSM hysteresis loops were recored at the maximum applied field of 200 G while the MOKE magnetization loops were recorded at the maximum applied field of 400 G.

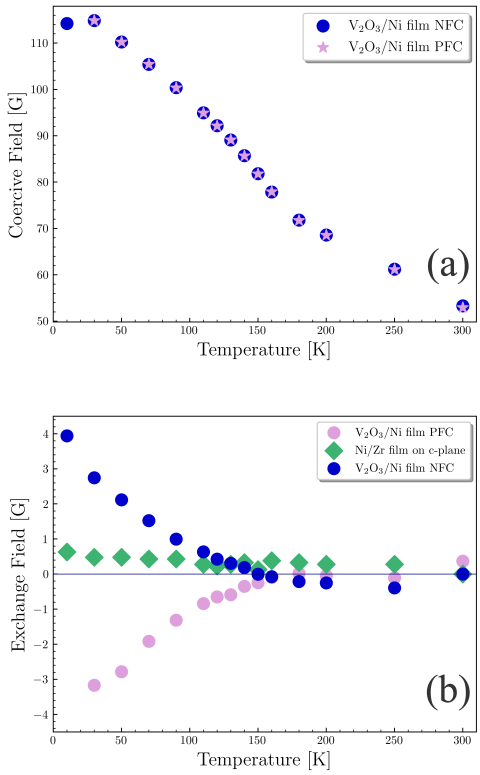

FIG. 6: (a) Coercivity and (b) exchange field for the V_2O_3/Ni/Zr film extracted from magnetization loops recorded using VSM as a function of increasing temperature after positive field cooling (PFC) under an applied field of 50 kG and negative field cooling (NFC) with a field of −50 kG. (b) includes the exchange bias recorded for a reference sample composed exclusively of Ni/Zr with the same dimensions. The reference sample showed no indication of an exchange bias and a typical decrease in coercivity with temperature (with respect to magnetic thin films) from $H_c = 52.2$ G at 10 K down to $H_c = 16.1$ G at room temperature (see supplementary graph). The presence of the in-plane exchange bias was verified by carrying out both MOKE and VSM measurements. No differences are observed in the coercivity of the films for both normal and field-cooled states as well as for sample orientations rotated in-plane 90°.

Fig. 6. The coercivity exhibits a decrease with increasing temperature as is generally observed for Ni films.

In addition to the expected gradual temperature dependent decrease in coercivity is a notable strain-related decrease at around 150 K is observed. This occurs at a temperature coinciding with the metal-insulator transition in the V_2O_3 at around 150 K [3, 14]. This temperature range corresponds well to the transition temperature determined initially by electrical resistance measurements [24].

At the transition temperature a clear onset of exchange bias is observed increasing with decreasing temperature (Fig. 6 (b)). The presence of the in-plane exchange bias was verified by carrying out both magneto-optic Kerr effect and vibrating sample magnetometry measurements. Heating the sample up to room temperature and subsequent cooling under an inverted external field results in an opposite and equal intensity exchange bias. The exchange bias was observed to be of the same magnitude for sample orientations rotated in-plane 90°. Comparative measurements were also performed on reference Ni/Zr films without an V_2O_3 layer which exhibited no sign of an exchange bias (see Fig. 6 (b)). The reference sample did not exhibit any exchange bias or anomalous changes in the coercivity, only displaying an expected gradual reduc-

tion in coercivity with increasing temperature (see supplementary material). In order to exclude possible measurement artifacts corroborative measurements were carried out at Uppsala University using custom-built temperature dependent MOKE setup. Both results demonstrate good agreement as can be seen in supplementary material (Figure S3).

Specular PNR measurements were performed in the saturated state (5 kG applied field) and the remanent (23 G) state. The spin-up and spin-down neutron spin channels were measured to investigate the magnetic moment of the sample aligned parallel to an external applied field. Additional spin-flip channels, which probe the magnetic moment perpendicular to the neutron polarization were recorded but showed no measurable signal, therefore revealing no evidence of canting of the magnetization. The PNR measurements were carried out at 10, 135, 145 and 300 K. Being complimentary to the XRR characterization the PNR measurements clarify additionally the magnetic properties of the films, namely the magnetization depth profile of the sample as a function of temperature. Any differences arising in the magnetization depth profile as the film progresses through the structural transition can therefore be observed.

Figure 7 (a) shows the polarized neutron reflectivity measurements recorded at 10 K under an external field of 5 kG for the V_2O_3/Ni/Zr film. The corresponding scattering length density (SLD) profile, determined by fitting the neutron data, is shown in Fig. 7 (b). The polarized neutron reflectivity data was fitted with the BoToFit software providing a model for both the nuclear and magnetic scattering length density (SLD) profile of the film. The resulting internal thicknesses of the film are in good agreement with results obtained from XRR where the thicknesses were determined to be V_2O_3(58.1 nm)/Ni(9.4 nm)/Zr(5.4 nm). The XRR data and fits are presented in supplementary material (Figure S4). After long exposure times the capping layer becomes oxidized and, therefore, all scans were fitted to a model which includes ZrO on top of the heterostructure. In order to obtain a good agreement between the experimental data and the simulation an interfacial layer, composed of Ni with a smaller density and higher roughness, at the Ni/V_2O_3 interface was needed, as is shown in Figure 7 (c). To understand the role of this interlayer, we compared two kinds of models. One in which there is an interface layer between Ni and V_2O_3 and a second without such an interfacial layer. For the latter case the fitting results of the magnetization SLD profile show a sharp Ni/V_2O_3 interface and less quality of fit. All fit attempts of the heterostructure model including the interfacial layer returned a relatively uniform magnetization profile through the Ni. The interface layer thickness was allowed to vary but converged at a thickness of approximately 2.6 nm. To allow for variations in the magnetization depth profile the ferromagnetic layer was split into several individual layers. In the final model two layers proved sufficient but more were tried without significantly improving the quality of the fit. The quality of the fit was evaluated using the reduced χ^2 figure of merit for each fit with a value 1.1. Comparing the neutron data recorded at different temperatures no changes were observed in the interface layer. The coercivity field, determined from hysteresis loops recorded as a function of field using PNR was in good agreement with the VSM and MOKE data within the experimental error. However, the value of the exchange field in the measured sample is relatively small, therefore precise

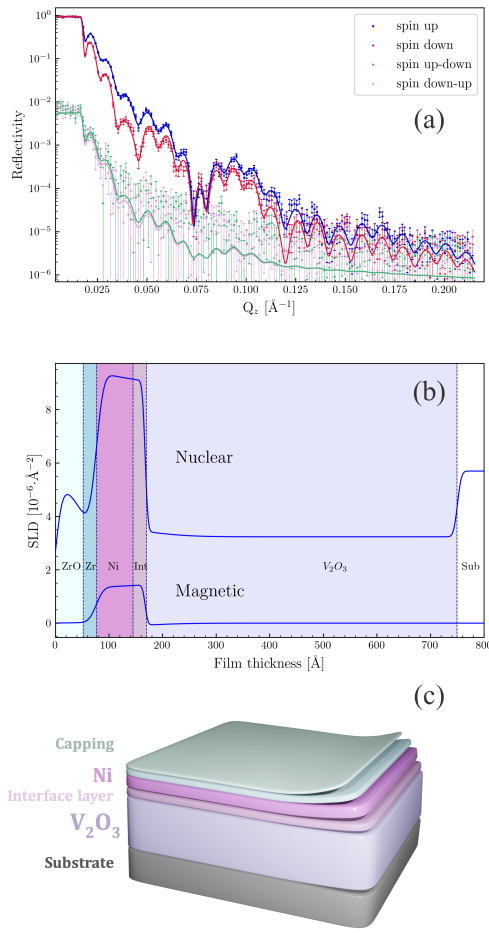

FIG. 7: Polarized neutron reflectivities recorded for the V_2O_3/Ni/Zr film. (a) Specular neutron reflectivities at a temperature of 10 K and 5 kG. The solid lines show the best fit to the experimental data obtained using the BoToFit software [20, 21]. (b) Corresponding scattering length density profiles derived from the fit. (c) Schematic illustration of the fitting model.

measurement of the weak induced moments at an antiferromagnetic interface remains challenging using polarized neutron reflectometry.

IV. CONCLUSIONS

In conclusion, we have investigated the microstructure and magnetic properties of a highly crystalline V_2O_3/Ni/Zr system grown on *c*-plane sapphire. The system reveals a lack of anisotropy due to the textured (1 1 1) layering of the Ni on the V_2O_3. Together with a strain-induced coercivity enhancement arising from the structural transition in the V_2O_3 layer we observe an exchange-bias field with an onset at the transition temperature. Characterization of the structural and magnetic profile of the hybrid heterostructure (using XRR and PNR) reveals the presence of a $\sim$ 2 nm thick interfacial layer at the V_2O_3/Ni interface. Although this interfacial layer could partially be composed of NiO we assume that the observed exchange bias is primarily not due to this layer as substantially thicker NiO is generally needed to induce an exchange bias in overlying ferromagnetic layers [29]. For example, measurable exchange bias (16 Oe) on an epitaxial Ni/NiO system was observed when the thickness of the antiferromagnetic NiO layer exceeded the critical value of 6-8 nm [5]. The onset of the exchange bias at the transition temperature is therefore attributed to the exchange bias effect occurring at the V_2O_3/Ni interface as the V_2O_3 transitions from a paramagnet to an antiferromagnet under an externally applied field. The exchange bias can be reversed upon heating the films to above the transition temperature followed by subsequent cooling under an inverted external magnetic field. Our results therefore reveal a reversible exchange bias which can be controlled by the structural transition in the V_2O_3 having implications with respect to antiferromagnetic spintronics [30, 31], Mott based memory devices [32] and neuromorphic computing [33].

Acknowledgements This work was supported by funding from the University of Iceland research fund, the Icelandic student innovation fund and the Icelandic Research Fund Grant No. 207111-051. Instrumentation funding from the Icelandic Infrastructure Fund is acknowledged. This work is based on experiments performed on SuperADAM at ILL, Grenoble, France.

Corresponding authors U. B. Arnalds (uarnalds@hi.is)

Conflict of Interest There is no conflict of interest to disclose.

Data Availability Statement The authors confirm that the data supporting the findings of this study are available within the article.

[1] Christian T Wolowiec, Juan Gabriel Ramírez, Min-Han Lee, Nicolas M Vargas, Ali C Basaran, Pavel Salev, and Ivan K Schuller. Stress-tailoring magnetic anisotropy of V_2O_3/Ni bilayers. arXiv preprint arXiv:2112.12826, 2021.

[2] Dustin A Gilbert, Juan Gabriel Ramírez, Thomas Saerbeck, Juan Trastoy, Ivan K Schuller, Kai Liu, and Jose de la Venta. Growth-induced in-plane uniaxial anisotropy in V_2O_3/Ni films. Scientific reports, 7(1):1–9, 2017.

[3] Valmianski, Ilya and Rodríguez, Arantxa Fraile and Rodríguez-Álvarez, Javier and Del Muro, Montserrat García and Wolowiec, Christian and Kronast, Florian and Ramírez, Juan Gabriel and Schuller, Ivan K and Labarta, Amílcar and Batlle, Xavier. Driving magnetic domains at the nanoscale by interfacial strain-induced proximity. Nanoscale, 13(9):4985–4994, 2021.

[4] Josep Nogués and Ivan K Schuller. Exchange bias. Journal of Magnetism and Magnetic Materials, 192(2):203–232, 1999.

[5] RA Lukaszew, M Mitra, Z Zhang, and M Yeadon. Exchange bias on epitaxial Ni films due to ultrathin NiO layer. The European Physical Journal B-Condensed Matter and Complex Systems, 45(2):181–184, 2005.

[6] Thomas Saerbeck, Jose de la Venta, Siming Wang, Juan Gabriel Ramírez, Mikhail Erekhinsky, Ilya Valmianski, and Ivan K Schuller. Coupling of magnetism and structural phase transitions by interfacial strain. Journal of Materials Research, 29(20):2353–2365, 2014.

[7] Eric E Fullerton, JS Jiang, M Grimsditch, CH Sowers, and SD Bader. Exchange-spring behavior in epitaxial hard/soft magnetic bilayers. Physical Review B, 58(18):12193, 1998.

[8] Fridrik Magnus, ME Brooks-Bartlett, R Moubah, RA Procter, Gabriella Andersson, TPA Hase, ST Banks, and Björgvin Hjörvarsson. Long-range magnetic interactions and proximity effects in an amorphous exchange-spring magnet. Nature communications, 7(1):1–7, 2016.

[9] Frances Hellman, Axel Hoffmann, Yaroslav Tserkovnyak, Geoffrey SD Beach, Eric E Fullerton, Chris Leighton, Allan H MacDonald, Daniel C Ralph, Dario A Arena, Hermann A Dürr, et al. Interface-induced phenomena in magnetism. Reviews of modern physics, 89(2):025006, 2017.

[10] Ulrich Nowak, Klaus-Dieter Usadel, Jan Keller, Peter Miltényi, Bernd Beschoten, and Gernot Güntherodt. Domain state model for exchange bias. I. theory. Physical review B, 66(1):014430, 2002.

[11] J De La Venta, Siming Wang, JG Ramirez, and Ivan K Schuller. Control of magnetism across metal to insulator transitions. Applied Physics Letters, 102(12):122404, 2013.

[12] J De La Venta, Siming Wang, T Saerbeck, JG Ramírez, I Valmianski, and Ivan K Schuller. Coercivity enhancement in V_2O_3/Ni bilayers driven by nanoscale phase coexistence. Applied Physics Letters, 104(6):062410, 2014.

[13] AS McLeod, E Van Heumen, JG Ramirez, S Wang, T Saerbeck, S Guenon, M Goldflam, L Anderegg, P Kelly, A Mueller, et al. Nanotextured phase coexistence in the correlated insulator V_2O_3. Nature Physics, 13(1):80–86, 2017.

[14] V Polewczyk, SK Chaluvadi, P Orgiani, G Panaccione, G Vinai, G Rossi, and P Torelli. Tuning the magnetic properties of V_2O_3/CoFeB heterostructures across the V_2O_3 structural transition. Physical Review Materials, 5(3):034413, 2021.

[15] B Sass, S Buschhorn, W Felsch, D Schmitz, and P Imperia. Thin layers of Fe, Co and Ni on V_2O_3 (112^- 0) and V_2O_3 (0 0 0 1): A comparison of the interfacial magnetic interactions. Journal of magnetism and magnetic materials, 303(1):167–177, 2006.

[16] UB Arnalds, JS Agustsson, AS Ingason, AK Eriksson, Kristinn B Gylfason, JT Gudmundsson, and S Olafsson. A magnetron sputtering system for the preparation of patterned thin films and in situ thin film electrical resistance measurements. Review of Scientific Instruments, 78(10):103901, 2007.

[17] Einar B Thorsteinsson, Seyedmohammad Shayestehaminzadeh, and Unnar B Arnalds. Tuning metal-insulator transitions in epitaxial V_2O_3 thin films. Applied Physics Letters, 112(16):161902, 2018.

[18] Gunnar Palsson, Gabriella Andersson, U. B Arnalds, Anton Devishvili, and Kristina Ignatova. Exploring the link between interface coupling and the magnetisation profile in V_2O_3/Ni magnetic heterostructures. Institut Laue-Langevin (ILL) doi:10.5291/ILL-DATA.CRG-2868, 2021.

[19] A Devishvili, K Zhernenkov, Andrew JC Dennison, BP Toperverg, Max Wolff, Björgvin Hjörvarsson, and H Zabel. Superadam: Upgraded polarized neutron reflectometer at the institut laue-langevin. Review of Scientific Instruments, 84(2):025112, 2013.

[20] A. Klechikov. BoToFit, Neutron Reflectivity fitting software. `https://github.com/Alexey-Klechikov/BoToFit`.

[21] BP Toperverg and V Derizlazov. Softwares for fitting of specular reflection and simulations of off-specular scattering are available on the instrument site, or from Boris.Toperverg@RUB.de. Unpublished.

[22] Einar B Thorsteinsson, Seyedmohammad Shayestehaminzadeh, Arni S Ingason, Fridrik Magnus, and Unnar B Arnalds. Controlling metal–insulator transitions in reactively sputtered vanadium sesquioxide thin films through structure and stoichiometry. Scientific Reports, 11(1):1–10, 2021.

[23] Hamidreza Hajihoseini, Einar B Thorsteinsson, Vilborg V Sigurjonsdottir, and Unnar B Arnalds. Strained interface layer contributions to the structural and electronic properties of epitaxial V_2O_3 films. Applied Physics Letters, 118(16):161602, 2021.

[24] MT Sultan, K Ignatova, EB Thorsteinsson, F Magnus, and UB Arnalds. Structural and electrical properties of V_2O_3 thin films on *c*-plane Al_2O_3 fabricated by reactive-HiPIMS and dcMS techniques. Journal of Physics D: Applied Physics, 54(42):425302, 2021.

[25] MT Sultan, K Ignatova, EB Thorsteinsson, and UB Arnalds. Structural morphology and electrical transitions of V_2O_3 thin films grown on SiO_2/Si by high power impulse magnetron sputtering. Thin Solid Films, 742:139048, 2022.

[26] I Yamaguchi, T Manabe, T Kumagai, W Kondo, and S Mizuta. Preparation of epitaxial V_2O_3 films on C-, A- and R-planes of α-Al_2O_3 substrates by coating-pyrolysis process. Thin Solid Films, 366(1-2):294–301, 2000.

[27] D Jiles. Introduction to magnetism and magnetic materials, 1998.

[28] Stephen Blundell. Oxford master series in condensed matter physics, 2001.

[29] ZY Liu and Shireen Adenwalla. Variation of domain formation in a 15 nm NiFe layer exchange coupled with nio layers of different thicknesses. Applied physics letters, 82(13):2106–2108, 2003.

[30] Jun-young Kim, Joel Cramer, Kyujoon Lee, Dong-Soo Han, Dongwook Go, Pavel Salev, Pavel N. Lapa, Nicolas M. Vargas, Ivan K. Schuller, Yuriy Mokrousov, Gerhard Jakob, and Mathias Kläui. Tuning Spin-Orbit Torques Across the Phase Transition in VO_2/NiFe Heterostructure. Advanced Functional Materials, n/a(n/a):2111555, 2022.

[31] V. Baltz, A. Manchon, M. Tsoi, T. Moriyama, T. Ono, and Y. Tserkovnyak. Antiferromagnetic spintronics. Rev. Mod. Phys., 90:015005, Feb 2018.

[32] Yue Wang, Kyung-Mun Kang, Minjae Kim, Hong-Sub Lee, Rainer Waser, Dirk Wouters, Regina Dittmann, J. Joshua Yang, and Hyung-Ho Park. Mott-transition-based RRAM. Materials Today, 28:63–80, 2019.

[33] You Zhou and Shriram Ramanathan. Mott memory and neuromorphic devices. Proceedings of the IEEE, 103(8):1289–1310, 2015.

Paper I: Supplementary information

Reversible exchange bias in epitaxial V_2O_3/Ni hybrid magnetic heterostructures

K. Ignatova, E.B. Thorsteinsson, B.A. Jósteinsson, N. Strandqvist, C. Vantaraki, V. Kapaklis, A. Devishvili, G. K. Pálsson, U.B. Arnalds

Journal of Physics: Condensed Matter (2022)

Reversible exchange bias in epitaxial V_2O_3/Ni hybrid magnetic heterostructures

Supplementary material

K. Ignatova,[1] E. B. Thorsteinsson,[1] B. A. Jósteinsson,[1] N. Strandqvist,[2] C. Vantaraki,[2] V. Kapaklis,[2] A. Devishvili,[2,3] G. K. Pálsson,[2] and U. B. Arnalds[1]

[1]*Science Institute, University of Iceland, Dunhaga 3, 107 Reykjavik, Iceland*
[2]*Department of Physics, Uppsala University, Uppsala SE-751 20, Sweden*
[3]*Institut Laue-Langevin, BP 156, 38042 Grenoble, France*

For a crystal structure the total magnetic energy of the system includes a magnetocrystalline energy term resulting in crystals possessing easy, medium and hard axes. For a cubic system the magnetocrystalline energy term in spherical coordinates is given by [1]

$$E = K_1\left(\frac{1}{4}\sin^2(\theta)\sin^2(2\phi) + \cos^2(\theta)\right)\sin^2(\theta) + \frac{K_2}{16}\left(\sin^2(2\phi)\sin^2(2\theta)\sin^2(\theta)\right) \quad (1)$$

where K_1 and K_2 are the first and second order anisotropy constants (higher order terms have been left out), θ is the polar angle and ϕ is the azimuthal angle, in a coordinate system aligned to the crystallographic axes. When K_1 is larger than zero in a cubic crystal the directions of the magnetic easy axes are <100>. However, when K_1 is negative and $K_2 < 9|K_1|\ /4$, as in Ni, the magnetic easy axes are <111> and the hard axes are <100>. Figure S1 shows the magnetocrystalline energy for Ni calculated using equation (1) and assuming the first and second order anisotropy constants for Ni to be $K_1 = -4.5\times10^3$ Jm^{-3} and $K_2 = 2.3\times10^3$ Jm^{-3} [2]. When Ni is rotated around the [111] direction, which is the out of plane direction in the samples in this study, a sixfold symmetry arises in the magnetocrystalline energy. The change in energy is however small, as seen in Figure S1, and the change is substantially larger when rotated around the [100] direction.

[1] Stephen Blundell. Oxford master series in condensed matter physics, 2001.
[2] D Jiles. Introduction to magnetism and magnetic materials, 1998.

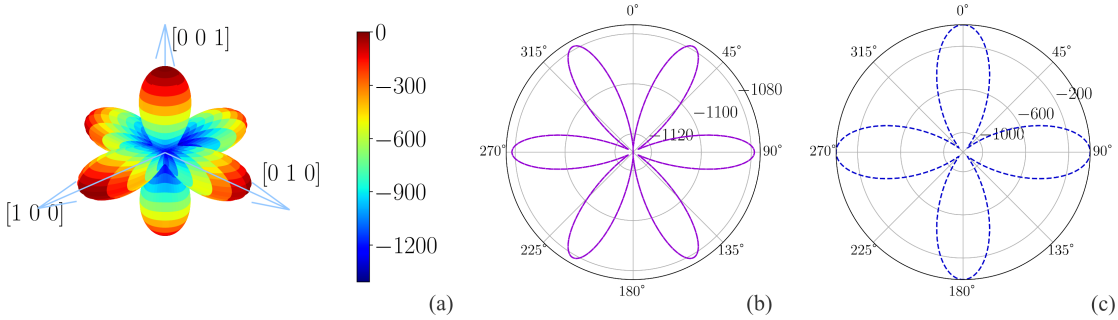

FIG. S1: (a) Anisotropy energy (in Jm^{-3}) surface for Ni (FCC) according to equation (1) using the first and second anisotropy constants for nickel $K_1 = -4.5\times10^3$ Jm^{-3} and $K_2 = 2.3\times10^3$ Jm^{-3} [2]. The [1 0 0], [0 1 0] and [0 0 1] crystallographic directions are indicated in the image. (b) Anisotropy energy around the [1 1 1] direction. (c) Anisotropy energy around the [1 0 0] direction.

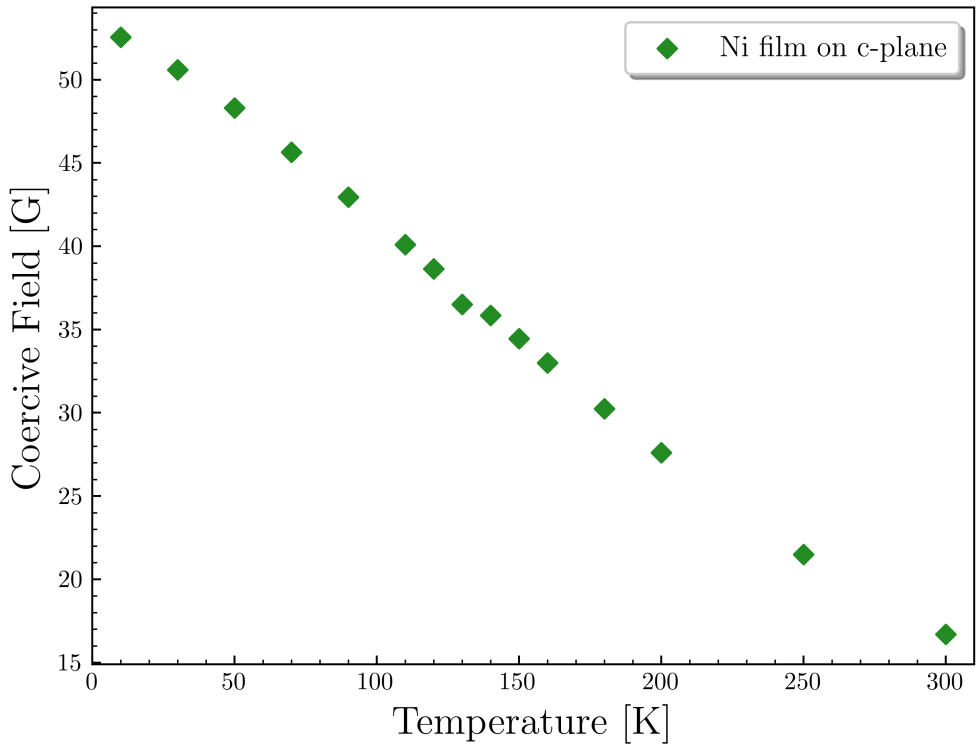

FIG. S2: Coercivity of the Ni/Zr film extracted from magnetization loops recorded using VSM as a function of increasing temperature after positive field cooling under an applied field of 50 kG . The reference sample showed a typical decrease in coercivity with temperature (with respect to magnetic thin films) from Hc = 52.2 G at 10 K down to Hc = 16.1 G at room temperature.

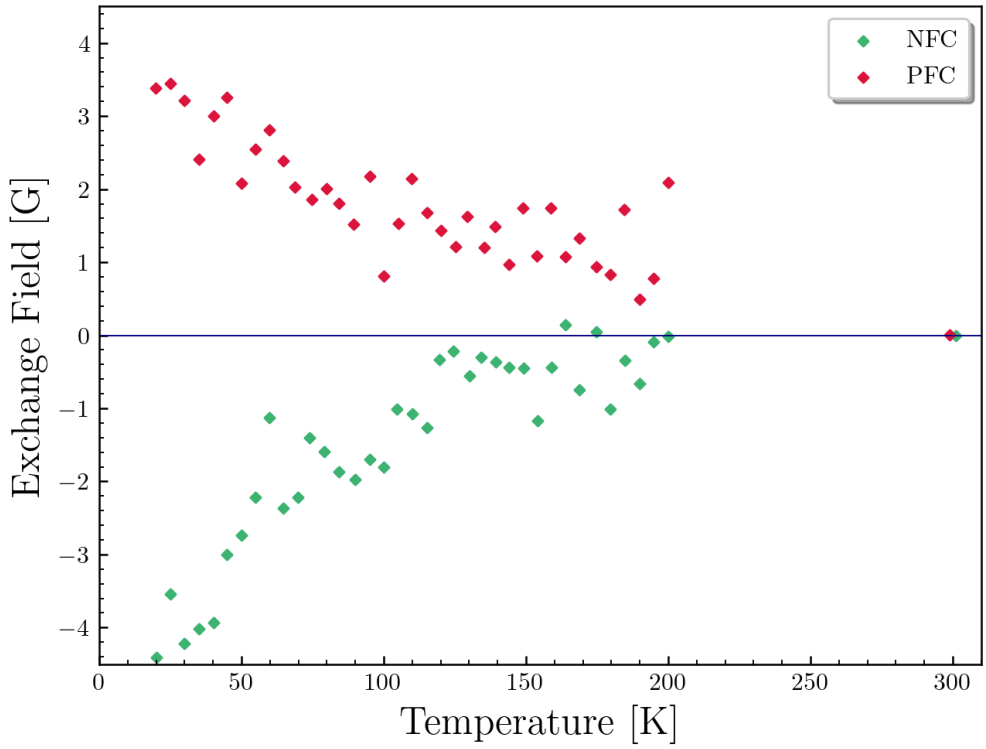

FIG. S3: Exchange field for the V_2O_3/Ni/Zr film extracted from magnetization loops recorded using temperature dependent MOKE as a function of increasing temperature after positive field cooling (PFC) and negative field cooling (NFC). These corroborative measurements were performed using a custom built MOKE setup at Uppsala University (the MOKE results discussed in the manuscript were recorded using a custom built setup at the University of Iceland). No notable differences are observed in the coercivity and exchange field of the films for both temperature dependent MOKE measurements.

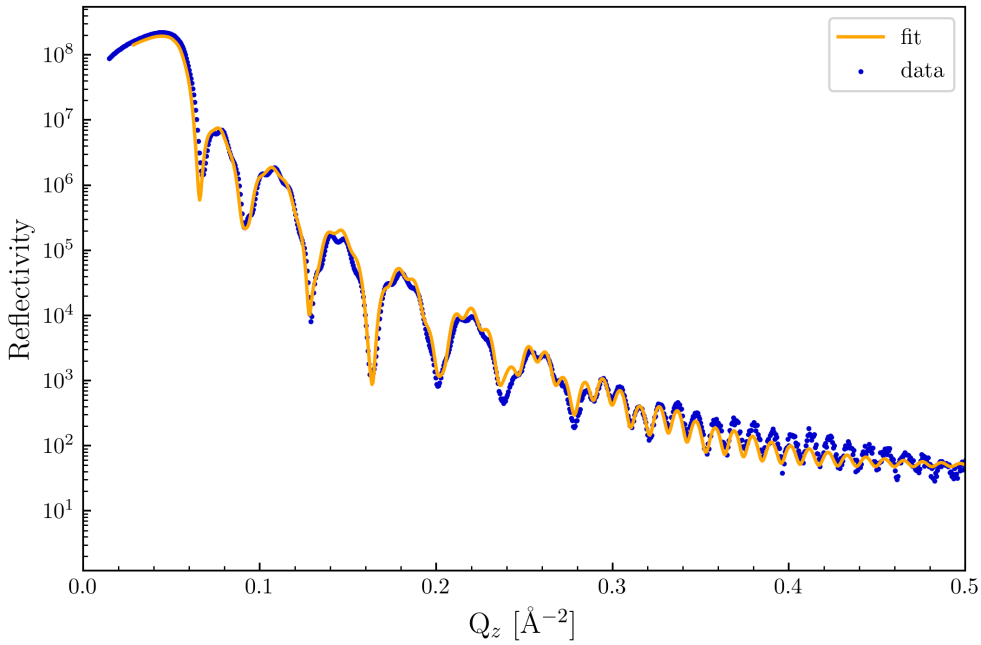

FIG. S4: Room temperature XRR data with fit for the V_2O_3/Ni/Zr film of thickness V_2O_3 = 58.1 nm , Ni = 9.4 nm , and Zr = 5.4 nm.

Paper II

Structural and magnetic characterization of epitaxial $V_2O_3/Ni_{80}Fe_{20}$ hybrid magnetic structuress

K. Ignatova, M.T. Sultan, A.O. Elvarsson, S. Ingvarsson, U.B. Arnalds

2022 International Semiconductor Conference (CAS) (2022)

Structural and magnetic characterization of epitaxial $V_2O_3/Ni_{80}Fe_{20}$ hybrid magnetic structures

K. Ignatova*, M. T. Sultan*, A. O. Elvarsson*, S. Ingvarsson*, U. B. Arnalds
*Science Institute, University of Iceland, Reykjavík, Iceland
Email: kri12@hi.is

***Abstract*—We study the structure and temperature dependent electrical and magnetic properties of highly epitaxial $V_2O_3/Ni_{80}Fe_{20}$ layers grown on *c*-plane Al_2O_3 by direct current magnetron sputtering. We focus our attention on the structural and magnetic properties of the $Ni_{80}Fe_{20}$ layer and their dependence on the deposition temperature. X-ray diffraction measurements reveal an epitaxial nature of the V_2O_3 layers with a (006) orientation. Electrical characterization of single layered V_2O_3 reveals a metal insulator transition at around ~ 150 K. All samples showed a strong epitaxial (1 1 1) peak showing that highly crystallized $Ni_{80}Fe_{20}$ layers can be deposited onto V_2O_3 at room temperature. Angular dependent magneto-optical Kerr effect characterization of the films reveals a uniaxial anisotropy in the films with a coercivity of the order of 1 Gauss. The first-order reversal curve method is used to analyze the magnetization reversal mechanism.**

***Index Terms*—$Ni_{80}Fe_{20}$, V_2O_3, strain, magnetic anisotropy, magnetic films, MIT**

I. Introduction

Permalloy, composed of $Ni_{80}Fe_{20}$, has long been the paradigm of soft magnetic materials and has been utilized in multiple research studies ranging from investigations in its thin film form [1], in magnetic nanostructures [2] as well as in biomedical applications. Several studies have been performed on the deposition of $Ni_{80}Fe_{20}$ on different substrates in order to investigate the role of the substrate surface on the magnetic and structural properties [3], [4]. In this work we investigate the use of a novel material as a substrate, fabricating highly crystalline hybrid heterostructures composed of V_2O_3 and $Ni_{80}Fe_{20}$. Although several investigations have been published on thin film $Ni_{80}Fe_{20}$ deposition on VO_2 layers, which share a similar structural nature [5], [6] work on deposition on V_2O_3 has been limited. Reactive magnetron sputtering has been shown to produce highly crystalline and atomically flat films of V_2O_3 onto *c*-plane sapphire substrates [7], [8], [9], [10]. We focus our attention on the structural and magnetic properties of the $Ni_{80}Fe_{20}$ layer when deposited at different deposition temperatures revealing that highly crystalline structures can be achieved even at room temperature. V_2O_3 exhibit a structural phase transitions at around ~ 150 K from a high temperature rhombohedral metallic state to a low temperature insulating monoclinic phase. Coupling this phase transition to magnetic layers therefore offers new routes for investigation including the effect of strain on the magnetic properties [11] as well as investigations on the spin orbit torque in hybrid structures through the metal-insulator transition [5].

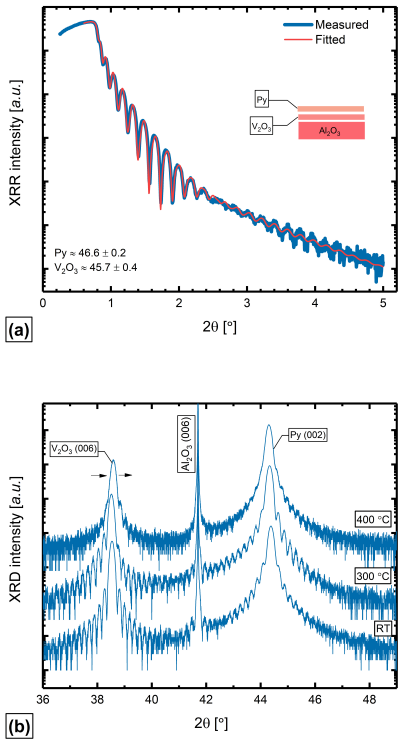

Fig. 1. (a) XRR plot for the film with $Ni_{80}Fe_{20}$ grown at 300°C. The blue and overlapped red line represent the measured and fitted data, respectively. (b) X-ray diffraction scans for structures with the $Ni_{80}Fe_{20}$ layer deposited at different temperatures. The vertical dashed lines illustrate the bulk peak positions.

II. Materials and Methods

The $V_2O_3/Ni_{80}Fe_{20}$ heterostructure thin films were grown on *c*-plane Al_2O_3 by direct current magnetron sputtering in a custom built high vacuum sputter chamber [12]. Prior to deposition the substrates were annealed at 600°C for 30 minutes followed by deposition of V_2O_3 at the same temperature synthesized from a vanadium target at a constant discharge power of 100 W. For the deposition of the V_2O_3 argon (Ar

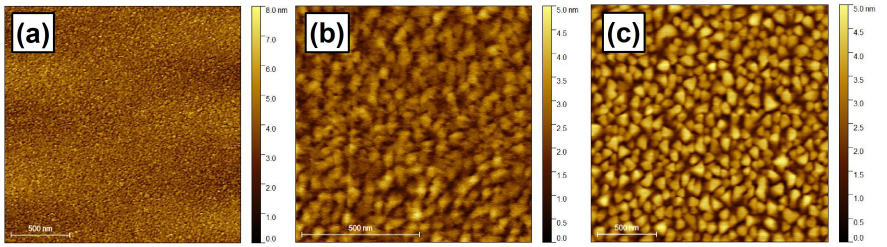

Fig. 2. (a-c) AFM images of the V_2O_3/$Ni_{80}Fe_{20}$ films deposited at room temperature, 300°C and 400°C (from left to right). The images were recorded over a scan area of 2 × 2 μm^2.

flow of 40 sccm) was used as the working gas and oxygen (O_2 flow of 0.85 sccm) as a reactive gas. During growth a throttle valve was adjusted to stabilize the deposition pressure at 0.7 Pa. The discharge parameters used for the deposition of the V_2O_3 were chosen based on previous works [10]. The $Ni_{80}Fe_{20}$ deposition was made using a $Ni_{80}Fe_{20}$ compound target at a constant power of 80 W, using Ar as working gas at a growth pressure of 0.7 Pa. The $Ni_{80}Fe_{20}$ layers were deposited at different temperatures from room temperature up to 400°C.

The structural properties of the films were characterized using x-ray reflectivity and x-ray diffraction using a Panalytical X'pert diffractometer (CuKα, 0.15406 nm). The surface morphology of the films was investigated using a Park System (PSIA XE-100) atomic force microscope. Electrical characterization as a function of temperature for single V_2O_3 layered films was carried out in a custom built helium cooled cryostat in vacuum.

The in-plane magnetic anisotropy of the films was investigated by recording hysteresis loops as a function of sample angle in a custom built longitudinal magneto-optical Kerr effect (MOKE) setup and FORC (first-order reversal curve) method. Temperature dependent magnetic properties were investigated using a second custom built, low temperature MOKE setup.

III. Results and Discussion

A. Structure characterization

Figure 1(a) shows a typical XRR scan of the structures ($Ni_{80}Fe_{20}$) film grown at 300°C along with results of fitting the data using the X-pert Reflectivity program. The thickness of films was determined from the fitting to be $\sim$ 45.7 nm and $\sim$ 46.6 nm for the V_2O_3 and $Ni_{80}Fe_{20}$ layers, respectively. Similar XRR results were obtained for the other film structures. Figure 1(b) shows XRD scans for structures where the $Ni_{80}Fe_{20}$ film was deposited at room temperature, 300°C and 400°C, respectively. The results reveal the highly epitaxial nature of the films with clear Laue fringes extending on both sides of the peaks for both the V_2O_3 (0 0 6) and $Ni_{80}Fe_{20}$ (1 1 1) layer peaks. For the $Ni_{80}Fe_{20}$ peak a shift in peak position towards lower 2θ values is observed with increasing deposition temperature implying an out-of plane tensile strain which can be attributed to the increase in growth temperature [13], [14]. The V_2O_3 peak position corresponds closely to the bulk standard value of 38.514° displaying a slight increase to higher values and a small shift from 38.53° to 38.58°.

Figure 2 shows the AFM analysis of the film stacks. The results reveal the films to have a low surface roughness with RMS roughness values determined from images to be 0.85 nm, 0.61 nm and 0.89 nm for the films deposited at room temperature, 300°C and 400°C, respectively. A clear evolution of the morphology of the films is observed from a small granular structure of the film deposited at room temperature to larger grains for the films deposited at elevated temperatures.

B. Room temperature magnetic properties

Figure 3 shows the coercivity and relative magnetic remanence ($M_{\rm rem}/M_{\rm sat}$) extracted from recorded hysteresis loops measured using MOKE with an in-plane applied magnetic field for in-plane sample angles in the range 0° - 360°. The results reveal the $Ni_{80}Fe_{20}$ layers to display soft magnetic properties with coercivities in all cases below 1.5 Gauss. The samples display a clear uniaxial anisotropy with an easy axis at $\sim$ 120° ($\sim$ 300°). For sputtered $Ni_{80}Fe_{20}$ films several different causes are known to induce a uniaxial anisotropy in addition to crystallographic properties [13] including substrate surface induced effects, growth under a tilt angle [15] and under an externally applied field [16]. As the films in this study are deposited under a perpendicular angle with the substrates facing directly the magnetron we rule out any role of tilted angle on the deposition inducing an anisotropy on the films. Step edges on Al_2O_3 substrate surfaces are known to induce an anisotropy in overlying magnetic layers, especially for sapphire substrates annealed in air at elevated temperatures [17]. As the V_2O_3 grows highly epitaxially on the Al_2O_3 substrate such step edges have the potential to traverse through the V_2O_3 layer affecting the anisotropy of the $Ni_{80}Fe_{20}$ layer [7]. However, as the films were deposited on substrates which did not undergo any annealing treatment beyond the 600°C annealing in vacuum we exclude any role of the Al_2O_3 surface on the anisotropy of the $Ni_{80}Fe_{20}$ films. The AFM analysis shown in figure 2 also did not reveal any stepped structure on the surface of the films.

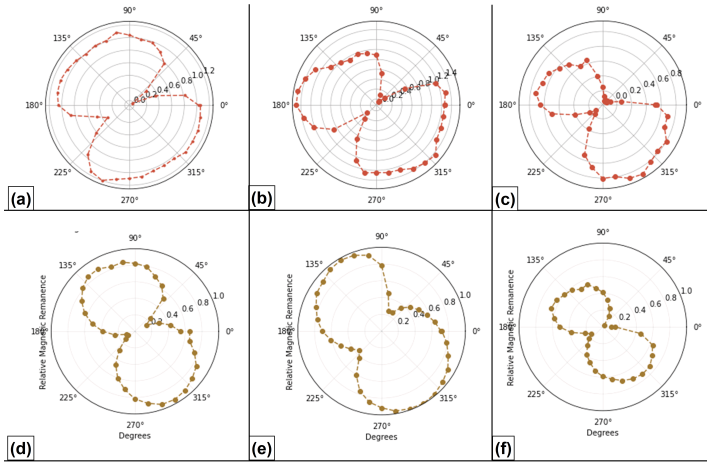

Fig. 3. In-plane polar plots for (a-c) coercivity in Gauss and (d-f) relative remanent magnetization for structures with $Ni_{80}Fe_{20}$ grown at RT, 300°C and 400°C, respectively. The values were determined from hysteresis loops recorded for varying in plane sample angle in the MOKE setup.

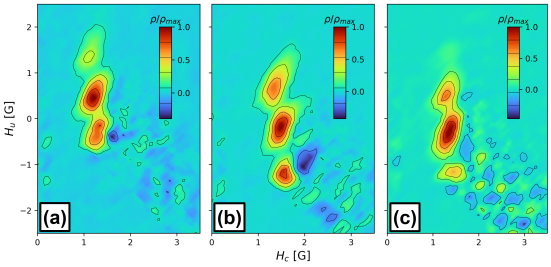

Fig. 4. FORC diagrams of $V_2O_3/Ni_{80}Fe_{20}$ films grown at room temperature (a), 300°C (b) and 400°C (c). Isolated peaks in the diagram indicate that all the films have weakly-interacting single domain grains.

Nonzero components of the FORC diagram reveal irreversible processes in the magnetic reversal mechanisms (see Fig.4). Isolated peaks in the diagram indicate that all the films have weakly-interacting single domain grains. The symmetric vertical spread of the peaks reveals that there is a local interaction field that is constant at a given particle site, but that varies randomly between particles [18]. Moreover, a stabilizing mean interacting field is observed to increase with the growth temperature, indicated by the downward shift of the peak positions. The middle and lower peak can be explained by irreversible annihilation and nucleation of the single domain grains, respectively. However, the presence of a third top peak is not fully understood. The features along the diagonal are an artefact that can arise when nucleation occurs at slightly different external magnetic fields [19].

C. Temperature dependent properties

Figure 5 shows the temperature dependent resistance of a single layer V_2O_3 layer deposited under the same conditions as for the $Ni_{80}Fe_{20}$ samples. The resistance change illustrates clearly the metal-insulator transition occurring in the material as it changes from a high temperature rhombohedral to a low temperature monoclinic crystal structure. The maximum in the transition occurs at a temperature of $\sim$ 150 K as expected for V_2O_3. Figure 5 also shows the coercivity of the $V_2O_3/Ni_{80}Fe_{20}$ structures along an easy axes for the room temperature deposited $Ni_{80}Fe_{20}$ layer. The results reveal a gradual increase in coercivity with reducing temperature as expected for all the samples grown at 400°C, 300°C and room temperature. Previous results on amorphous magnetic layers grown on on V_2O_3 films (on c-plane sapphire) have show a strain induced increase in coercivity occuring at the transition [11]. Similarly, magnetic heterostructures deposited on r-plane sapphire have shown an increased strain related coercivity as well as a nanoscale phase formation induced coercivity enhancement at the transition arising from an increased roughness of the V_2O_3 film [20], [21]. The coercivity data depicted in figure 5 reveals no indication of an increased coercivity in the $Ni_{80}Fe_{20}$ film occurring at the transition. This results therefore shows that the strain induced by the structural transition occurring in the V_2O_3 has a limited effect on the magnetic properties of the $Ni_{80}Fe_{20}$.

IV. Conclusions

In summary we have investigated the structural and magnetic properties of $V_2O_3/Ni_{80}Fe_{20}$ bilayer structures deposited using dc-magnetron sputtering on c-plane Al_2O_3 substrates. The results reveal similar textured $Ni_{80}Fe_{20}$ films with soft magnetic properties with limited dependence on the deposition temperature of the $Ni_{80}Fe_{20}$ layer. Magnetic characteriza-

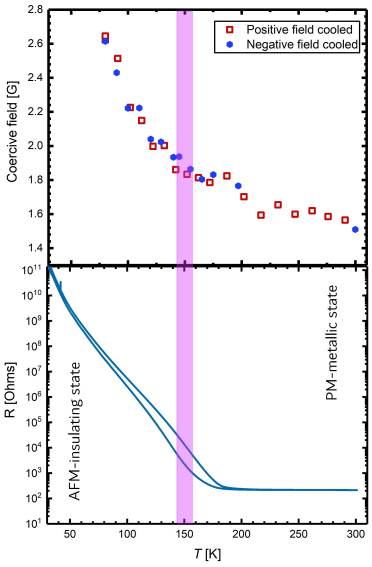

Fig. 5. (Lower graph) Resistance as a function of temperature (measured using gold contacts on the sample edges [8]) for a reference single layer V_2O_3 film deposited onto c-plane Al_2O_3 with the same deposition parameters as the $Ni_{80}Fe_{20}$ samples. The line and the shaded area highlight the metal-insulator transition temperature (obtained using Gaussian fitting of the $\mathrm{d}(\ln(R))/\mathrm{d}T$ data). (Upper graph) Coercivity as a function of temperature along an easy axes for the $V_2O_3/Ni_{80}Fe_{20}$ film grown at RT. The blue squares and red dots denote coercivity values extracted from hysteresis loops recorded for increasing temperature after cooling under an externally applied positive and negative field, respectively.

tion as a function of in-plane sample angle reveals uniaxial anisotropy axis. These results therefore show that using dc-magnetron sputtering high quality permalloy layers can be achieved even at room temperature. Temperature dependent magnetic characterization shows an increased coercivity with reducing temperature but does not reveal strong indications of strain induced effects arising from the structural transition occurring in the V_2O_3.

V. Acknowledgements

This work was supported by funding from the Icelandic Research Fund Grant Nos. 207111-051, 218029-051 and 228951-051.

References

[1] F Legall, C Morice, W Jahjah, A Bivic, N Ryon, J Richy, ARE Prinsloo, CJ Sheppard, A Fessant, J-Ph Jay, et al. Magnetization Reversals of $Fe_{81}Ga_{19}$-Based Flexible Thin Films Under Multiaxial Mechanical Stress. Physical Review Applied, 15(4):044028, 2021.

[2] M Xing, Jeotikanta Mohapatra, J Elkins, D Guragain, SR Mishra, and J Ping Liu. Exchange bias and Verwey transition in Fe_5C_2/Fe_3O_4 core/shell nanoparticles. Nanoscale, 13(37):15837–15843, 2021.

[3] Movaffaq Kateb, Hamidreza Hajihoseini, Jon Tomas Gudmundsson, and Snorri Ingvarsson. Comparison of magnetic and structural properties of permalloy $Ni_{80}Fe_{20}$ grown by dc and high power impulse magnetron sputtering. Journal of Physics D: Applied Physics, 51(28):285005, 2018.

[4] JCA Huang, YM Hu, and CC Yu. Magnetic and structural characterizations of HCP permalloy films grown by molecular beam epitaxy. Journal of applied physics, 83(11):7046–7048, 1998.

[5] Jun-young Kim, Joel Cramer, Kyujoon Lee, Dong-Soo Han, Dongwook Go, Pavel Salev, Pavel N Lapa, Nicolas M Vargas, Ivan K Schuller, Yuriy Mokrousov, et al. Tuning Spin-Orbit Torques Across the Phase Transition in VO_2/NiFe Heterostructure. Advanced Functional Materials, page 2111555, 2022.

[6] Guodong Wei, Xiaoyang Lin, Zhizhong Si, Dong Wang, Xinhe Wang, Xiaofei Fan, Kun Deng, Kai Liu, Kaili Jiang, Na Lei, Yanxue Chen, Stephane Mangin, Eric Fullerton, and Weisheng Zhao. Optically induced phase change for magnetoresistance modulation. Advanced Quantum Technologies, 3(3):1900104, 2020.

[7] Einar B Thorsteinsson, Seyedmohammad Shayestehaminzadeh, and Unnar B Arnalds. Tuning metal-insulator transitions in epitaxial V_2O_3 thin films. Applied Physics Letters, 112(16):161902, 2018.

[8] Einar B Thorsteinsson, Seyedmohammad Shayestehaminzadeh, Arni S Ingason, Fridrik Magnus, and Unnar B Arnalds. Controlling metal–insulator transitions in reactively sputtered vanadium sesquioxide thin films through structure and stoichiometry. Scientific Reports, 11(1):1–10, 2021.

[9] Hamidreza Hajihoseini, Einar B Thorsteinsson, Vilborg V Sigurjonsdottir, and Unnar B Arnalds. Strained interface layer contributions to the structural and electronic properties of epitaxial V_2O_3 films. Applied Physics Letters, 118(16):161602, 2021.

[10] MT Sultan, K Ignatova, EB Thorsteinsson, F Magnus, and UB Arnalds. Structural and electrical properties of V_2O_3 thin films on c-plane Al_2O_3 fabricated by reactive-HiPIMS and dcMS techniques. Journal of Physics D: Applied Physics, 54(42):425302, 2021.

[11] V Polewczyk, SK Chaluvadi, P Orgiani, G Panaccione, G Vinai, G Rossi, and P Torelli. Tuning the magnetic properties of V_2O_3/CoFeB heterostructures across the V_2O_3 structural transition. Physical Review Materials, 5(3):034413, 2021.

[12] UB Arnalds, JS Agustsson, AS Ingason, AK Eriksson, Kristinn B Gylfason, JT Gudmundsson, and S Olafsson. A magnetron sputtering system for the preparation of patterned thin films and in situ thin film electrical resistance measurements. Review of Scientific Instruments, 78(10):103901, 2007.

[13] Movaffaq Kateb, Jon Tomas Gudmundsson, and Snorri Ingvarsson. Effect of atomic ordering on the magnetic anisotropy of single crystal $Ni_{80}Fe_{20}$. AIP advances, 9(3):035308, 2019.

[14] Mitsuru Ohtake, Takahiro Tanaka, Katsuki Matsubara, Fumiyoshi Kirino, and Masaaki Futamoto. Epitaxial growth of permalloy thin films on MgO single-crystal substrates. In Journal of Physics: Conference Series, volume 303, page 012015. IOP Publishing, 2011.

[15] Movaffaq Kateb, Egill Jacobsen, and Snorri Ingvarsson. Application of an extended Van der Pauw method to anisotropic magnetoresistance measurements of ferromagnetic films. Journal of Physics D: Applied Physics, 52(7):075002, 2018.

[16] Jose M. Porro, Aritz Villar, Carolina Redondo, Natalia A. Río-López, Andoni Lasheras, Daniel Salazar, Rafael Morales, and Eduardo Fernández-Martín. Competition of magnetic anisotropies in permalloy antidot lattices. Magnetochemistry, 8(5), 2022.

[17] Xu Xu, Lichuan Jin, Tianlong Wen, Yulong Liao, Xiaoli Tang, Huaiwu Zhang, and Zhiyong Zhong. Effects of substrate annealing on uniaxial magnetic anisotropy and ferromagnetic resonance frequency of $Ni_{80}Fe_{20}$ films deposited on self-organized periodically rippled sapphire substrates. Vacuum, 186:110047, 2021.

[18] Roberts Pike. Verosub characterizing interactions in fine magnetic particle systems using first order reversal curves j. Appl. Phys, 85:6660, 1999.

[19] Merlin Pohlit, Paul Eibisch, Maryam Akbari, Fabrizio Porrati, Michael Huth, and Jens Müller. First order reversal curves (FORC) analysis of individual magnetic nanostructures using micro-Hall magnetometry. Review of Scientific Instruments, 87(11):113907, 2016.

[20] J De La Venta, Siming Wang, T Saerbeck, JG Ramírez, I Valmianski, and Ivan K Schuller. Coercivity enhancement in V_2O_3/Ni bilayers driven by nanoscale phase coexistence. Applied Physics Letters, 104(6):062410, 2014.

[21] AS McLeod, E Van Heumen, JG Ramirez, S Wang, T Saerbeck, S Guenon, M Goldflam, L Anderegg, P Kelly, A Mueller, et al. Nanotextured phase coexistence in the correlated insulator V_2O_3. Nature Physics, 13(1):80–86, 2017.

Paper III

Phase coexistence induced surface roughness in V_2O_3/Ni magnetic heterostructures

K. Ignatova, E. Vlasov, S.D. Seddon, N. Gauquelin, J. Verbeeck, D. Wermeille, S. Bals, T.P.A. Hase, U.B. Arnalds

APL Materials (2024)

APL Materials ARTICLE pubs.aip.org/aip/apm

Phase coexistence induced surface roughness in V_2O_3/Ni magnetic heterostructures

Cite as: APL Mater. 12, 041118 (2024); doi: 10.1063/5.0195961
Submitted: 4 January 2024 • Accepted: 27 March 2024 •
Published Online: 15 April 2024

K. Ignatova,[1] E. Vlasov,[2] S. D. Seddon,[3] N. Gauquelin,[2] J. Verbeeck,[2] D. Wermeille,[4,5] S. Bals,[2] T. P. A. Hase,[6] and U. B. Arnalds[1,a)]

AFFILIATIONS

[1] Science Institute, University of Iceland, Dunhaga 3, 107 Reykjavik, Iceland
[2] EMAT and NANOlab Center of Excellence, University of Antwerp, Groenenborgerlaan 171, Antwerp, Belgium
[3] TU Dresden, Institute of Applied Physics, Nöthnitzer Strasse 61, 01187 Dresden, Germany
[4] XMaS, The UK Materials Science Facility, European Synchrotron Radiation Facility, F-38043 Grenoble, France
[5] Department of Physics, University of Liverpool, Oliver Lodge, Liverpool L69 7ZE, United Kingdom
[6] Department of Physics, University of Warwick, Coventry CV4 7AL, United Kingdom

[a)] Author to whom correspondence should be addressed: uarnalds@hi.is

ABSTRACT

We present an investigation of the microstructure changes in V_2O_3 as it goes through its inherent structural phase transition. Using V_2O_3 films with a well-defined crystal structure deposited by reactive magnetron sputtering on *r*-plane Al_2O_3 substrates, we study the phase coexistence region and its impact on the surface roughness of the films and the magnetic properties of overlying Ni magnetic layers in V_2O_3/Ni hybrid magnetic heterostructures. The simultaneous presence of two phases in V_2O_3 during its structural phase transition was identified with high resolution x-ray diffraction and led to an increase in surface roughness observed using x-ray reflectivity. The roughness reaches its maximum at the midpoint of the transition. In V_2O_3/Ni hybrid heterostructures, we find a concomitant increase in the coercivity of the magnetic layer correlated with the increased roughness of the V_2O_3 surface. The chemical homogeneity of the V_2O_3 is confirmed through transmission electron microscopy analysis. High-angle annular dark field imaging and electron energy loss spectroscopy reveal an atomically flat interface between Al_2O_3 and V_2O_3, as well as a sharp interface between V_2O_3 and Ni.

I. INTRODUCTION

Transition metal oxides in the vanadium oxide family comprise an interesting class of materials that exhibit multiple oxidation states.[1] These materials are primarily recognized for their triple transitions: a first-order metal–insulator transition (MIT), a structural phase transition (SPT), and a magnetic transition. These transitions typically occur simultaneously but can be modified or suppressed through techniques such as doping and applying stress.[2–6] In both bulk and thin film forms, vanadium oxides have found applications in memristors, battery electrodes, supercapacitors,[7] and other memory-related technologies. The incorporation of vanadium oxide composite thin films with a magnetic layer presents numerous additional possibilities for utilizing nano-devices in sensor technology, antiferromagnetic spintronics,[8,9] medical applications,[10] Mott-based memory devices,[11] and neuromorphic computing.[12–14]

Extensive research has been conducted to understand the underlying mechanisms of the MIT and the SPT in vanadium oxide as well as to investigate the impact of phase transitions in vanadium oxides on the magnetic characteristics of hybrid magnetic heterostructures.[15] The underlying phase transitions are emerging as an increasingly potent mechanism for manipulating the essential characteristics of epitaxial heterostructures containing vanadium oxide.[16–20] Experimental evidence has demonstrated that structural phase transitions and surface-induced roughness can directly influence magnetic overlayers, leading to alterations in their internal anisotropy and coercivity as well as an emerging exchange bias.[16,19–23] Gaining a comprehensive understand-

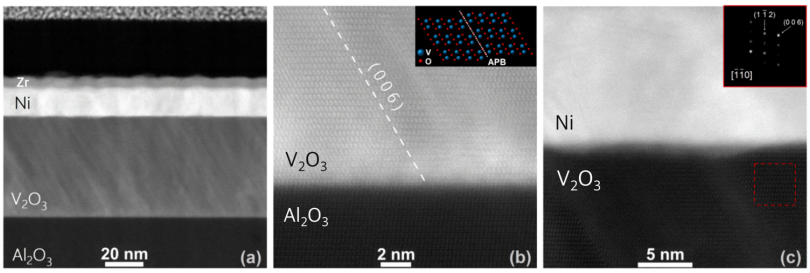

FIG. 1. HAADF-STEM images of (a) the cross section of the V_2O_3/Ni/Zr thin film on the Al_2O_3 *r*-plane substrate, (b) the Al_2O_3/V_2O_3, and (c) the V_2O_3/Ni interfaces. The HAADF-STEM signal intensity is proportional to the atomic number and portrayed in the grayscale of the images. The dashed line in (b) illustrates the placement of an antiphase boundary in the V_2O_3, with the possible atom arrangement schematics illustrated in the inset. The inset in (c) shows a diffractogram obtained by Fourier transforming the image from the red square region in the V_2O_3 layer indexed as rhombohedral V_2O_3.

ing of the intricate, detailed microstructure–property relationships is crucial for fully exploiting the effects of phase transitions in vanadium oxides on systems integrated with these phase-change materials.

For our study, we focus on thin film vanadium sesquioxide (V_2O_3) with a well-defined crystal structure that undergoes a structural transition from a low-temperature insulating/antiferromagnetic phase to a high-temperature metallic/paramagnetic phase. During this transition, the crystalline structure of V_2O_3 undergoes a transformation from a single monoclinic (MC) phase to a coexistence of rhombohedral and monoclinic phases at ~130 K, which eventually transitions into a single rhombohedral (RH) phase structure.[21] Here, we investigate the interplay between the microstructure of the V_2O_3 films and their structural properties during the phase transition. In particular, we examine the changes in the microstructure during the phase coexistence region of the V_2O_3 layer and how these changes correlate with alterations in the magnetic properties of overlying magnetic layers in V_2O_3/Ni heterostructures.

II. MATERIALS AND METHODS

The V_2O_3 and V_2O_3/Ni films were grown on *r*-plane Al_2O_3 [1$\bar{1}$02] substrates using reactive direct current (dc) magnetron sputtering for the V_2O_3 layer and conventional dc magnetron sputtering for the Ni layer. In addition, a Zr capping layer was deposited to prevent oxidation of the Ni layer. The substrates were annealed in air at 1200 °C for 24 h. The growth process was carried out in a custom-built chamber,[24] utilizing high-purity 3-in. vanadium (99.99%) and high-purity 3-in. nickel (99.99%) sputtering targets. Prior to deposition, the base pressure of the chamber was below 4×10^{-6} Pa. The substrates underwent pre-baking under vacuum in the sputtering chamber at a temperature of 610 °C for ~60 min prior to any growth. The V_2O_3 was deposited at a temperature of 610 °C, while the Ni and Zr layers were deposited at room temperature after allowing the sample to cool down under an ultra-high vacuum. An identical reference sample consisting solely of the V_2O_3 layer was deposited following the same recipe. X-ray reflectivity (XRR) analysis showed the heterostructure film stack to be composed of a 49 nm thick V_2O_3 layer, followed by a 13 nm Ni layer, and finally a 6 nm thick Zr capping layer.

The structural properties of the V_2O_3 and V_2O_3/Ni films were examined as a function of temperature using high-resolution double-axis x-ray diffraction (XRD) and reflectivity (XRR) measurements at the BM28 (XMaS) beamline at the European Synchrotron Radiation Facility (ESRF) in Grenoble, France.[25] The photon energy was chosen to be 12.4 keV, corresponding to a wavelength of 1 Å. The XRR profiles were fitted using the GenX software.[26] High-resolution three-dimensional reciprocal space mapping (3D-RSM) was employed to investigate the crystal microstructure and its structural evolution across the temperature-driven phase transition in the V_2O_3 and V_2O_3/Ni films. The surface morphology of the specimens was examined using atomic force microscopy (AFM) in contact mode at room temperature.

The stoichiometric composition and crystalline quality at the sub-nm lateral scale of the films were investigated by scanning transmission electron microscopy (STEM), using high-angle annular dark-field (HAADF-STEM) imaging, energy dispersive x-ray analysis (STEM-EDX), and electron energy loss spectroscopy (EELS). The HAADF-STEM imaging, EELS, and STEM-EDX measurements were conducted on a double aberration-corrected Thermo Fischer Scientific X-Ant-EM instrument operated at 120 kV and equipped with a GIF Enfinium EELS spectrometer. The TEM lamellas were prepared by focused ion beam (FIB) milling. The magnetic properties of the V_2O_3/Ni bilayer were characterized using the longitudinal magneto-optical Kerr effect (MOKE) as a function of azimuth angle at room temperature. Furthermore, temperature-dependent magnetic characterization was performed using vibrating sample magnetometry (VSM) and a custom-built system for measuring the longitudinal MOKE signal at low temperatures.

III. EXPERIMENTAL RESULTS

A. Phase and microstructure investigation

Figure 1(a) shows an overview cross-sectional HAADF-STEM image of the V_2O_3/Ni/Zr heterostructure on the Al_2O_3 substrate. Figures 1(b) and 1(c) show higher magnification images at the Al_2O_3/V_2O_3 and V_2O_3/Ni interfaces, respectively. The data clearly

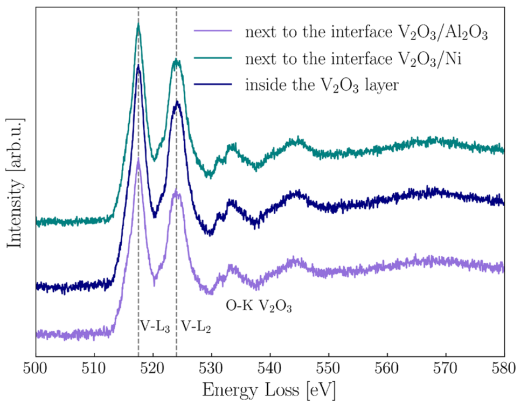

FIG. 2. STEM-EELS spectra with indicated V–L and O–K edges taken from the V_2O_3/Ni interface and the V_2O_3 interior. The spectra are corrected for background and taken at room temperature for the V_2O_3/Ni film grown on the *r*-plane of the Al_2O_3 substrate.

reveal both the crystalline nature of the film and the high quality of the interfaces. The TEM images were taken along the [$\bar{1}$10] zone axis of the Al_2O_3 sapphire substrate.

The chemical and oxidation states of the V_2O_3 and Ni layers were investigated using EELS. EELS spectra were recorded at different locations of the V_2O_3, in the middle of the layer, and near both interfaces, as shown in Fig. 2. The observed V–L_3 energy loss edge is 517.48 eV, and the O–K edges consist mainly of two peaks, which correspond well with the fingerprint feature of rhombohedral corundum V_2O_3.[27–29] At the nanoscale, the EELS analysis indicates that the oxidation state of vanadium does not vary across the entire film (see Fig. 2), revealing no evidence of other non-stoichiometric parasitic phases of vanadium oxide in the film. We can, therefore, conclude that the V_2O_3 layer is chemically homogeneous in our samples. EELS structure evolution spectra recorded for the Ni and other interfaces in the film are shown in Figs. S1 and S2 of the supplementary material. After extended exposure, the top capping layer undergoes oxidation, as confirmed by the EELS analysis. Consequently, all scans were analyzed using a model that incorporates ZrO_2 atop the heterostructure. Notably, there is no presence of a NiO layer across the film (see Fig. S1 of the supplementary material). The analysis of the HAADF images together with line profiles retrieved from EELS reveals the quality of the interfaces. It is evident that the Al_2O_3/V_2O_3 interface is atomically flat, and the V_2O_3/Ni interface has a well-defined boundary between the layers with negligible intermixing. The extent of interdiffusion between the V_2O_3 and Ni layers does not exceed 1.5 nm (see Figs. S1 and S2 of the supplementary material). The thicknesses of the V_2O_3/Ni film obtained from the STEM measurements are in agreement with thicknesses determined from XRR data performed at room temperature of 49 and 13 nm, respectively.

The STEM images show striped patterns with staircase-like features in the V_2O_3 layer [Fig. 1(b)]. This structural feature is a typical signature of the presence of symmetry-breaking anti-phase boundaries (APB) that emerge at the Al_2O_3/V_2O_3 interface, with the displacement vector parallel to the ⟨001⟩ direction.[30,31] Neighboring domains separated by the APB are displaced by half of a unit cell along the (006) plane, as demonstrated schematically in the inset in Fig. 1(b). Other microstructure symmetry-breaking effects, such as crystallographic twinning, have been found previously in VO_2 films grown on *c*-plane Al_2O_3 substrates.[32] In our case, a similar parallel columnar-like microstructure of the V_2O_3 layer is observed for the V_2O_3 films grown on *c*-plane sapphire substrates (see Fig. S3 of the supplementary material) with no presence of twinning or APB defects. Further details on the structural and magnetic properties of the *c*-plane V_2O_3/Ni heterostructure can be found elsewhere.[20] Figure 1(b) reveals no twinning in the V_2O_3 layer grown on the Al_2O_3*r*-plane, only showing anti-phase boundaries at an angle of 59.04° with the surface plane corresponding well to the angle between the film surface normal (012) and (006) planes of 58.59°. APBs in V_2O_3 films grown on Al_2O_3*c*-plane substrates have been previously observed, with APBs being identified in the planar view of the *c*-plane.[33] Multiple mechanisms can induce the formation and nucleation processes of APBs. Typically, the formation of APBs occurs during thin film growth.[34,35] For V_2O_3 films deposited onto annealed Al_2O_3 substrates, the most likely reason for the formation of APBs in the V_2O_3 layer is related to the Al_2O_3*r*-plane substrate due to its multi-step, terrace-like surface structure formed by the annealing at 1200 °C, as shown in Fig. 3.

B. Structural evolution

The crystal structural evolution of the film through the phase transition was investigated by performing x-ray diffraction measurements as a function of temperature from 30 to 277 K. Figure 4 shows a sub-set of the XRD scans recorded along the surface normal from 70 to 180 K. The data show clear single phase behavior at low and high temperatures arising from the low temperature monoclinic and high temperature rhombohedral phases. Additional powder-like peaks originating from the Be vacuum capsule are evident across the entire temperature range (see Fig. 4). It is crucial to note that the Ni layer exhibits a textured (111) orientation, as evidenced by a weak

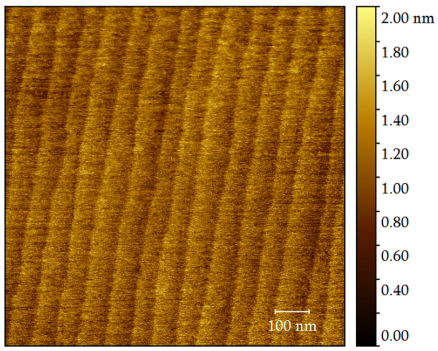

FIG. 3. 5 × 5 μm^2 atomic force microscopy image of an *r*-plane sapphire Al_2O_3 substrate annealed for 24 h at 1200 °C. The annealed surface exhibits atomically flat terraces, with each terrace ~100 nm in width.

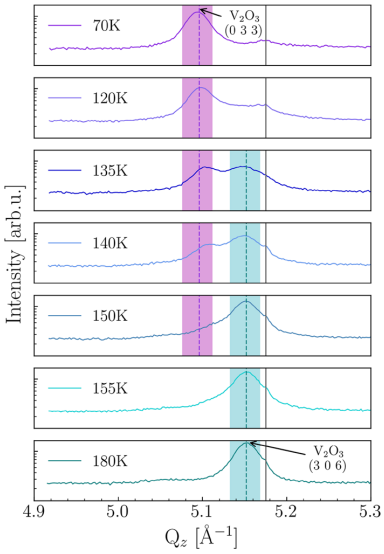

FIG. 4. Temperature-dependent x-ray diffraction scans recorded for the V_2O_3/Ni film as a function of temperature across the SPT of V_2O_3. Pink and cyan bars indicate the diffraction peaks for the monoclinic and rhombohedral phases of V_2O_3 at low and high temperatures, respectively. Broken lines indicate the XRD peak positions derived by the fitting with a Pearson-type VII function of the monoclinic V_2O_3 (0 3 3) at low temperatures and the rhombohedral V_2O_3 (3 0 6) at high temperatures. Straight gray lines indicate Be powder peak positions arising from scattering from the beryllium vacuum capsule.

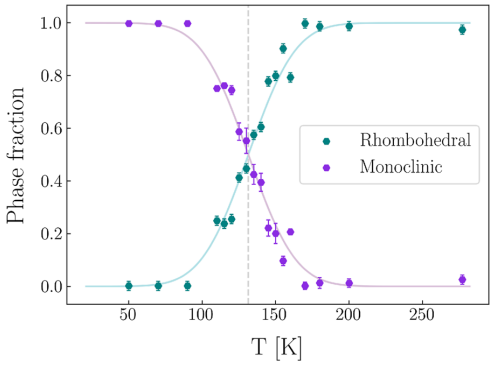

FIG. 5. Relative intensities of V_2O_3 (0 3 3) and V_2O_3 (3 0 6) Bragg peaks observed upon heating in the V_2O_3/Ni film. The dashed line indicates the temperature where the ratio of monoclinic and rhombohedral V_2O_3 phases is equal, and it is at ~130 K. The dependency of the phase fractions on temperature was modeled using a cumulative skewed normal distribution function. The function is symmetric within uncertainty, with a transition width of 12.7 K, centered at 131.4 K.

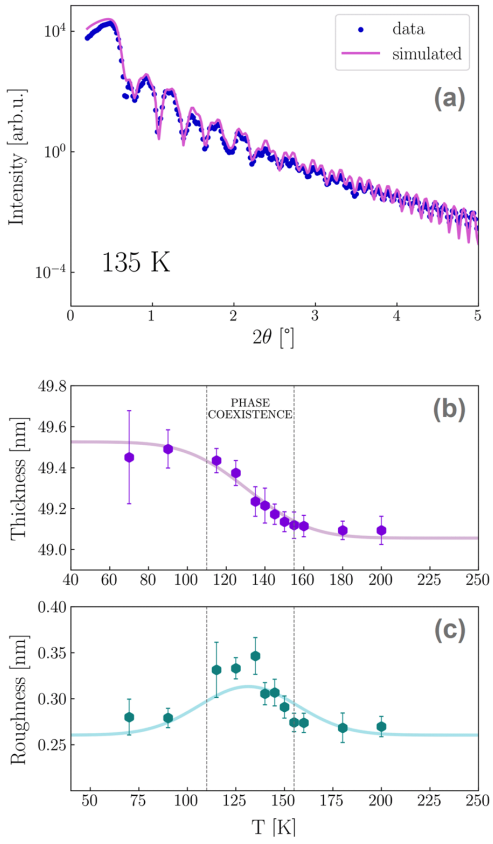

FIG. 6. (a) XRR data recorded for the V_2O_3/Ni structure at 135 K and fit using GenX.[26] The corresponding x-ray scattering length density profile of the film at 135 K is shown in Fig. S6 of the supplementary material. (b) and (c) show the thickness and the roughness values of the V_2O_3 layer derived from the fit of the XRR profiles as a function of temperature, respectively. The error bars represent estimated systematic errors calculated in the fitting. Dashed lines indicate where the fractions of either of the two coexisting phases correspond to 5%.

peak observed around 44.5°, which can be attributed to the Ni (111) reflection (see Fig. S4 of the supplementary material).

The transition from the low temperature phase begins at about 110 K and extends up to about 155 K, at which point the layer has fully transformed to the rhombohedral phase (see Fig. 4). The peak intensities and locations of the two phases (indicated by dashed lines in the graphs) were extracted by fitting the XRD data to the sum of two Pearson VII peaks. Figure 5 shows the crystallographic phase fractions determined from fits to the peaks shown in Fig. 4 and normalized by their sum. The dependence of the phase fractions on temperature was modeled using a cumulative skewed normal distribution function to account for any asymmetry, with α as a parameter

that determines the degree and direction of skewness. Further details regarding the definition of a skewed normal distribution can be found in the supplementary material [Eq. (1)]. Both data were fitted simultaneously with the phase fraction of the rhombohedral phase assumed to follow the complementary function of the monoclinic phase fraction. Although the fit function has no physical meaning, it captures the overall features of the structural transition well. The function was found to be symmetric within uncertainty with the shape parameter $\alpha = -0.1 \pm 0.6$. The standard deviation, or width, of the transition is 12.7 ± 0.3 K, and the center of the transition, determined using the center of mass of the fit function, is 131.4 ± 0.5 K. The corresponding temperature for the non-capped V_2O_3 layer is ~133 K (see Fig. S5 of the supplementary material). XRR intensity profiles for the single V_2O_3 layer film and the V_2O_3/Ni film were acquired at different temperatures upon heating from 30 to 200 K. The thickness and roughness values were derived by fitting the XRR data using the GenX software package,[26] with an example shown in Fig. 6(a). The thickness and roughness of the V_2O_3 layer in the V_2O_3/Ni film as a function of temperature are shown in Figs. 6(b) and 6(c). A slight decrease in layer thickness by 1.5% upon heating is observed for both specimens, which is consistent with changes in the lattice parameters of the monoclinic and rhombohedral phases.[36,37] The same function that was used to model the phase fractions determined from XRD in Fig. 5 is redrawn in Fig. 6(b), simply scaled in amplitude. The close agreement of the line with the data shows that there is a clear correlation between the phase fraction and the thickness of the V_2O_3 layer. Simultaneously, across the phase coexistence region, an elevation in the roughness of the V_2O_3 layer determined from the XRR fitting was also observed, which was maximized at the midpoint of the transition. The correlation between the phase fractions and the roughness enhancement at the middle of the transition is further demonstrated in the solid line shown in Fig. 6(c), which is the scaled derivative of the fit function used to model the phase fractions in Fig. 5 and the layer thickness in Fig. 6(b).

C. Reciprocal space mapping

In order to observe the coexistence of both phases and investigate further any lateral changes in the crystal or film structure, 3D-reciprocal space volumes of the scattering around the symmetric

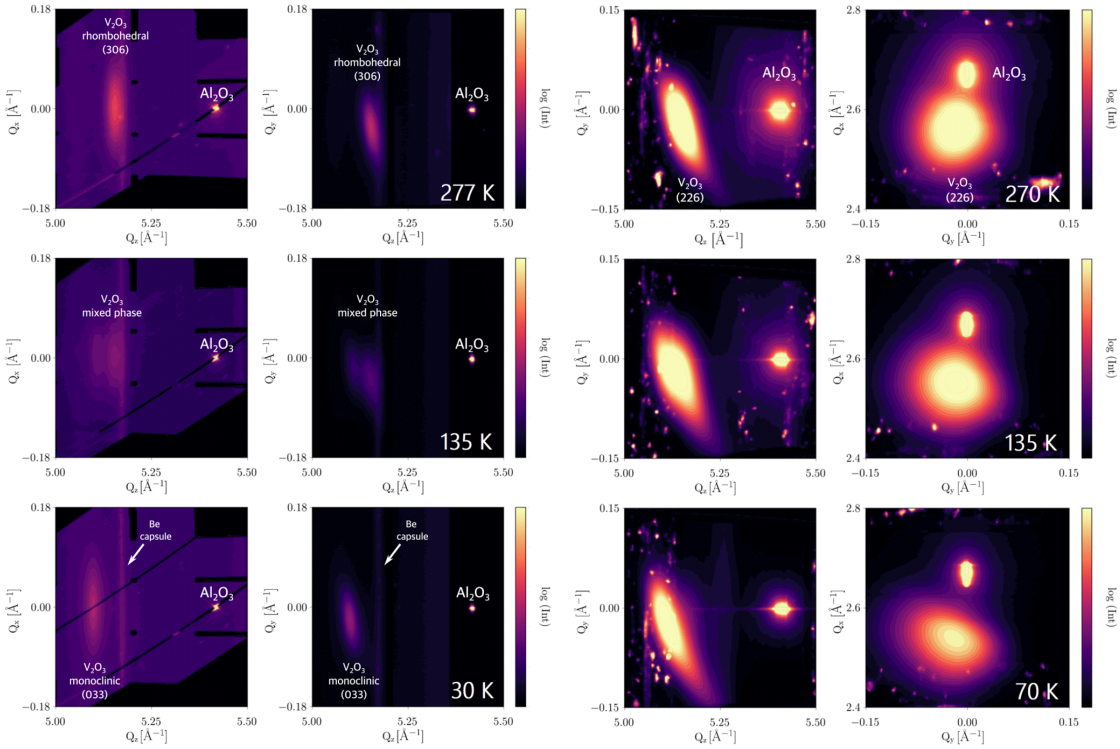

FIG. 7. 2D projections of 3D reciprocal space maps of the V_2O_3/Ni film recorded at different temperatures upon heating across the phase transition. Peaks are indexed to the rhombohedral structure for convenience. Left: RSM scans recorded for the symmetric (3 0 6) peak of V_2O_3 together with the Al_2O_3 substrate peak. Right: RSM scans recorded for the asymmetric (2 2 6) peak of V_2O_3. The scans for the symmetric (3 0 6) peak reveal a clear splitting for the two phases, as in the XRD scans shown in Fig. 4.

and asymmetric V_2O_3 Bragg reflections were recorded as a function of temperature. Reciprocal space volumes were also recorded for single layer films (see Fig. S7 of the supplementary material). Several scans were combined and data binned into cubic voxels of reciprocal space defined in the laboratory frame with the Q_z aligned with the surface normal and with Q_x and Q_y orthogonal directions in the plane of the sample with Q_x coincident with the incident beam. With respect to the rhombohedral crystal planes, Q_z is parallel to the 306 direction, and Q_x is aligned to the $\bar{1}20$ direction.

Figure 7 shows representative reciprocal space maps (RSMs) reduced into 2D by integrating the third reciprocal space direction for the V_2O_3/Ni film. The RSMs are shown for temperatures below the transition, at the transition midpoint, and above the transition. The data are generally clearer in the RSMs recorded in the vicinity of the symmetric peaks, which are displayed in the left-hand panel in Fig. 7. The sapphire substrate is the sharp peak at $Q_z = 5.41$ Å^{-1} and $Q_x = Q_y = 0$ Å^{-1}. The film peaks are seen as weaker reflections at lower Q_z. The splitting, corresponding to the transition between the low and high temperature phases seen in the one-D projections shown in Fig. 4, is again clear. The weak streak at $Q_z = 5.17$ Å^{-1} is the powder line from the Be vacuum dome. However, the projections for the asymmetric peak mask the clear splitting due to the projection of the scattering vector into these directions, but a distinct broadening is observed during the transition, accompanied by a shift in the peak position from the low-temperature to the high-temperature phase.

In addition to the out-of-plane Q_z information, the RSMs provide further information on the lateral properties of the film through projections into Q_x and Q_y. Such in-plane data includes details on the mosaic, any lateral crystallographic periodicities or correlations, and also film strain. Thus, any domain formation in the V_2O_3 that could arise during the transition can, therefore, be observed in changes to the RSM film peak in the Q_x and Q_y directions as the material progresses between the two different phases. In particular, any lateral periodic domain formation (e.g., discussed in Ref. 38) would result in secondary peaks observed in the Q_x and Q_y scans, while incoherent domain formation[39] would result in changes in the peak widths or forms. The scans show no secondary peaks or changes in the lateral spread of the RSM peaks, therefore eliminating any short length scale periodicity or domain formation during the nano-scale phase formation, and the mosaic dominates the peak structure at all temperatures and remains unchanged during the phase transition.

D. Magnetic properties across the SPT

Any change to the surface morphology of the V_2O_3 layer will impact any crystalline overlayer by introducing interface strain. In the case of a magnetic material such as Ni, roughness contributes a significant factor, with the enhanced roughness arising from the height difference of different domains during the transition inducing pinning centers, thereby enhancing the coercivity of the magnetic material. Figure 8 shows the coercivity of the magnetic layer derived from hysteresis loops recorded as a function of temperature. A representative magnetic hysteresis curve measured at 130 K is presented in the supplementary material (see Fig. S8). The coercivity exhibits the expected decrease with increasing temperature, as is generally observed for Ni films as more thermal energy becomes available. In addition to the expected temperature dependent decrease, a notable perturbation in the coercivity is observed across the mixed phase region, with a peak occurring at a temperature coinciding with the structural phase transition in the V_2O_3. This temperature range of enhanced coercivity corresponds well to the phase coexistence region observed from XRD and the increased roughness seen in the XRR data, as highlighted by the shaded region, which corresponds to the 90% confidence interval determined from the phase fraction function shown in Fig. 4.

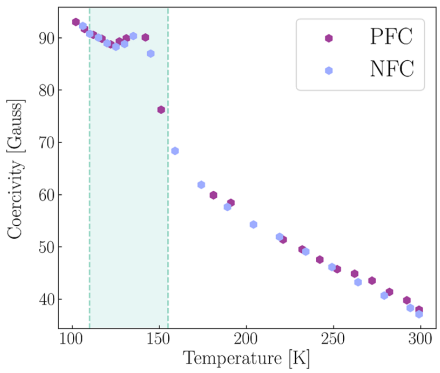

FIG. 8. Coercivity of the V_2O_3/Ni film extracted from magnetization loops recorded using low-temperature MOKE measurements as a function of increasing temperature after positive field cooling (PFC) under an applied field of 400 G and negative field cooling (NFC) with a field of −400 G along the easy axis. In addition to the general trend of reduced coercivity with increasing temperature, from $H_c = 92$ G at 80 K down to $H_c = 35$ G at room temperature, the presence of a clear peak in coercivity in the temperature range of the SPT of the V_2O_3 layer is observed. This coercivity maximum across the SPT was verified by carrying out both MOKE and VSM measurements. Cyan dashed lines indicate the 90% confidence interval determined from the phase fraction function shown in Fig. 4.

IV. DISCUSSION

The temperature of the SPT is defined as that where the rhombohedral and the monoclinic phases are equally determined. As illustrated in Fig. 4, the center of the transition is at a temperature of ~130 K. Similar analysis of data for the V_2O_3 single layer film (see Fig. S5 of the supplementary material) yields a transition temperature of 133 K. These results are consistent with the expected phase transformation of V_2O_3 as observed in structural characterization, resistivity, and magnetic changes.[20,21,40]

Within the region where both phases coexist, an increase in the roughness of the V_2O_3 layer is observed [Fig. 6(c)], with a maximum located at the transition midpoint. The increased roughness is attributed to the coexistence of the two phases in different regions of the film. A further analysis of the XRD data shows no apparent differences in the peak widths in Q_z for both phases (Fig. 4) across the entire temperature range. This indicates that when part of the film transitions, it does so across the entire film thickness. There is also little change in the in-plane scattering, as shown in the RSMs, suggesting that the lateral size of the transitioning regions is greater than

the coherence length of the x-rays, which is some tens of micrometers. The V_2O_3 surface in the mixed-phase regime is, therefore, composed of pillars of the expanded rhombohedral phase and the original monoclinic phase. This results in an uneven interface profile that evolves with temperature and is most disordered when the ratio of the two phases is equal, i.e., at the midpoint of the transition corresponding to the SPT.

The coercivity, shown in Fig. 8, exhibits a clear peak at a temperature corresponding to the structural phase transition in the V_2O_3, with a maximum of 135 K driven by the morphology of the V_2O_3/Ni interface. The peak in coercivity extends to ~155 K, and at higher temperatures, it follows a general trend of reduced coercivity with increasing temperature. In addition to the peak in coercivity, the data show a strain related shift in coercivity below and above the transition, as has been observed in similar systems.[20,22]

Confirmation of the importance of the roughness is found by comparing this study of the coercivity with our previous work on V_2O_3/Ni films grown on sapphire Al_2O_3 substrates with *c*-plane [0001] surface orientation under the same conditions as those reported here on sapphire *r*-plane [$1\bar{1}02$] substrates with nearly the same V_2O_3 thickness of ~58 nm.[20] While the V_2O_3 undergoes the same mixed phase transition for the two cases, when grown on the *c*-plane [0001], the expansion of the V_2O_3 film along the surface normal is significantly reduced due to the epitaxy. Thus, the morphology of the interface is smoother and more uniform, with much less disorder introduced into the epitaxial Ni overlayer, resulting in V_2O_3/Ni heterostructures grown on the *c*-plane having more isotropic magnetic properties. In contrast, and as described here, the *r*-plane V_2O_3/Ni films display a stronger tendency for nanoscale phase formation due to the increased interface roughness of the V_2O_3 layer during the transition. HAADF-STEM imaging also showed clear signs of anti-phase boundaries within the V_2O_3 layer on *r*-plane substrates, while such boundaries were not observed for identical *c*-plane film structures. These boundaries can act as phase coexistence boundaries for adjacent regions undergoing transitions at different temperatures, thereby contributing to the observed increase in surface roughness during the transition.

V. CONCLUSIONS

In conclusion, we have investigated the microstructure and structural phase coexistence of the V_2O_3 layer in the V_2O_3/Ni system grown on *r*-plane sapphire, as well as the magnetic properties of the magnetic Ni layer in relation to the microstructure and structural behavior of the V_2O_3 during the SPT. As the V_2O_3 transitions from the low-temperature phase to the high-temperature phase, the film thickness determined from XRR measurements decreases in accordance with the phase fractions determined from XRD measurements. Within the phase coexistence region, an increase in the roughness of the V_2O_3 layer is observed, reaching its maximum in the middle of the transition. This increased roughness is attributed to the different thicknesses of the two concurrent phases in V_2O_3 during the transition. The observed enhanced roughness follows the derivative of the skewed normal distribution function used to fit the phase fraction data, illustrating that the roughness takes a maximum value in the middle of the transition.

In the temperature range of 110–155 K, corresponding to the phase coexistence of V_2O_3, a notable peak of enhanced coercivity is observed. This peak is attributed to the transition occurring in the phase coexistence region, which is accompanied by increased roughness in the V_2O_3 layer, causing significant strain in the magnetic Ni layer. These pronounced changes and strain effects in the Ni layer result in a peak in coercivity.

When analyzing the reciprocal space map across the SPT, we observe a clear splitting of the V_2O_3 peak and a diagonal shift in the peak position along the Q_y direction, deviating from the anticipated symmetric pattern. This can be attributed to the presence of anti-phase boundaries, which introduce structural disorder and disrupt the regular lattice arrangement. As a result, deviations from the expected symmetry and stress distribution occur within the material. Our results reveal no periodic structural distortions in the reciprocal space map due to the simultaneous existence of two phases in the V_2O_3 layer. This could be attributed to the fact that the notable structural changes associated with the competing phases occur at a mesoscale, which exceeds the resolution capability of our measurement technique.

SUPPLEMENTARY MATERIAL

See the supplementary material for structural measurements of the reference single-layer V_2O_3 sample. It also presents HAADF-STEM images of the V_2O_3/Ni film grown on the Al_2O_3*c*-plane, along with detailed magnetic and structural data for the V_2O_3/Ni heterostructure deposited on the sapphire *r*-plane and fitting information.

ACKNOWLEDGMENTS

This work was supported by the funding from the University of Iceland Research Fund, the Icelandic Research Fund Grant No. 207111. Instrumentation funding from the Icelandic Infrastructure Fund is acknowledged. This work was based on experiments performed at the BM28 (XMaS) beamline at the European Synchrotron Radiation Facility, Grenoble, France. XMaS is a National Research Facility funded by the UK EPSRC and managed by the Universities of Liverpool and Warwick. This project has received funding from the European Union's Horizon 2020 research and innovation program under Grant Agreement No. 823717—ESTEEM3.

AUTHOR DECLARATIONS

Conflict of Interest

The authors have no conflicts to disclose.

Author Contributions

K. Ignatova: Conceptualization (equal); Data curation (lead); Formal analysis (lead); Investigation (equal); Visualization (equal); Writing – original draft (equal); Writing – review & editing (equal). **E. Vlasov**: Data curation (equal); Investigation (equal); Writing – review & editing (equal). **S. D. Seddon**: Formal analysis (equal); Software (equal); Writing – review & editing (equal). **N. Gauquelin**: Data curation (equal); Investigation (equal); Writing – review &

editing (equal). **J. Verbeeck**: Writing – review & editing (equal). **D. Wermeille**: Data curation (equal); Investigation (equal); Writing – review & editing (equal). **S. Bals**: Writing – review & editing (equal). **T. P. A. Hase**: Conceptualization (equal); Data curation (equal); Investigation (equal); Methodology (equal); Supervision (equal); Writing – review & editing (equal). **U. B. Arnalds**: Conceptualization (equal); Data curation (equal); Funding acquisition (equal); Investigation (equal); Methodology (equal); Supervision (equal); Writing – review & editing (equal).

DATA AVAILABILITY

The data that support the findings of this study are available from the corresponding author upon reasonable request.

REFERENCES

[1] C. Griffiths and H. Eastwood, J. Appl. Phys. **45**, 2201 (1974).
[2] D. Lee, B. Chung, Y. Shi, G.-Y. Kim, N. Campbell, F. Xue, K. Song, S.-Y. Choi, J. Podkaminer, T. Kim *et al.*, Science **362**, 1037 (2018).
[3] M. Yang, Y. Yang, B. Hong, L. Wang, K. Hu, Y. Dong, H. Xu, H. Huang, J. Zhao, H. Chen *et al.*, Sci. Rep. **6**, 23119 (2016).
[4] P. Homm, M. Menghini, J. Seo, S. Peters, and J.-P. Locquet, APL Mater. **9**, 021116 (2021).
[5] S. Shin, S. Suga, M. Taniguchi, M. Fujisawa, H. Kanzaki, A. Fujimori, H. Daimon, Y. Ueda, K. Kosuge, and S. Kachi, Phys. Rev. B **41**, 4993 (1990).
[6] M. Marezio, D. B. McWhan, J. Remeika, and P. Dernier, Phys. Rev. B **5**, 2541 (1972).
[7] Z. Khan, P. Singh, S. A. Ansari, S. R. Manippady, A. Jaiswal, and M. Saxena, Small **17**, 2006651 (2021).
[8] J.-y. Kim, J. Cramer, K. Lee, D.-S. Han, D. Go, P. Salev, P. N. Lapa, N. M. Vargas, I. K. Schuller, Y. Mokrousov *et al.*, Adv. Funct. Mater. **32**, 2111555 (2022).
[9] V. Baltz, A. Manchon, M. Tsoi, T. Moriyama, T. Ono, and Y. Tserkovnyak, Rev. Mod. Phys. **90**, 015005 (2018).
[10] J. Guo, H. Zhou, J. Wang, W. Liu, M. Cheng, X. Peng, H. Qin, J. Wei, P. Jin, J. Li *et al.*, Artif. Cells, Nanomed., Biotechnol. **46**, 58 (2018).
[11] Y. Wang, K.-M. Kang, M. Kim, H.-S. Lee, R. Waser, D. Wouters, R. Dittmann, J. J. Yang, and H.-H. Park, Mater. Today **28**, 63 (2019).
[12] Y. Zhou and S. Ramanathan, Proc. IEEE **103**, 1289 (2015).
[13] M. Lee, "New materials and techniques for resistive switching devices and neuromorphic computing," Ph.D. thesis, UC San Diego, 2021.
[14] J. Lappalainen, J. Mizsei, and M. Huotari, J. Appl. Phys. **125**, 044501 (2019).
[15] Y. Kalcheim, N. Butakov, N. M. Vargas, M.-H. Lee, J. Del Valle, J. Trastoy, P. Salev, J. Schuller, and I. K. Schuller, Phys. Rev. Lett. **122**, 057601 (2019).
[16] C. T. Wolowiec, J. G. Ramírez, M.-H. Lee, N. Ghazikhanian, N. M. Vargas, A. C. Basaran, P. Salev, and I. K. Schuller, Phys. Rev. Mater. **6**, 064408 (2022).
[17] D. A. Gilbert, J. G. Ramírez, T. Saerbeck, J. Trastoy, I. K. Schuller, K. Liu, and J. de la Venta, Sci. Rep. **7**, 13471 (2017).
[18] J. de La Venta, S. Wang, J. Ramirez, and I. K. Schuller, Appl. Phys. Lett. **102**, 122404 (2013).
[19] J. de La Venta, S. Wang, T. Saerbeck, J. Ramírez, I. Valmianski, and I. K. Schuller, Appl. Phys. Lett. **104**, 062410 (2014).
[20] K. Ignatova, E. Thorsteinsson, B. Jósteinsson, N. Strandqvist, C. Vantaraki, V. Kapaklis, A. Devishvili, G. K. Pálsson, and U. Arnalds, J. Phys.: Condens. Matter **34**, 495001 (2022).
[21] A. McLeod, E. Van Heumen, J. Ramirez, S. Wang, T. Saerbeck, S. Guenon, M. Goldflam, L. Anderegg, P. Kelly, A. Mueller *et al.*, Nat. Phys. **13**, 80 (2017).
[22] V. Polewczyk, S. Chaluvadi, P. Orgiani, G. Panaccione, G. Vinai, G. Rossi, and P. Torelli, Phys. Rev. Mater. **5**, 034413 (2021).
[23] G. Wei, X. Lin, Z. Si, N. Lei, Y. Chen, S. Eimer, and W. Zhao, Appl. Phys. Lett. **114**, 012407 (2019).
[24] U. B. Arnalds, J. S. Agustsson, A. S. Ingason, A. K. Eriksson, K. B. Gylfason, J. T. Gudmundsson, and S. Olafsson, Rev. Sci. Instrum. **78**, 103901 (2007).
[25] O. Bikondoa, L. Bouchenoire, S. D. Brown, P. B. J. Thompson, D. Wermeille, C. A. Lucas, M. J. Cooper, and T. P. A. Hase, Philos. Trans. R. Soc., A **377**, 20180237 (2019).
[26] M. Björck and G. Andersson, J. Appl. Crystallogr. **40**, 1174 (2007).
[27] D. S. Su and R. Schlögl, Catal. Lett. **83**, 115 (2002).
[28] J. Li, B. Gauntt, J. Kulik, and E. Dickey, Microsc. Microanal. **15**, 1004 (2009).
[29] G. Sun, X. Cao, X. Gao, S. Long, M. Liang, and P. Jin, Appl. Phys. Lett. **109**, 143903 (2016).
[30] B. W. Cahn, J. Nucl. Mater. **21**, 356 (1967).
[31] B. W. David and C. B. Carter, *Transmission Electron Microscopy: A Textbook for Materials Science* (Springer Science+Business Media, LLC, 1996).
[32] X. Li, A. Gloter, H. Gu, X. Cao, P. Jin, and C. Colliex, Acta Mater. **61**, 6443 (2013).
[33] J. Schoiswohl, M. Sock, S. Surnev, M. Ramsey, F. Netzer, G. Kresse, and J. N. Andersen, Surf. Sci. **555**, 101 (2004).
[34] M. Luysberg, R. Sofin, S. Arora, and I. Shvets, Phys. Rev. B **80**, 024111 (2009).
[35] C. Xu, H. Du, A. J. van der Torren, J. Aarts, C.-L. Jia, and R. Dittmann, Sci. Rep. **6**, 38296 (2016).
[36] P. Dernier and M. Marezio, Phys. Rev. B **2**, 3771 (1970).
[37] L. Eckert and R. Bradt, J. Appl. Phys. **44**, 3470 (1973).
[38] D. Rusu, J. J. Peters, T. P. Hase, J. A. Gott, G. A. Nisbet, J. Strempfer, D. Haskel, S. D. Seddon, R. Beanland, A. M. Sanchez *et al.*, Nature **602**, 240 (2022).
[39] I. Valmianski, A. F. Rodríguez, J. Rodríguez-Álvarez, M. G. del Muro, C. Wolowiec, F. Kronast, J. G. Ramírez, I. K. Schuller, A. Labarta, and X. Batlle, Nanoscale **13**, 4985 (2021).
[40] E. B. Thorsteinsson, S. Shayestehaminzadeh, and U. B. Arnalds, Appl. Phys. Lett. **112**, 161902 (2018).

Paper III: Supplementary information

Phase coexistence induced surface roughness in V_2O_3/Ni magnetic heterostructures

K. Ignatova, E. Vlasov, S.D. Seddon, N. Gauquelin, J. Verbeeck, D. Wermeille, S. Bals, T.P.A. Hase, U.B. Arnalds

APL Materials (2024)

Phase coexistence induced surface roughness in V_2O_3/Ni magnetic heterostructures

Supplementary material

K. Ignatova,[1] E. Vlasov,[2] S. D. Seddon,[3] N. Gauquelin,[2] J. Verbeeck,[2]
D. Wermeille,[4,5] S. Bals,[2] T. P. A. Hase,[6] and U. B. Arnalds[1]

[1]*Science Institute, University of Iceland, Dunhaga 3, 107 Reykjavik, Iceland*
[2]*EMAT and NANOlab Center of Excellence, University of Antwerp, Groenenborgerlaan 171, Antwerp, Belgium*
[3]*TU Dresden, Institute of Applied Physics, Nöthnitzer Strasse 61, 01187 Dresden, Germany*
[4]*XMaS, The UK Materials Science Facility, European Synchrotron Radiation Facility, F-38043 Grenoble, France*
[5]*Dept of Physics, University of Liverpool, Oliver Lodge, Liverpool L69 7ZE, United Kingdom*
[6]*Department of Physics, University of Warwick, Coventry CV4 7AL, United Kingdom*

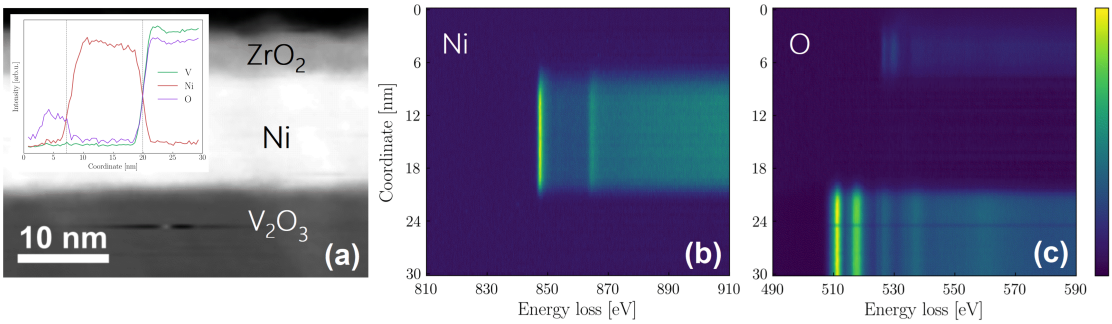

FIG. S1: (a) Experimental HAADF-STEM image of the cross-section of the V_2O_3/Ni/Zr film; the inset shows corresponding V-, Ni-, and O- elemental profiles obtained by EELS. EELS structure evolution across the film and the interfaces for (b) Ni $L_{2,3}$-edge, (c) O K-edge. After extended exposure, the top capping layer undergoes oxidation, as confirmed by the analysis. Consequently, all scans were analyzed using a model that incorporates ZrO_2 atop the heterostructure. Notably, there is no presence of a NiO layer across the film.

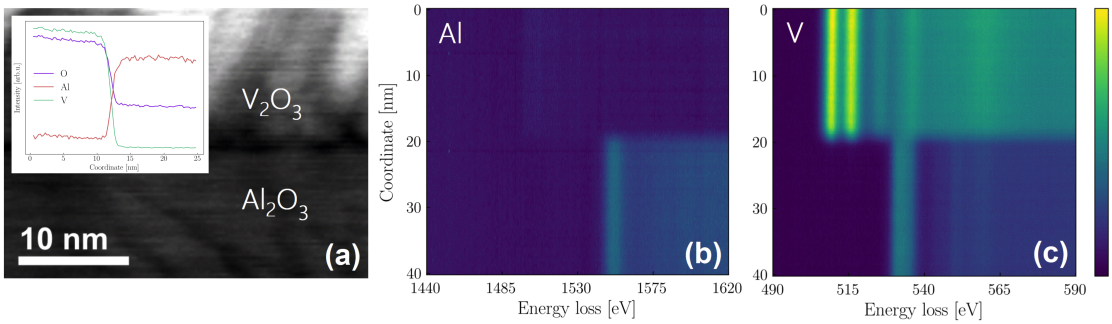

FIG. S2: (a) Experimental HAADF-STEM image of the cross-section of the Al_2O_3/V_2O_3 interface; the inset shows corresponding V-, Al-, and O- elemental profiles obtained by EELS. EELS structure evolution across the interface for (b) Al K-edge, (c) V $L_{2,3}$-edge. The analysis reveals an atomically flat interface between Al_2O_3 and V_2O_3 layers.

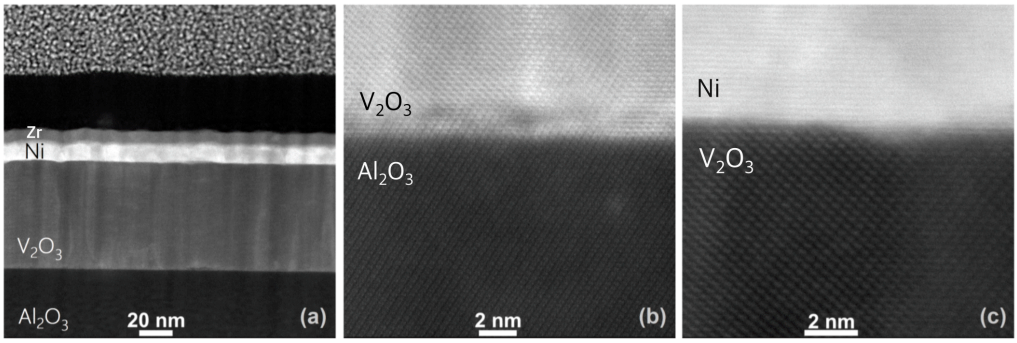

FIG. S3: Experimental HAADF-STEM image of (a) the cross-section of the V_2O_3/Ni/Zr thin film on Al_2O_3 *c*-plane substrate, (b) the Al_2O_3/V_2O_3 interface, and (c) the V_2O_3/Ni interface. The Al_2O_3/V_2O_3 interface appears atomically flat, while the V_2O_3 layer exhibits a columnar structure. The V_2O_3/Ni interface is sharp, and both the Ni and capping Zr layers follow the roughness of the V_2O_3. HAADF-STEM signal intensity (image grayscale) is proportional to atomic number.

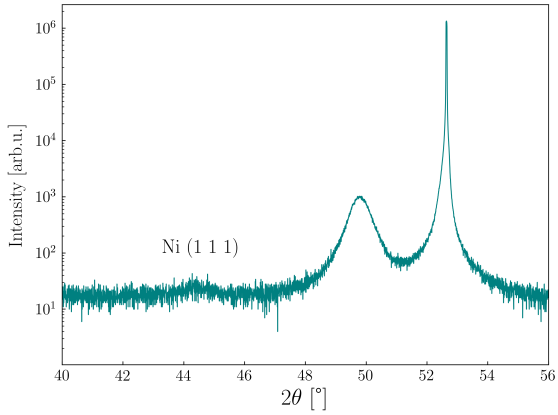

FIG. S4: X-ray diffraction scan recorded for the Al_2O_3/V_2O_3/Ni/Zr film structure. A weak peak, indicative of a textured Ni (111) orientation, was observed around 44.5°.

The skewed normal distribution probability density function is defined as follows:

$$f(x) = \frac{2}{\sigma}\phi\left(\frac{x-\mu}{\sigma}\right)\Phi\left(\alpha\left(\frac{x-\mu}{\sigma}\right)\right) \tag{1}$$

where:

- x is the variable,
- μ is the location parameter (mean),
- σ is the scale parameter (standard deviation),
- α is the shape parameter (skewness),
- $\phi(\cdot)$ is the standard normal PDF,
- $\Phi(\cdot)$ is the standard normal CDF.

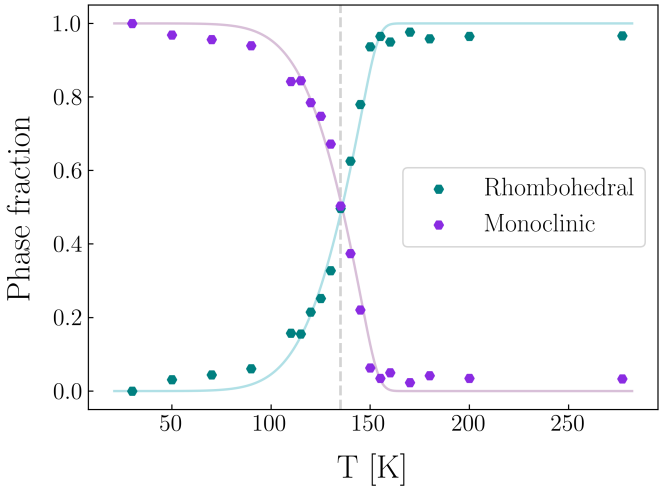

FIG. S5: Relative intensities of V_2O_3 (0 3 3) and V_2O_3 (3 0 6) Bragg peaks observed upon heating in the single V_2O_3 layer film. The dashed line indicates where peaks from both the monoclinic and the rhombohedral V_2O_3 phases have equal intensities. The dependency of phase fractions on temperature was modeled using a cumulative skewed normal distribution function. The centre of the transition, determined using the centre of mass of the fit function, is 132.7 ± 0.5 K.

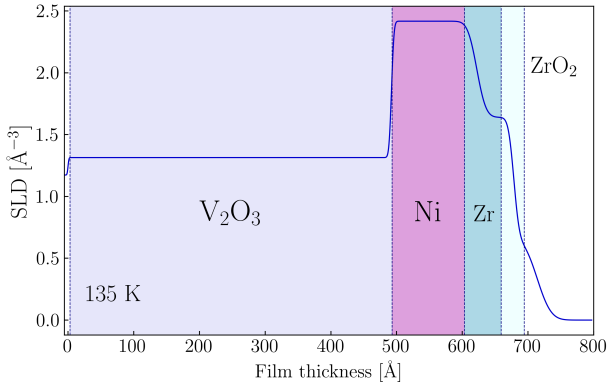

FIG. S6: X-ray scattering length density (SLD) profile of the V_2O_3/Ni/Zr film at a temperature of 135 K. After extended exposure, the top capping layer undergoes oxidation, which was confirmed by HAADF-STEM. Consequently, all scans were analyzed using a model that incorporates ZrO_2 atop the heterostructure.

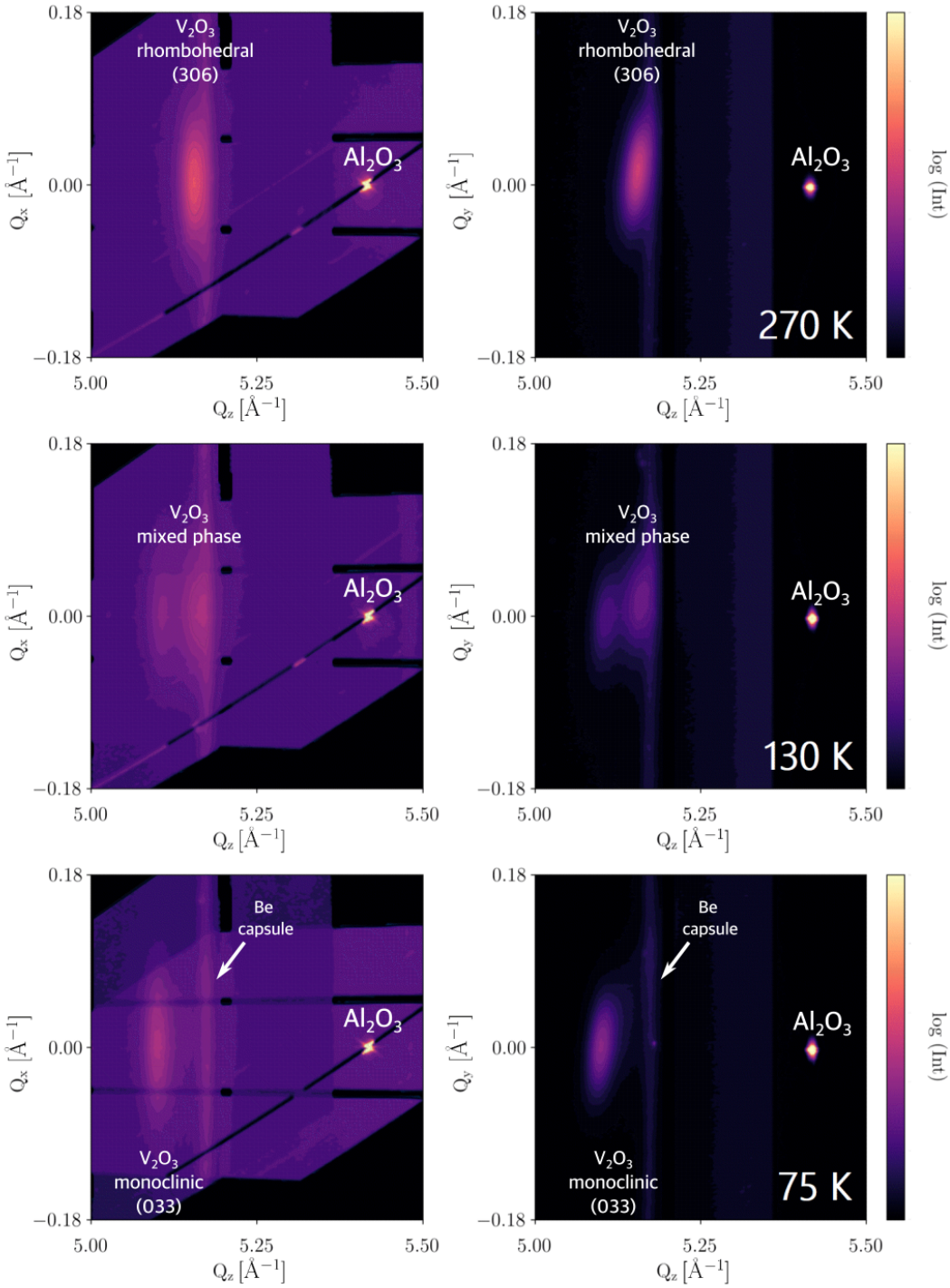

FIG. S7: 2D projections of 3D reciprocal space maps of the V_2O_3 single layer film recorded at different temperatures upon heating across the phase transition. Peaks are indexed to the rhombohedral structure for convenience. RSM scans recorded for the symmetric (3 0 6) peak of V_2O_3 together with the Al_2O_3 substrate peak.

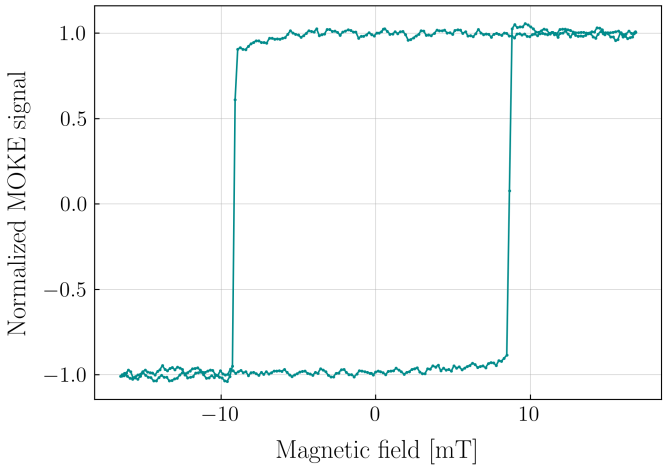

FIG. S8: An exemplary magnetic hysteresis curve of the V_2O_3/Ni/Zr film grown on Al_2O_3 sapphire r-plane, measured at 130 K using MOKE upon heating.

Paper IV

Angular-dependent exchange bias in V_2O_3/Ni magnetic heterostructures

K. Ignatova, E.B. Thorsteinsson, U.B. Arnalds

In manuscript, 2024

Angular-dependent exchange bias in V_2O_3/Ni magnetic heterostructures

K. Ignatova,[1] E. B. Thorsteinsson,[1] and U. B. Arnalds[1]

[1] *Science Institute, University of Iceland, Dunhaga 3, 107 Reykjavik, Iceland*

In this study we examine the angular dependence of coecivity and exchange bias in a V_2O_3/Ni magnetic bilayer film grown on r-plane sapphire (α-Al_2O_3) substrates using reactive dc-magnetron sputtering. We investigate the directional angular dependence and differences in the response of the magnetic layer through the structural phase transition in the V_2O_3. Distinct variations in angular dependence is observed between the exchange field and the coercivity across the structural phase transition in V_2O_3, depending on different field cooling states. A peak in coercivity, occurring at a temperature corresponding to the phase coexistence region of the V_2O_3 transition, is observed only along the main easy axis of the film, disappearing at other angles and remaining independent of the field cooling state. Temperature-dependent measurements, with the applied cooling field along different angles, revealed that the onset of exchange bias at the structural phase transition of V_2O_3 occurs irrespective of the cooling field state, yet demonstrates a complex angular dependence based on the orientation of the applied cooling field. The cooling field orientation influences the exchange bias's anisotropy, magnitude, and direction; notably, a typical unidirectional symmetry emerges at 80 K when the cooling field aligns with the secondary easy axis (90° / 270°) of the film, which nearly aligns with the magnetic moment of V_2O_3. Our results highlight the intricate relationship between the antiferromagnetic state of V_2O_3 and magnetic properties of adjacent magnetic layers.

I. INTRODUCTION

Vanadium sesquioxide (V_2O_3) is an intriguing material that has gathered significant attention in the field of condensed matter physics and material science. It exhibits multiple simultaneous phase transitions, including a metal-insulator transition (MIT), structural phase transition (SPT), and paramagnetic/antiferromagnetic (PM/AFM) transition, making it a subject of multitude of different investigations. V_2O_3 is a prototypical transition metal oxide that undergoes an MIT at a critical temperature of around 150 K[1–3]. The underlying mechanisms driving this transition are still under active research, with various theories proposed, including the Mott-Hubbard and Slater models, as well as Peierls instability[4–7]. Upon cooling, V_2O_3 undergoes an SPT from a paramagnetic metallic state to an insulating and antiferromagnetic state. This magnetic transition from paramagnetic to antiferromagnetic is particularly intriguing when considering V_2O_3 in a bilayer with a magnetic material such as nickel (Ni). At low temperatures the ferromagnetic nature of Ni interacts with the antiferromagnetic low-temperature phase of V_2O_3 with a potential for an exchange bias to be observed at the interface.

When a conventional FM/AFM system is cooled below the Néel temperature of the AFM the spins of the AFM align with those of the FM to minimize the interface exchange interaction. This leads to a single stable configuration for the FM spins, inducing a unidirectional anisotropy known as exchange anisotropy or exchange bias with significant technological implications, particularly in the development of magnetic devices and spintronic applications[8–10].

As V_2O_3 is not a conventional AFM material the onset of the AFM state does not occur as the material is cooled below its Néel temperature but as it undergoes an SPT with a concomitant paramagnetic to antiferromagnetic first order phase transition. As an interface effect, exchange bias is influenced by structural parameters that can significantly impact magnetic coupling, including roughness and chemical intermixing[11,12]. These structural factors play a crucial role in determining the strength and behavior of the exchange bias phenomenon at the interface between the AFM and FM materials. Considering these aspects, the role of structural factors becomes even more complex and crucial, particularly given that V_2O_3 undergoes an SPT. Notably, within V_2O_3, there is a specific region where both structural phases coexist – a phase coexistence region with a width of roughly 10 K[13]. In this region magnetic properties are profoundly influenced as altering the structure via the SPT in V_2O_3 can lead to significant changes in the magnetic properties of the adjacent magnetic layer[14–19].

In this study, we investigate the temperature and angular dependence of the magnetic properties of V_2O_3(50 nm)/Ni(13 nm) bilayer structures deposited on r-plane sapphire Al_2O_3 substrates. Previously, several studies have investigated the temperature dependence of magnetic properties across phase transitions in the V_2O_3 layer, revealing a coercivity enhancement manifested as a peak around the middle of the structural phase transition of the V_2O_3 at around $\sim$ 131 K and attributed to strain and subsequent changes in surface roughness during the SPT[13]. However, most of the investigations have primarily focused on magnetic properties along a single direction of the film with only a few studies investigating the angular dependence, with findings that tend to vary, indicating a need for further research[20,21].

II. MATERIALS AND METHODS

The deposition of the single Ni layer sample and V_2O_3/Ni film was performed on r-plane Al_2O_3 ($1\bar{1}02$)

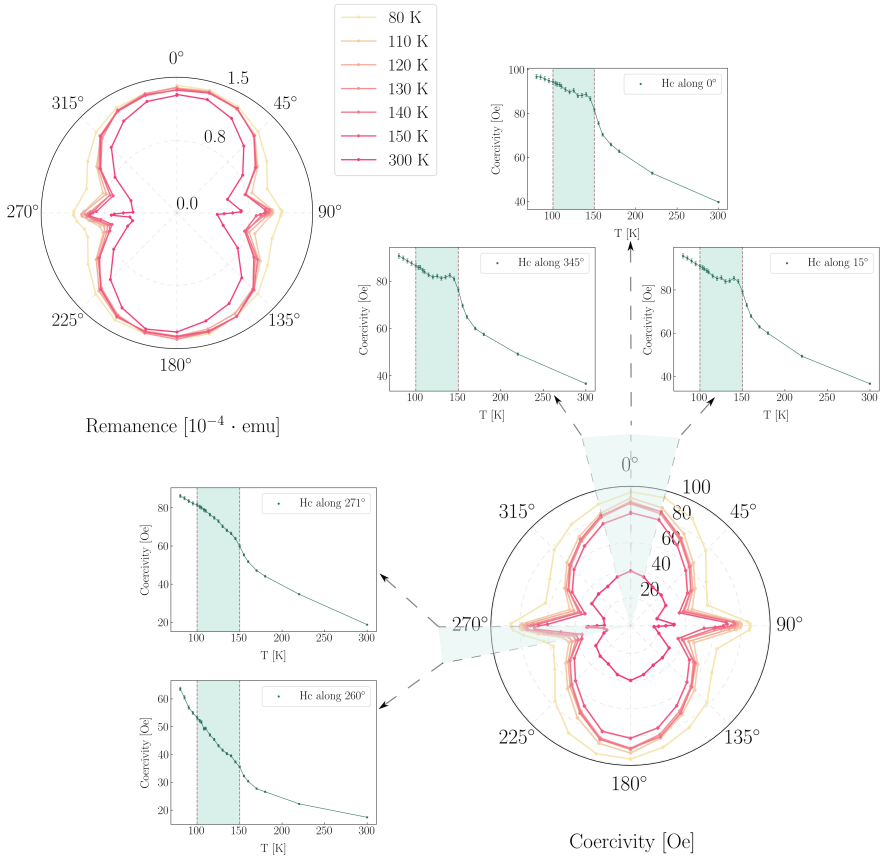

FIG. 1. Temperature and azimuth angular dependence of magnetic properties: Coercivity and remanent magnetization M_{rem} for the V_2O_3/Ni film grown on the r-plane of Al_2O_3 substrate annealed at 1200°C. Measurements were performed as a function of increasing temperature through the temperature of the SPT of the V_2O_3 after positive field cooling (PFC) under an applied field of +5 kOe along 90°.The effective magnetic anisotropy exhibits a gradual transition throughout the SPT of V_2O_3, without any abrupt changes. The graph insets show representative scans of the temperature dependent coercivity across the SPT of the V_2O_3 along the hard and easy axes. The error bars in the figures are determined based on field accuracy measurements, defined as 1 % of the reading. Cyan dashed line areas indicate phase coexistence regions in the V_2O_3 during the SPT.

substrates using reactive direct current (dc) magnetron sputtering for the V_2O_3 layer and conventional dc-magnetron sputtering for the Ni and Zr capping layer. A custom-built chamber[22] was used for the growth process, employing high-purity 3-inch vanadium (99.99%) and nickel (99.99%) sputtering targets. The substrates were annealed at 1200°C in air for 24 hours. Prior to deposition, the chamber's base pressure was maintained below 4×10^{-6} Pa. The substrates were pre-baked in vacuum at a temperature of 610°C for approximately 60 minutes before the growth process. The V_2O_3 layer was deposited at 610°C with working pressure of 0.7 Pa of 5N Ar and O_2 gases at 20 sccm and 1.05 sccm flow rates, respectively. The Ni and Zr layers were deposited at room temperature after cooling down under vacuum. A reference sample, composed of only magnetic Ni layer without V_2O_3, was deposited following the same recipe directly onto annealed r-plane sapphire substrates. The film stack in the heterostructure consists of a $\sim$ 50 nm V_2O_3 layer, followed by a 13 nm layer of Ni, and capped with a 6 nm layer of Zr[13].

In-plane temperature-dependent magnetic hysteresis loops were measured at various azimuthal angles upon heating using a vibrating sample magnetometer (VSM; VSM 8600 series, Lake Shore Cryotronics). The measurements covered a temperature range from room tempera-

ture down to 80 K, encompassing the entire SPT of the V_2O_3. The temperature-dependent magnetization curves were recorded upon heating with a field step of 2 Oe. Between temperature steps, where hysteresis loops were recorded, and during field cooling a temperature sweep rate of 2 K/min was used. Two cooling protocols were applied: field-cooling (FC), where samples were cooled from room temperature to 80 K with an applied magnetic field, and zero-field-cooling (ZFC), where they were cooled under the same conditions but without a magnetic field. Magnetic fields were applied in-plane along three different azimuthal angles (φ): 0°, 45°, and 90°. During the FC process, measurements were conducted with both positive +5 kOe and negative −5 kOe applied magnetic fields, resulting in positive field-cooled (PFC) and negative field-cooled (NFC) states, respectively.

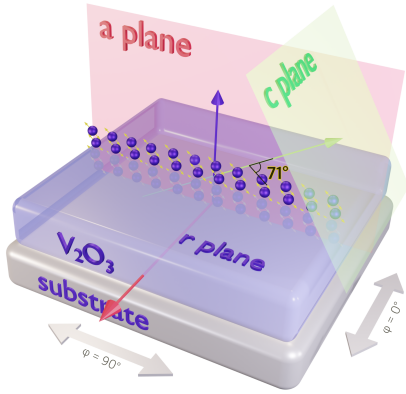

FIG. 2. 3D schematic illustration of a film stack with the orientation of crystallographic planes and corresponding axes (based on XRD and FFT analyses from HAADF-STEM[13]. The yellow arrows suggest the general direction of vanadium magnetic moments at low-temperature AFM phase (perpendicular to the rhombohedral a-axis and inclined at an angle of 71° to the rhombohedral c-axis[23]). The grey arrows denote the in-plane azimuthal φ angles. The cooling field was applied at distinct orientations of $\varphi = 0°$, 45°, and 90°. The illustration magnifies the position of vanadium atoms above the layer for visual emphasis.

III. RESULTS AND DISCUSSION

A. Coercivity

As mentioned earlier, previous studies have revealed a coercivity enhancement, observed as a peak in the phase coexistence region during the transition of the V_2O_3, along a specific direction in the film[13]. Figure 1 shows results for the temperature-dependent evolution of the in-plane magnetic anisotropy within the V_2O_3/Ni magnetic heterostructure across the SPT. The insets display representative scans detailing the behavior of the coercive field across the SPT along the 0° and 270° in-plane angles, and in their vicinity. The depicted measurements were conducted following a PFC protocol under an applied field of +5 kOe along 90°. In the high-temperature paramagnetic phase of the V_2O_3, the V_2O_3/Ni film displays a biaxial anisotropy in coercivity with a slight opening at 90° and 270°. The reference sample, consisting of a single Ni layer grown on the Al_2O_3 r-plane substrate, exhibits an identical but more defined biaxial anisotropy (see supplementary material). The inclusion of the V_2O_3 layer leads to a significant increase in the coercive field at room temperature, roughly twice as much compared to when the V_2O_3 is absent. As illustrated in Fig. 1, the V_2O_3/Ni film at room temperature demonstrates a diminished biaxial anisotropy when compared to the reference sample. Despite being weaker, biaxial anisotropy is still evident in the film. As previously observed through HAADF-STEM measurements in this V_2O_3/Ni magnetic heterostructure, the V_2O_3 layer exhibits step-like terrace antisite defects, specifically antiphase boundaries (APB)[13]. The APBs, having a displacement vector parallel to the <001> direction, are related with the sapphire r-plane substrate due to its multi-step surface structure. The easy axes of the magnetization in the film were determined to be oriented at 0° (180°) and 90° (270°). The secondary easy axis at 90° (270°) is oriented along the a-plane [11$\bar{2}$0] Al_2O_3 and perpendicular to the a axis.

Previously, a similar weak frozen biaxial magnetic anisotropy at room temperature, associated with this terraced microstructure, was observed in the V_2O_3/Ni bilayer, where the anisotropy constants were found to be less dependent on temperature during the cooling process towards the SPT[16]. As can be seen in Fig. 1, the magnetic anisotropy does not exhibit abrupt changes during the SPT of the V_2O_3, contrary to previous findings where a significant change in anisotropy occurred during the structural phase transition of the V_2O_3[16,24]. In our case, as the temperature increases across the SPT, the magnetic anisotropy becomes slightly more pronounced, accompanied by the anticipated temperature-dependent decrease in the coercivity of the Ni layer upon heating. One possible reason for this might be the reduced thickness of the V_2O_3 layer. A thickness of 50 nm could be critical, lessening the impact of the structural phase transition on the coercive field and anisotropy of the magnetic layer[25]. Additionally, it was previously demonstrated that adjusting the ratio between the thicknesses of V_2O_3 and the magnetic layer has a notable impact on anisotropy. Specifically, increasing the proportion of the magnetic layer in relation to V_2O_3 tends to diminish the impact of the SPT on magnetic anisotropy[17]. Figure 1 (lower right) displays representative temperature dependence scans along the two axes and in their vicinity. As observed in the insets of Fig. 1, a closer examination of the temperature-dependent coercive field reveals dis-

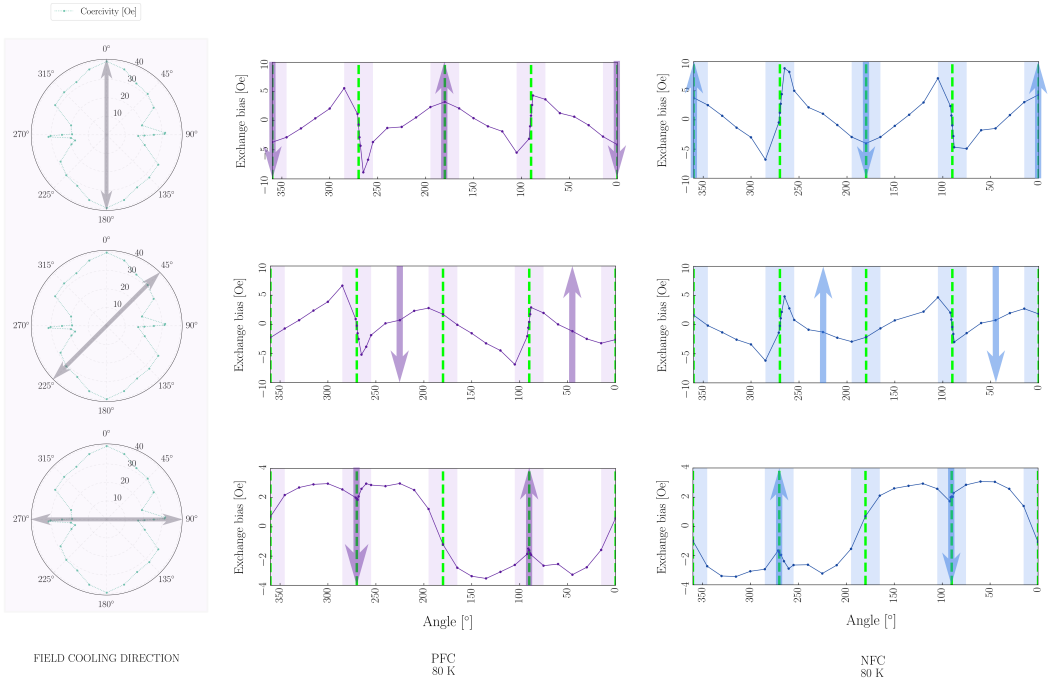

FIG. 3. The in-plane angle dependence of H_{EB} at 80 K in response to both positive and negative field cooling modes with different applied field directions along 0°, 45°, and 90°. The applied magnetic field was -5 kOe (NFC) and +5 kOe (PFC). Measurements were conducted for increasing temperature. Arrows indicate the direction of field cooling. Dashed green lines denote the position of the easy axes of the film at 0° (180°) and 90° (270°).

tinct peaks of coercivity enhancement within the region corresponding to structural phase coexistence in V_2O_3 along the easy axes at 0° (180°). In contrast, along the 90° (270°) axes the coercivity shows less sensitivity and, therefore, a smoother change in the coercivity behavior at the region where both phases coexist at the same time during the transition. The transition was previously defined for this sample to be at around 131 K for increasing temperature[13]. As the angle approaches values closer to the primary easy axes angles, the peaks of coercivity become more distinguishable. While the overall in-plane magnetic anisotropy of the system remains relatively stable, there is still a significant response in the coercive field along specific directions, indicating a clear directional dependence of the response to the SPT. The inhomogeneous distribution of metallic rhombohedral and insulating monoclinic states in the V_2O_3 layer during the phase coexistence region[1] leads to an uneven stress distribution in the Ni layer. Previous experimental findings demonstrate that the SPT significantly influences the magnetic domain configuration within the Ni layer. Specifically, the spatial variability in V_2O_3's domain structure leads to localized variations in the magnetic properties of the Ni layer[24]. The observed directional difference in coercivity in this work, manifesting as a peak across the SPT exclusively along 0° (180°) and its vicinity, contrasted with the smooth change observed at 90° (270°), can be attributed to an inhomogeneous domain distribution in V_2O_3. This distribution causes differential stress transfer to the Ni layer, resulting in distinct magnetic responses depending on the orientation affecting the angular dependence of the coercivity during the phase coexistence.

B. Exchange Bias

Exchange bias values were extracted from hysteresis loops recorded for increasing temperatures (after a field cooling protocol) spanning across the V_2O_3 transition temperature, where it undergoes a transition from an antiferromagnetic state to a paramagnetic state. Figure 2 shows a three dimensional schematic illustration of a film stack with included orientations of crystallographic planes and corresponding axes, as identified by XRD and FFT from HAADF-STEM, detailed in[13]. It also depicts the alignment of vanadium magnetic moments in the low-temperature monoclinic phase, perpendicular to the rhombohedral a-axis and angled at 71°

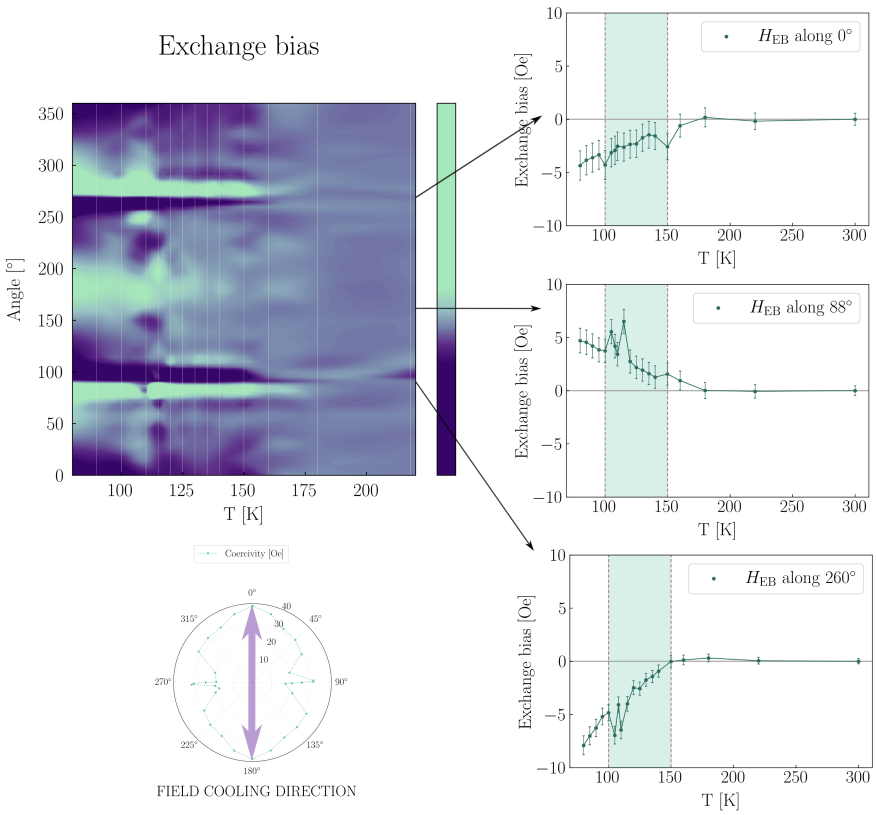

FIG. 4. Temperature and angular dependence of exchange bias for the V_2O_3/Ni film. Measurements were performed for increasing temperature through the temperature of the SPT of the V_2O_3 after positive field cooling (PFC) under an applied field of +5 kOe along the 0° sample direction. The graphs on the right show representative temperature dependent values of the exchange field across the SPT of the V_2O_3 along the easy axes. Two peaks in exchange bias along the 90° (270)° axis are observed within the phase coexistence region. The error bars in the figures are determined based on field accuracy measurements, defined as 1 % of the reading. Cyan dashed line areas indicate phase coexistence regions in the V_2O_3 during the SPT. Vertical lines in the contour plot indicate the temperature values the hysteresis loops were recorded at.

to the rhombohedral c-axis, according to[23]. The grey arrows represent the in-plane azimuthal φ angles. The cooling field was applied at orientations of 0°, 45°, and 90°. The magnitude of the applied magnetic field was ±5 kOe. Regarding field cooling states, whether the applied field is positive or negative, it only affects the direction of the exchange bias. Therefore, by applying a field, either positive or negative, we can manipulate the direction of the exchange bias.

Exchange bias in V_2O_3 based hybrid magnetic heterostructures has been reported by Sass et al.[26], who observed an exchange bias field in V_2O_3/Ni films grown on c-sapphire substrates. The exchange bias field appeared at the transition temperature of V_2O_3 in their case as well, with a strength of about 70 Oe. This was observed with a magnetic layer 5 nm thick and a V_2O_3 layer that was about three times thinner than for our case. It's important to highlight that the phenomenon of exchange bias is roughly inversely proportional to the thickness of the FM layers[8] and that the exchange bias value correlates with the thickness of the AFM layer[27–30]. The magnetic transition in V_2O_3, as demonstrated by[31], is also sensitive to the V_2O_3 layer's thickness. Thus, with a magnetic layer almost three times thicker, we anticipate a reduced magnitude of exchange bias in our system.

In heterostructures with identical layer thickness ratios, particularly in the V_2O_3/Ni magnetic heterostructure grown on a c-plane Al_2O_3 (0006) substrate, the onset of exchange bias exhibiting a magnitude of ~ 6 Oe was previously established in[18]. From Figure 3, it is evident that applying the cooling field along 0° (180°) results in an exchange bias at 80 K, displaying a complex unidi-

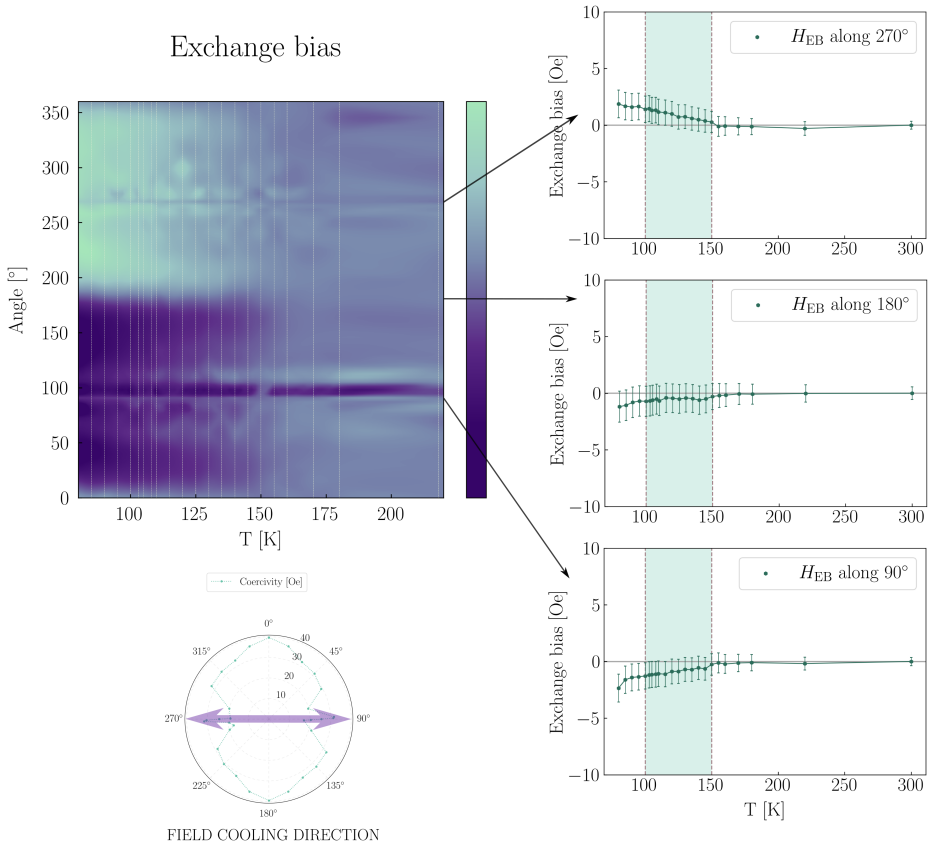

FIG. 5. Exchange field as a function of temperature and in plane sample angle after positive field cooling (+5 kOe) along 90°. The temperature dependent exchange bias displays a smooth reduction with increasing temperature towards zero at the V_2O_3 transition temperature and no peaks as observed for the 0° field cooling state (Fig. 4).

rectional symmetry. The ZFC state occurs and behaves similarly to applying FC along 0° (180°) direction. When the cooling field is rotated to 45°, there is a slight shift in the orientation of the exchange bias towards the direction of the cooling field. However, the overall shape of the exchange bias still maintains its unidirectional symmetry. Applying a cooling field along 90° (270°) results in a significant and notable change. As depicted in Figure 3 (lowest row), the exchange bias undergoes a complete transformation in shape, becoming almost fully unidirectional in nature. Figure 4 and 5 show contour plots that illustrate the exchange bias intensity as a function of both temperature and azimuthal angle under two distinct field cooling conditions, along the primary easy axis at 0° (180°) and along the easy axis at 90° (270°), including plots with the detailed temperature and angular behavior of exchange bias along different angles. In the plot corresponding to the field cooling direction along the 90° (270°) axis (see Fig. 5), the intensity seems to be more uniform across the phase transition. In contrast, the field cooling direction along the primary easy axis at 0° (180°) (see Fig. 5) shows more variation in intensity with azimuthal angle especially in the inhomogeneous transition region where both phases coexist. The applied field cooling direction has a significant effect on the exchange bias. The onset of exchange bias appears to be at the transition temperature in V_2O_3 for all the cooling states and along all the angles, as can be seen from the temperature dependence exchange bias graphs in Figure 4 and Figure 5. Significantly, when cooling the sample with an applied field along 0° (180°), the exchange bias exhibits peaks along and in the vicinity of the axis at 90° (270°), where coercivity behaves rather smoothly without displaying any peaks. Conversely, along the primary easy axes, where coercivity exhibits peaks in the phase coexistence region, the peaks in exchange bias are less

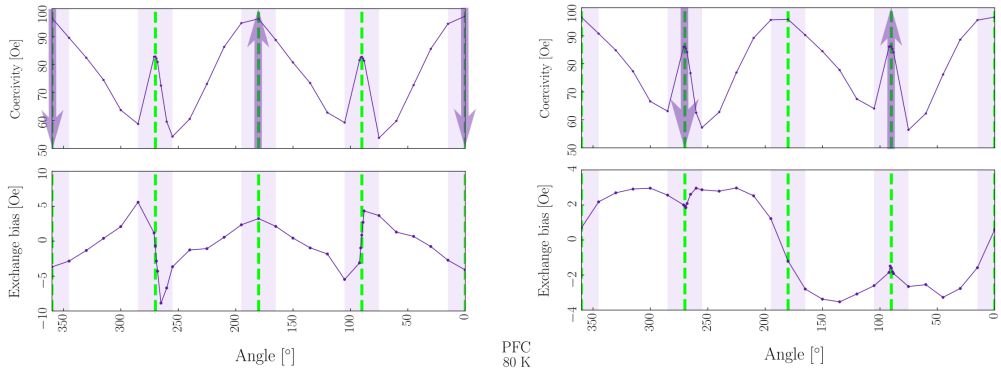

FIG. 6. The azimuthal dependence of coercivity and exchange bias in Oe at 80 K for two positive field cooling states of +5 kOe: along the primary easy axis at 0° (180°) and along the secondary axis at 90° (270°). Arrows represent the field cooling direction. Dashed green lines denote easy axes at 0° (180°) and 90° (270°).

pronounced. This observation suggests a strong correlation between the coercivity and exchange bias behavior along different crystallographic directions. This pronounced correlation fades when the cooling field is oriented along the 90° (270°) axis, as seen in Figure 5, and it exhibits a more stable behavior across the temperature range with reduced anisotropy. Here, the exchange bias incrementally increases during cooling, with the absence of sharp changes during phase transition in V_2O_3.

Previous studies have shown that larger exchange coupling is expected near the axes, where the coercivity is higher and along which the sample was field-cooled[9]. From Figure 6, both coercivity and exchange bias as functions of azimuth angles at 80 K for different cooling states are depicted, revealing similar correlations between exchange bias and coercivity as those observed in previous studies[9,20,32]. Moreover, it becomes evident, by analyzing the cooling field direction and its impact on exchange bias shapes, that no rapid changes occur when the sample is cooled with the applied field along axes where coercivity does not reach its maximum values, and the exchange coupling is more affected when the cooling field is applied along 0° (180°) and 90° (270°) directions, corresponding to the maximum values of the coercive field.

The ordered magnetic moments of V in the monoclinic phase have been observed to orient perpendicular to the hexagonal a-axis, at an angle of approximately 71° from the hexagonal c-axis (see Figure 2)[23,33]. Therefore, cooling with an applied field along the 90° (270°) direction, coinciding with the spin alignment plane of the V moments leads to a more commonly expected in-plane angular behavior of the exchange bias, correlated with the coercivity[9,20,32]. However, the magnitude of exchange bias is observed to be higher when applying cooling field is along the primary easy axis at 0° (180°). We assume that in this cooling field state along the primary easy axis, during the phase coexistence region, the inhomogenous distributions of phases of the V_2O_3 layer results in a correspondingly non-uniform V_2O_3/Ni structural interface, thereby causing an uneven magnetic interface. When a cooling field is applied along the 90° (270°) axis, which is nearly aligned with the V magnetic moments, it tends to support magnetic exchange coupling, as the field direction complements the existing moment alignment. On the other hand, applying a cooling field along the primary easy axis, which is perpendicular to the V moment alignment and presumably less effective in contributing to the coupling, results in more sensitivity to structural variations during the SPT. This leads to a less uniform and more inhomogeneous exchange bias across the phase coexistence region (as shown in Fig. 4).

IV. CONCLUSIONS

Our study has revealed the intricate angular dependence of coercivity, exchange bias, and field cooling direction in V_2O_3/Ni heterostructures. A pronounced coercivity peak is observed specifically along the main easy axes (0°/180°), highlighting the directional dependence within the heterostructure. This peak contrasts with the more gradual changes observed along the secondary easy axis at 90° (270°), where coercivity exhibits a smoother transition without abrupt shifts. Temperature dependent investigations of the exchange bias reveal the onset of exchange bias to occur at the SPT of V_2O_3 across all angles and for all cooling field states. The orientation of the applied cooling field plays a pivotal role in dictating the shape, magnitude, and orientation of the exchange bias. Notably, when the cooling field is applied along the secondary easy axis (90°/270°), coinciding with the alignment of the V magnetic moments, exchange bias at 80 K displays a characteristic unidirectional symmetry. Our

results reveal the complex interplay between the angular dependence of exchange bias, coercivity, and field cooling direction with the underlying crystallographic orientation of the V_2O_3 layer and highlight the potential V_2O_3 based magnetic heterostructures have for engineering and controlling the magnetic properties and response of bilayer films.

Acknowledgements This work was supported by funding from the University of Iceland research fund and the Icelandic Research Fund Grant No. 207111. Instrumentation funding from the Icelandic Infrastructure Fund is acknowledged.

Corresponding authors
U. B. Arnalds (uarnalds@hi.is)

Conflict of Interest There is no conflict of interest to disclose.

Data Availability Statement The authors confirm that the data supporting the findings of this study are available within the article.

[1] A. McLeod, E. Van Heumen, J. Ramirez, S. Wang, T. Saerbeck, S. Guenon, M. Goldflam, L. Anderegg, P. Kelly, A. Mueller, et al., Nature Physics **13**, 80 (2017).
[2] E. B. Thorsteinsson, S. Shayestehaminzadeh, and U. B. Arnalds, Applied Physics Letters **112**, 161902 (2018).
[3] M. Sultan, K. Ignatova, E. Thorsteinsson, F. Magnus, and U. Arnalds, Journal of Physics D: Applied Physics **54**, 425302 (2021).
[4] N. Mott, Contemporary Physics **14**, 401 (1973).
[5] A. Zylbersztejn and N. F. Mott, Physical Review B **11**, 4383 (1975).
[6] J. Slater, Physical Review **82**, 538 (1951).
[7] R. E. Peierls, Quantum theory of solids, Vol. 9 (Clarendon Press, 1964).
[8] J. Nogués and I. K. Schuller, Journal of Magnetism and Magnetic Materials **192**, 203 (1999).
[9] T. Ambrose, R. Sommer, and C. Chien, Physical Review B **56**, 83 (1997).
[10] Y.-C. Lau, D. Betto, K. Rode, J. Coey, and P. Stamenov, Nature nanotechnology **11**, 758 (2016).
[11] W. Kuch, L. I. Chelaru, F. Offi, J. Wang, M. Kotsugi, and J. Kirschner, Nature materials **5**, 128 (2006).
[12] S. R. Ali, M. B. Janjua, M. Fecioru-Morariu, D. Lott, C. J. P. Smits, and G. Güntherodt, Phys. Rev. B **82**, 020402 (2010).
[13] K. Ignatova, E. Vlasov, S. D. Seddon, N. Gauquelin, J. Verbeeck, D. Wermeille, S. Bals, T. P. A. Hase, and U. B. Arnalds, "Phase coexistence induced surface roughness in V_2O_3/Ni magnetic heterostructures," (2024), submitted to APL Materials, under review.
[14] J. De La Venta, S. Wang, J. Ramirez, and I. K. Schuller, Applied Physics Letters **102**, 122404 (2013).
[15] J. De La Venta, S. Wang, T. Saerbeck, J. Ramírez, I. Valmianski, and I. K. Schuller, Applied Physics Letters **104**, 062410 (2014).
[16] C. T. Wolowiec, J. G. Ramírez, M.-H. Lee, N. Ghazikhanian, N. M. Vargas, A. C. Basaran, P. Salev, and I. K. Schuller, Physical Review Materials **6**, 064408 (2022).
[17] V. Polewczyk, S. Chaluvadi, P. Orgiani, G. Panaccione, G. Vinai, G. Rossi, and P. Torelli, Physical Review Materials **5**, 034413 (2021).
[18] K. Ignatova, E. B. Thorsteinsson, N. Strandqvist, C. Vantaraki, V. Kapaklis, A. Devishvili, G. K. Pálsson, U. B. Arnalds, et al., Journal of Physics: Condensed Matter (2022), https://doi.org/10.1088/1361-648X/ac9946.
[19] T. Saerbeck, J. de la Venta, S. Wang, J. G. Ramírez, M. Erekhinsky, I. Valmianski, and I. K. Schuller, Journal of Materials Research **29**, 2353 (2014).
[20] H. Xi, M. H. Kryder, and R. M. White, Applied Physics Letters **74**, 2687 (1999).
[21] C. Marrows, F. Stanley, and B. Hickey, Sensors and Actuators A: Physical **81**, 49 (2000).
[22] U. Arnalds, J. Agustsson, A. Ingason, A. Eriksson, K. B. Gylfason, J. Gudmundsson, and S. Olafsson, Review of Scientific Instruments **78**, 103901 (2007).
[23] R. Moon, Journal of Applied Physics **41**, 883 (1970).
[24] I. Valmianski, A. F. Rodríguez, J. Rodríguez-Álvarez, M. G. Del Muro, C. Wolowiec, F. Kronast, J. G. Ramírez, I. K. Schuller, A. Labarta, and X. Batlle, Nanoscale **13**, 4985 (2021).
[25] A. Pofelski, S. Valencia, Y. Kalcheim, P. Salev, A. Rivera, C. Huang, M. A. Mawass, F. Kronast, I. K. Schuller, Y. Zhu, et al., arXiv preprint arXiv:2312.09051 (2023), https://doi.org/10.48550/arXiv.2312.09051.
[26] B. Sass, S. Buschhorn, W. Felsch, D. Schmitz, and P. Imperia, Journal of magnetism and magnetic materials **303**, 167 (2006).
[27] R. Stamps, Journal of Physics D: Applied Physics **33**, R247 (2000).
[28] J. Van Driel, F. De Boer, K.-M. Lenssen, and R. Coehoorn, Journal of Applied Physics **88**, 975 (2000).
[29] O. Allegranza and M.-M. Chen, Journal of Applied Physics **73**, 6218 (1993).
[30] H. Xi and R. M. White, Journal of Applied Physics **87**, 410 (2000).
[31] B. A. Frandsen, Y. Kalcheim, I. Valmianski, A. S. McLeod, Z. Guguchia, S. C. Cheung, A. M. Hallas, M. N. Wilson, Y. Cai, G. M. Luke, et al., Physical Review B **100**, 235136 (2019).
[32] F. Radu, A. Westphalen, K. Theis-Bröhl, and H. Zabel, Journal of Physics: Condensed Matter **18**, L29 (2005).
[33] P. Dernier and M. Marezio, Physical Review B **2**, 3771 (1970).

Paper IV: Supplementary information

Angular-dependent exchange bias in V_2O_3/Ni magnetic heterostructures

K. Ignatova, E.B. Thorsteinsson, U.B. Arnalds

In manuscript, 2024

Angular-dependent exchange bias in V_2O_3/Ni magnetic heterostructures

Supplementary material

K. Ignatova,[1] E. B. Thorsteinsson,[1] and U. B. Arnalds[1]

[1]*Science Institute, University of Iceland, Dunhaga 3, 107 Reykjavik, Iceland*

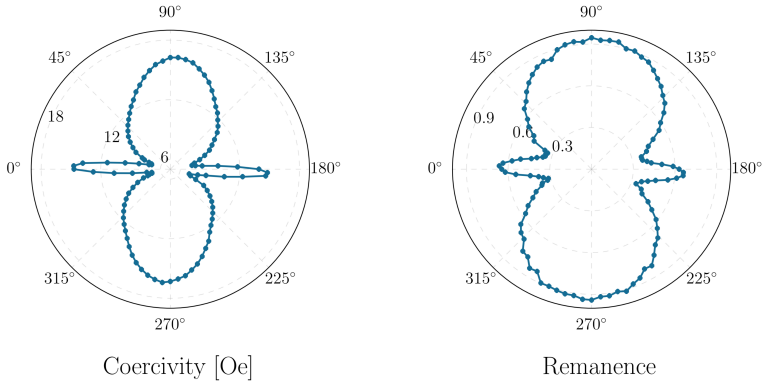

FIG. S1: Coercivity in Oe and normalized remanent magnetization at room temperature for the single Ni layer film grown on the r-plane of Al_2O_3 substrate annealed at 1200°C as a function of the azimuth angle.

Paper V

Structural and electrical properties of V_2O_3 thin films on c-plane Al_2O_3 fabricated by reactive-HiPIMS and dcMS techniques

M.T. Sultan, K. Ignatova, E.B. Thorsteinsson, F. Magnus, U.B. Arnalds

Journal of Physics D: Applied Physics (2021)

Structural and electrical properties of V_2O_3 thin films on c-plane Al_2O_3 fabricated by reactive-HiPIMS and dcMS techniques

M. T. Sultan[1], K. Ignatova[1], E. B. Thorsteinsson[1], F. Magnus[1], and U. B. Arnalds[1]

[1]Science Institute, University of Iceland, Dunhaga 3, 107 Reykjavik, Iceland

June 19, 2021

Abstract

The study presents the synthesis of epitaxial V_2O_3 thin films on c-plane Al_2O_3 substrates by reactive high-power impulse (HiPIMS) and direct current (dcMS) magnetron sputtering. The results reveal that for fixed deposition conditions and discharge power, well defined epitaxial layers can be attained using both HiPIMS and dcMS. For dcMS we observe the formation of these epitaxial films down to flow rate values of 1.3 sccm while for HiPIMS we observe an extended operation window down to much lower oxygen flow of 0.5 sccm without sacrificing the structural quality of the films. Furthermore, the effect of varying HiPIMS discharge parameters i.e. repetition frequency and average power for fixed O_2 flow setting, were explored in order to determine their effect on the structural quality and electrical characteristics of films. The magnitude of the metal-insulator transition (MIT) and the transition temperature is correlated to the film stoichiometry which can be fine-tuned by mapping the HiPIMS discharge parameters, displaying a total change in resistance of ~ 7 decades over the studied temperature range. The MIT temperature and magnitude obtained for films fabricated by HiPIMS, even for low O_2 flow settings (down to $0.6-0.5$ sccm), displayed superior characteristics compared to films fabricated by dcMS where a minimum O_2 flow of 1.3 sccm was needed.

Keyword: V_2O_3, HiPIMS, thin-films, metal-insulator transition, XRD, AFM

1 Introduction

Vanadium sesquioxide (V_2O_3) is a widely recognized system displaying Mott-Hubbard physics [1, 2] and serves as an important model for studying correlated electron systems [3]. V_2O_3 is a transition metal-oxide which undergoes a first-order structural phase transition from a high temperature (HT) rhombohedral paramagnetic metal to a low temperature (LT) monoclinic anti-ferromagnetic insulating state [3, 4]. Such a structural transition is linked to the metal-insulator transition (MIT) and can be observed through the resistivity change of the material as a function of temperature. For bulk V_2O_3 the transition temperature (T_{MIT}) is around ~ 155 K, and the change in resistivity can extend up to 7 orders of magnitude [3, 5, 6]. As the MIT is linked to the structural transition the application of pressure, doping and stoichiometry can affect the electrical transition. For instance, titanium doping and vanadium vacancies both shift the T_{MIT} to lower temperature and eventually can lead to the suppression of the insulating phase [7]. In contrast,

chromium doping increases the T_{MIT} and can create a paramagnetic insulating phase near room temperature (RT) [8, 3] or alternatively can promote excess of oxygen in films, stabilizing the metallic state [5, 9]. Apart from doping, for V_2O_3 films deposited on single crystalline substrates the choice of deposition method and fabrication conditions, substrate material and film thickness can also alter the MIT properties [1, 10]. Films with varying transport properties have been fabricated where the change in MIT magnitude and T_{MIT} have been correlated to strain induced by lattice mismatch, c/a ratio, film thickness and by altering the stoichiometric composition of the film(as the transition is sensitive to vanadium and oxygen vacancies and /or interstitials) [11, 7].

For the deposition of V_2O_3 films the most common substrate of choice is c-plane Al_2O_3, sharing a similar rhombohedral crystal symmetry with an approximately 4.1% smaller in-plane lattice constant [1]. For thin film growth on such substrates, in-plane strain induced by the substrate is expected along with strain arising from variations in the stoichiometry [2, 5]. Several deposition methods have been employed for the thin film fabrication of metastable stoichiometric V_2O_3 including e-beam evaporation [12], thermal evaporation [13], reactive magnetron sputtering [5, 14, 15], pulsed laser deposition[6, 4] and molecular beam epitaxy [7, 8, 3]. Out of these, magnetron sputtering (MS) is the most versatile method, as it provides better quality of the films through control of discharge parameters, along with a high level of automation and a good compatibility with industrial processes [16, 17]. A rather recent variation of the magnetron sputtering technique, so-called high power impulse magnetron sputtering (HiPIMS), has been demonstrated to give superior control over the properties of the sputtered species and deposited films by yielding a discharge with increased ionization, having a sufficiently large amount of energetic ions. In HiPIMS, high power is applied to the magnetron target in short unipolar pulses at low repetition frequency (f_R) and low duty cycle while keeping the time averaged power about 2-orders of magnitude lower than the peak power [18]. This results in a higher ionization fraction of the sputtered species and a high plasma density [19, 20]. This allows better control of the film growth by controlling the energy and direction of the sputtered species [21], providing denser films, with smoother surface and of higher crystallinity [22, 23], in comparison to conventional MS methods. During reactive sputtering, the reactive gas tends to form compound films over the target surface, referred to as target poisoning. Due to this target coverage the reactive sputtering is unstable and represents well-known hysteresis curve [24]. Three different modes of operation can be observed during reactive HiPIMS sputtering i.e., metal, transition and poisoned mode. In metal mode i.e., sputtering at low reactive gas flow or high pumping speed, there is insignificant reaction of reactive gas with the target and the supplied reactive gas is incorporated in the deposited film. Increasing the gas flow, a compound film forms over the target surface, and the effective etching rate of the compound is lower than the pure metal and the process is referred to as poisoned mode[24, 19]. During the poisoned mode the discharge current is carried out by the electrons rather than the ions, thereby increasing the cathode current when sputtering in compound/poisoned mode, along with a reduction in deposition rate [19, 25]. However, it has been debated whether the deposition of compound films at relatively high deposition rates can be obtained within the transition zone, between metal and poisoned mode[19]. Within the transition zone there is a balance between the formation and removal of the compound film over the target surface. A detailed description of the three modes of reactive HiPIMS operation along with the current and voltage waveforms can be found in studies [26, 25, 24]. Considering the discharge current and voltage waveforms, the general trend observed is that the electron density increases when transitioning from metal mode to the poisoned mode. In the metal mode the electron density and or the discharge current increase at the initial pulse-on followed by a steady plateau, which in case of transition and or poisoned mode tends to increase with cathode current peaking at the end of the pulse [26, 25]. It has been further documented in a study by Gudmundsson *et al.* [21] that the contribution and composition of different ions to the discharge current alters between the metal and the poisoned mode in reactive HiPIMS sputtering. That is, in case of metal

mode the discharge current is dominated by recycling metal ions, however due to low self-sputter yield the discharge current is maintained at lower amplitudes. In the case of poisoned mode a triangular shape of waveform having a high discharge current, can be explained on the fact that the discharge current is dominated by the Ar^+ ions, out of which two third is being recycled and the return probability of the working gas in poisoned mode is close to unity. An example of metal and poisoned mode of sputtering is shown in Figure S1c.

To our knowledge, limited or no work deals with the fabrication of V_2O_3 films using HiPIMS deposition. In this study we investigate the structural and electrical properties of V_2O_3 thin films (of thickness $\sim 22 \pm 2$ nm) grown by HiPIMS and dcMS techniques under varying O_2 flow rates and discharge parameters at a fixed growth temperature (T) of 600°C. We observe that the variation in oxygen flow settings and discharge parameters i.e. power and repetition f_R (in case of HiPIMS), influence the MIT characteristics of the films in a similar and controllable manner. Furthermore, a correlation between the structural quality of the films with the discharge parameters and O_2 flow settings was observed. Thus, the possibility of tuning the electrical properties (i.e. metal-insulator transition) have been demonstrated in this study by rigorous mapping of the HiPIMS deposition parameters along with structural and electrical characterization.

2 Experimental

2.1 Material and method

The study incorporates two variants of MS, i.e. direct current (dcMS) and high-power impulse (HiPIMS) magnetron sputtering. For dcMS an Advanced Energy MDX500 power supply was utilized, whereas for HiPIMS the power was supplied using a SPIK1000A pulse unit (Melec GmbH) operating in unipolar negative mode at a constant square wave pulses of constant voltage, which in turn was charged by a DC power supply (ADL GS30). The discharge current and voltage were monitored using a combined current transformer and a voltage divider unit (Melec GmbH) and the data were monitored and recorded with a digital storage oscilloscope (Agilent 54624A) and the PCI-e DAQ card, respectively.

The V_2O_3 films were fabricated onto single crystalline sapphire substrates with c-plane [0001] surface orientations, by reactive magnetron sputtering from a vanadium target using a custom built sputtering system [27]. Prior to deposition the substrate was prebaked at 600°C for 30 minutes and the chamber was held at a base pressure of 7×10^{-6} Pa. During sputtering, an Argon (Ar) gas of 5N purity was used as the working gas along with oxygen (O_2) gas of 5N purity, while keeping the substrate temperature at 600°C. The flow rates for Ar (q_{Ar}= 40 sccm) and O_2 (q_{O_2} in range of 0.35 to 1.5 sccm) were controlled by a mass flow controller and throttle valves were adjusted to stabilize the growth pressure of 0.7 Pa during deposition. After deposition the substrates were allowed to cool down *in-situ* before *ex-situ* characterization.

For each variant of magnetron sputtering the growth temperature, growth pressure, and the film thickness (of $\sim 22 \pm 2$ nm), were kept constant. The reactive dcMS deposition for V_2O_3 was made in a constant-power mode of 150 and 200 W, at varying O_2 flow rates. Whereas, for HiPIMS the deposition was made at a fixed pulse length of 100 μs while varying:

1. the O_2 flow from 0.35 to 1.3 sccm, at a fixed f_R and average power (150 Hz and 375 W, respectively).

2. f_R (ranging from $100 - 550$ Hz) at a constant average power of 200 W and O_2 flow setting of 0.6 sccm.

3. the average power (from $150 - 375$ W) for fixed f_R and O_2 flow (150 Hz and 0.6 sccm, respectively).

2.2 Characterization

Structural characterization was conducted using X-ray reflectivity (XRR) and X-ray diffraction (XRD) using a Panalytical X'pert diffractometer (CuKα, 0.15406 nm). For XRD, a 2×Ge (220) asymmetrical hybrid monochromator utilizing line focus, a divergence slit (1/4°), and a parallel plate collimator (0.27°) was used. Atomic force microscopy (AFM), from Park System (PSIA XE-100) was utilized for surface analysis. For electrical characterization, a custom built setup was utilized employing a cryogenic pump (Leybold-Heraeus RG 210), and the samples with co-planar electrical contacts were mounted on a cooling stage with an insulating sample holder.

3 Results and discussion

Three variables were considered for HiPIMS deposited structures, (1) variation of the O_2 flow setting, (2) f_R at low duty cycles and (3) average power. The pulse length was chosen to be 100 μs, which lies suitably in the range of pulse lengths quoted for thin film deposition [20]. For the case of (1) varying O_2 flow rates, the repetition frequency (150 Hz) and pulse length (100 μs) were kept constant (at a duty cycle of 0.015). The constant average power of 375 W over the target area was maintained having the peak current and power density of 1.7 ± 0.2 A/cm^2 and 1010 ± 10 W/cm^2, respectively, with cathode voltage approximately varying within 510 ± 15 V in order to keep a constant average power. For the case of (3) varying average power (150 - 375 W), the repetition frequency and pulse length of 150 Hz and 100 μs with an O_2 flow setting of 0.6 sccm was kept constant. Subjected to (2) variation in f_R (ranging from 100 to 550 Hz), a constant pulse length of 100 μs (and therefore a resulting low duty cycle of 0.01 to 0.055, respectively) was employed with an average power and O_2 flow rate of 200 W and 0.6 sccm, respectively.

The discharge parameters were selected to attain a metallic mode of deposition. The recorded waveforms for varying O_2 and power are provided in supplementary information (Figure S1(a,c)) and is in good agreement with studies in [26, 25]. Figure 1(a) shows the HiPIMS current and voltage waveforms in metal mode for varying f_R. The discharge current reaches a peak value in the initial regime of the pulse which then decays to lower values until the end of the pulse. The obtained peak current and power density, which both decrease with increasing f_R, are plotted in Figure 1(b, c)). These results are in good agreement with previous work related to reactive HiPIMS with metal targets [19, 28, 29, 21], and is attributed to increased secondary electron emission yield as a result of oxide formation on the target surface at low f_R.

3.1 Structural characterization

The epitaxial quality of the films deposited by dcMS and HiPIMS was investigated by x-ray diffraction analysis. Figure 2a shows XRD scans for V_2O_3 thin films grown on *c*-plane Al_2O_3 by reactive HiPIMS for various O_2 flows. The XRD scans for HiPIMS deposited structures at varying f_R and power can be found in supplementary information (Figure S2(a,b)). For all HiPIMS deposited structures, the films displayed an epitaxial nature displaying a clear V_2O_3 (006) peak along with Laue fringes extending on both sides. The epitaxial nature of the films can further be perceived in Figure 2c (blue open square), which shows the ratio of the mean size of crystalline domains in the vertical direction (i.e. coherence length, obtained by the width of the X-ray peak and the Scherrer formula and of the film thickness (as determined by XRR) as a function of O_2 flow rates. The coherence length as a function of f_R is also presented in Figure 2d. The above analysis of the epitaxial quality of films is in good agreement with the data obtained via reciprocal space mapping and the phi-scan profiles (not shown here) and has already been explored in our earlier work over similar structures [[10, 30], fabricated via dcMS sputtering.

Figure 2b shows XRD scans for varying O_2 flow rates for the dcMS deposited films, at constant power of 150 and 200 W. The epitaxial nature obtained by dcMS deposition is found to be strictly dependent on both the power setting and specific O_2 flow rate[10]. That is, films deposited at 200 W with a 1.5 sccm O_2 flow rate showed similar structural quality

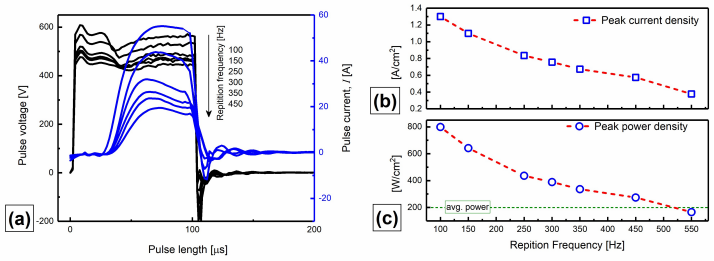

Figure 1: Discharge cathode current and voltage waveforms during HiPIMS deposition for V_2O_3 films at constant O_2 of 0.6 sccm, pulse length of 100 μs and an average power over target of 200 W for varying repetition frequency. (b) Peak discharge current density and (c) peak power density, recorded for varying repetition frequency.

(epitaxial nature) as that obtained at a lower power and O_2 flow setting of 150 W and 1.0 sccm, respectively. A detailed description for varying dcMS power can be found elsewhere [5, 10]. However, it is worth mentioning here that, in dcMS the reactive sputtering operational window (i.e. O_2 flow rate) showing epitaxial nature, is much smaller than that obtained for HiPIMS deposited structures i.e. 1.3 - 0.5 sccm (highlighted is the extended range) complementing its merit. A similar observation in study [31] on the fabrication of Al_2O_3 from an Al-target in Ar/O_2 atmosphere, has shown that the HiPIMS operational window can extend beyond the dcMS critical gas flow settings. Even though similar deposition conditions were utilized the deposition rate for dcMS is higher (i.e. 4.7 nm/min) than the HiPIMS (i.e. 3.2 nm/min) which can affect the shift in the O_2 process window. However, to further validate this a higher repetition frequency was also studied in this context wherein a deposition rate of 4.1 nm/min was obtained (see later discussion). Akin to HiPIMS structures the coherence length as a function of O_2 flow rates for dcMS structures is also incorporated in Figure 2c. Moreover, to elaborate the distinct advantage of HiPIMS compared to that of dcMS , structures with thickness between $\geq$ 60 nm and $\leq$ 100 nm were deposited and analysed for x-ray diffraction. An evident presence of Laue fringes can be seen for structures deposited via HiPIMS while films deposited by dcMS for similar deposition conditions (see Figure S2c, in supplementary information) reveal a limited presence of Laue fringes. This result is in agreement with expectations for HiPIMS growth as it provides a high ionization fraction along with better control over the energy and direction of sputtered species, resulting in improved quality of films [23, 21].

The V_2O_3 (0 0 6) peak positions are plotted in Figure 2(e,f) as a function of dcMS and HiPIMS discharge variables and O_2 flow rates with respect to the V_2O_3 (0 0 6) bulk value i.e. 38.514° . For HiPIMS and dcMS (at 200 W) it was observed that with decreasing O_2 flow a shift in the V_2O_3 (0 0 6) peak position to higher values was observed indicating a reduction in the out-of-plane c-lattice parameter. We attribute this reduction to small changes in the stoichiometry of the films with films grown at lower oxygen flows having a reduced oxygen content [32]. Furthermore, considering the in plane lattice constants of Al_2O_3 which are lower than that of high temperature corundum V_2O_3, the coherent growth of films (at least for those showing an epitaxial nature), can be thought of to be under compressive in-plane strain [32], especially close to the interface [30]. However, the effect of variation in V_2O_3 stoichiometry cannot be neglected which can further contribute to strain and will be discussed in a later section. It is to acknowledge here that, for HiPIMS deposition compared to dcMS, the upper O_2 oper-

ational limit was selected to be 1.3 sccm, as above this value the discharge tends to operate in transition and eventually in poisoned mode, which tends to result in a VO_x phase with higher oxygen content than the intended V_2O_3 phase. The above statement is supported by the triangular discharge current-voltage waveform obtained for O_2 flow settings of 1.5 sccm and is supported by data in studies on reactive HiPIMS sputtering [33, 19, 25]. Additionally, the XRD scans and related extracted values for films deposited at O_2 flow of 0.9 and 1.2 sccm,are not included as to avoid cluttering the Figure 2(a, c and e). However will be discussed in section 3.3, for electrical characterization.

Varying the f_R from 100 - 550 Hz at a constant O_2 flow of 0.6 sccm, an unusual trend in peak position was observed and is characterized in three distinct regions as can be seen in Figure 2f. In region I, the peak position shifts to higher angles with a maximum of 38.65° for up to 300 Hz f_R, followed by a shift to lower values as the f_R increases to the 350 - 450 Hz (region II). For region I, the shift in peak position to higher angle can be explained in light of results presented by Kubart et al. [34] which show that at high repetition frequency the reduction in gas density is lower due to lower peak current (see Figure 1b). The resulting effect is a more pronounced possibility towards target poisoning at low f_R, which has been supported by results from [35, 36] i.e., with increased time between pulses (i.e. lower f_R) there is more time available for target poisoning. Based on this, one can therefore expect an increased metal flux with increased f_R up tp 300 Hz, i.e. the vanadium to oxide (V/O) ratio will increase.

In region II, with f_R >300 Hz the peak shifts to lower angles. Such a reduction in peak position can be attributed to increased gas rarefaction (i.e. decrease in gas density in front of the target [28]) and reduced gas refill time, as a consequence of increased number of pulses (implying shorter pulse off time between pulses) and/or to a hot target surface [36]. Such an effect in turn leads to a reduction in the number of available ions for sputtering due to lower density of the working gas in front of the target (i.e. reduced metal flux)[19]. Thus, one can assume more oxygen to be available for sputtered species reaching the substrate, and hence a reduction in the V/O ratio.

Increasing further the f_R up to 550 Hz (region III), a drastic change-over of peak position to higher angle can be seen. This is understood in reference to Figure 1c, where an evident lowering of the peak power density is observed. In such a case, even though the gas-rarefaction effect is still dominant, a further reduction in the working gas ions near the target surface results in a loss of intended ionized physical vapour deposition characteristics [28], and the process conducts itself more as a pulsed dc-magnetron sputtering process. Such a behaviour is further illustrated by comparing the 550 Hz deposited structure to that of dcMS at similar O_2 flow of 0.6 - 0.8 sccm, which shows a similar peak position. However, it should be noted that the structural quality of the films is better for the HiPIMS deposited ones.

It is important to note here that in the case of HiPIMS only a slight variation in peak position was observed and that the peak positions are closer to the bulk value (of 38.514°) over the studied O_2 range of 0.5 - 1.3 sccm compared to that of dcMS, where the peaks are more shifted to higher angles. This observation is in good agreement with the previously reported results stating that, considering the hysteresis for reactive sputtering, dcMS has a relatively wide unstable region compared to HiPIMS which is substantially smaller [37] and can be further reduced with increased f_R [19, 26, 38]. To validate the preceding statement, XRD peak positions are plotted for structures at varying O_2 flow rate for higher f_R (i.e. 350 Hz, also incorporated in Figure 2e, open pentagons symbols). Compared to structure deposited at 150 Hz, a relatively small change in peak position was observed. Such a reduction in variation of peak position or instability at higher f_R for HiPIMS has been studied by Kubart et al. [34] and is explained in terms of gas rarefaction and gas refill time [38]. Although several other variations in controlling the discharge parameters can give the intended discharge stability, only the repetition frequency of 350 Hz is considered here for illustration.

Supplementary Figures S1 and S3a show the peak power density and the XRD data for structures deposited at varying average power. It is observed

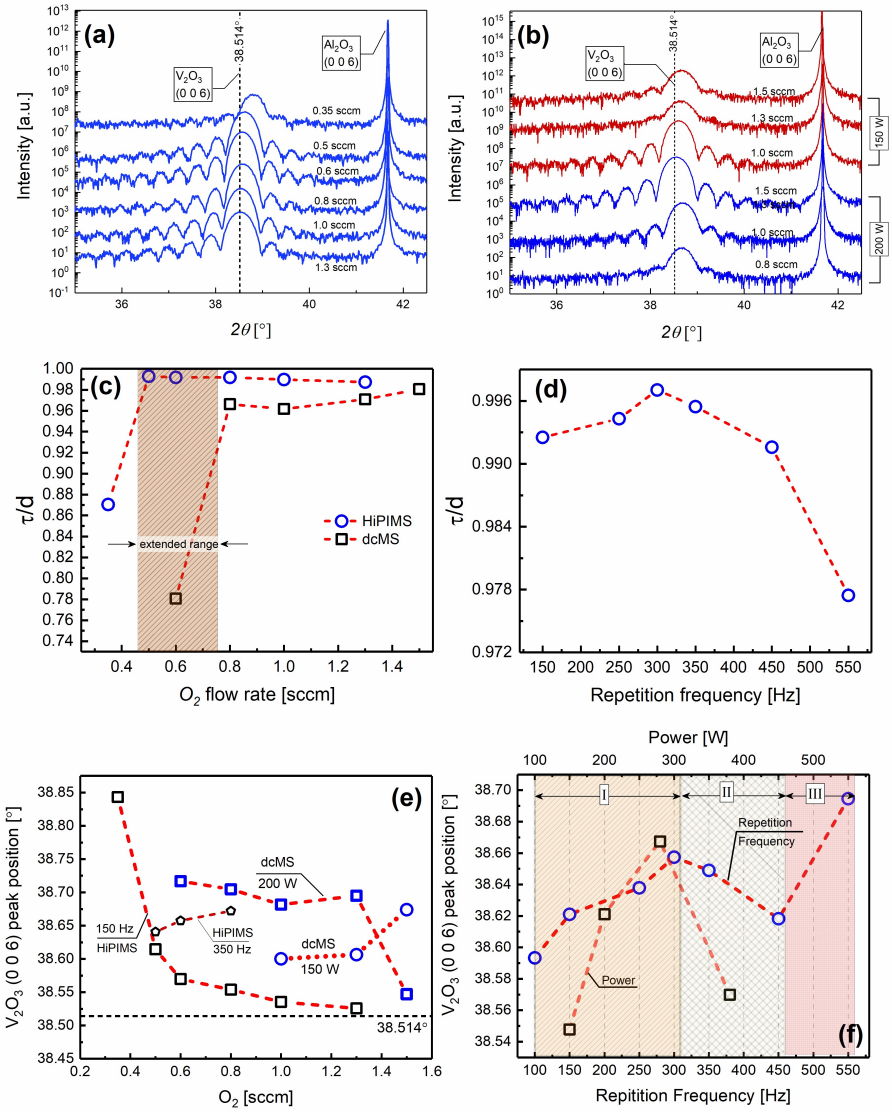

Figure 2: X-ray diffraction scans recorded for V_2O_3 films deposited by (a) HiPIMS and (b) dcMS, for varying O_2 flow rates (ranging from 0.35 – 1.5 sccm) and fixed working gas i.e. Ar flow rate of 40 sccm. The growth pressure was 0.74 Pa. In (b) the XRD graph incorporates dcMS structures deposited at 200 W (blue) and 150 W(red). Ratio of the mean size of the crystalline domains in the vertical direction, (τ), to the film thickness, d, as a function of (c) O_2 flow rate for both HiPIMS and dcMS sputtered films and (d) as a function of repetition frequency. V_2O_3 (0006) angular peak position as function of (e) O_2 flow rate for both HiPIMS and dcMS (indicated in the plot); (f) repetition frequency and average power. The vertical and horizontal dashed lines in (a, b and e) indicate the angular peak position of bulk V_2O_3 (00-034-0187 JCPDS data file; R-3c space group).

that with increase in peak power density the crystal structure is significantly affected [39] i.e. alteration in XRD peak position and coherence length Figure 2(d,f). With increase in average power up to 280 W an evident shift in peak position to higher 2θ values can be seen. This may be attributed to the increase in kinetic energy of the impinging atoms that may result in increased bombardment of the atoms on to the substrate surface during growth, thus resulting in an increased probability of oxygen re-sputtering [40]. This increased re-sputtering of oxygen results in increased oxygen vacancies as a function of power. Thus, an increase in V/O ratio is expected due to oxygen re-sputtering and increased deposition rates. However, with further increase in peak power to 380 W a shift in peak position to lower values is observed. This shift is attributed to the self-sputtering process attained at higher peak power densities[41]. That is, with an increase in peak power density, electron temperature will increase leading to a higher ionization rate with a higher chance of multiply charged metal ions (MCMI) [41, 42]. This increase in multiply charged metal ions gives rise to secondary electron emission resulting in a subsequent transition of the discharge to a higher current regime [42] i.e. a pulse current of up to 78 A, approximately twice that obtained for 150 W (Figure S1b). Furthermore, there is less probability that such MCMI can escape the negative potential of the target, and will therefore return to the target causing self-sputtering and a resulting reduction of the deposition rate. Thus, there is less metal flux and more oxygen for oxidation close or similar to that what is obtained at 150 W.

3.2 AFM analysis

The surface morphology of all samples was investigated by atomic force microscopy. The measurements were repeated for each sample on different reference areas in order to validate the reproducibility of these features. Representative topographic images (AFM contact mode) of the surface morphology of V_2O_3 films grown on Al_2O_3 are shown in Figure 3 . For the HiPIMS and dcMS deposited films considered in this study, the RMS roughness values were approximately 0.16±0.05 nm and 0.20±0.03 nm, respectively. Such values are limited by equipment resolution; however, a qualitative visualization can be made through selected AFM micrograph in Figure 3 showing an atomically flat terraced surface for all the films.

3.3 Electrical characterization

Figure 4 shows the resistance as a function of temperature for films fabricated under different O_2 conditions. For both deposition methods it was observed that the room temperature (RT) resistance increases as a function of decreasing O_2 flow rate (Figure S4a), in good agreement with previously published results [7, 3]. In the case of structures fabricated via HiPIMS three different types of electrical transitions were observed (Figure 4b), similar to that observed in other studies [11, 10]. For structures deposited towards the upper regime of O_2 flow rates i.e. 1.0 to 1.3 sccm, a metal-metal transition was observed, i.e. a decrease in resistance with increase in temperature having a slight jump at around 120 K, followed by a stabilized metallic state (type I) at lower temperature. A corresponding suppression of the insulating phase i.e. stabilization of metallic phase can be correlated with strain in the films and the film stoichiometry. In the literature the MIT alteration has been associated with the non-stoichiometry of V_2O_3 films and formulated as $V_2O_{3+\delta}$ or $V_{2-y}O_3$. For increased oxygen level it is believed that the electrical characteristics can change significantly and that the low temperature insulating phase can be suppressed with excess oxygen [8, 43]. That is, in a recent study it was observed that the excess oxygen can sit at interstitial sites, giving increased strain in the *a*-lattice parameter while having less impact on the *c*-lattice parameter [10]. The disorder created by these oxygen defects as parts of O Frenkel pairs in V_2O_3 lowers the energy cost of the transition, hence shifting the energy balance of the crystal towards the high temperature metallic phase, thereby reducing the temperature of the transition [44]. Similar metallic behaviour and suppression of the LT phase has already been studied for thinner films [13, 45, 46, 30].

Film deposited at reduced O_2 flow rates, rang-

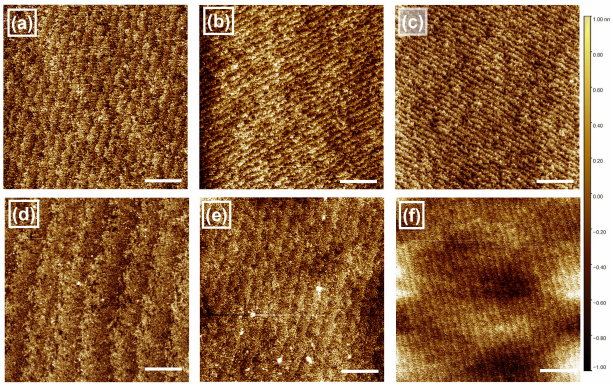

Figure 3: 5×5 μm^2 AFM images of V_2O_3 thin-films grown by HiPIMS (a-c) at varying O_2 flow setting i.e. 1.3, 1.0 and 0.6 sccm at fixed f_R and average power (150 Hz and 375 W, respectively) and (d) at 0.6 sccm for 350 Hz at 200 W. (e, f) grown by dcMs at 200 W (at 1.5 and 1.3 sccm). The scale bar provided is 1 μm. For all the images the z-scale bar is provided on the right-hand side.

ing from $\sim$ 0.5 to 0.9 sccm, all display a clear abrupt metal-insulator transition (type II) with varying magnitudes and T_{MIT} of which the sharpest and most dominant transition is obtained for 0.5 sccm. For these films, the resistance change of the transition ranges up to $\sim$ 4-orders of magnitude, and the films display a total resistance change of up-to 7-orders of magnitude (limited by the compliance of the measurement setup). For Films displaying a type-II transition, an evident dependence on the stoichiometry of the films was attained and that the transition can be

fine-tuned by controlling the oxygen interstitials [10, 5]. Moreover, Brockman et al. [7] showed a similar behaviour, i.e. increase in transition temperature and room temperature resistance (R_{RT}), with decreasing oxygen partial pressure. There, the changes were attributed to strong localization as a result of increased number of defects (oxygen vacancies and/or vanadium interstitials) which in turn would set-off an earlier onset of the vanadium sesquioxide insulating phase.

With further reduction in O_2 flow rate down to 0.35 sccm, the R_{RT} increases to $\sim 10^4$, and an insulator-insulator transition (type III) can be seen where the resistance increases with decreasing temperature. These results can be correlated to the structural analysis which revealed a low crystallinity and a broad 2θ peak with only a slight hint of Laue fringes. Thus, we can expect the film to be textured with domain boundaries acting as scattering centres for electron conduction [10, 1].

Our results reveal that the main controlling factor in the MIT of the films is the film stoichiometry [5, 10, 7, 47]. However, the effect of strain cannot be neglected. This can be discussed in terms of the c/a lattice parameter ratio which has been shown to affect the transition behaviour [10]. It is accepted that the a-axis of the HT corundum V_2O_3 phase expands and the c-axis shrinks through the structural phase transition from the HT-PM phase to the LT-AFI phase [6]. Moreover, in the case of epitaxial film growth on c-plane sapphire, the a-axis of the film is firmly clamped by the substrate, resulting in impeded lattice deformation. Additionally, the difference in thermal expansion coefficient between film and substrate contributes to increased c/a ratio [8, 48] for films grown at elevated temperatures. Other parameters affecting the c/a ratio include temperature, oxy-

gen content and thickness of the film [13], where the c/a ratio has been found to be larger for higher deposition temperature, increased oxygen content and thinner films, in agreement with our results.

Considering the above criteria it is logical to say that at higher O_2 flow rates the incorporation of oxygen interstitials will tend to increase the strain in the a-plane stabilizing the metallic state [5, 10, 6]. A reduction in the c/a ratio as in films of type-II accompanied with a reduction in the amount of oxygen interstitials results in a shift of T_{MIT} to higher temperature [6], eventually leading to a stabilization of the insulating phase.

In contrast, for dcMS deposited structures (at 200 W, Figure 4e) an evident metal-insulator transition (type-II) was observed at higher O_2 flow rates ranging from 1.5 to 1.0 sccm with resistance change for transition of about 3-orders of magnitude. However, in contrast to HiPIMS deposition, lowering the O_2 flow rate in dcMS from 0.8 to 0.6 sccm, changes the transition to type-III, i.e. an insulator-insulator transition. A detailed description for dcMS deposited structures at varying O_2 flow and power settings, is provided in previous studies [10, 5]. For exploration purposes the MIT plots for dcMS deposited structures at 150 W are provided in supplementary information (see Figure S3). It is to mention here that the O_2 flow setting for HiPIMS deposited structures were studied for maximum of 1.3 sccm, compared to dcMS for 1.5 sccm. As any further increase in O_2 for HiPIMS deposition as mentioned previously, causes the discharge to operate in transition or poisoned mode (see Figure S1c), manifesting an unintended VO_x phase. Additionally, since the transition to insulating phase is being suppressed already at 1.0 to 1.3 sccm range, any further increase in oxygen is expected to further stabilization of the metallic phase.

Figure 4c shows the MIT plots for films deposited by HiPIMS under different average power settings while maintaining other deposition settings fixed. As has been detailed before, the main controlling parameter affecting the electrical properties of the films is their stoichiometry, which is controlled by the discharge parameters [10]. For 100 to 280 W power settings at a fixed O_2 flow rate, the increase in average power increases the proportion of sputtered metallic flux from the target, thereby increasing the V/O ratio as can also be visualized by the shift in peak positions (see Figure 2f, open squares). This implies a reduction in oxygen interstitials along with a reduction in the c/a ratio, with the films thereby showing an increased transition magnitude and temperature (Figure S5(b)) as a function of increased power. However, as mentioned earlier that for increased power up to 380 W there is a higher probability for the formation MCMI causing self-sputtering which in turn reduces the deposition rate. Thus, implying a reduction in V/O ratio, as highlighted by the shift in peak position towards lower angles, close to that obtained from 150 W (see Figure 2f). However, the steepness of the MIT slope is higher for 380 W than for 150 W, due to a reduced amount of oxygen interstitials compared to that of 150 W and thereby shows less suppression of the insulating phase.

Based on the above presented results, power and O_2 flow setting values which resulted in the sharpest MIT and reasonable room temperature resistance values were chosen as fixed values for varying the repetition frequency f_R, see Figure 4d.

Here an evident increase in R_{RT} (Figure S4c) and increased MIT magnitude (Figure 4d) with shift in T_{MIT} towards higher values (Figure 4(d, f)) is observed for the f_R range up to 300 Hz which with further increase in f_R to 350 - 450 Hz resulted in a deviation of T_{MIT} towards lower values. The T_{MIT} values were obtained by plotting $\mathrm{d}(\ln R)/\mathrm{d}T$ as a function of temperature, an example of which can be found in supplementary information Figure S5(a). The alteration in transition temperature with varying repetition f_R can be directly associated with the oxygen content in the film. That is with increase in f_R from 150 to 300 Hz, as stated in section 2.1, the metallic flux increases due to reduced possibility of target poisoning. Hence, we can assume a reduction in oxygen interstitials with increased f_R.

Increasing f_R further to 350 and 450 Hz results in a reduction of the peak power density closer to average power giving rise to gas rarefaction implying a high V/O ratio and shifting the peak position towards lower angles (region II, Figure 2f) and hence the T_{MIT} to a lower temperature (Figure 4(d, f)). At $f_R = 550$ Hz, as stated before, one can predict a

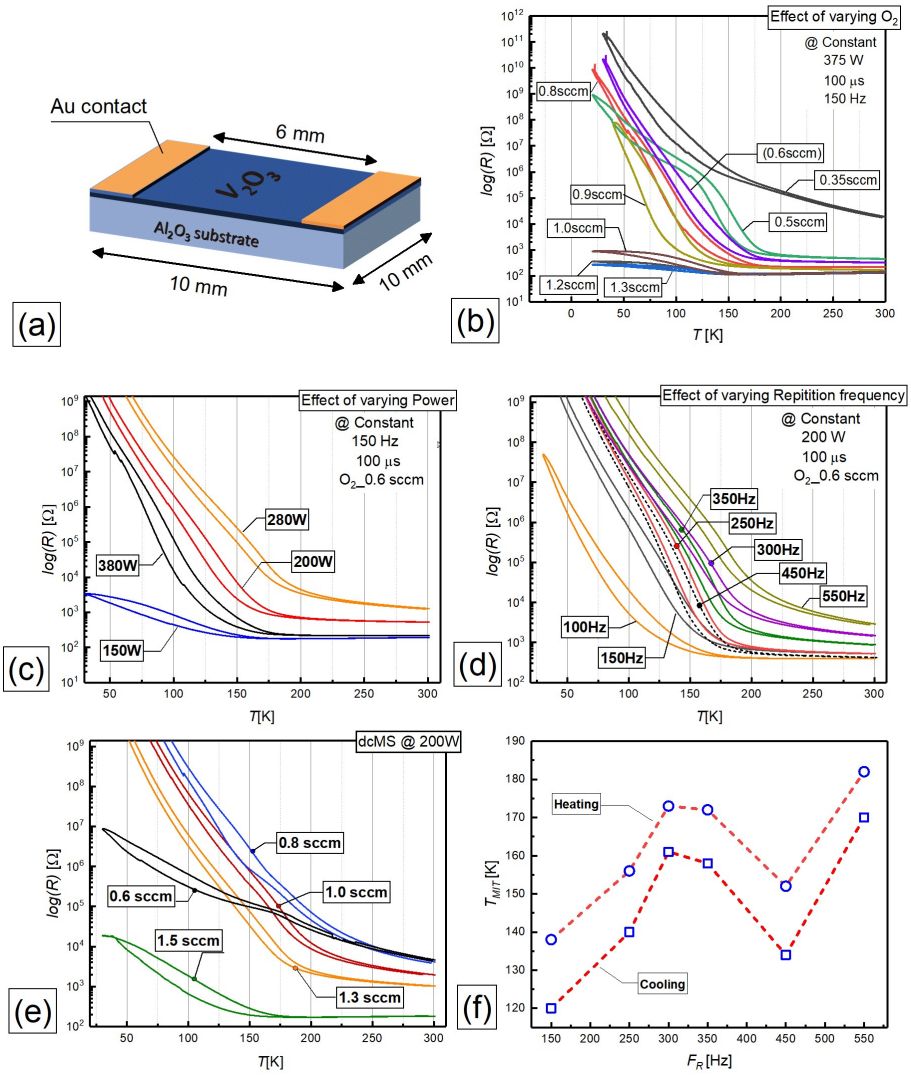

Figure 4: (a) Schematic illustration of the sample structure where the resistance of the films was measured using 100 nm thick and 2 mm wide gold contacts deposited along the edges of the films. Resistance as a function of temperature for the $\sim 22\pm 2$ nm V_2O_3 thin films deposited via HiPIMS (b) under different oxygen conditions, (c) at varying sputtering power, and (d) at varying repetition frequency. (e) Resistance as a function of temperature for V_2O_3 thin films deposited by dcMS technique under varying O_2 flow rates at 200 W. (f) T_{MIT} values both for cooling and heating cycles for HiPIMS deposited structures at varying f_R presented in (d).

dcMS nature of the deposition even though the structural quality of the film is preserved (see Figure S2). For this film a similar MIT behaviour, as for dcMS films deposited for an O_2 setting of 0.8 sccm is observed. This similarity is further illustrated by the V_2O_3 peak positions for the corresponding structures (see Figure 2(e, f)).

Finally, considering the electrical properties of films deposited at higher f_R, a minor alteration in MIT characteristics for structures deposited at 350 Hz for varying O_2, ranging from 0.5 - 0.8 sccm was observed (see Figure S3b). These results support the statement in section 3.1. regarding the reduction in the instability of reactive HiPIMS deposition at higher f_R.

4 Conclusions

In summary, we present an investigation of the use of HiPIMS for the fabrication of flat, epitaxial V_2O_3 thin films on sapphire for O_2 flow settings ranging from 0.35 to 1.3 sccm. Our results show that, fine-tuning of the MIT magnitude and T_{MIT} is possible by controlling the HiPIMS discharge parameters i.e. average power and f_R, which in turn determines the stoichiometry (i.e. oxygen interstitials or vanadium vacancies) and the strain in the films.

We compare our results to the structural and electrical properties of thin film structures deposited by HiPIMS to those deposited using dcMS approach (Figure S6). An evident edge of using HiPIMS, compared to that of dcMS at the similar average power, is the reduction in O_2 flow rate (i.e. extended operation window as low as ~ 0.5 sccm) while offering a finer control over the tunability and magnitude of the MIT via the HiPIMS discharge parameters, without sacrificing the films structural quality.

5 Acknowledgements

This work was supported by funding from the Icelandic Research Fund Grant No. 207111-051 and the University of Iceland Research fund.

Corresponding authors
Unnar Bjarni Arnalds (uarnalds@hi.is)
Muhammad Taha Sultan (muhammad@hi.is)

Conflict of Interest

There is no conflict of interest to disclose.

References

[1] J. Brockman, M. G. Samant, K. P. Roche, and S. S.P. Parkin. Substrate-induced disorder in V_2O_3 thin films grown on annealed c-plane sapphire substrates. Applied Physics Letters, 101(5):051606, 2012.

[2] B. Qi, H. P. Gunnlaugsson, S. Ólafsson, H. P. Gislason, E. B. Thorsteinsson, U. B. Arnalds, R. Mantovan, I. Unzueta l, D. V. Zyabkin, K. Bharuth Ram, K. Johnston, P. B. Krastev, T. E. Mølholt, H. Masenda, A. Tarazaga Martín-Luengo, D. Naidoo, and J. Schell. Metal-insulator transition in crystalline V_2O_3 thin films probed at atomic-scale using emission Mössbauer spectroscopy. Thin Solid Films, 714:138389, nov 2020.

[3] L. Dillemans, R. R. Lieten, M. Menghini, T. Smets, J. W. Seo, and J. P. Locquet. Correlation between strain and the metal-insulator transition in epitaxial V_2O_3 thin films grown by Molecular Beam Epitaxy. In Thin Solid Films, volume 520, pages 4730–4733. Elsevier, may 2012.

[4] Joe Sakai, Maxime Bavencoffe, Beatrice Negulescu, Patrice Limelette, Jérôme Wolfman, Akinori Tateyama, and Hiroshi Funakubo. Strain-induced resistance change in V_2O_3 films on piezoelectric ceramic disks. Journal of Applied Physics, 125(11):115102, mar 2019.

[5] Einar B. Thorsteinsson, Seyedmohammad Shayestehaminzadeh, and Unnar B. Arnalds. Tuning metal-insulator transitions in epitaxial V_2O_3 thin films. Applied Physics Letters, 112(16):161902, apr 2018.

[6] Joe Sakai, Patrice Limelette, and Hiroshi Funakubo. Transport properties and c/a ratio of V_2O_3 thin films grown on C- and R-plane sapphire substrates by pulsed laser deposition. Applied Physics Letters, 107(24):241901, dec 2015.

[7] J. Brockman, N. P. Aetukuri, T. Topuria, M. G. Samant, K. P. Roche, and S. S.P. Parkin. Increased metal-insulator transition temperatures in epitaxial thin films of V_2O_3 prepared in reduced oxygen environments. Applied Physics Letters, 98(15):152105, apr 2011.

[8] P. Homm, L. Dillemans, M. Menghini, B. Van Bilzen, P. Bakalov, C. Y. Su, R. Lieten, M. Houssa, D. Nasr Esfahani, L. Covaci, F. M. Peeters, J. W. Seo, and J. P. Locquet. Collapse of the low temperature insulating state in Cr-doped V_2O_3 thin films. Applied Physics Letters, 107(11):111904, sep 2015.

[9] M. Yethiraj, S. A. Werner, W. B. Yelon, and J. M. Honig. Phase transitions in pure and Cr-doped V_2O_3. Physica B+C, 136(1-3):458–460, jan 1986.

[10] Einar B. Thorsteinsson, Seyedmohammad Shayestehaminzadeh, Arni S. Ingason, Fridrik Magnus, and Unnar B. Arnalds. Controlling metal–insulator transitions in reactively sputtered vanadium sesquioxide thin films through structure and stoichiometry. Scientific Reports, 11(1):1–10, dec 2021.

[11] B. S. Allimi, M. Aindow, and S. P. Alpay. Thickness dependence of electronic phase transitions in epitaxial V_2O_3 films on (0001) $LiTaO_3$. Applied Physics Letters, 93(11):112109, sep 2008.

[12] H. Schuler, S. Klimm, G. Weissmann, C. Renner, and S. Horn. Influence of strain on the electronic properties of epitaxial V_2O_3 thin films. Thin Solid Films, 299(1-2):119–124, may 1997.

[13] Qiang Luo, Qinlin Guo, and E. G. Wang. Thickness-dependent metal-insulator transition in V_2O_3 ultrathin films. Applied Physics Letters, 84(13):2337–2339, mar 2004.

[14] Armando Rúa, Karla Echeverría, Brian Ayala, Gabriel A. Goenaga, Sergiy Lysenko, and Félix E. Fernández. Toward reproducible metal-insulator transition characteristics in V_2O_3 thin films sputter-deposited on glass. Journal of Applied Physics, 124(20):205301, nov 2018.

[15] I. Valmianski, Juan Gabriel Ramirez, C. Urban, X. Batlle, and Ivan K. Schuller. Deviation from bulk in the pressure-temperature phase diagram of V_2O_3 thin films. Physical Review B, 95(15):155132, apr 2017.

[16] F. Borghi, A. Podestà, M. Di Vece, C. Piazzoni, and P. Milani. Cluster-assembled materials: From fabrication to function. In Encyclopedia of Interfacial Chemistry: Surface Science and Electrochemistry, pages 417–427. Elsevier, jan 2018.

[17] Ioan Valentin Tudose, Florin Comanescu, Petronela Pascariu, Stefan Bucur, Laurentiu Rusen, Felicia Iacomi, Emmanuel Koudoumas, and Mirela Petruta Suchea. Chemical and physical methods for multifunctional nanostructured interface fabrication. In Functional Nanostructured Interfaces for Environmental and Biomedical Applications, pages 15–26. Elsevier, may 2019.

[18] André Anders. Discharge physics of high power impulse magnetron sputtering. Surface and Coatings Technology, 205(SUPPL. 2):S1–S9, jul 2011.

[19] J. T. Gudmundsson, N. Brenning, D. Lundin, and U. Helmersson. High power impulse magnetron sputtering discharge. Journal of Vacuum Science & Technology A: Vacuum, Surfaces, and Films, 30(3):030801, may 2012.

[20] Jon Tomas Gudmundsson and Daniel Lundin. Introduction to magnetron sputtering. In High Power Impulse Magnetron Sputtering: Fundamentals, Technologies, Challenges and Applications, pages 1–48. Elsevier, jan 2019.

[21] J. T. Gudmundsson, D. Lundin, N. Brenning, M. A. Raadu, Chunqing Huo, and T. M. Minea. An ionization region model of the reactive Ar/O_2 high power impulse magnetron sputtering discharge. Plasma Sources Science and Technology, 25(6):065004, oct 2016.

[22] B. Agnarsson, F. Magnus, T.K. Tryggvason, A.S. Ingason, K. Leosson, S. Olafsson, and J.T. Gudmundsson. Rutile TiO_2 thin films grown by reactive high power impulse magnetron sputtering. Thin Solid Films, 545:445–450, oct 2013.

[23] M. T. Sultan, J. T. Gudmundsson, A. Manolescu, V. S. Teodorescu, M. L. Ciurea, and H. G. Svavarsson. Obtaining SiGe nanocrystallites between crystalline TiO_2 layers by HiPIMS without annealing. Applied Surface Science, 511:145552, may 2020.

[24] J. T. Gudmundsson. Physics and technology of magnetron sputtering discharges, nov 2020.

[25] D. Lundin, J. T. Gudmundsson, N. Brenning, M. A. Raadu, and T. M. Minea. A study of the oxygen dynamics in a reactive Ar/O2 high power impulse magnetron sputtering discharge using an ionization region model. Journal of Applied Physics, 121(17), may 2017.

[26] Tomáš Kubart, Jon Tomas Gudmundsson, and Daniel Lundin. Reactive high power impulse magnetron sputtering. In High Power Impulse Magnetron Sputtering: Fundamentals, Technologies, Challenges and Applications, pages 223–263. Elsevier, jan 2019.

[27] U. B. Arnalds, J. S. Agustsson, A. S. Ingason, A. K. Eriksson, K. B. Gylfason, J. T. Gudmundsson, and S. Olafsson. A magnetron sputtering system for the preparation of patterned thin films and in situ thin film electrical resistance measurements. Review of Scientific Instruments, 78:103901, 2007.

[28] Daniel Lundin and Kostas Sarakinos. An introduction to thin film processing using high-power impulse magnetron sputtering, mar 2012.

[29] F. Magnus, O. B. Sveinsson, S. Olafsson, and J. T. Gudmundsson. Current-voltage-time characteristics of the reactive Ar/N_2 high power impulse magnetron sputtering discharge. Journal of Applied Physics, 110(8):083306, oct 2011.

[30] H. Hajihoseini, Einar B. Thorsteinsson, Vilborg V. Sigurjonsdottir, and Unnar B. Arnalds. Strained interface layer contributions to the structural and electronic properties of epitaxial V_2O_3 films. Appl. Phys. letters (in press), 2021.

[31] E. Wallin and U. Helmersson. Hysteresis-free reactive high power impulse magnetron sputtering, jul 2008.

[32] Darshana Wickramaratne, Noam Bernstein, and I. I. Mazin. Impact of biaxial and uniaxial strain on V_2O_3. Physical Review B, 100(20):205204, nov 2019.

[33] Asim Aijaz, Yu Xia Ji, José Montero, Gunnar A. Niklasson, Claes G. Granqvist, and Tomáš Kubart. Low-temperature synthesis of thermochromic vanadium dioxide thin films by reactive high power impulse magnetron sputtering. Solar Energy Materials and Solar Cells, 149:137–144, may 2016.

[34] T. Kubart, M. Aiempanakit, J. Andersson, T. Nyberg, S. Berg, and U. Helmersson. Studies of hysteresis effect in reactive HiPIMS deposition of oxides. Surface and Coatings Technology, 205(SUPPL. 2):S303–S306, jul 2011.

[35] Yan Yuan, Lizhen Yang, Zhongwei Liu, and Qiang Chen. High power impulse magnetron sputtering and its applications. Plasma Science and Technology, 20(6):065501, jun 2018.

[36] S. Shayestehaminzadeh. Growth of Functional Thin Films by HiPIMS : Fundamentals, Challenges, Applications. PhD thesis, University of Iceland, 2015.

[37] M. Fekete, K. Bernátová, P. Klein, J. Hnilica, and P. Vašina. Influence of sputtered species ionisation on the hysteresis behaviour of reactive

HiPIMS with oxygen admixture. Plasma Sources Science and Technology, 29(2):025027, feb 2020.

[38] Daniel Lundin, Ante Hecimovic, Tiberiu Minea, André Anders, Nils Brenning, and Jon Tomas Gudmundsson. Physics of high power impulse magnetron sputtering discharges. In High Power Impulse Magnetron Sputtering: Fundamentals, Technologies, Challenges and Applications, pages 265–332. Elsevier, jan 2019.

[39] Shuliang Dou, Weiyan Zhang, Feifei Ren, Jinxin Gu, Hang Wei, Xi Chen, Gaoping Xu, Xiangqiao Yan, Yaohui Zhan, Jiupeng Zhao, and Yao Li. The infrared optical performance of VO_2 film prepared by HiPIMS. Materials Chemistry and Physics, 259:124042, feb 2021.

[40] Veena Mounasamy, Ganesh Kumar Mani, Dhivya Ponnusamy, Kazuyoshi Tsuchiya, Arun K. Prasad, and Sridharan Madanagurusamy. Template-free synthesis of vanadium sesquioxide (V_2O_3) nanosheets and their room-temperature sensing performance. Journal of Materials Chemistry A, 6(15):6402–6413, apr 2018.

[41] Saeed Ghasemi, Pourya Seyfi, Alireza Farhadizadeh, and Hamid Ghomi. The experimental approach into the influence of external inductance on the discharge characteristic of HiPIMS. Journal of Theoretical and Applied Physics, 13(4):289–297, dec 2019.

[42] Montri Aiempanakit, Asim Aijaz, Daniel Lundin, Ulf Helmersson, and Tomáš Kubart. Understanding the discharge current behavior in reactive high power impulse magnetron sputtering of oxides. In Journal of Applied Physics, volume 113, page 133302. American Institute of PhysicsAIP, apr 2013.

[43] Leander Dillemans, Tuan Tran, Md Nurul Kabir Bhuiyan, Tomas Smets, Mariela Menghini, Ruben Lieten, Jin Won Seo, and Jean Pierre Locquet. Epitaxial growth of V_2O_3 on Al_2O_3 by reactive MBE. In Materials Research Society Symposium Proceedings, volume 1292, pages 61–66. Cambridge University Press, 2011.

[44] Darshana Wickramaratne, Noam Bernstein, and I. I. Mazin. Role of defects in the metal-insulator transition in VO_2 and V_2O_3. Physical Review B, 99(21):214103, jun 2019.

[45] S. Autier-Laurent, B. Mercey, D. Chippaux, P. Limelette, and Ch Simon. Strain-induced pressure effect in pulsed laser deposited thin films of the strongly correlated oxide V_2O_3. Physical Review B - Condensed Matter and Materials Physics, 74(19):195109, nov 2006.

[46] C. Grygiel, Ch Simon, B. Mercey, W. Prellier, R. Fŕsard, and P. Limelette. Thickness dependence of the electronic properties in V_2O_3 thin films. Applied Physics Letters, 91(26):262103, dec 2007.

[47] Jun Wang, Guus Rijnders, and Gertjan Koster. Complex plume stoichiometry during pulsed laser deposition of $SrVO_3$ at low oxygen pressures. Applied Physics Letters, 113(22):223103, nov 2018.

[48] L. J. Eckert and R. C. Bradt. Thermal expansion of corundum structure Ti_2O_3 and V_2O_3. Journal of Applied Physics, 44(3470), 1973.

Paper VI

Structural morphology and electrical transitions of V_2O_3 thin films grown on SiO_2/Si by high power impulse magnetron sputtering

M.T. Sultan, K. Ignatova, E.B. Thorsteinsson, U.B. Arnalds

Thin Solid Films (2022)

Thin Solid Films 742 (2022) 139048

Contents lists available at ScienceDirect

Thin Solid Films

journal homepage: www.elsevier.com/locate/tsf

Structural morphology and electrical transitions of V_2O_3 thin films grown on SiO_2/Si by high power impulse magnetron sputtering

M.T. Sultan *, K. Ignatova, E.B. Thorsteinsson, U.B. Arnalds

Science Institute, University of Iceland, Dunhaga 3, Reykjavik 107, Iceland

ARTICLE INFO

Keywords:
Vanadium sesquioxide
High power impulse magnetron sputtering
Metal-insulator transition
X-Ray diffraction
Atomic force microscopy,

ABSTRACT

The study presents the synthesis of V_2O_3 films on thermally oxidized Si(001) substrates by reactive high power impulse magnetron sputtering. The effect of film thickness and oxygen variation were explored at fixed discharge parameters. X-ray diffraction (XRD), grazing incidence-XRD and pole scans reveal the films to be textured. The results show that for a critical thickness up to ~ 5 nm, highly strained V_2O_3 films are obtained, and with increased thickness the film exhibit increased surface roughness and the formation of a granular structure arising from strain relaxation in the films. With increasing thickness the films exhibit a variation in the lattice parameters affecting their electrical characteristic i.e. metal-insulator transition (MIT). Subject to variation in O_2 flow setting we observe the MIT magnitude and transition temperatures to be strongly dependent on the film stoichiometry and lattice parameters which can be fine tuned by mapping the O_2 flow settings. The most dominant transition out of the studied structures was observed for those having film thickness of ~ 36 nm with an O_2 flow setting ranging from 0.8 to 0.95 sccm and displaying a low c/a lattice ratio. The MIT observed for these structures displayed a change in resistance of up to ~ 4 decades with a total change in resistance of ~ 7 decades.

1. Introduction

Vanadium sesquioxide (V_2O_3) is a recognized material system exhibiting Mott-Hubbard physics [1], whose electronic properties have been actively studied both theoretically [2] and experimentally [3–5]. V_2O_3 is a transition metal oxide which shows a first-order structural phase transition from a high temperature rhombohedral paramagnetic metal to low temperature monoclinic anti-ferromagnetic insulating state [3,6]. The interest in V_2O_3 stems from the fact that coupled to the structural transition it undergoes an abrupt change in resistance i.e. metal to insulator transition (MIT)[7], which for bulk V_2O_3 can show a change in resistance of up to 7 order of magnitude at a transition temperature (T_{MIT}) of ~ 155K. These properties open exciting application possibilities for V_2O_3 films for instance in bolometers, sensors and energy storage [8–10].

As the MIT observed in V_2O_3 is linked to the structural transition, several studies have been performed on the effect of for instance, doping (with for instance Ti, Cr and W [11,12]), oxygen vacancies and/or vanadium interstitials [2,7,12], film thickness [13,14], the choice of substrate [1] and the resulting interface[15] along with the fabrication method [4]. All these methods have been shown to influence the electrical properties of the films. Various synthesis methods have been employed for metastable stoichiometric V_2O_3 thin film growth including electron-beam evaporation [16], thermal evaporation [14], sol-gel [17], reactive magnetron sputtering [7,18], pulsed laser deposition [19] and molecular beam epitaxy [6,20]. Of these, magnetron sputtering (MS) is the most versatile method as it provides high levels of automation and a good compatibility with industrial processes [21] while providing finer control of discharge parameters. In this study a relatively recent variation of MS that is high power impulse magnetron sputtering (HiPIMS) is utilized which has been shown to give improved control over the properties of grown films, with increased ionization fraction of sputtered species and large amount of energetic ions [22]. A more detailed exploration of V_2O_3 films grown on Al_2O_3 substrates by HiPIMS at 600 °C for various discharge parameters and O_2 flow settings using HiPIMS can be found elsewhere [5].

The majority of the work in the literature has focused on growth of V_2O_3 on sapphire as it has a similar rhombohedral crystal symmetry

Abbreviations: V_2O_3, Vanadium sesquioxide; HiPIMS, High Power impulse magnetron sputtering; MIT, Metal insulator transition; XRD, X-ray diffraction; AFM, Atomic force microscopy.

* Corresponding author.
E-mail address: muhammad@hi.is (M.T. Sultan).

https://doi.org/10.1016/j.tsf.2021.139048
Received 30 April 2021; Received in revised form 7 December 2021; Accepted 8 December 2021
Available online 12 December 2021

with a ~ 4.1% lower in-plane lattice constant [1]. However, in contrast to VO_2 [23–26] little work has been reported for V_2O_3 [18] thin films grown on amorphous thermally grown SiO_2 which is known as the highest quality oxide [25], can remain amorphous up to high temperatures, and is compatible with already existing Si-based technology [27]. The interest in using thick buffer oxide stems from the fact that it can provide a quality interface between the substrate and the film due to low density of states and defects present at the Si/SiO_2 boundary, as compared to ill-defined SiO_x native oxide [28]. The fast growing need of switching speed of many proposed vanadium oxide devices such as resistive and thermal switches, bolometers resistive memory elements, neuromorphic computing and many others [29–31], and the ability to grow thin films of materials while maintaining the pronounced MIT is of prime importance. Thus films grown on Si or SiO_2 substrates are important for the incorporation of these devices at large scale with already existing silicon technology while reducing the cost of fabrication [23]. Several factors have been shown to affect the growth of vanadium oxides on SiO_2/Si which need to be taken into consideration for their utilization. Foremost of these are the lattice mismatch, the large difference in thermal expansion coefficient and the difficulty in obtaining highly crystalline vanadium oxide films on amorphous SiO_2 [23].

In this study we investigate the fabrication of V_2O_3 films having varying thickness and O_2 flow setting during deposition on technology relevant silicon oxide surfaces by reactive high power impulse magnetron sputtering. The films are deposited at a growth temperature of 700 °C, higher than what has been utilized for growth of V_2O_3 on Al_2O_3 in our previous work. The results reveal that films grown within an O_2 flow setting window of 0.8 to 0.95 sccm, having a thickness of ~ 36 nm gives a T_{MIT} close to that of bulk with pronounced magnitude of transition of approximately 4 orders of magnitude and a total change in resistance of ~ 7-orders of magnitude.

2. Experimental

2.1. Material and method

The V_2O_3 thin films were fabricated by reactive HiPIMS from a vanadium target using a custom-built sputtering chamber [32] on 10 × 10 mm^2 Si (001) substrate with a ~ 100 nm thermally grown oxide. Prior to loading into the chamber, the substrates were cleaned in an ultrasonic bath using acetone, methanol and isopropanol followed by rinsing with de-ionized-water and blow-drying with N_2.

For deposition, the HiPIMS power was supplied via a SPIK1000A pulse unit by Melec GmbH, operating in a unipolar negative mode at a constant pulse voltage, where the unit was charged by a direct current power supply (ADL GS30). The discharge current and voltage were monitored using a combined current transformer and a voltage divider unit (Melec GmbH) and the data was recorded with a digital storage oscilloscope (Agilent 54624A).The depositions were performed with a constant average power of 200 W over the target area using a square voltage waveform at a pulse length of 100 μs and repetition frequency of 150 Hz, while varying the:

- O_2 flow setting from 0.5 − 1.3 sccm at a fixed thickness of 36 nm (giving a growth rate of ~ 2.3 nm/min)
- Thickness ($d_{V_2O_3}$ between 2.5 − 100 nm) for a fixed O_2 flow setting of 0.9 sccm.

Prior to deposition the samples were pre-baked to 700 °C, and the chamber was held at a base pressure of 10^{-6} Pa. During sputtering, Argon of 5N purity was utilized as the working gas and the substrate temperature was held at 700 °C. The V target was pre-sputtered for a few minutes prior to the introduction of O_2 gas of 5N purity into the chamber. Mass flow controllers were utilized to adjust the flow rates of Ar ($q_{Ar} = 40$ sccm) and O_2 (q_{O_2} in range of 0.35 to 1.5 sccm), and a throttle valve on the pumping side was adjusted to stabilize the growth pressure of 0.7 Pa during deposition. After deposition the samples were allowed to cool down in-situ.

2.2. Characterization

The structural properties of the films were investigated by X-ray diffraction (XRD) using a Philips X'pert diffractometer (CuKα, 0.15406 nm). For X-ray diffraction analysis, a 2 × Ge (220) asymmetrical hybrid monochromator utilizing line focus, a divergence slit (1/4°), and a parallel plate collimator (0.27°) was used. The measurement run was made with a step size of 0.005° and time per step of 1.2 s.The surface morphology of the films was investigated by atomic force microscopy (AFM) (Park System PSIA XE-100) in contact mode. The thickness of the films was determined using X-ray reflectometery (XRR) analysis and the measured data was simulated using the X'Pert reflectivity software 1.3a. For electrical characterization co-planar contacts of Cr(~ 5 nm)/Au(~ 100 nm) were deposited using electron beam evaporation onto the films (see Fig. 1). Electrical characterization were performed in a custom built setup comprising a cryogenic pump (Leybold-Heraeus RG 210), a cryostat connected to a source meter and an electrometer (Keithley 2400 and 617 series) along with a temperature controller.

3. Results and discussion

3.1. Discharge characteristics

The V_2O_3 films were deposited via reactive HiPIMS on Si substrates with thermally grown SiO_2 (~100 nm). The discharge parameters, i.e. pulse length of 100 μs and repetition frequency f_R of 150 Hz, were adjusted giving an average power of 202 ± 3 W and duty cycle of 0.015. The recorded pulse waveforms for varying O_2 flow settings are presented in Fig. 2a, and the obtained peak power density in Fig. 2b. The cathode voltage varied from 500 to 556 V, with increased O_2 flow setting, in order to keep the average power constant. A detailed discussion of the HiPIMS discharge parameters i.e. f_R, power and varying O_2 flow setting for V_2O_3 thin films grown on Al_2O_3 substrates can be found elsewhere [5].

Increasing the O_2 flow setting from 0.5 to 1.0 sccm the discharge was maintained in metallic mode. Increasing the O_2 flow further, from 1.1 - 1.15 sccm, a transition regime can be seen (highlighted as green), eventually leading to the discharge transitioning to a poisoned mode (highlighted as red) for increased O_2 flow setting of ≥ 1.2 sccm. Such a behaviour is also observed in Fig. 4 and will be discussed further. The increase in peak power density, or reduction in cathode current, is in good agreement with previous studies [22,33]. That is, for metallic mode the discharge current reaches a peak value in the initial stages of the pulse which then decays to lower values until the end of the pulse. The obtained peak current density for the case of metallic mode was approximately 1.0 ± 0.1 A/cm^2. For the transition regime i.e. O_2 flow setting of up to 1.15, the current increases and eventually saturates with increase in the cathode current, giving a peak current density of ~ 1.2 A/cm^2. A further an increase in O_2 flow, up to approximately 1.2 sccm,

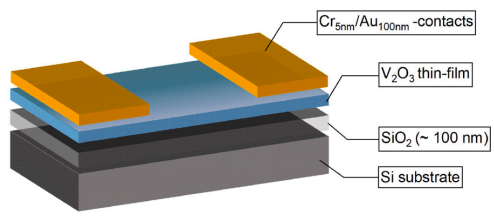

Fig. 1. Schematic illustration of a deposited structure of the $V_2O_3/SiO_2/Si$ films with co-planar Au/Cr contacts, deposited by electron-beam evaporation.

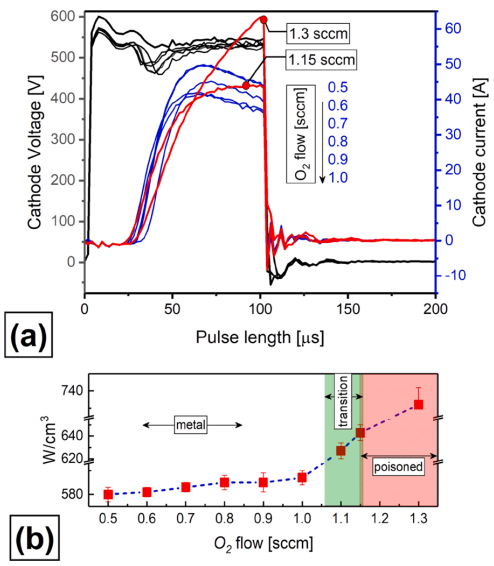

Fig. 2. (a) Discharge cathode current and voltage waveforms during HiPIMS deposition for V_2O_3 films for varying O_2 flow settings with a fixed pulse length, f_R and average power of 200 W. (b) Discharge peak power density, recorded for varying O_2 flow settings.

results in a continuous increase in the current until the end of the pulse (see Fig. 2a), revealing the poisoned nature of the discharge [33], with a peak current density of $\geq$ 1.5 A/cm^2.

3.2. Structural characterization

XRR scans were performed on the films in order to determine their thickness, density and surface roughness. A typical XRR scan and fit is shown in Fig. 3. Fig. 4a shows the X-ray diffraction scans for V_2O_3 thin films ($\sim$ 36 nm thick) deposited at varying O_2 flow settings. Films deposited with an O_2 flow setting up to 1.15 sccm showed a peak position (Fig. 4b) in close proximity to that of the (006) bulk V_2O_3 value i.e. 38.514° (JCPDS card no. 00-034-0187) [34]. Grazing incidence XRD scans (GiXRD) performed on the films (see Fig. 5a), showed standard

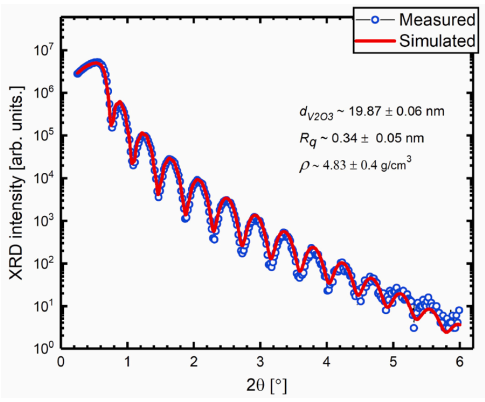

Fig. 3. XRR scan over structure having ~20 nm V_2O_3 on SiO_2/Si substrate at O_2 flow setting of 0.9 sccm. The values for thickness (d_{V2O3}), roughness(Rq) and density(ρ) were extrated by fitting the measured data using the X'Pert reflectivity software.

tabulated peaks positioned at 32.9°, 38.514°, 53.9 ° and 71.5° depicting a fiber textured structured, with (0 0 6) orientation being out of plane. The textured nature of the films was further confirmed through pole scans performed around the (1 0 4) and (1 1 6) orientations which revealed ring patterns at the expected χ angles of 39.2° and 43.3° with respect to the (0 0 6) crystallographic orientation. The pole scans are shown in Fig. 6.

Since the lattice constant of V_2O_3 is larger than that of SiO_2, one could expect a compressive out-of-plane strain in the film. Additionally, as the thermal expansion coefficient of V_2O_3 (3.2×10^{-5}/K [35]) is larger than that of SiO_2 and Si [36], the film can further experience an in-plane tensile strain. The possible formation of silicates i.e. (V_xSi_yO) at the interface between the film and substrate contributing to strain, cannot be neglected and has been discussed regarding the deposition of VO_2 films[15,37]. The oxygen stoichiometry of the films, furthermore, plays a vital role in altering the strain nature of films. Such an effect of stoichiometry over strain can be perceived in light of the study by [4] and further by extracting the c and a lattice parameters of films from the (0 0 6) and (1 1 6) planes, presented in Fig. 4a and 5 a. The derived lattice parameters and c/a ratios are plotted in Fig. 7a.

A clear trend of the peak position towards bulk values are observed with increase in O_2 ranging from 0.5 to 0.8 sccm. This shift indicates the development of out-of-plane compressive strain as the oxygen content is reduced (see Fig. 4) [7,12]. However, with further increase in O_2 from 0.9 up to 1.0 sccm, the peak position is in close proximity to that of bulk values indicative of a good stoichiometry obtained in film and relaxed lattice parameters with values closer to that of bulk. Any further increase in the O_2 (up to 1.15 sccm) flow setting results in the peak shifting at higher angles indicative of the formation of compressive strain. Such a transition having out-of-plane compressive strain can be discussed considering the reactive HiPIMS discharge mode, which was found to be in the transition regime (see Fig. 2), for which the XRD peak position of films shifted to higher angles. Such a shift in peak position and an increase in the V/O ratio can be argued on the well-studied fact, that a reactive HiPIMS discharge operating in transition mode can result in good stoichiometric compound films with a higher deposition rate. Additionally, the ionized fraction of sputtered metal at the end of the pulse was determined to be higher in transition mode as compared to that in metallic mode of the discharge. With an increase in O_2 flow setting up to 1.3 sccm, the XRD peak shifts to higher angles corresponding to VO_2 peak (0 0 2), according to JCPD card no. 00-033-1441. At this O_2 flow setting the discharge was observed to be operating in poisoned mode (Fig. 2), resulting in a reduction of the V/O ratio significantly i.e. the possibility of sputtering compound is highly likely (i.e. instead of sputtering pure vanadium the compound layer formed on the target is being sputtered [22,33]) thereby suppressing the formation of V_2O_3.

GiXRD scans performed for films of varying thickness are shown in Fig. 5b. The results reveal that for thinner films up to 20 nm in thickness the films showed the presence of broad humps, which with increasing thickness from 36 to 100 nm showed the presence of peaks at the V_2O_3 standard tabulated peak positions (32.9°, 38.514°, 53.9° and 71.5°, JCPDS card no. 00-034-0187). The extracted lattice parameters, determined from Gaussian fitting of the XRD peaks, are plotted in Fig. 7b. For the thinner films, the film can be thought of as under compressive strain with a large c/a ratio due to the formation of intrinsic stress as a consequence of interface stress, surface reconstruction and due to difference in thermal expansion coefficient between the film and substrate [38–40]. With increasing thickness (in our case up to ~20 nm) the films relax with a reduction in the c/a ratio. However, the c/a ratio increases to higher values for films of thickness $\geq$ 60 nm with the development of compressive strain in the films. Such a transition in the lattice parameters is discussed further later in light of the AFM analysis revealing a Volmer-Weber growth mode for films above a critical thickness. From the above analysis it can be understood that the competing effects from

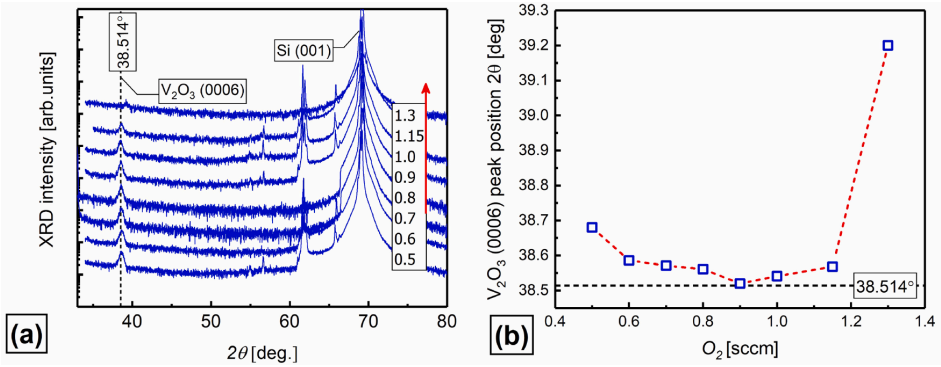

Fig. 4. (a)X-ray diffraction scans recorded for V_2O_3 films grown on Si/SiO_2 for varying O_2 flow rates (ranging from 0.5 - 1.3 sccm) and fixed working gas i.e. Ar flow rate of 40 sccm. The growth pressure was 0.7 Pa. (b) V_2O_3 (0006) angular peak position as a function of O_2 flow rate. The dotted and solid line in (a, b) corresponds to the V_2O_3 (0006) bulk value. The peaks observed at higher angles correspond to the crystalline silicon substrates.

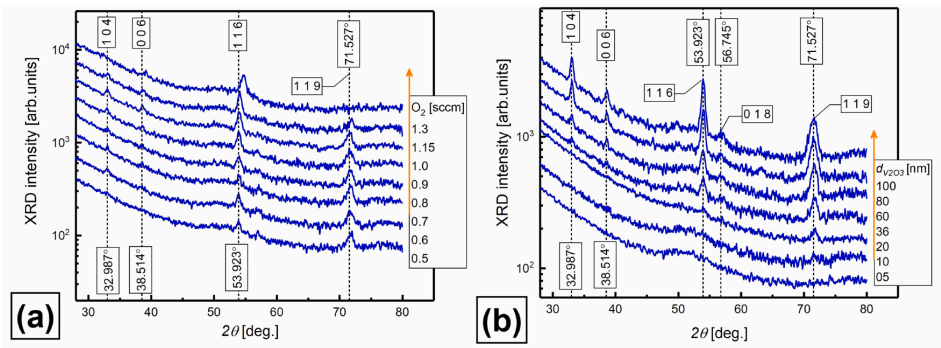

Fig. 5. GiXRD scans for films (a)at varying O_2 flow setting for constant thickness of approximately 36 nm and (b) having varying thickness at fixed O_2 flow of ~ 0.9 sccm. The vertical dotted line represents the standard bulk V_2O_3 values according to JCPD card no.: 00-034-0187.

the substrate, oxygen stoichiometry, film thickness and crystalline quality of film, will determine the nature of strain in the films. This in turn affects the magnitude and the transition temperature (T_{MIT}) of the films and will be discussed further in the following sections.

3.3. AFM Analysis

Fig. 8 shows representative topographic images (obtained by AFM in contact mode) of structures with varying V_2O_3 thickness. The images were recorded over a scan area of $2 \times 2\ \mu m^2$. The scans were repeated over different reference areas in order to validate the observed features. The root mean square roughness values R_q were determined over the entire surface region and the size of nanoislands (NI) were measured via line scans (see Fig. 9).

For thin films up to thickness of ~ 5 nm the surface showed no obvious presence of nanostructures implying the two-dimensional growth of a strained film. With an increase in thickness to between 20 and 100 nm, the AFM images showed the presence of nanoislands, the size of which increases with increasing thickness in accordance with Ostwald ripening. The size of nanoislands (NI) i.e. width and height were measured via line scans and are plotted in Figure9(b, c). The AFM images obtained here were utilized in Section 3.4 to explain the variation in the lattice parameters and its effect on the MIT behaviour. However, it was observed that the nanoislands with thickness up to 36 nm formed metastable spherical nanoislands which transform to elongated ones, with increased thickness. Such a transformation can be explained by the fact that the film growth is not an equilibrium process and the kinetics and thermodynamic strains imposed by the deposition methods, thickness and substrate of choice, can lead to the emergence of metastable nanostructures as a consequence of strain relaxation and surface reconstruction [16,41,42]. For thin film deposition, it was observed that the total deposited coverage and thermal activation are of vital importance in obtaining nanogeometries having varying size and shapes [42]. Moreover, the choice of substrate, its orientation and the surface symmetry play an important role in determining the geometric shape of the nanostructures, as a result of constraints imposed by the substrate anisotropy and lattice mismatch. Further, it has been documented for vanadium oxide that the film thickness can influence the film crystallographic orientation [43]. Thus, increasing the film thickness the islands are oriented along the preferred 104, 116 and 119 orientation as can be visualized by GiXRD analysis in Fig. 5b. Additionally, the increase in the lateral size of the nanoislands has been attributed to grain-boundary migration resulting in an increased lateral grain size with increased film thickness [15].

3.4. Electrical characterization

Fig. 10 (a, b). shows the resistance as a function of temperature for films of varying thicknesses (2.5 -100 nm), for a fixed O_2 flow setting of 0.9 sccm. Although there is a possibility of variation in O_2 stoichiometry the effect of strain is considered dominant in such a case and can be visualized in light of the films c/a ratio extracted from the XRD scans

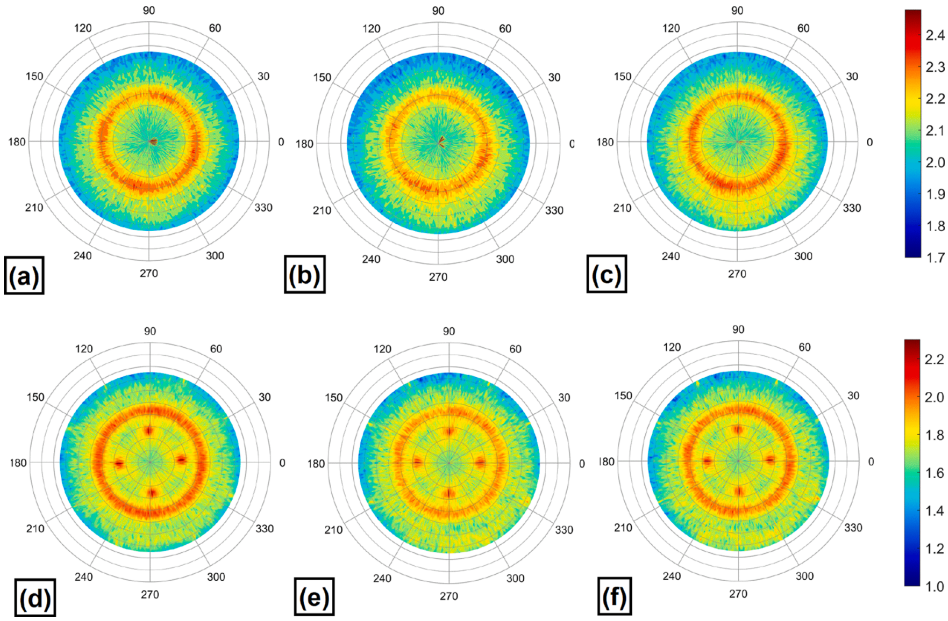

Fig. 6. Pole scans around the (a-c) 1 0 4 and (d-f) 1 1 6 peaks, for structures deposited at O_2 flow settings of 0.8, 0.9 and 0.6 sccm, respectively from left to right.

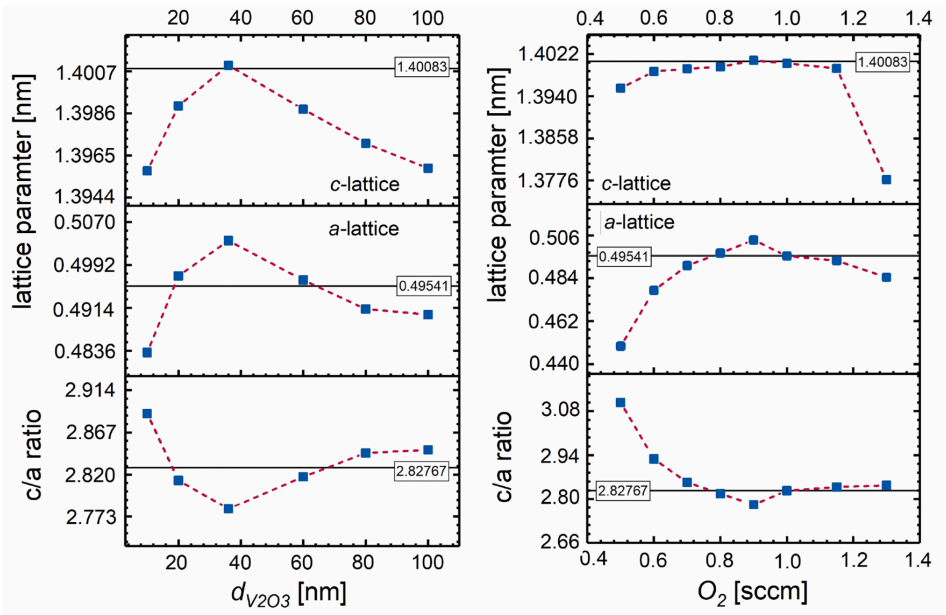

Fig. 7. Plots for lattice parameters c, a and c/a ratio extracted from (0 0 6) and (1 1 6) peaks for films (a) having varying thickness at fixed O_2 flow of ~ 0.9 sccm and (b) at varying O_2 flow setting for constant thickness of approximately 36 nm. The solid horizontal lines correspond to bulk lattice values of V_2O_3 i.e. c=1.40083 nm and a=0.49541.

(Fig. 7b). For films with varying thickness it was observed that the resistance reduces and later stabilizes as a function of increased thickness (Fig. 11a), and is in good agreement with the study by Hajihoseini *et al.* [40]. Fig. 10c shows the transition temperature T_{MIT} as a function of thickness, with T_{MIT} having a maxima at ~ 36 nm. The corresponding variation in T_{MIT} with respect to increasing thickness can be explained in light of surface-growth-mode-induced strain in films [41], which in turn affects the c/a ratio, thereby altering the MIT characteristics. During the initial stages of the film growth (up to 5 nm), the film grows two dimensionally (see AFM micrograph Fig. 8(a, b)). In this case the film is

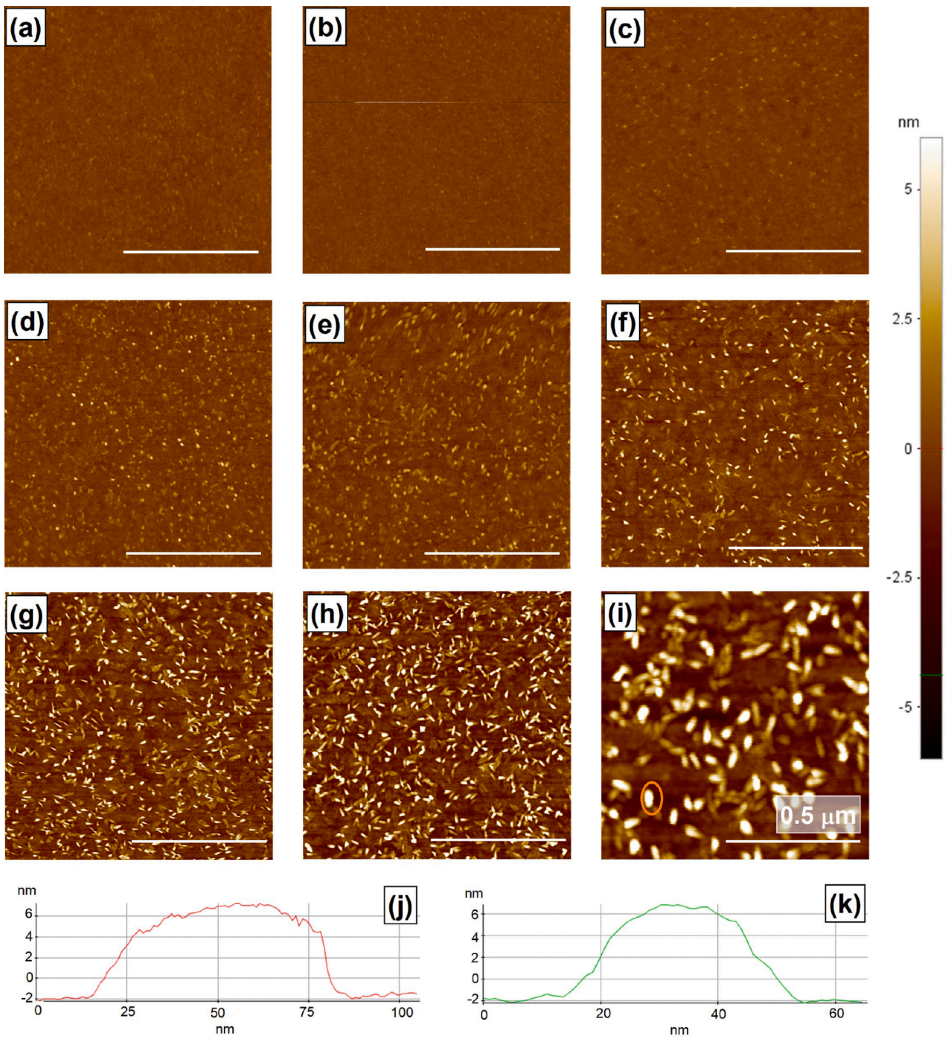

Fig. 8. $2 \times 2\ \mu m^2$ AFM images of V_2O_3 films grown by HiPIMS having varying thickness (a) 2.5 (b) 5 (c) 10 (d) 20 (e) 36 (f) 60 (g) 80 and (h) 100 nm, at constant O_2 flow setting of 0.9 sccm. (i) Shows the structure in (h) at higher magnification and resolution (image size, $1 \times 1\ \mu m^2$). (j, k) Line profile over a NI highlighted in (i). The scale bar in (a-h) is 1 µm.

under large compressive strain due to the development of intrinsic stress. Since the film is not firmly clamped to the substrate as in the case of epitaxial film grown on Al_2O_3 substrates [38], the film will deform elastically as a consequence of stress at the film- substrate interface, substrate surface i.e., SiO_2 reconstruction and the difference in thermal expansion coefficient between the film and the substrate [15,38,39]. This results in a large c/a ratio, and suppression of the metallic phase (for the 2.5 nm film) and/or broadening of the MIT hysteresis (for films with thickness $\geq$ 5 nm). The results are in good agreement with published works [11,35,40] dealing with V_2O_3 films on Al_2O_3 and in studies [44–46] for V_2O_3 films on Si/SiO_2 substrates. However, in our case later work is more relevant considering the choice of substrate. It has been detailed that thinner films are under large compressive strain exhibiting stabilization of the insulating phase and that the film relaxes as the thickness increases.

With increased film thickness, the island growth mode (i.e. Volmer-Weber growth mode [42,47]) is preferred as to reduce stress in the film. Such an evolution for thicknesses in the range $\sim$ 10 to 36 nm can be seen in Fig. 8(c, e), where clear nanoislands are observed. The formation of these nanoislands tends to relax the films i.e. increase the out-of-plane tensile strain and reduce the c/a ratio (see Fig. 7b). Furthermore, at this point the islands are isolated with sizes $\sim$ 26 to 32 nm in width and $\sim$ 2 to 5 nm in height, having no strain between them (Fig. 9).

A further increase in thickness ($\geq$ 60 nm) results in a shift of the T_{MIT} to lower temperature and can be attributed to the development of c-axis compressive strain i.e. increase in c/a ratio. In such a case, with increased deposition coverage the islands start to coalesce with increase in size for up to 100 nm thick films (see AFM micrograph in Fig. 8(h, i)). This in turn causes the a-axis lattice to expand as to balance the grain boundary free energy and the surface energy of the islands. However, according to volume conservation out-of-plane compressive strain is induced to balance the in-plane tensile strain. Thus, with increase in

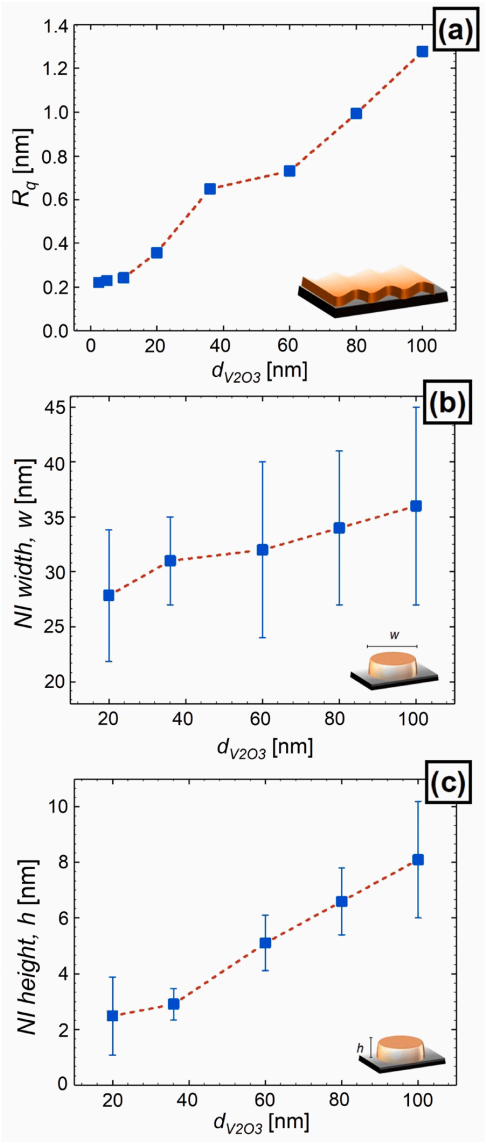

Fig. 9. (a) Root mean square roughness (R_q) obtained from AFM micrographs for structures with varying V_2O_3 thicknesses. Nanoislands (b) width and (c) height as a function of increasing V_2O_3 thickness. The representative error bars were extracted via line scans over several NI distributed randomly over the entire surface area.

thickness the compressive strain becomes dominant. Such an effect has been documented in study by Yang *et al.* [41] for VO_2 films. Moreover, in studies [14,16], it has been documented that above a thickness of ~50 nm, the relaxation or increase in tensile strain is restricted due to the formation of tension and misfit dislocations. Thus, for deposition coverage at or above 60 nm, the islands start to coalesce forming bigger nanoisland accompanied with defects and misfit dislocations, which in turn transforms the shape of nanoislands, along with an increase in unit cell volume thereby altering the c/a ratio. Additionally, for thicker films, the microstructure with localized defects differing from that at the film-substrate interface and the surface, leads to a varying strain state within the structure itself [13,37]. Moreover, the effect of grain boundaries, can also effect the absolute value of the change in resistance, the hysteresis width and the sharpness of transition [8,47–49]. That is, an increase in grain boundary area as a result of smaller grain size, will cause reduced carrier mobility, and therefore an increase in overall resistance [50]. Such a behaviour can be observed in Fig. 11a, for films with increase thickness and consequent increase in grain sizes (as discussed in Section 3.3). Various models on such reversibility of stress for Volmer-weber films have been argued in the study by Koch *et al.* [51], of which we assume the most probable is the one dealing with the stress due to surface chemical potential dependent changes in adatom population, where the compressive stress in the pre- and post-coalescence stages, and a tensile during island nucleation stage of Volmer-Weber growth have been discussed.

The data presented here demonstrate that the morphological evolution of nanostructures provides a possibility of surface induced strain engineered control of MIT characteristics of V_2O_3 films deposited on technologically relevant Si substrates for their application in nanoelectronic applications [46,52–54]. Furthermore, a potential application of these 3D-nanoislands in hybrid structures for instance Ni over V_2O_3 is of technological relevance as it can prompt significant effect of nanoisland size on the electronic as well as magnetic properties of these hybrid structures [55–57].

Fig. 10 (d, e) shows the resistance as a function of temperature for films deposited at varying O_2 flow settings having a fixed thickness of ~ 36 nm. The room temperature resistance of the films decreases as a function of O_2 flow setting, in good agreement with the study by Brockman *et al.* [12] and is plotted in Fig. 11b. Considering the metal-insulator transition, films deposited at O_2 flow settings of 0.7 to 1.15 sccm, displayed a clear abrupt MIT behaviour with varying magnitude and T_{MIT} (Fig. 10d) of which the sharpest and most dominant ones i.e. close to that of bulk are observed for O_2 flow settings ranging from 0.8 to 0.9 sccm (plotted separately in Fig. 10e). Fig. 10f is plotted with T_{MIT} as a function of varying O_2 flow settings, where the T_{MIT} values were extracted by differentiating the plots in Fig. 10(d, e) followed by Gaussian fitting of the peaks. For these films a resistance change of up to ~4 orders of magnitude were observed, with a total change in resistance of ~ 7 orders of magnitude limited by the compliance of the measurement setup. The transition in these films reveals a clear dependence on the oxygen stoichiometry and can be fine-tuned by varying the O_2 flow settings i.e. the amount of oxygen interstitials [2,7,12].

The observed shift in T_{MIT} to lower temperature from O_2 flow settings of 0.5 - 1.0 sccm can be correlated with the strain in the film and the film stoichiometry. Generally, the alteration in MIT characteristics and a shift in T_{MIT} has been associated with the oxygen non-stoichiometry of the V_2O_3 films typically formulated as V_2O_{3+x} or $V_{2-y}O_3$, and that any small variation can cause a large shift in T_{MIT}. In case of increased oxygen concentration in film the electrical characteristics can be significantly altered, and that the low temperature-insulating phase can be suppressed with the presence of excess oxygen [4,12,20]. In recent studies [2,4] it has been argued that the excess oxygen sits at interstitial sites as a part of an O Frenkel pair. This gives rise to strain in the *a*-lattice parameter while having less impact on the *c*-lattice creating a disorder in lattice structure[2]. Thereby shifting the energy balance towards the metallic phase i.e., a shift in T_{MIT} towards lower temperature as in the case of the film deposited at 1.0 sccm. For films deposited at O_2 flow settings of 0.8 -0.5 sccm, the XRD scans show a shift in peak position towards higher angle displaying an expansion in the out-of-plane direction and implying metal enrichment[4,5]. Considering the above criteria, it is logical to say that with the reduction in oxygen interstitials at low O_2 flow down to 0.8 to 0.5 sccm, a shift in T_{MIT} to higher temperature is observed, eventually resulting in the stabilization of the Mott-insulating phase at 0.5 sccm. Such a behaviour was well documented in a recent study by Ha *et al.* [39] for similar textured V_2O_3 films on SiO_2 at varying oxygen partial pressures. Their results show that with

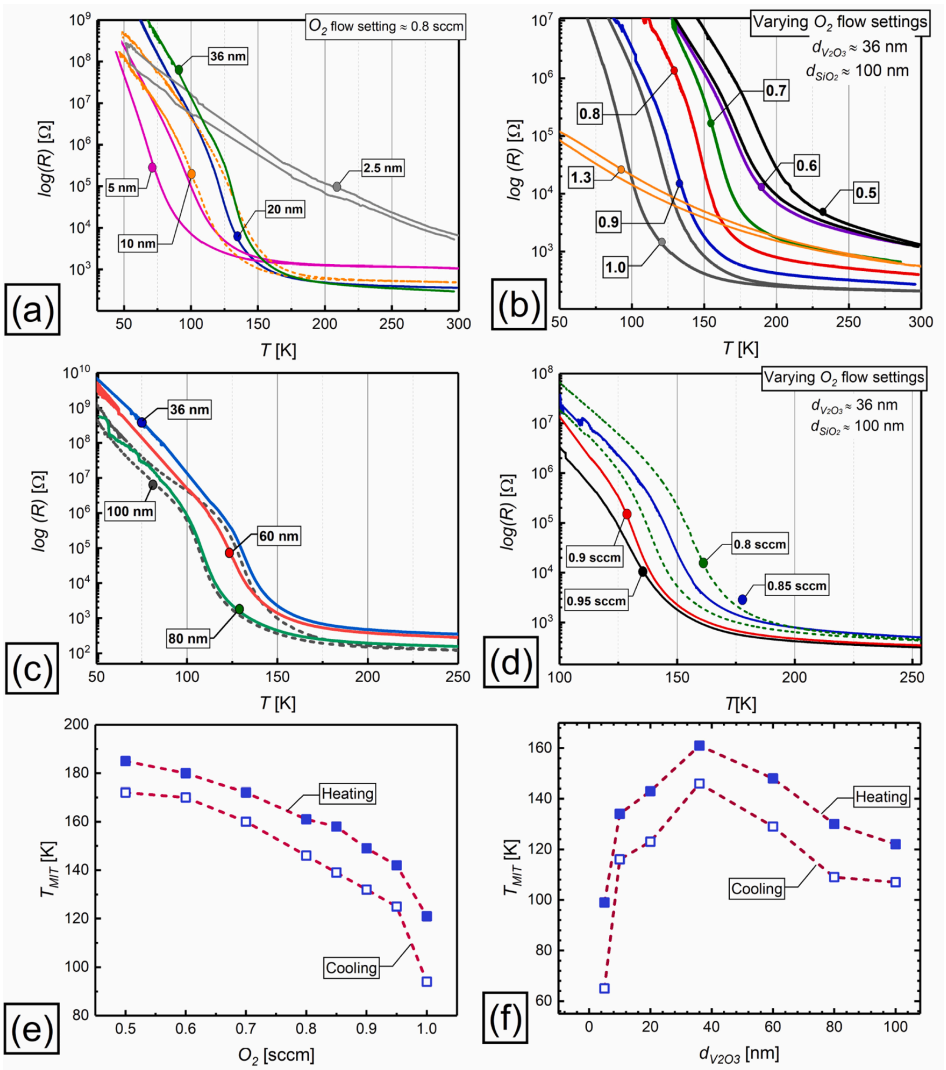

Fig. 10. Resistance as a function of temperature for V_2O_3 thin films deposited via HiPIMS for varying thickness ($d_{V_2O_3}$) under fixed oxygen condition (~ 0.9 sccm) i.e. (a) ranging from 2.5 - 36 nm, and (b) ranging from 36 - 100 nm, respectively. (c) T_{MIT} values obtained from differentiating plots in (a, b) given by function dlnR/dT. Resistance as a function of temperature for the 36 ± 1 nm V_2O_3 thin films deposited via HiPIMS under different oxygen conditions i.e. (d) for a broad range from 0.5 - 1.3 sccm, and (e) narrow range from 0.8 - 0.95 sccm, respectively.(f) T_{MIT} values obtained from differentiating plots in (d, e) given by function $dlnR/dT$.

reduced oxygen content the *a*-lattice parameter expands [39,45] and that the variation in the *a*-lattice parameter is ~4 times lager than that observed in the *c*-lattice parameter (thus complementing our results). Furthermore, transmission electron microscopy carried out on their structures have shown the presence of stacking faults distributed parallel to the film surface and that the reduced oxygen causes an imbalance in V/O ratio. Thus, increased defect density in the film causes lattice strain over the entire film area. Additionally, the observed room temperature resistivity increases with reduced oxygen along with an *a*-lattice expansion thereby suppressing the metallic phase. Moreover, since the MIT transition in V_2O_3 is linked to the structural change because of vanadium (V)-ion shift forming V-V dimers[58]. The distance between V-V bonds in the rhombohedral structure along the *c*-axis is larger than in the monoclinic insulating phase[59]. Therefore, as a consequence of oxygen vacancy the V-V bond distance reduces resulting in broadening of bandwidth and suppression of electron-electron correlation thereby suppressing the metallic phase. The above results for reducing O_2 flow settings are well aligned with studies [2,5,12] where increased number of defects i.e., oxygen vacancies would shift the energy balance resulting in an earlier onset of vanadium sesquioxide insulating phase (i.e., transition to insulating phase occur at higher temperature) along with an increase in room temperature resistance.

Even though the main steered factor at this point is O_2 flow settings the effect of strain cannot be neglected contributing to variation in the c/a ratio. It has been highlighted in study[60] that, in case of systems displaying non-stoichiometry and strain in the V_2O_3 films the strain plays a dominant role on the global MIT feature. Moreover, it has been argued that the MIT characteristics of textured thin films is better than

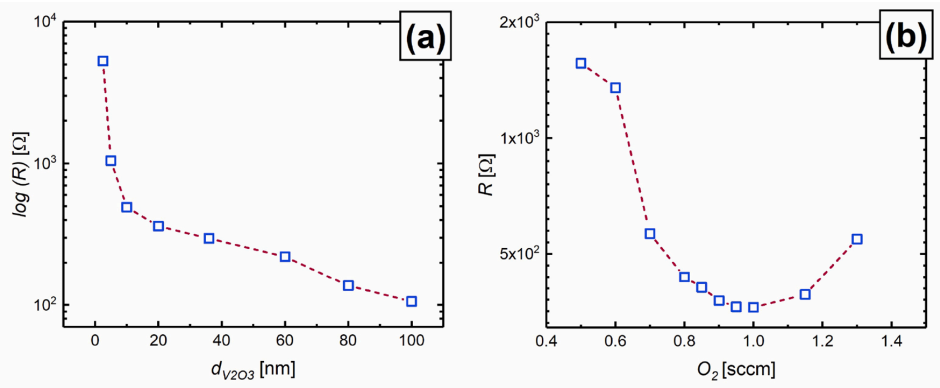

Fig. 11. Room temperature (RT) resistance as a function of varying (a) film thickness and (b) O_2 flow settings, extracted from data plotted in Fig. 10(a-d).

that demonstrated by epitaxial films. Thus, in our case for films displaying non-stoichiometric nature i.e., 0.5 to 0.7 sccm one would expect strain in the structures as a consequence of a large lattice distortion in the *a*-axis as discussed earlier. Other contributing factors affecting the *c* /*a* ratio include, for instance, differences in thermal expansion coefficient between the film and substrate for films grown at elevated temperatures, the oxygen content and the film thickness (for which the c/a ratio is found to be highest for thinner films[14]).

In contrast for films with 36 nm thickness showing good stoichiometry supported by XRD analysis (i.e. for 0.9 ± 0.5 sccm) displaying a T_{MIT} close to that of the bulk value for V_2O_3[24], it is imperative to consider that for such films the observed transition can be attributed only to Mott-type transition with little if any effect arising from strain in the films[44]. Since as has already discussed above that at such thickness (of 36 nm) the strain in films tends to relax by forming isolated nanoislands. For films deposited at an O_2 flow setting of 1.15 sccm, it has already been argued that a discharge operating in the transition regime will result in a decreased V/O ratio, i.e. shift in XRD peak position towards higher angles (Fig. 4b). Thus, the T_{MIT} shifts to higher temperatures (represented by a dotted line) close to films at lower O_2 flow settings of ~ 0.85 sccm. The film having ~ 1.3 sccm of O_2 flow, results in the formation of the VO_2 phase as evident by XRD analysis and thereby a disappearance of the MIT is observed.

4. Conclusions

In summary, V_2O_3 films were fabricated on SiO_2/Si substrates, via HiPIMS at a growth temperature of 700 °C. The MIT characteristics were found to be strongly dependent on the V_2O_3 film thickness and O_2 flow setting, which in turn determines the resultant lattice parameters of the films. It was observed that the surface morphology and the film's strain state are strongly dependent on $d_{V_2O_3}$. That is, the films with lowest thickness exhibiting two-dimensional growth show a much higher room temperature resistance, which for higher thickness(~ 36 nm) results in the formation of isolated nanoislands due to strain relaxation, increasing the magnitude and T_{MIT} of the metal-insulator transition. However, for $d_{V_2O_3}$ extending on both sides respective to 36 nm, a shift in T_{MIT} to lower temperatures was observed and attributed to increased strain i.e. *c* /*a* ratio in the films. Varying the O_2 flow settings reveals a fine-tunability of the MIT magnitude and temperature value by controlling the O_2 partial pressure governing the stoichiometry and the strain in the films.

V_2O_3 films of thickness ~ 36 nm were shown to be optimal with respect to obtaining a strong MIT transition when deposited within an O_2 flow window of ~ 0.8 to 0.95 sccm. Our results demonstrate the possibility of the incorporation of such structure in well established Si-based technologies. Nevertheless, there is still a debate on decreasing the thermal budget for fabrication of V_2O_3 films on amorphous SiO_2. As a future proof of concept, the presented issue can be overcome by utilizing HiPIMS discharge with increased frequency and/or power [5,61], thereby further providing a possibility of reducing the substrate temperature during fabrication as well as reducing the oxygen to obtain good stoichiometry, as previously studied in our work [4,5].

Data availability statement

The data that supports the findings of this study are available within the article.

CRediT authorship contribution statement

M.T. Sultan: Conceptualization, Data curation, Formal analysis, Funding acquisition, Investigation, Methodology, Software, Validation, Visualization, Writing – original draft. **K. Ignatova:** Data curation. **E.B. Thorsteinsson:** Formal analysis. **U.B. Arnalds:** Conceptualization, Formal analysis, Funding acquisition, Project administration, Resources, Software, Supervision, Validation, Visualization, Writing – review & editing.

Declaration of Competing Interest

There is no conflict of interest to disclose.

Acknowledgements

This work was supported by funding from the Icelandic Research Fund Grant Nos. 207111-051 and 218029-051.

References

[1] J. Brockman, M.G. Samant, K.P. Roche, S.S. Parkin, Substrate-induced disorder in v_2o_3 thin films grown on annealed c-plane sapphire substrates, Appl Phys Lett 101 (5) (2012) 051606, https://doi.org/10.1063/1.4742160.
[2] D. Wickramaratne, N. Bernstein, I.I. Mazin, Role of defects in the metal-insulator transition in VO_2 and v_2o_3, Physical Review B 99 (21) (2019) 214103, https://doi.org/10.1103/PhysRevB.99.214103.
[3] J. Sakai, M. Bavencoffe, B. Negulescu, P. Limelette, J. Wolfman, A. Tateyama, H. Funakubo, Strain-induced resistance change in v_2o_3 films on piezoelectric ceramic disks, J Appl Phys 125 (11) (2019) 115102, https://doi.org/10.1063/1.5083941.
[4] E.B. Thorsteinsson, S. Shayestehaminzadeh, A.S. Ingason, F. Magnus, U.B. Arnalds, Controlling metal-insulator transitions in reactively sputtered vanadium sesquioxide thin films through structure and stoichiometry, Sci Rep 11 (1) (2021) 1–10, https://doi.org/10.1038/s41598-021-85397-x.
[5] M.T. Sultan, K. Ignatova, E.B. Thorsteinsson, F. Magnus, U.B. Arnalds, Structural and electrical properties of V2O3 thin films on c-plane al2o3 fabricated by reactive-Hipims and dcms techniques, J Phys D Appl Phys 54 (42) (2021), https://doi.org/10.1088/1361-6463/ac1463.

[6] L. Dillemans, R.R. Lieten, M. Menghini, T. Smets, J.W. Seo, J.P. Locquet, Correlation between strain and the metal-insulator transition in epitaxial V_2O_3 thin films grown by Molecular Beam Epitaxy. Thin Solid Films volume 520, Elsevier, 2012, pp. 4730–4733, https://doi.org/10.1016/j.tsf.2011.11.064.

[7] E.B. Thorsteinsson, S. Shayestehaminzadeh, U.B. Arnalds, Tuning metal-insulator transitions in epitaxial v_2o_3 thin films, Appl Phys Lett 112 (16) (2018) 161902, https://doi.org/10.1063/1.5023180.

[8] C. Grygiel, C. Simon, B. Mercey, W. Prellier, R. Fŕsard, P. Limelette, Thickness dependence of the electronic properties in v_2o_3 thin films, Appl Phys Lett 91 (26) (2007) 262103, https://doi.org/10.1063/1.2824465.

[9] X. Liu, R. Liu, L. Zeng, X. Huang, X. Chen, C. Zheng, Y. Xu, Q. Qian, M. Wei, Q. Chen, Facile preparation of a v_2o_3/carbon fiber composite and its application for long-term performance lithium-ion batteries, New J. Chem. 41 (13) (2017) 5380–5386, https://doi.org/10.1039/c7nj00320j.

[10] N. Hassan, J. Riaz, M.T. Qureshi, A. Razaq, M. Rahim, A.M. Toufiq, A. Shakoor, Vanadium oxide (v_2o_3) for energy storage applications through hydrothermal route, Journal of Materials Science: Materials in Electronics 29 (18) (2018) 16021–16026, https://doi.org/10.1007/s10854-018-9689-5.

[11] P. Homm, M. Menghini, J.W. Seo, S. Peters, J.P. Locquet, Room temperature mott metal-insulator transition in v_2o_3 compounds induced via strain-engineering, APL Mater 9 (2) (2021) 021116, https://doi.org/10.1063/5.0035865.

[12] J. Brockman, N.P. Aetukuri, T. Topuria, M.G. Samant, K.P. Roche, S.S. Parkin, Increased metal-insulator transition temperatures in epitaxial thin films of v_2o_3 prepared in reduced oxygen environments, Appl Phys Lett 98 (15) (2011) 152105, https://doi.org/10.1063/1.3574910.

[13] B.S. Allimi, M. Aindow, S.P. Alpay, Thickness dependence of electronic phase transitions in epitaxial v_2o_3 films on (0001) litaov$_3$, Appl Phys Lett 93 (11) (2008) 112109, https://doi.org/10.1063/1.2978352.

[14] Q. Luo, Q. Guo, E.G. Wang, Thickness-dependent metal-insulator transition in v_2o_3 ultrathin films, Appl Phys Lett 84 (13) (2004) 2337–2339, https://doi.org/10.1063/1.1690107.

[15] G.J. Kovács, D. Bürger, I. Skorupa, H. Reuther, R. Heller, H. Schmidt, Effect of the substrate on the insulator-metal transition of vanadium dioxide films, J Appl Phys 109 (6) (2011) 063708, https://doi.org/10.1063/1.3563588.

[16] H. Schuler, S. Klimm, G. Weissmann, C. Renner, S. Horn, Influence of strain on the electronic properties of epitaxial v_2o_3 thin films, Thin Solid Films 299 (1–2) (1997) 119–124, https://doi.org/10.1016/S0040-6090(96)09399-6.

[17] Y.X. Guo, C.W. Zou, Y.F. Liu, Y.Q. Xu, X.L. Wang, J.Y. Yu, Z.Y. Yang, F. Zhang, R. Zhou, Facile preparation of vanadium oxide thin films on sapphire(0001) by sol-gel method, J Solgel Sci Technol 70 (1) (2014) 40–46, https://doi.org/10.1007/s10971-014-3271-2.

[18] A. Rúa, K. Echeverría, B. Ayala, G.A. Goenaga, S. Lysenko, F.E. Fernández, Toward reproducible metal-insulator transition characteristics in v_2o_3 thin films sputter-deposited on glass, J Appl Phys 124 (20) (2018) 205301, https://doi.org/10.1063/1.5051195.

[19] J. Sakai, P. Limelette, H. Funakubo, Transport properties and c/a ratio of v_2o_3 thin films grown on C- and R-plane sapphire substrates by pulsed laser deposition, Appl Phys Lett 107 (24) (2015) 241901, https://doi.org/10.1063/1.4937456.

[20] P. Homm, L. Dillemans, M. Menghini, B. Van Bilzen, P. Bakalov, C.Y. Su, R. Lieten, M. Houssa, D. Nasr Esfahani, L. Covaci, F.M. Peeters, J.W. Seo, J.P. Locquet, Collapse of the low temperature insulating state in cr-doped v_2o_3 thin films, Appl Phys Lett 107 (11) (2015) 111904, https://doi.org/10.1063/1.4931372.

[21] F. Borghi, A. Podestà, M. Di Vece, C. Piazzoni, P. Milani, Cluster-assembled Materials: From Fabrication to Function. Encyclopedia of Interfacial Chemistry: Surface Science and Electrochemistry, Elsevier, 2018, pp. 417–427, https://doi.org/10.1016/B978-0-12-409547-2.12935-X.

[22] J.T. Gudmundsson, N. Brenning, D. Lundin, U. Helmersson, High power impulse magnetron sputtering discharge, Journal of Vacuum Science & Technology A: Vacuum, Surfaces, and Films 30 (3) (2012) 030801, https://doi.org/10.1116/1.3691832.

[23] D.H. Youn, J.W. Lee, B.G. Chae, H.T. Kim, S.L. Maeng, K.Y. Kang, Growth optimization and electrical characteristics of VO_2 films on amorphous SiO_2/si substrates, J Appl Phys 95 (3) (2004) 1407–1411, https://doi.org/10.1063/1.1637935.

[24] Z. Yang, C. Ko, S. Ramanathan, Oxide electronics utilizing ultrafast metal-Insulator transitions, Annu Rev Mater Res 41 (1) (2011) 337–367, https://doi.org/10.1146/annurev-matsci-062910-100347.

[25] S.J. Yun, J.W. Lim, J.S. Noh, B.G. Chae, H.T. Kim, Vanadium dioxide films deposited on amorphous SiO_2 and al_2o_3-coated si substrates by reactive RF-magnetron sputter deposition, Jpn J Appl Phys 47 (4 PART 2) (2008) 3067–3069, https://doi.org/10.1143/JJAP.47.3067.

[26] G. Sun, X. Cao, S. Long, R. Li, P. Jin, Optical and electrical performance of thermochromic v_2o_3 thin film fabricated by magnetron sputtering, Appl Phys Lett 111 (5) (2017) 053901, https://doi.org/10.1063/1.4997323.

[27] M.T. Sultan, A.V. Maraloiu, I. Stavarache, J.T. Gudmundsson, A. Manolescu, V. S. Teodorescu, M.L. Ciurea, H.G. Svavarsson, Fabrication and characterization of si1-xgex nanocrystals in as-grown and annealed structures: a comparative study thesis, Beilstein J Nanotechnol 10 (2019) 1873–1882, https://doi.org/10.3762/bjnano.10.182.

[28] P. Tejedor, V.M. Fuenzalida, F. Briones, Effect of SiO_2 buffer layers on the structure of srtio$_3$ films grown on silicon by pulsed laser deposition, Citation: J. Appl. Phys 80 (1996) 7–907, https://doi.org/10.1063/1.363198.

[29] L.V. Yakovkina, S.V. Mutilin, V.Y. Prinz, T.P. Smirnova, V.R. Shayapov, I. V. Korol'kov, E.A. Maksimovsky, N.D. Volchok, MOCVD Growth and characterization of vanadium dioxide films, J Mater Sci 52 (7) (2017) 4061–4069, https://doi.org/10.1007/s10853-016-0669-y.

[30] T. Hennen, D. Bedau, J.A. Rupp, C. Funck, S. Menzel, M. Grobis, R. Waser, D. J. Wouters, Switching speed analysis and controlled oscillatory behavior of a Cr-doped V_2O_3 threshold switching device for memory selector and neuromorphic computing application. 2019 IEEE 11th International Memory Workshop, IMW 2019, Institute of Electrical and Electronics Engineers Inc., 2019, https://doi.org/10.1109/IMW.2019.8739556.

[31] P. Salev, J. del Valle, Y. Kalcheim, I.K. Schuller, Giant nonvolatile resistive switching in a mott oxide and ferroelectric hybrid, Proceedings of the National Academy of Sciences 116 (18) (2019) 8798–8802, https://doi.org/10.1073/pnas.1822138116.

[32] U.B. Arnalds, J.S. Agustsson, A.S. Ingason, A.K. Eriksson, K.B. Gylfason, J. T. Gudmundsson, S. Olafsson, A magnetron sputtering system for the preparation of patterned thin films and in situ thin film electrical resistance measurements, Rev. Sci. Instrum. 78 (10) (2007) 103901, https://doi.org/10.1063/1.2793508.

[33] D. Lundin, J.T. Gudmundsson, N. Brenning, M.A. Raadu, T.M. Minea, A study of the oxygen dynamics in a reactive ar/o_2 high power impulse magnetron sputtering discharge using an ionization region model, J Appl Phys 121 (17) (2017) 171917, https://doi.org/10.1063/1.4977817.

[34] National bureau of standards (US) monograph 25 (108) (1983).

[35] Y.D. Ji, T.S. Pan, Z. Bi, W.Z. Liang, Y. Zhang, H.Z. Zeng, Q.Y. Wen, H.W. Zhang, C. L. Chen, Q.X. Jia, Y. Lin, Epitaxial growth and metal-insulator transition of vanadium oxide thin films with controllable phases, Appl Phys Lett 101 (7) (2012) 071902, https://doi.org/10.1063/1.4745843.

[36] H. Tada, A.E. Kumpel, R.E. Lathrop, J.B. Slanina, P. Nieva, P. Zavracky, I. N. Miaoulis, P.Y. Wong, Thermal expansion coefficient of polycrystalline silicon and silicon dioxide thin films at high temperatures, J Appl Phys 87 (9 I) (2000) 4189–4193, https://doi.org/10.1063/1.373050.

[37] B.G. Chae, H.T. Kim, S.J. Yun, B.J. Kim, Y.W. Lee, K.Y. Kang, Comparative analysis of VO2 thin films prepared on sapphire and SiO_2/si substrates by the sol-gel process, Japanese Journal of Applied Physics, Part 1: Regular Papers and Short Notes and Review Papers 46 (2) (2007) 738–743, https://doi.org/10.1143/JJAP.46.738.

[38] R.C. Cammarata, Surface and interface stress effects on the growth of thin films, Journal of Electronic Materials 1997 26:9 26 (9) (1997) 966–968, https://doi.org/10.1007/S11664-997-0232-3.

[39] J.H. Ha, H.W. Kim, Y.S. Jo, S.W. Kim, J.I. Hong, Tunable metal-insulator transition of v_2o_3 thin films strained by controlled inclusion of crystallographic defect, Applied Materials Today 22 (2021) 100984, https://doi.org/10.1016/J.APMT.2021.100984.

[40] H. Hajihoseini, E.B. Thorsteinsson, V.V. Sigurjonsdottir, U.B. Arnalds, Strained interface layer contributions to the structural and electronic properties of epitaxial v_2o_3 films, Appl Phys Lett 118 (16) (2021) 161602, https://doi.org/10.1063/5.0043941.

[41] M. Yang, Y. Yang, B. Hong, L. Wang, Z. Luo, X. Li, C. Kang, M. Li, H. Zong, C. Gao, Surface-growth-mode-induced strain effects on the metal-insulator transition in epitaxial vanadium dioxide thin films, RSC Adv 5 (98) (2015) 80122–80128, https://doi.org/10.1039/c5ra13490k.

[42] I. Berbezier, A. Ronda, J.-N. Aqua, T. Favre, Sige nanostructures, Pan Stanford Publishing, 2014, https://doi.org/10.1201/b15634.

[43] Y.J. Park, K.S. Ryu, N.G. Park, Y.S. Hong, S.H. Chang, RF-Sputtered Vanadium oxide films effect of film thickness on structural and electrochemical properties, J Electrochem Soc 149 (2002) 5–597, https://doi.org/10.1149/1.1466860.

[44] M. Querré, E. Janod, L. Cario, J. Tranchant, B. Corraze, V. Bouquet, S. Deputier, S. Cordier, M. Guilloux-Viry, M.P. Besland, Metal-insulator transitions in (V1-xcrx) 2O3 thin films deposited by reactive direct current magnetron co-sputtering, Thin Solid Films 617 (2016) 56–62, https://doi.org/10.1016/J.TSF.2015.12.043.

[45] J.A. Rupp, E. Janod, M.P. Besland, B. Corraze, A. Kindsmüller, M. Querré, J. Tranchant, L. Cario, R. Dittmann, R. Waser, D.J. Wouters, Competition between v_2o_3 phases deposited by one-step reactive sputtering process on polycrystalline conducting electrode, Thin Solid Films 705 (2020) 138063, https://doi.org/10.1016/J.TSF.2020.138063.

[46] J.A.J. Rupp, B. Corraze, M.-P. Besland, L. Cario, J. Tranchant, D.J. Wouters, R. Waser, E. Janod, Control of stoichiometry and morphology in polycrystalline v_2o_3 thin films using oxygen buffers, Journal of Materials Science 2020 55:30 55 (30) (2020) 14717–14727, https://doi.org/10.1007/S10853-020-05028-0.

[47] B.S. Allimi, S.P. Alpay, D. Goberman, T. Huang, J.I. Budnick, D.M. Pease, A. I. Frenkel, Growth of v_2o_3 thin films on a-plane (110) and c-plane (001) sapphire via pulsed-laser deposition, J Mater Res 22 (10) (2007) 2825–2831, https://doi.org/10.1557/jmr.2007.0378.

[48] D. Brassard, S. Fourmaux, M. Jean-Jacques, J.C. Kieffer, M.A. El Khakani, Grain size effect on the semiconductor-metal phase transition characteristics of magnetron-sputtered VO2 thin films, Appl Phys Lett 87 (5) (2005) 051910, https://doi.org/10.1063/1.2001139.

[49] J. Narayan, V.M. Bhosle, Phase transition and critical issues in structure-property correlations of vanadium oxide, J Appl Phys 100 (10) (2006) 103524, https://doi.org/10.1063/1.2384798.

[50] H.H. Park, T.J. Larrabee, L.B. Ruppalt, J.C. Culbertson, S.M. Prokes, Tunable electrical properties of vanadium oxide by hydrogen-Plasma-Treated atomic layer deposition, ACS Omega 2 (4) (2017) 1259–1264, https://doi.org/10.1021/acsomega.7b00059.

[51] R. Koch, D. Hu, A.K. Das, Compressive stress in polycrystalline volmer-Weber films, Phys. Rev. Lett. 94 (14) (2005) 146101, https://doi.org/10.1103/PhysRevLett.94.146101.

[52] I. Mjejri, A. Rougier, M. Gaudon, Low-Cost and facile synthesis of the vanadium oxides v_2o_3, VO_2, and v_2o_5 and their magnetic, thermochromic and electrochromic

properties, Inorg Chem 56 (3) (2017) 1734–1741, https://doi.org/10.1021/ACS.INORGCHEM.6B02880.
[53] A.P. Peter, K. Martens, G. Rampelberg, M. Toeller, J.M. Ablett, J. Meersschaut, D. Cuypers, A. Franquet, C. Detavernier, J.P. Rueff, M. Schaekers, S. Van Elshocht, M. Jurczak, C. Adelmann, I.P. Radu, Metal-insulator transition in ALD VO 2 ultrathin films and nanoparticles: morphological control, Adv Funct Mater 25 (5) (2015) 679–686, https://doi.org/10.1002/ADFM.201402687.
[54] G. Xu, X. Wang, X. Chen, L. Jiao, Facile synthesis and phase transition of v_2o_3 nanobelts, RSC Adv 5 (23) (2015) 17782–17785, https://doi.org/10.1039/C4RA13707H.
[55] L. Sutton, J. Lauzier, J. de la Venta, Magnetic properties of hybrid v_2o_3/ni composites, J Appl Phys 123 (8) (2018) 083902, https://doi.org/10.1063/1.5018586.
[56] J. de la Venta, S. Wang, T. Saerbeck, J.G. Ramírez, I. Valmianski, I.K. Schuller, Coercivity enhancement in V2O3/ni bilayers driven by nanoscale phase coexistence, Appl Phys Lett 104 (6) (2014) 062410, https://doi.org/10.1063/1.4865587.
[57] R.V. Gorev, O.G. Udalov, Micromagnetic simulation of the magnetoelastic effect in submicron structures, Physics of the Solid State 2019 61:9 61 (9) (2019) 1563–1571, https://doi.org/10.1134/S1063783419090087.
[58] W. Liang, Z. Zhuo, Y. Ji, C. Lu, M. Gao, H. Yang, C. Chen, F. Pan, Y. Lin, In-plane orientation-dependent metal-insulator transition in vanadium dioxide induced by sublattice strain engineering, npj Quantum Materials 2019 4:1 4 (1) (2019) 1–8, https://doi.org/10.1038/s41535-019-0176-x.
[59] M.M. Qazilbash, A.A. Schafgans, K.S. Burch, S.J. Yun, B.G. Chae, B.J. Kim, H. T. Kim, D.N. Basov, Electrodynamics of the vanadium oxides VO_2 and v_2o_3, Physical Review B - Condensed Matter and Materials Physics 77 (11) (2008), https://doi.org/10.1103/physrevb.77.115121.
[60] B. Qi, H.P. Gunnlaugsson, S. Ólafsson, H.P. Gislason, E.B. Thorsteinsson, U. B. Arnalds, R. Mantovan, I. Unzueta l, D.V. Zyabkin, K.B. Ram, K. Johnston, P. B. Krastev, T.E. Mølholt, H. Masenda, A.T. Martín-Luengo, D. Naidoo, J. Schell, Metal-insulator transition in crystalline v_2o_3 thin films probed at atomic-scale using emission mössbauer spectroscopy, Thin Solid Films 714 (2020) 138389, https://doi.org/10.1016/j.tsf.2020.138389.
[61] M.T. Sultan, J.T. Gudmundsson, A. Manolescu, V.S. Teodorescu, M.L. Ciurea, H. G. Svavarsson, Obtaining sige nanocrystallites between crystalline TiO_2 layers by hipims without annealing, Appl Surf Sci 511 (2020) 145552, https://doi.org/10.1016/j.apsusc.2020.145552.